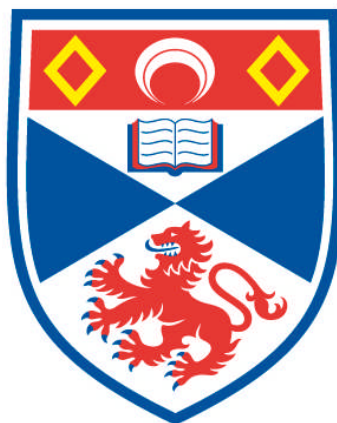


**STRUCTURAL AND CATALYTIC STUDIES OF NOVEL  
AU/NI ENANTIOSELECTIVE CATALYSTS**

**Aoife Geraldine Trant**

**A Thesis Submitted for the Degree of PhD  
at the  
University of St Andrews**



**2008**

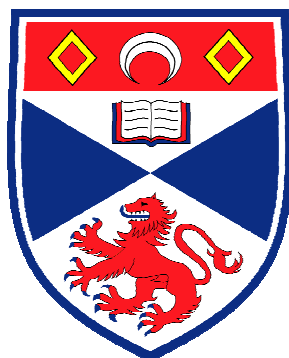
**Full metadata for this item is available in  
Research@StAndrews:FullText  
at:**

**<http://research-repository.st-andrews.ac.uk/>**

**Please use this identifier to cite or link to this item:**

**<http://hdl.handle.net/10023/854>**

**This item is protected by original copyright**



University  
of  
St Andrews

---

**STRUCTURAL AND CATALYTIC STUDIES OF  
NOVEL AU/NI ENANTIOSELECTIVE  
CATALYSTS**

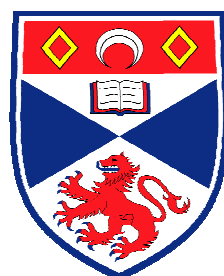
---

**AOIFE GERALDINE TRANT**

A thesis submitted in accordance with the requirements  
of the University of St-Andrews for the degree of Doctor of Philosophy.

July 2008

Funded by the EPSRC (GR/R16198/01) & University of St-Andrews  
under the supervision of Dr. C. J. Baddeley.



University  
of  
St Andrews



# DECLARATION

The work presented in this thesis is the original work of the author, under the direction of Dr. C. J. Baddeley and due reference has been made, where necessary, to the work of others. No part of this thesis which is approximately 54,000 words in length has been previously submitted to this or any other third level Institute.

**DATE:**

**SIGNATURE OF CANDIDATE:**

The author was admitted as a research student in January 2003 and as a candidate for the degree of Ph.D. in October 2003. The higher study for which was carried out in the School of Chemistry, University of St Andrews between 2003 and 2006.

**DATE:**

**SIGNATURE OF CANDIDATE:**

I, Dr. C.J. Baddeley, hereby certify that the candidate has fulfilled the conditions of the Resolution and Regulations appropriate for the degree of Ph.D. in the University of St Andrews and that the candidate is qualified to submit this thesis in application for that degree.

**DATE:**

**SIGNATURE OF SUPERVISOR:**

In submitting this thesis to the University of St Andrews, we understand that we are giving permission for it to be made available for use in accordance with the regulations of the University Library and that a copy of this thesis may be made and supplied to any *bona fide* library. This thesis has an embargo on both the printed and electronic copies for a fixed period of one year on the grounds that publication would preclude future publications.

**SIGNATURE OF SUPERVISOR:**

**SIGNATURE OF CANDIDATE:**

# ABSTRACT

Heterogeneous enantioselective catalysis strives to create new successful catalysts. One of the most researched examples is the hydrogenation  $\beta$ -ketoesters using nickel-based catalysts. A hindrance in the industrial scale-up of this enantioselective hydrogenation reaction is the lack of exact details of how chirality is bestowed onto this achiral metal surface. While a number of mechanisms have been proposed to explain the enantioselective behaviour of this system, these are predominantly based on catalytic studies. An alternative approach is through surface science studies examining the morphology, structure and composition of this catalytic system. A range of ultrahigh vacuum based model studies investigating the structure and composition of ultrathin Ni films and Ni/Au surface alloys on Au{111} using the techniques of Scanning Tunnelling Microscopy (STM) and Medium Energy Ion Scattering (MEIS) are presented in this thesis. In addition, the adsorption of the chiral modifier (*S*)-glutamic acid has been studied on these surfaces using vibrational spectroscopy (Reflection Absorption Infrared Spectroscopy (RAIRS)) and Temperature Programmed Desorption (TPD). Furthermore, MEIS has been used to investigate the influence of (*S*)-glutamic acid on the surface composition of Au/Ni model catalysts detecting effects such as adsorbate induced segregation and de-alloying behaviour.

In addition, colloidal preparative routes have been used to synthesise bimetallic Au/Ni nanoparticles supported on mesoporous silica. The catalysts are then modified by the adsorption of the chiral ligand, (*R,R*)-tartaric acid. Finally, the catalysts are tested for their activity and enantioselectivity with respect to methylacetoacetate hydrogenation. At each stage the catalysts are characterised by a combination of Extended X-ray Absorption Fine Structure (EXAFS); Transmission Electron Microscopy (TEM), Energy Dispersive X-ray Spectrometry (EDS) and Atomic Absorption Spectroscopy (AAS).

# ACKNOWLEDGEMENTS

I owe a debt of gratitude to my supervisor, Dr. Chris Baddeley, for the privilege of undertaking this research project. A thousand thanks for all your help and encouragement. You have the patience of a saint! Moreover, your enthusiasm for this subject is admirable and was certainly an additional motivation during my studies. But most of all, thanks for creating an enjoyable working environment.

My sincere thanks to my postdoc, Dr. Tim Jones, for his generous assistance throughout the entirety of my Ph.D. studies. Thanks for all your help, from teaching me how to use the UHV chambers to having a few pints in the Jigger. It was all greatly appreciated.

Huge thanks to the Surface Science group, especially Dr. Steve Francis. My thanks to Prof. Neville Richardson for use of his STM & RAIRS chamber; Dr. Paul Wright for use of his laboratory & EXAFS time; Dr. Paul Bailey & Dr. Tim Noakes (MEIS technical support); Dr. Wuzong Zhou & Mr. Ross Blackley (TEM analysis); Mrs. Sylvia Williamson (AAS analysis) and Dr. Rob Hodgkins for the helpful discussions on mesoporous solids.

My time in St. Andrews has been enjoyable due to good friends. My gratitude to the following people for all the banter and memorable times: Dee, Tim, Lorna & Bob, Peter, Steve & Paul, and flatmates Nathan and Emilie.

In addition, for those back home in Ireland:

Go raibh mile a maith agat go Ger, Carol & Laura agus Catz & Carm for all the laughs had. To my family; Aaron, Ruth, Jarlath, Saoirse, Marcus & Clara; thanks for all the encouragement and support. Last but not least, much love and appreciation to my parents, Carol & Gerald who made everything possible.

# LIST OF PUBLICATIONS

Thermal treatment of glutamic acid modified Ni nanoclusters on Au{111} leads to the formation of 1-D metal organic co-ordination networks.

A.G. Trant, T.E. Jones and C.J. Baddeley; *Journal of Physical Chemistry C*, **111**, (2007) 10534.

Growth and alloying behaviour of ultrathin Ni films on Au{111} – an investigation with Scanning Tunnelling Microscopy and Medium Energy Ion Scattering.

A.G. Trant, T.E. Jones, T.C.Q. Noakes, P.Bailey and C.J. Baddeley; *Surface Science* (in preparation).

Adsorption of (*S*)-glutamic acid on ultrathin Ni films and Ni/Au surface alloys on Au{111}.

A.G. Trant, T.E. Jones, T.C.Q. Noakes, P.Bailey and C.J. Baddeley; *Journal of Physical Chemistry C* (in preparation).

# LIST OF ACRONYMS

AAS	Atomic Absorption Spectroscopy
AES	Auger Electron Spectroscopy
bcc	body-centred cubic
EDS	Energy Dispersive X-ray analysis
EXAFS	Extended X-ray Absorption Fine Structure
fcc	Face-centred cubic
GC	Gas Chromatography
hcp	Hexagonal close packed
LEED	Low Energy Electron Diffraction
MEIS	Medium Energy Ion Scattering
RAIRS	Reflective-Adsorption Infra-Red Spectroscopy
STM	Scanning Tunnelling Microscopy
TEM	Transmission Electron Microscopy
TPD	Temperature Programmed Desorption
UHV	Ultra-High Vacuum

# LIST OF SYMBOLS

$\text{\AA}$	Ångstrom
$A$	Current
$d$	Distance
$eV$	Electron Volts
$E$	Electronic charge
$F$	Fermi function
$K$	Kelvin
$L$	Langmuir
$M$	Mass of an electron
$M$	Molarity
$ML$	Monolayer
$mL$	Millilitre
$nA$	Nanoampere
$nm$	Nanometer
$V$	Voltage
$\delta$	Delta function
$\pi$	Pi
$\mu m$	Micrometer (micron)
$\{hkl\}$	Planes of form in crystals
$[uvw]$	Indices of direction

# AIMS & OBJECTIVES

The aims & objectives of this research project are as follows:

1. To examine the relevant literature on enantioselective heterogeneous hydrogenation nickel catalysis.
2. To provide a succinct overview of the characterisation techniques utilised in this research project.
3. To examine the morphology, structure and composition of Au{111}/Ni bimetallic surfaces as a function of annealing temperature/nickel deposition temperature using Scanning Tunnelling Microscopy and Medium Energy Ion Scattering.
4. To examine the morphology, structure & composition, adsorption & desorption properties of (*S*)-glutamic acid adsorbed onto Au{111}/Ni bimetallic surfaces as a function of annealing temperature/nickel deposition temperature using Scanning Tunnelling Microscopy, Medium Energy Ion Scattering, Reflective-Adsorption Infra-Red Spectroscopy and Temperature Programmed Desorption.
5. To synthesise bimetallic Au/Ni nanoparticles supported on mesoporous silica; to chirally modify these catalysts by the adsorption of (*R,R*)-tartaric acid and to test for their activity and enantioselectivity with respect to methylacetoacetate hydrogenation.

# TABLE OF CONTENTS

Declaration.....	iii
Abstract.....	iv
Acknowledgements.....	v
List of Publications.....	vi
List of Acronyms.....	vii
List of Symbols.....	viii
Aims & Objectives.....	ix

## CHAPTER 1 INTRODUCTION

<b>Synopsis .....</b>	<b>1</b>
<b>1.1 Importance of Chirality .....</b>	<b>2</b>
<b>1.2 Motivation.....</b>	<b>4</b>
<b>1.3 Chiral Metal Surfaces .....</b>	<b>5</b>
1.3.1 Chiral supports.....	5
1.3.2 Chiral surfaces of achiral structures.....	5
1.3.3 Adsorption of chiral modifiers.....	7
<b>1.4 Hydrogenation of <math>\beta</math>-Ketoesters over Modified Nickel Catalysts .....</b>	<b>8</b>
1.4.1 Modification variables.....	9
1.4.2 Reaction variables .....	13
1.4.4 Summary of modified Ni catalysts .....	13
<b>1.5 Proposed Models of Enantioselective Hydrogenation of Modified Nickel catalysts.....</b>	<b>14</b>
<b>1.6 Surface Science Investigations of Chiral Modifiers Adsorbed onto Metal Surfaces .....</b>	<b>16</b>
1.6.1 Adsorption of ( <i>R,R</i> )-tartaric acid .....	17
1.6.2 Adsorption of ( <i>S</i> )-glutamic acid .....	22
1.6.3 Bonding of the reactant MAA to modified Ni surfaces.....	25
<b>1.7 Overview of Thesis .....</b>	<b>30</b>
<b>Bibliography .....</b>	<b>34</b>

## CHAPTER 2 EXPERIMENTAL TECHNIQUES

Synopsis .....	40
2.1 Introduction .....	41
2.2 Preparation of single crystal surfaces .....	42
2.3 Auger Electron Spectroscopy.....	43
2.4 Low Energy Electron Diffraction .....	46
2.5 Scanning Tunnelling Microscopy.....	50
2.6 Medium Energy Ion Scattering .....	53
2.7 Reflection Absorption Infrared Spectroscopy .....	63
2.8 Temperature Programmed Desorption.....	65
2.9 Transmission Electron Microscopy.....	66
2.10 Energy Dispersive X-ray Spectrometry .....	68
2.11 Extended X-ray Absorption Fine Structure.....	69
2.12 Atomic Absorption Spectroscopy .....	74
2.13 Gas Chromatography .....	76
Bibliography .....	78

## CHAPTER 3 STRUCTURAL & COMPOSITIONAL ANALYSIS OF BIMETALLIC AU{111}/NI SURFACES

Synopsis .....	80
3.1 Introduction .....	81
3.1.1 Surface alloying of immiscible metals.....	81
3.1.2 Au{111} reconstructed surfaces for metal-on-metal growth .....	84
3.1.3 Aim of research .....	86
3.2 Experimental.....	86
3.2.1 STM experiments .....	87
3.2.2 MEIS experiments .....	87
3.3 Results .....	92
3.3.1 STM studies .....	92
3.3.2 MEIS studies .....	103
3.3.2.1 Surface & subsurface composition.....	103

3.3.2.2 Surface & subsurface structure .....	115
<b>3.4 Discussion .....</b>	<b>127</b>
3.4.1 Morphology of bimetallic Au{111}/Ni surfaces.....	127
3.4.2 Composition of bimetallic Au{111}/Ni surfaces.....	129
<b>Bibliography .....</b>	<b>131</b>

## CHAPTER 4 CHARACTERISATION OF AU{111}/NI SURFACES MODIFIED WITH (S)-GLUTAMIC ACID

<b>Synopsis .....</b>	<b>134</b>
<b>4.1 Introduction .....</b>	<b>135</b>
4.1.1 Metal-organic frameworks .....	135
4.1.2 Adsorbate induced segregation at bimetallic surfaces.....	136
4.1.3 Aim of research .....	137
<b>4.2 Experimental.....</b>	<b>140</b>
3.2.1 STM & RAIRS experiments .....	140
3.2.2 TPD experiments .....	141
3.2.2 MEIS experiments .....	142
<b>4.3 Results .....</b>	<b>143</b>
<b>4.3.1 Submonolayer Deposition of Ni onto Au{111} Surfaces .....</b>	<b>143</b>
4.3.1.1 STM studies .....	143
4.3.1.2 RAIRS studies .....	147
4.3.1.3 TPD studies .....	149
<b>4.3.2 Deposition of Ultrathin Films of Ni onto Au{111} Surfaces ..</b>	<b>152</b>
4.3.2.1 RAIRS studies .....	152
4.3.2.2 TPD studies .....	153
4.3.2.2 MEIS studies .....	155
<b>4.3.3 Deposition of Ni onto Au{111} Surfaces at Elevated Temperatures.....</b>	<b>159</b>
4.3.3.1 TPD studies .....	159
4.3.3.2 MEIS studies .....	161
4.3.3.2.1 Compositional analysis .....	161
4.3.3.2.2 Structural analysis .....	163

<b>4.4</b>	<b>Discussion .....</b>	<b>167</b>
4.4.1	Morphology & proposed model of (S)-GA on Au{111}/Ni surfaces .....	167
4.4.2	Adsorption & thermal stability of (S)-GA on Au{111}/Ni surfaces .....	175
4.4.3	Adsorbate-induced segregation .....	178
<b>4.5</b>	<b>Implications for Enantioselective Catalysis.....</b>	<b>179</b>
<b>4.6</b>	<b>Summary.....</b>	<b>180</b>
	<b>Bibliography .....</b>	<b>182</b>

## CHAPTER 5 CATALYSIS BY COLLOIDS

	<b>Synopsis .....</b>	<b>186</b>
<b>5.1</b>	<b>Introduction.....</b>	<b>187</b>
5.1.1	Mesoporous silica supports .....	188
5.1.2	Bimetallic Au/Ni catalysis.....	190
5.1.3	Aim of research.....	191
<b>5.2</b>	<b>Experimental.....</b>	<b>192</b>
5.2.1	Preparation of SBA-15.....	192
5.2.2	Co-impregnation & co-reduction of Au/Ni supported colloids ...	193
5.2.2.1	Turkevich method .....	193
5.2.2.2	Impregnation .....	194
5.2.2.3	Hydrazine hydrate reduction .....	194
5.2.2.4	Hydrogen reduction .....	194
5.2.3	Modification of Au/Ni nanoparticles .....	195
5.2.4	Catalytic testing.....	195
<b>5.3</b>	<b>Results .....</b>	<b>196</b>
5.3.1	<b>TEM &amp; EDS studies .....</b>	<b>196</b>
5.3.1.1	Turkevich method .....	196
5.3.1.2	Hydrazine hydrate reduction .....	199
5.3.1.2.1	SBA-15 supported catalysts .....	199
5.3.1.2.2	SiO <sub>2</sub> supported catalysts.....	206
5.3.1.3	Hydrogen reduction .....	210
5.3.1.3.1	SBA-15 supported catalysts .....	210

5.3.1.3.2 SiO <sub>2</sub> supported catalysts .....	214
<b>5.3.2 EXAFS studies.....</b>	<b>217</b>
<b>5.3.3 AAS &amp; GC studies .....</b>	<b>227</b>
<b>5.4 Discussion .....</b>	<b>231</b>
5.4.1 Particle Size & morphology <i>versus</i> preparation method .....	231
5.4.2 Composition of nanoparticles <i>versus</i> preparation method .....	233
5.4.3 Influence of the support .....	236
5.4.4 Influence of gold .....	237
<b>5.5 Implications for Enantioselective Catalysis.....</b>	<b>239</b>
<b>5.6 Summary.....</b>	<b>240</b>
<b>Bibliography .....</b>	<b>242</b>

## CHAPTER 6 CONCLUSIONS & OUTLOOK

Synopsis .....	246
<b>6.1 Conclusions .....</b>	<b>247</b>
<b>6.2 Outlook .....</b>	<b>248</b>

# Chapter 1

## *Introduction*

### **SYNOPSIS**

*In the following chapter, molecular chirality is introduced and the enantioselective hydrogenation of  $\beta$ -ketoesters over nickel based catalysts is examined with particular attention to the modification and reaction variables that effect the performance of these systems. Surface science studies of amino and carboxylic acids adsorbed onto single crystal metal surfaces are discussed. In addition, a brief outline of the uses of gold as a catalytic metal is given. There are many examples where bimetallic catalysts are known to outperform their monometallic counterparts and this is considered in relation to bimetallic Au/Ni catalysis.*

## 1.1 IMPORTANCE OF CHIRALITY

Enantioselective catalysis is a topic of particular current importance. Research and technological applications of enantioselective catalysis has developed at a rapid pace during the twentieth century. One of the major triumphs of modern enantioselective catalysis is the Monsanto synthesis of the L-isomer of 3,4-dihydroxyphenylalanine, otherwise referred to as L-dopa. This is the first industrial homogenous chiral catalytic process and the product is used in the treatment of Parkinson's disease. Its importance was recently reflected by the 2001 Nobel Prize for Chemistry awarded to Knowles and Noyori for their work in enantioselective hydrogenation reactions and Sharpless for his work on enantioselective oxidation reactions.<sup>[1]</sup>

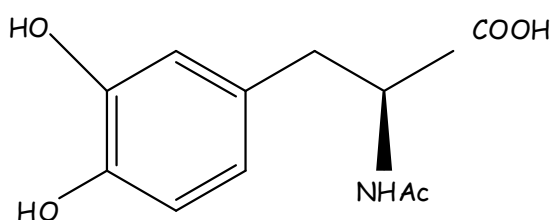


**Figure 1-1** The first product of industrial homogenous chiral catalysis, L-dopa.

Chirality is a geometric attribute and refers to molecules as a whole rather than to a particular atom. A molecule is either chiral or achiral. The word chiral is derived from the ancient Greek for 'hand' and means handedness, reflecting the left and right-handedness of molecules that are chiral in nature. An achiral molecule does not have this property. The mirror image of a chiral molecule cannot be superimposed on the molecule itself, whereas, the mirror image of an achiral molecule is identical with or superimposable on the molecule itself.

Enantiomers are a pair of chiral molecules related as non-superimposable mirror images. Neither enantiomer can be superimposed on the other by translation or rotation. An enantiomer contains a stereogenic centre. The absolute configuration of such chiral

centres can be labelled R (for rectus) or S (for sinister) as determined by the Cahn-Ingold-Prelog rules.

From a practical perspective, the importance of molecular chirality arises from the fact that two enantiomers can have the same physical properties such as melting point, boiling point and density but may possess different biological effects. Limonene (4-isopropenyl-1-methyl-1-cyclohexene), for example, is a chiral molecule and exists as a pair of enantiomers as illustrated in figure 1-2. The two enantiomers of limonene differ greatly. One form smells of lemons but the other of oranges.

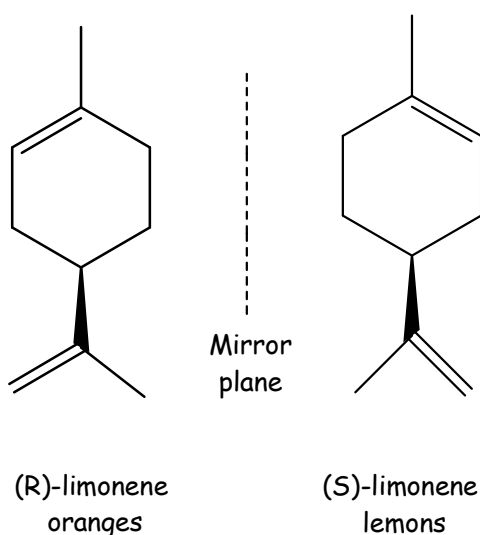


**Figure 1-2** Two enantiomers of limonene.

While there are examples, where both enantiomers of a pharmaceutical drug have similar therapeutic properties, for instance ibuprofen; there are cases where one of the enantiomers can cause serious side effects. The Parkinson's disease drug L-dopa is marketed in the enantiomerically pure form because the D-form causes serious side effects such as granulocytopenia (a loss of white blood cells that leaves patients prone to infections).

The most devastating example of the relationship between pharmacological activity and molecular chirality was provided by the tragic administration of thalidomide to pregnant

women in the 1950s. The drug was prescribed to counter morning sickness and was administered as a racemic mixture (equimolar concentrations of both enantiomers). Tragically, while the (*R*)-isomer had the desired anti-nausea effects, the (*S*)-form was a teratogenic and caused foetal abnormalities, such as severely underdeveloped limbs. Recent studies suggest that even the marketing of the *R*-enantiomer of the drug may not have averted the thalidomide tragedy as the drug is known to racemize within the body.<sup>[2]</sup>

## 1.2 MOTIVATION

Increasingly, pharmaceuticals and vitamins, agrochemicals, flavours and fragrances are produced as enantiomerically pure compounds. The reason for this is the often superior performance of the pure enantiomers and/or because regulations demand the evaluation of both enantiomers of a biologically active compound before its approval. This trend highlights the economical importance of the enantioselective synthesis of chiral chemicals. According to a survey by Frost & Sullivan, worldwide revenues due to chiral chemistry, which amounted to \$4.8 billion in 1999, will more than triple by 2009.<sup>[3]</sup>

The current industrial route for enantioselective processes involves either homogeneous or enzyme catalysis. However, heterogeneous catalysis would be preferable due to several practical advantages related to separation, handling, stability, recovery and re-use. Using a small amount of catalyst, large amounts of desired products can be attained selectively often with values of enantiomeric excess (ee) exceeding 95%. This is the driving force for developing heterogeneous enantioselective catalysts and research in this area has intensified.

## 1.3 CHIRAL METAL SURFACES

There are several ways to transfer chirality onto metal surfaces. The insertion of metals into chiral supports like quartz, silk and polymers is one such method. Chiral surfaces prepared from achiral bulk crystals is another. The most successful and developed method combines catalytically active metals with chiral organic molecules. The organic molecule binds to the catalyst surface and the chirality of the molecule causes the resulting functionalised catalyst to be chiral, whilst the catalytic metal shows no enantioselectivity in the absence of the chiral molecules.

### 1.3.1 CHIRAL SUPPORTS

The use of naturally occurring chiral materials such as catalytic supports was one of the very first attempts to develop heterogeneous enantioselective catalysts. Dating back to 1932, Schwab used copper, nickel, palladium and platinum on quartz to dehydrogenate racemic 2-butanol.<sup>[4]</sup> Albeit the enantioselectivity was low (<10% ee), nonetheless one enantiomer of the substrate had reacted preferentially. Chiral crystal surfaces lack a centre of symmetry. The chirality of quartz arises from the helical arrangement of corner-linked silicon dioxide (SiO<sub>2</sub>) tetrahedra in the bulk structure. More recently, palladium supported on chiral silk in the hydrogenation of benzylidene oxazolidone yielded a 66% ee.<sup>[5]</sup> While the natural chirality of these supports is evident, its application however, to enantioselective heterogeneous catalysis is problematic. Metal atoms would have to be in very close contact to the support e.g. as an epitaxial growth and such preparation techniques are not yet readily available.

### 1.3.2 CHIRAL SURFACES OF ACHIRAL STRUCTURES

Metals have achiral bulk structures. Single crystal metal surfaces exposing chiral sites of one handedness can be created by cleavage along specific planes. Cleavage of a face

centred cubic (fcc) lattice along a high Miller index plane exposes terrace-step-kink structures and it is these structures that are chiral. McFadden *et al.*,<sup>[6]</sup> were the first to demonstrate this phenomenon using silver single crystals. McFadden *et al.*, denoted  $\text{Ag}\{643\}^{\text{R}}$  and  $\text{Ag}\{643\}^{\text{S}}$  in analogy with Cahn-Ingold-Prelog rules used in the nomenclature of organic stereoisomers as highlighted in figure 1-3. These surfaces are non-superimposable mirror images of one another and are therefore chiral.

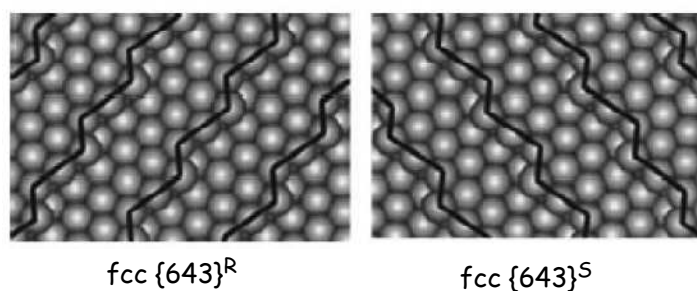


**Figure 1-3** Diagrammatic illustration of  $\text{fcc Ag}\{643\}^{\text{R}}$  and  $\text{fcc Ag}\{643\}^{\text{S}}$  Image adapted from reference [9].

Sholl carried out atomistic simulations of small chiral hydrocarbons on chiral platinum surfaces. He concluded that enantioselectivity on the aforementioned surfaces was possible as the enantiospecific adsorption energies for chiral molecules on such chiral surfaces should be observable.<sup>[7]</sup> Experimental evidence for this was provided by Attard *et al.*, with the electro-oxidation of D- and L-glucose on platinum.<sup>[8]</sup> More recently, Gellman *et al.*, examined chiral molecules adsorbed onto naturally chiral copper surfaces. R-3-methylcyclohexanone exhibited measurable enantiospecific differences in its desorption energy from  $\text{Cu}\{643\}^{\text{R}}$  and  $\text{Cu}\{643\}^{\text{S}}$  surfaces.<sup>[9]</sup> There are a number of practical limitations associated with this method of induced chirality. The percentage of chiral kinks produced is too low for enantioselective catalysis as the overall metal surface is achiral, statistically favouring the corresponding racemic reaction. Secondly, the stability of these chiral kinks under catalytic reaction conditions is questionable; it is probable the chiral kinks would reconstruct thereby losing their chirality.

### 1.3.3 ADSORPTION OF CHIRAL MODIFIERS

Conventional metal catalysts contain no inherent chirality. Chirality can be bestowed by adsorbing from solution chiral organic molecules (modifiers) onto a conventional metallic catalyst. Although the mechanisms and adsorbate/substrate interactions are not fully understood, there are two principal families of synthetically useful systems as represented in figure 1-4. Nickel catalysts modified with  $\alpha$ -hydroxy acids (e.g. tartaric acid) and  $\alpha$ -amino acids (e.g. alanine, glutamic acid etc) are useful for the liquid phase hydrogenation of  $\beta$ -functionalised ketones with optical yields of up to 95%.<sup>[10]</sup> Secondly, platinum catalysts modified with cinchona alkaloids and related modifiers are successful for the liquid phase hydrogenation of  $\alpha$ -functionalised ketones with optical yields up to 98%. Preparation of enantioselective nickel catalysts is relatively straightforward.<sup>[10]</sup> The supported nickel (or Raney Ni) is pre-treated in air at 800 K for 10 hrs. The supported catalyst is suspended in an aqueous solution of the chiral modifier at a controlled pH. Following this, the modified catalyst is washed with deionised water and filtered. The hydrogenation reaction proceeds at high hydrogen pressures in a solution of the  $\beta$ -ketoester and a reaction solvent such as tetrahydrofuran (THF).

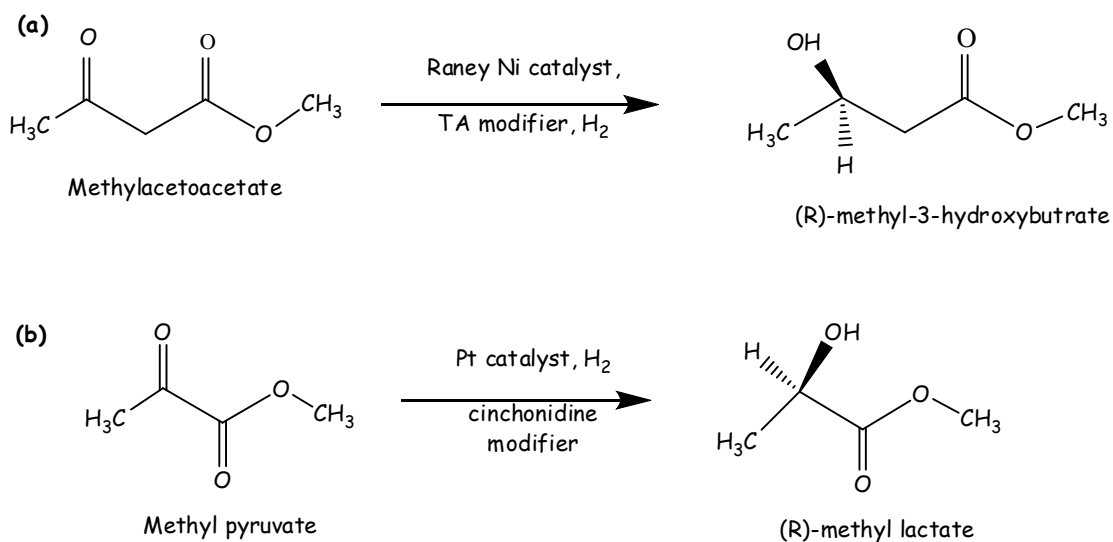


**Figure 1-4** (a) Hydrogenation of methylacetoacetate with tartaric acid modified Raney Ni catalyst giving *R*-methyl-3-hydroxybutyrate in 95% enantiomeric excess. (b) Hydrogenation of methyl pyruvate with Pt catalysts modified with cinchona alkaloids giving (*R*)-methyl lactate in 98% enantiomeric excess.<sup>[10]</sup>

## 1.4 HYDROGENATION OF $\beta$ -KETOESTERS OVER MODIFIED NICKEL CATALYSTS

The enantioselective hydrogenation of methylacetoacetate (MAA) to *R*-methyl-3-hydroxybutyrate (MHB) over modified Raney Ni catalysts gives 95% ee under optimised conditions. MHB is an important intermediate in the synthesis of a carbonic anhydrase inhibitor MK-0507 used in the treatment of glaucoma. Moreover, 3-hydroxyacids produced by hydrolysis of the chiral ester are useful building blocks in chiral synthesis.

It has taken over fifty-five years to understand the general features of the modified Raney Ni catalyst and to improve its ee from 15% to 95%. In the quest to find a nickel catalyst with high activity and enantioselectivity, considerable effort has been undertaken to screen out efficient modifiers, optimise modification and reactions conditions such as solvents, pressure and temperature. This system has been researched at length in Japan since the late 1950s primarily by Izumi,<sup>[10]</sup> Tai and Harada.<sup>[11,12]</sup> In Europe, Nitta,<sup>[13-15]</sup> Sachtler,<sup>[16,17]</sup> Webb,<sup>[18,19]</sup> and Keane<sup>[20-23]</sup> have made significant contributions. Despite the extensive

research carried out by the different groups, there remains little consensus regarding the interaction of the metallic surface with the chiral modifiers and the nature of the resulting chirally modified Ni surface. Model surface science studies by Raval and co-workers<sup>[24-27]</sup> and Baddeley and co-workers<sup>[28-35]</sup> have made significant contributions in understanding the behaviour of these chiral modifiers on achiral single crystal metal surfaces.

### 1.4.1 MODIFICATION VARIABLES

In the enantioselective conversion of MAA to MHB over modified Raney Ni and silica supported nickel catalysts, the degree of enantioselectivity is hugely dependent upon the modification conditions. The effects of temperature, time, pH and use of co-modifiers are all intertwined. There is general agreement that two kinds of enantioselective sites functioning in opposite directions exist on the catalyst surface and that the proportion of these two sites change depending upon the modifying conditions. Consequently, the overall enantioselectivity and direction of configuration may change significantly.

Early studies pioneered by Izumi focused on various chiral modifiers such as  $\alpha$ -amino and  $\alpha$ -hydroxy acids and their derivatives.<sup>[10]</sup> The direction of enantioselectivity is dependent upon the modifier used. For example, (*R*)-hydroxy and (*S*)-amino acids yield excesses of (*R*)-MHB, whereas (*S*)-hydroxy and (*R*)-amino acid modifiers yield excesses of (*S*)-MHB. Overall, tartaric acid gave the highest enantiomeric excess.

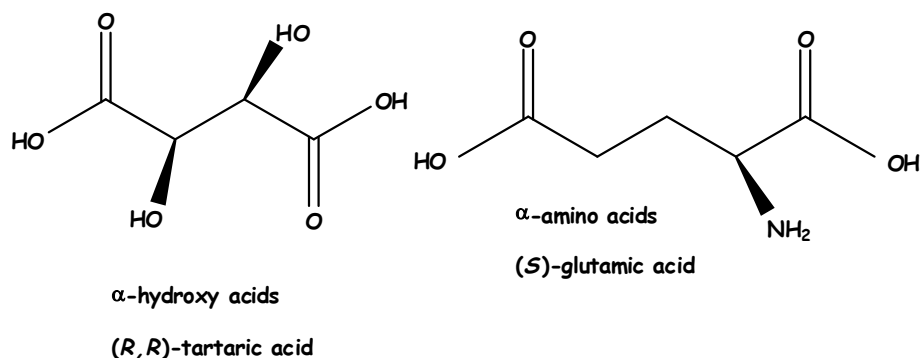


**Figure 1-6** Chiral organic modifiers used in the hydrogenation of MAA over Ni catalysts.

The temperature of the modification process can also affect the enantioselectivity in a manner that is dependent upon the modifier structure. For instance, (*S*)-glutamic acid modified below 353 K gave (*R*)-MHB whereas, when modified above 353 K (*S*)-MHB was dominant. This switch in preferred product is not observed following modification with tartaric acid.<sup>[10]</sup>

Hoek and Sachtler<sup>[16]</sup> examined the influence of temperature and the nature of the ambient atmosphere during the modification process. Using Raney Ni and Ni/SiO<sub>2</sub> catalysts, the highest enantioselectivities were achieved at a modification temperature of 373 K. There are two possible explanations for this. Firstly, at elevated temperatures a nickel-tartaric acid surface complex is formed which differs in structure from the complex formed at lower temperatures or alternatively, the same complex is formed but to a higher degree at elevated temperatures. Hoek and Sachtler also noted that catalysts modified in air had three times larger enantioselectivities than catalysts modified under hydrogen or nitrogen. More interestingly, they established that modified Ni/SiO<sub>2</sub> catalysts gave comparable enantioselectivities to Raney Ni. Their research suggests that a silica support has a relatively minor effect on the enantioselectivity of modified nickel catalysts.

Modification with slightly acidic tartaric acid solution, pH adjusted to 3.5 with sodium hydroxide gives optimum enantioselectivities for modified Raney Ni. Below pH 5, tartaric acid corrodes the surface leaching aluminium from the Raney Ni catalyst thereby

establishing a surface suitable for enantioselectivity. Residual aluminium was initially thought to be detrimental to the enantioselective process. However, studies that are more recent show it may potentially block the unmodified sites. Conversely, above pH 3, tartaric acid adsorbs onto the nickel surface as an appropriate species for enantioselectivity.<sup>[11]</sup> These factors highlight the importance of a controlled nickel surface and pH 3-5 is the optimum pH region where the favourable conditions of these two factors overlap for Raney Ni catalysts.

Keane<sup>[19]</sup> found that for Ni/SiO<sub>2</sub> catalysts, modification in slightly basic conditions yielded higher levels of enantioselectivity than observed for modification in acidic conditions. Modification is a corrosive process, characterised by the leaching of Ni into the modifying solution. Analysis of post-modification solutions by atomic absorption spectroscopy (AAS) revealed less leaching of Ni in basic conditions. It is probable that the more severe acidic tartaric acid treatment removes all weakly bound enantioselective sites during modification.

The corrosive nature of the modification process results in the extraction of nickel atoms from the metal lattice. This is evident as the colour of the solution changes from clear to light green. Extensive research to interpret the causes and effects of nickel leaching during the modification procedure has been carried out. Nitta *et al.*, showed that nickel leaching results in the selective dissolution of small < 2 nanometre (nm) particles from the catalyst as determined by electron microscopy and selective chemisorption measurements.<sup>[12]</sup> This suggests that large nickel particles are preferred for enantioselectivity.<sup>[13-15]</sup> Spectroscopic data suggests that tartaric acid adsorbs onto the metal surface as a carboxylate. Hoek and Sachtler were the first to suggest the possibility that tartaric acid interacts with the surface to form a nickel tartrate complex. This complex can either remain on the silica support to form an enantioselective site or diffuse into the modifying solution.<sup>[16]</sup> Keane and Webb

found that under identical conditions, nickel tartrate leached during modification, without any pretreatment proved both catalytically active and enantioselective.<sup>[22]</sup>

The extent of tartaric acid adsorption onto the nickel surface is dependent upon both modification time and temperature. In general, the time required for tartaric acid adsorption equilibrium decreases with increasing temperature and concentration. While modification for thirty minutes at 373 K is sufficient for Raney Ni,<sup>[12]</sup> a more lengthy treatment of an hour and a half is required for supported nickel catalysts.<sup>[22]</sup> Keane and Webb calculated that for optimum enantioselectivity a concentration of approximately 0.05-0.08 ML of tartaric acid is required (where 1 ML means 1 tartaric acid per surface Ni atom).<sup>[22]</sup>

Harada serendipitously discovered that sodium salts were effective as secondary modifying reagents.<sup>[11]</sup> Among those examined, sodium bromide (NaBr) was the best causing strong enhancement of the enantioselectivity of the catalyst even though it has no enantioselective ability itself. The inclusion of sodium bromide in the modifying reagent is well documented and its mode of action is still under debate. Harada and Izumi<sup>[10,11]</sup> proposed that sodium bromide preferentially blocked sites on the catalyst surface that are unmodified (non-enantioselective), since the ratio of modified (enantioselective) to unmodified sites determines the overall optical yield. As unmodified sites yield a racemic mixture of products, they concluded that sodium bromide is adsorbed onto these sites thereby lowering the hydrogenation activity from these areas and in doing so increasing the overall optical yield. Whilst Bostelaar *et al.*,<sup>[10,11]</sup> interpret the effects of sodium bromide to alteration of the stereochemistry of the product determining surface complex, Keane and Webb have demonstrated with thiophene-poisoned catalysts that the addition of sodium bromide as a secondary modifying reagent still results in increased enantioselectivity.<sup>[22-23]</sup> From this, they concluded that the function of sodium bromide is

not merely as a site-blocking agent. Keane further suggested that sodium bromide possibly increases the stability of the nickel tartrate complex in addition to blocking the unmodified sites on the nickel surface.

## 1.4.2 REACTION VARIABLES

The enantioselective hydrogenation of MAA is preferably carried out in the liquid phase. Hydrogenation reactions performed in gaseous phase gave significantly lower enantiomeric excesses.<sup>[10]</sup> While Izumi *et al.*, performed the hydrogenation of MAA without solvents; others used methanol, ethanol or butanol without major effects.<sup>[10,11,12]</sup> Later, semipolar aprotic solvents such as THF and ethyl acetate appeared to give much higher enantioselectivity values than alcohols. In the hydrogenation of MAA, infiltration of water significantly decreases the enantioselectivity while small amounts of carboxylic acids such as acetic acid raise the enantioselectivity. There is general agreement that optimum enantioselectivity in the Ni/tartaric acid system is achieved at a hydrogenation temperature of approximately 335 K. This temperature corresponds to dissociation of hydrogen bonding. At higher temperatures, a disruption of the hydrogen bonding between MAA and tartaric acid on the catalyst surface occurs. Transesterification and decomposition of the  $\beta$ -ketoester MAA at higher temperatures has been reported.<sup>[36-38]</sup>

## 1.4.3 SUMMARY OF MODIFIED NI CATALYSTS

Tartaric acid is the superior modifier and sodium bromide is an obligatory co-modifier for high ee's. Raney Ni is the catalyst of choice although supported nickel catalysts are suitable. Modifier pH, temperature, and time are crucial for good catalyst performance. Aprotic semipolar solvents, especially THF give the highest enantiomeric excesses. A reaction temperature of 350 K and hydrogen pressures of 90 bar yield good enantioselectivities.

## 1.5 PROPOSED MODELS FOR THE ENANTIOSELECTIVE HYDROGENATION OF TA MODIFIED NI CATALYSTS

Trying to understand the mode of action of a catalyst is a challenging endeavour. This is particularly true for heterogeneous catalysis and even more so for enantioselective catalysis. Sachtler and co-workers were the first to recognise that the modification procedure was corrosive.<sup>[17]</sup> They proposed that for enantioselectivity, the formation of a Na-Ni-tartrate complex on the surface of the catalyst was necessary. The sodium ions are obtained by the addition of NaOH to adjust the pH in the modification step and by the addition of sodium bromide. The complex has an overall octahedral arrangement, possessing available sites for the interaction of both MAA and hydrogen atoms. This seems feasible due to the leaching of nickel during the modification procedure.<sup>[17]</sup>

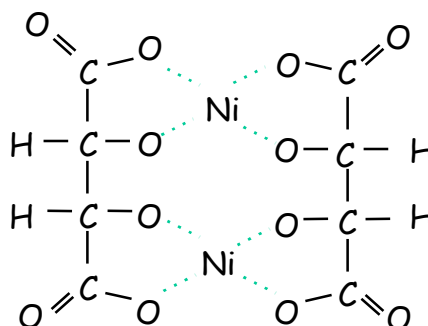
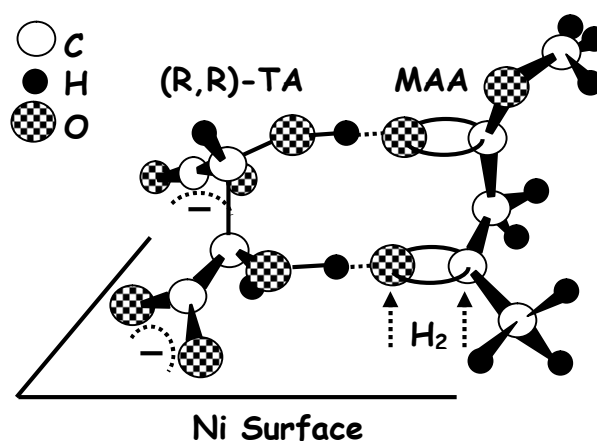


Figure 1-6 Proposed binuclear Ni-tartrate complex.<sup>[17]</sup>

In order to explain the stereochemistry of the enantioselective hydrogenation over modified Raney Ni, a one-to-one interaction model for methylacetoacetate was proposed by Tai *et al.*<sup>[11,12]</sup> based upon spectroscopic studies. This is illustrated in figure 1-7. Tartaric acid is adsorbed as a bitartrate species. One of the hydroxyl groups of tartaric acid comes close to the nickel catalyst surface and the second hydroxyl group is somewhat removed from the surface. In the hydrogenation reaction, methylacetoacetate is proposed to be

adsorbed through two hydrogen bonds between the two hydroxyl groups of tartaric acid and the two carbonyl groups of methylacetoacetate. The carbonyl group of methylacetoacetate to be hydrogenated is fixed at site 1. The methylacetoacetate thus adsorbed is hydrogenated to give the *R*-form of MHB. This model indicates that two hydrogen bonds between tartaric acid and methylacetoacetate are necessary for attaining a high optical yield.<sup>[39-41]</sup>

It is not clear why methylacetoacetate would adopt the aforementioned geometry in favour of the 180 ° rotated geometry exposing the other enantioface to the nickel surface. In addition, the role of sodium ions was not addressed.



**Figure 1-7** Mode of enantioselectivity over TA modified RNi in the hydrogenation of MAA.<sup>[11]</sup>

A template model has been proposed by Webb and Wells<sup>[19]</sup> for the enantioselective hydrogenation of pyruvate esters over cinchonidine modified platinum catalysts. Although this model is now thought to be inaccurate for the platinum catalysed system, studies by Lorenzo *et al.* (albeit on Cu{110})<sup>[26,27]</sup> indicate that this type of model may have considerable relevance in the tartaric acid modified nickel system. In the template model, adsorption of the modifier (cinchonidine) was proposed to produce a 2D array on the platinum surface. This is illustrated in figure1-9 (Site A). It is proposed that the L-shaped footprint of the modifier is not close packed thereby leaving small chiral regions on the

surface where methyl pyruvate could enter. Site A is a chiral cavity where methyl pyruvate is bound to two or three cinchonidine molecules in an ordered array. Site B represents a second model also proposed by Webb *et al.*<sup>[42]</sup> called the 1:1 interaction between methyl pyruvate and a single cinchonidine molecule. Site C is a racemic site. The orientation of the modifier imposes a chiral environment that favours one particular adsorption geometry of methyl pyruvate consequently introducing enantioselectivity to the system.

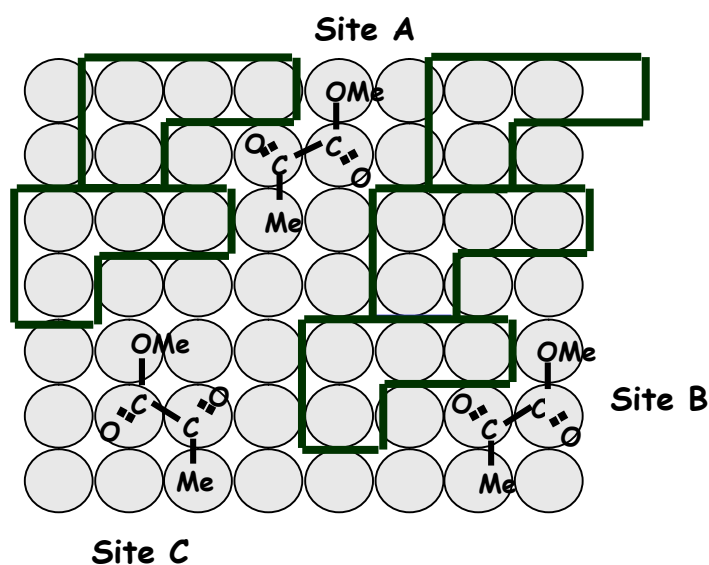


**Figure 1-8** A proposed scheme for the adsorption sites in the enantioselective hydrogenation of pyruvate esters over cinchonidine modified platinum catalysts.<sup>[19]</sup>

## 1.6 SURFACE SCIENCE INVESTIGATIONS OF CHIRAL MODIFIERS ADSORBED ONTO METAL SURFACES

Key questions relating to how a chiral organic molecule bonds to the surface, its molecular orientation and surface structure are of huge importance to enantioselective heterogeneous catalysis. A detailed understanding of catalytic mechanisms and kinetics, adsorbate-surface interactions and identification of catalytic active sites is fundamental. Understanding these processes in a microscopic or atomistic way is a formidable challenge. Industrial processes frequently operate at high temperatures and pressures. The

catalysts are in the form of highly dispersed powders, frequently involving transition metals on oxide supports and may include the addition of promoters, which greatly enhance the efficiency of the catalyst. Surface science techniques study simplified versions of these conditions. The advent of sophisticated surface science techniques such as Reflection Absorption Infrared Spectroscopy (RAIRS), Scanning Tunnelling Microscopy (STM) and Low Energy Electron Diffraction (LEED) has enabled a detailed insight into the adsorption of chiral organic molecules. This involves taking flat, usually low Miller index, faces of single crystals of the material of interest and studying the adsorption or co-adsorption of small quantities of atoms and molecules in an Ultra-High Vacuum (UHV) environment.

### **1.6.1 ADSORPTION OF (R,R)-TARTARIC ACID**

(R,R)-tartaric acid can exist in three different forms, the neutral bi-acid form, the monotartrate form where one of the carboxylic groups has deprotonated to give a carboxylate moiety and the bitartrate form, in which both acid groups have deprotonated. The carboxylic acid groups are capable of sustaining hydrogen bonds with other acid and alcohol groups, which can lead to a number of intermolecular interactions.<sup>[24]</sup>

Initial investigations in this area examined the adsorption behaviour of (R,R)-TA on Cu{110} using LEED, STM, and RAIRS by Raval, Baddeley and co-workers.<sup>[26,27]</sup> A series of ordered structures were observed dependent upon sample temperature and modifier coverage. The monotartrate species is favoured by lower adsorption temperatures (~300 K) and higher coverages, while the bitartrate species is favoured by lower coverages and higher adsorption temperatures (~350 K and above). The monotartrate species bonds to the surface via a single carboxylate functionality while the bitartrate species is doubly deprotonated and bonded with both carboxylate groups to the surface.

Although the bitartrate species is thermodynamically preferred at low coverages, the monotartrate species forms upon initial adsorption at room temperature due to kinetic factors and only upon annealing to 350 K is the bitartrate phase created. The evident temperature dependencies of (R,R)-TA on Cu{110} is important to note, as enantioselectivity in the nickel system is optimised by modification at 350 K. STM topographic images of Cu{110} exposed to a low coverage of (R,R)-TA bitartrate species at 350 K revealed self assembled rows of three, each rows stacking in parallel, forming long chains along the  $\bar{[114]}$  direction. LEED confirmed the bitartrate species adopted a (9 0, 1 2) adlayer unit cell. The adsorption of (S,S)-TA bitartrate species under the identical conditions gave the mirror image of the (R,R)-TA bitartrate species. This was indicated by the (S,S)-TA bitartrate adsorption along the  $\bar{[114]}$  direction and an observed LEED pattern corresponding to (9 0, -1 2) unit cell. Figure 1-9 shows the corresponding STM images.

Of particular interest is that this adsorption phase of (R,R)-TA or (S,S)-TA covers the entire achiral Cu{110} surface. Lorenzo *et al.*, propose in light of the template model that between the rows of the adsorbed tartaric acid, lie empty channels of exposed copper. It is at these sites which MAA could potentially dock in a preferential orientation with subsequent enantioselective hydrogenation occurring. Support for this theory is provided by the examination of the amino acid (S)-alanine on Cu{110}. A similar growth direction and arrangement covering the entire surface was observed.<sup>[43]</sup>

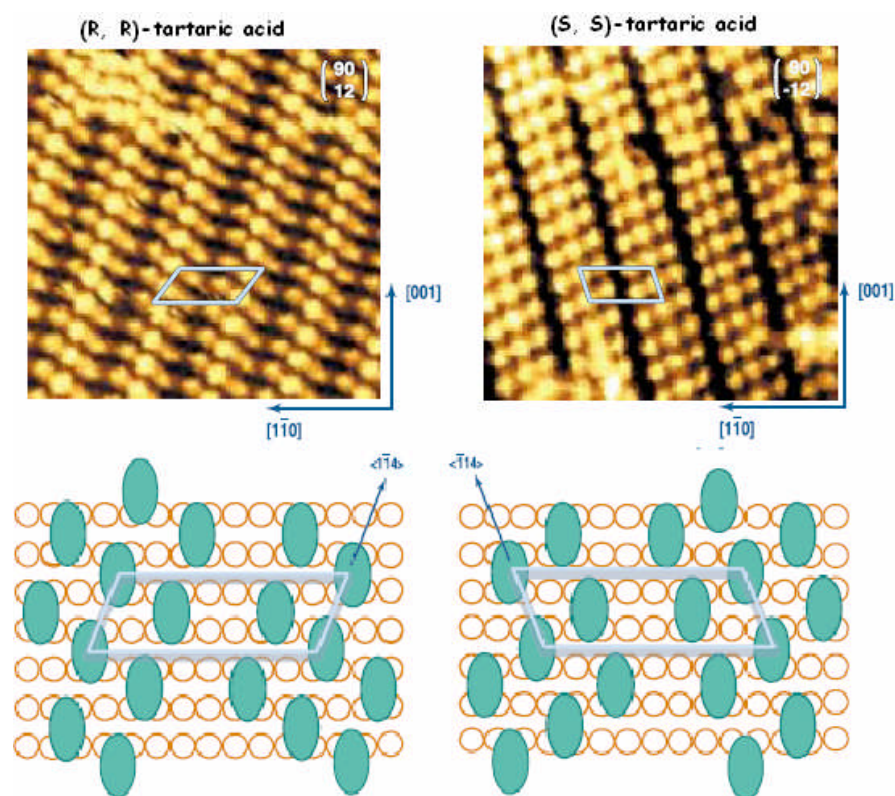


**Figure 1-9** STM images and schematic illustration of (R,R)-TA and (S,S)-TA on Cu{111} at 350 K.<sup>[28]</sup>

Wan *et al.*, examined the adsorption of TA on Cu{111} with electrochemical STM in solution. It was found that (R,R)-TA and (S,S)-TA formed ordered adlayers with mirror image equivalents on the Cu{111} surface with a (4 x 4) periodicity. From the EC-STM data, Wan *et al.* concluded that two TA molecules form a dimer through intermolecular hydrogen bonds.<sup>[44,45]</sup> Of particular interest is that each TA molecule can leave one hydroxyl group to form hydrogen bonds with other reactants e.g MAA. Therefore, (R,R)-TA and (S,S)-TA can provide a chiral template on the Cu{111} surface in the liquid phase and this is consistent with the theory of the template model in heterogeneous catalysis.

Jones and Baddeley studied the adsorption of (R,R)-TA on Ni{111} using STM, RAIRS, and Temperature Programmed Desorption (TPD).<sup>[35]</sup> Ni{111} is a more relevant system in catalytic terms, as copper has not been used in the enantioselective hydrogenation of MAA and has generally found to be a poor hydrogenation catalyst overall. In addition, the most thermodynamically stable nanoparticles are truncated octahedra exposing {111} and

{100} facets. Studies by Jones and Baddeley therefore represent the most realistic model study thus far for the chiral modification of nickel nanoparticles.

Jones and Baddeley observed that the growth of (*R,R*)-TA was dependent on sample adsorption temperature and coverage, as was the case with the Cu{110} system. This may be relevant to the dependency on modification temperature and time in the optimisation of enantioselectivity over nickel catalysts. Two ordered adlayer structures were detected; monotartrate and bitartrate species that are stabilised by intermolecular hydrogen bonding interactions. These structures were observed for sub-monolayer coverages and were confined to relatively small areas of the nickel surface.<sup>[35]</sup> This is in contrast to the Cu{110} system. Investigations by Humblot *et al.*, who examined (*R,R*)-TA on Ni{110}, also reported no long-range ordering of (*R,R*)-TA molecules.<sup>[46]</sup>

Jones and Baddeley found that with a local coverage of 0.20 ML at 300 K, areas of bare nickel surface within the monotartrate species measured  $\sim 8 \text{ \AA}$  in diameter. As an MAA molecule has a length of  $\sim 7 \text{ \AA}$ , it is possible that incoming MAA molecules could interact with the nickel sites. This is reminiscent of the template model proposed by Webb *et al.*, for the enantioselective hydrogenation of  $\beta$ -ketoesters in the Pt/ cinchona catalytic system.<sup>[42]</sup> With a local coverage of 0.18 ML at 300 K, areas of bare nickel between the monotartrate species were measured to be  $\sim 4 \text{ \AA}$ . Whilst these areas are too small for incoming MAA molecules to attach to the nickel surface, the possibility of reconstructing the overlayer is feasible. At 350 K, a bitartrate species was detected and the areas of bare nickel between overlayers ( $\sim 3 \text{ \AA}$ ) were also too small for incoming MAA molecules to attach to the nickel surface.

Humblot *et al.* investigated the adsorption of (*R,R*)-TA on Ni{110}.<sup>[46]</sup> No long range ordering of the modifier was observed. DFT theoretical simulations indicated the nickel surface atoms could undergo relaxation or reconstruction upon TA adsorption. They

proposed that chirality is bestowed onto the achiral surface by the TA modifier resulting in enantioselectivity. The chirality of the reconstructed surface would be retained even if the tartaric acid adsorbate were removed; however no concrete evidence was presented by Humblot *et al.*, to support such theories. TA modification of nickel catalysts is a corrosive process resulting in the leaching of nickel into the modifier solution. The nickel atoms are effectively etched, thereby producing a nickel tartrate species as suggested by Sachtler and co-workers.<sup>[16,17]</sup> Taking the aforementioned into consideration, it is plausible that a chiral arrangement of metal atoms may result in enantioselectivity. L-lysine on Cu{100} is another such example of adsorbate-induced reconstruction of metal surfaces.<sup>[47]</sup> More recently, the group of Besenbacher presented elegant STM studies of cysteine adsorbed onto Au{110} surface. The cysteine molecules etched the Au surface thereby inducing chirality onto the metal surface.<sup>[48]</sup>

Chiral modification of nickel catalysts occurs in aqueous solution and in air. A passivating oxide layer will cover the nickel nanoparticles as a result. Similarly, exposure to water vapour or aqueous conditions results in the formation of hydroxide-terminated surfaces. Jones and Baddeley modelled the interaction of the liquid-solid interface by investigating the adsorption (R,R)-TA on nickel oxidised surfaces (Ni{111}-NiO{111}). RAIRS data indicated the formation of nickel (II) tartrate. Jones and Baddeley concluded that the formation of such a species might be the key factor in the etching of the nickel nanoparticles during chiral modification.<sup>[29]</sup>

In previous studies, Jones and Baddeley observed with STM corrosion of the nickel surface at step edges resulting in a serrated step edge when (R,R)-TA is adsorbed onto Ni{111}. Corrosion was not observed when imaging the clean nickel surface. The etching of nickel nanoparticles by the chiral nickel (II) tartrate could possibly result in a chiral array of exposed nickel similar to the chiral step-kink surfaces described by McFadden *et*

*al.*<sup>[6]</sup> Indeed, it is feasible that these chiral arrays could partially contribute to the overall enantioselectivity observed in the catalytic reaction as the removal of nickel atoms by corrosion could leave behind chiral defects which may possess enantioselective catalytic properties.

Very interestingly, they also found that the adsorption of (R,R)-TA on oxidised nickel surfaces has a decomposition temperature  $\sim 130$  K higher than on clean Ni{111}. This suggests that the tartrate species is more thermodynamically stable on oxidised nickel.<sup>[29]</sup>

## 1.6.2 ADSORPTION OF (S)-GLUTAMIC ACID

Amino acids are similar to carboxylic acids (COOH) but with an additional amino (NH<sub>2</sub>) group, thereby providing two different functional groups which potentially could bond to a metal surface. The chemical form of amino acids can vary from cationic to zwitterionic to anionic to di-anionic according to their pH environment. As a result, it is important to determine in which chemical form the amino acid adsorbs when studying their behaviour on metal surfaces. In the gas phase, most amino acids are present in the neutral form while in the solid form at room temperature and atmospheric pressures (liquid form) they are usually present as a zwitterion. The latter form of amino acids can make strong intermolecular hydrogen bonds. All amino acids with the exception of glycine are chiral.<sup>[30]</sup>

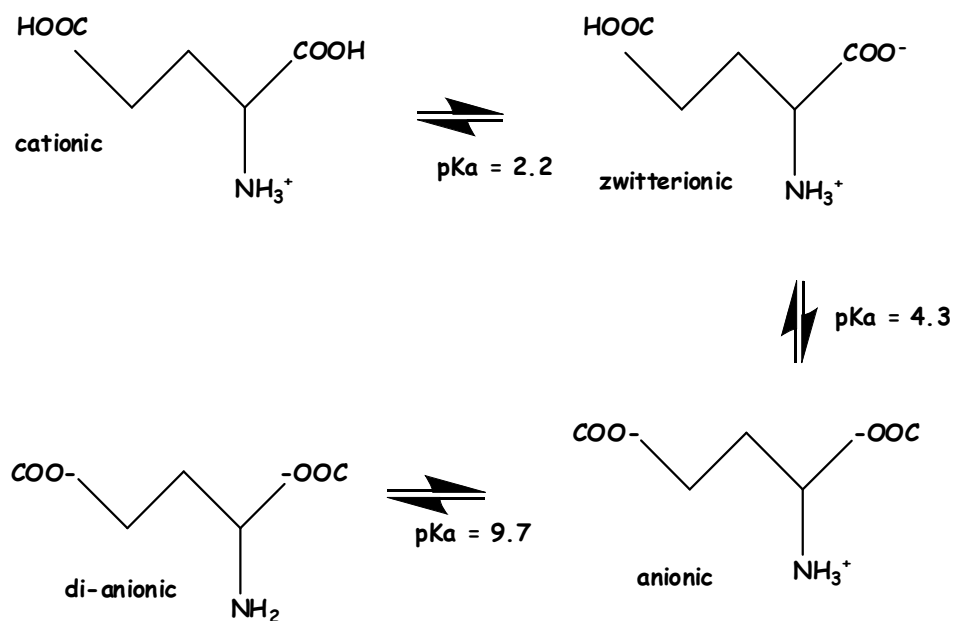
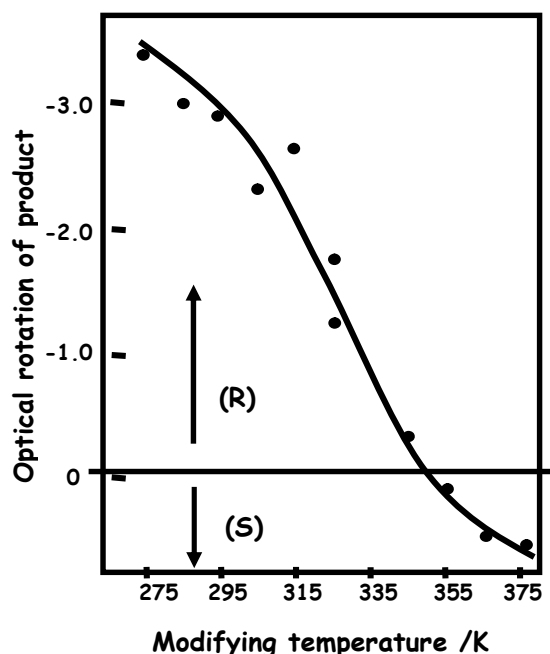


Figure 1-10 The chemical forms of amino acids.

Amino acids have been identified as potentially useful chiral modifiers for catalytic surfaces. In particular, the adsorption of glycine and alanine has been examined on single crystal metal surfaces such as copper,<sup>[49-60]</sup> gold,<sup>[61-63]</sup> silver,<sup>[64,65]</sup> platinum<sup>[65-68]</sup> and palladium.<sup>[69]</sup> Overall, the amino acid adsorption geometry was found to be coverage dependent. In all cases, the amino acid adsorbed in the anionic form with the surface-molecule interaction being via the carboxylate only; or via both the carboxylate and the –NH<sub>2</sub> group. Jones and Baddeley have more recently examined the adsorption of (*S*)-glutamic acid (herein denoted (*S*)-GA) on Ag{110}.<sup>[30]</sup> Similar ordered structures were observed between the adlayers produced on Ag{110} compared to those formed by analogous molecules on Cu{110}.

Jones and Baddeley have investigated the adsorption of (*S*)-GA on Ni{111} using RAIRS and STM as a function of adsorption temperature.<sup>[33]</sup> (*S*)-GA is an interesting modifier in that the dominant enantiomer produced in the reaction is dependent upon the modification temperature as illustrated in figure 1-11.<sup>[10]</sup> Jones and Baddeley found that low coverage adsorption of (*S*)-GA on Ni{111} at 300 K occurred in the zwitterionic form. With increasing coverage, infrared data indicated an anionic species with the amino

and carboxylate groups bonded to the Ni surface. STM images showed the initial growth of (*S*)-GA primarily occurred at step edges when adsorbed at 300 K. At higher coverages, short-ranged ordering was observed. The extent of ordering increased with annealing to 350 K. These ordered structures were limited to only 10- 20 % of the nickel surface and are too tightly packed to accommodate the reactant MAA.<sup>[53]</sup> This lack of long range ordering and adequate spacing for MAA has also been reported for (*R,R*)-TA on Ni{111}<sup>[55]</sup> and Ni{110}.<sup>[46]</sup> This is in contrast to (*S*)-GA on Ag,<sup>[30]</sup> and for (*R,R*)-TA<sup>[26,27]</sup> and several other amino acids on Cu surfaces.



**Figure 1-11** Illustration of (*S*)-glutamic acid modified below 353 K giving (*R*)-MHB whereas, when modified above 353 K, (*S*)-MHB dominates.<sup>[10]</sup>

Adsorption of (*S*)-GA at 350 K led to significant corrosion of the step edges at 350 K. Such corrosion was not evident at 300 K. This etching of the step edges is thought to induce chiral faceting of the metal surface and an example of this is lysine on Cu{100}.<sup>[47]</sup> It is conceivable that this behaviour may contribute to the unusual dependency of enantioselectivity on modification temperature in the case of (*S*)-GA. The enantioselectivity of the chiral catalyst modified at 300 K would differ to that modified at

350 K. This behaviour highlights the possible role of step-kink sites in the enantioselective process. Corrosion of the nickel nanoparticles could yield an excess of one type of chiral step-kink site thereby contributing to the overall enantioselective reaction. Jones and Baddeley further postulate that the enantioselectivity could be originating from more than one mechanism and that the different mechanisms compete with each other.<sup>[33]</sup>

### 1.6.3 BONDING OF THE REACTANT MAA TO MODIFIED NI SURFACES

MAA can exist in the diketo form or as an enol. The latter species is stabilised by the possibility of the formation of a six membered ring via hydrogen bonding between the OH group of the enol and the carbonyl group of the ester moiety. Jones and Baddeley have carried out the only examination to date on the adsorption of the  $\beta$ -ketoester, methylacetoacetate onto (*R,R*)-TA modified Ni{111} surfaces using TPD, STM, RAIRS and Photoelastic Modulation Infrared Reflection Spectroscopy (PM-RAIRS).<sup>[32, 34]</sup>

MAA absorbs mainly in its enol form at low coverages with high sticking probability at 300 K on Ni{111}. No ordered structures were observed using STM. MAA is stable on nickel surfaces up to its decomposition temperature of  $\sim$ 400 K. Adsorption at 300 K onto Ni{111}, pre-covered with a saturated dose of (*R,R*)-TA displays a low sticking probability. This is of huge importance as it questions the role of ordered modifiers in the nickel system and casts doubt on the application of the template model to this system.<sup>[32]</sup>

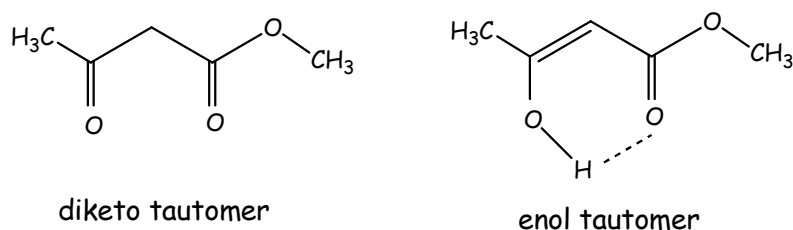


**Figure 1-12** Molecular structure of the diketo and enol tautomer of MAA.

Adsorption of MAA at low coverage (sub monolayer) of (R,R)-TA on Ni{111} is within areas of disordered tartrate species by the displacement of CO from the surface. Jones and Baddeley deem the presence of CO disrupts the intermolecular bonding between tartrate species and hence is possibly responsible for the lack of order in the adlayers at low coverage. Two ordered structures were detected upon the co-adsorption of MAA and (R,R)-TA on Ni{111}. Neither structures were previously observed in the adsorption of (R,R)-TA or MAA individually. The first, as shown in figure 1-13 (a) is a sub-molecular resolution STM image of MAA with a local coverage is 0.133 ML (0.067 ML (R,R)- TA and 0.067 ML MAA). As the coverage of MAA is increased, a second ordered structure is observed as shown in figure 1-13 (b). This structure has a local coverage is 0.17 ML (0.06 ML (R,R)- TA and 0.11 ML MAA).

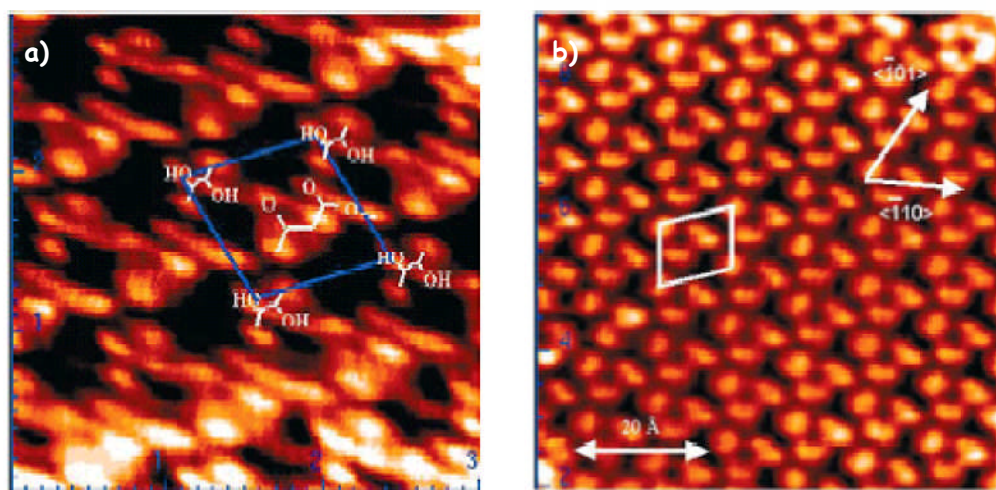


**Figure 1-13** STM images of MAA and (R,R)-tartaric acid on Ni {111} (a) corresponds to a low coverage of MAA and (b) corresponds to a high coverage of MAA.<sup>[32]</sup>

Jones and Baddeley propose that at lower coverages, MAA rearranges the initially disordered tartrate species into an ordered array held together by intermolecular interactions between the ketone group of MAA and an  $\alpha$ -hydroxy group of (R,R)-TA. It is suggested four bitartrate species sit in the corners of the unit cell with one MAA molecule fitting in the centre. No STM images have been observed for the co-crystalline

structure in which the opposite face of MAA is bound to the surface. As all MAA species are in the same orientation within this structure, hydrogenation would yield (*R*)-MHB. If this model existed on the nickel nanoparticles, under catalytic conditions, this could explain the observed enantioselectivity. Conversely, the second structure at a higher coverage (figure 1-13 b) is proposed to contain four bitartrate species sitting in the corners of the unit cell with two MAA molecules fitting in the centre. If the unit cell consists of two MAA molecules of opposite faces, hydrogenation would yield a racemic product.<sup>[32]</sup>

Jones *et al.*, also investigated the adsorption from solution, (*R,R*)-TA as a function of modifier pH and temperature and the adsorption of MAA from solution onto (*R,R*)-TA pre-modified Ni{111} surfaces using PEM-RAIRS.<sup>[34]</sup> It is not possible to adequately model the effect of modifier pH on Ni{111} surfaces in an UHV environment and consequently this solution based RAIRS study by Jones *et al.*, is a more realistic investigation. Overall, the adsorption of (*R,R*)-TA onto Ni{111} surfaces from solution results in the formation of nickel tartrate at low pH and nickel and/or sodium tartrate at high pH. Of particular interest is that several ML of nickel tartrate is formed and this is indicative of extensive etching of the nickel surface. After washing (analogous to the modification procedure), the Ni{111} surface contains submonolayer quantities of the adsorbate (*R,R*)-TA. At 350 K, the washed/ modified surface displays larger amounts of hydrogen tartrate than at 300 K. When the aforementioned surfaces are exposed to MAA, the presence of the protonated tartrate species correlates with an enhancement in the diketone to enol tautomeric ratio of MAA. Jones *et al.*, also investigated the addition of sodium bromide into the modification/ washing solution. Exposure of such surfaces to MAA resulted in an increase in the diketone to enol ratio also. Jones *et al.*, postulate that sodium bromide stabilises the diketone tautomer of MAA.<sup>[34]</sup>

Jones and Baddeley also examined the adsorption of MAA onto Ni{111} surfaces pre-modified by (*S*)-GA using UHV-RAIRS. Previous RAIRS studies by the same group examining the absorption geometry of (*S*)-GA on Ni{111} at 300 K confirmed that at low coverage, (*S*)-GA adsorbed in the zwitterionic form whilst at higher coverages in the zwitterionic and anionic form whereas with saturated coverages of (*S*)-GA adsorption was in the anionic form. No long-range ordering was observed. At the higher modification temperature of 350 K (*S*)-GA adsorbs preferentially in the anionic form.<sup>[33]</sup>

Adsorption of MAA onto Ni{111} with a saturated coverage of (*S*)-GA revealed that MAA has a sticking probability close to zero at 300 K suggesting that MAA adsorption requires metal ensembles. This is of great consequence as it casts doubt on the importance of ordered domains of chiral modifiers in the nickel catalytic system. Looking back at the work of Lorenzo *et al.* who examined the adsorption behaviour of (*R,R*)-TA on Cu{110}; it was proposed that the ordered arrays of tartrate were necessary to provide chiral docking sites for the MAA reactant molecule. However, both the current case and (*R,R*)-TA on Ni{111} suggest otherwise. The local coverages of (*R,R*)-TA on Ni {111} was in the range of 0.18-0.20 ML and similarly for (*S*)-GA on Ni{111} was in the range of 0.11 ML-0.14 ML. It is only under these high coverages that ordered structures are created. Yet calculations by Keane and Webb conclude that a tartrate coverage of 0.05 ML gives optimum enantioselectivity. This is substantially below the coverage range where Jones and Baddeley observed ordered structures of tartrate and glutamate on Ni{111}. Consequently, Jones and Baddeley propose it is not likely that ordered structures contribute to the catalytic reaction and thereby question the role of the template model to this system.<sup>[33]</sup>

Low coverage adsorption of (*S*)-GA is in the zwitterionic form at 300 K and subsequent adsorption of MAA at 300 K is in the diketo tautomeric form as detected by RAIRS. This

would lead to a geometry that would favour the formation of the (*R*)-product. RAIRS data confirmed an interaction between the two ketone groups of MAA and the  $-\text{NH}_3^+$  and the aliphatic  $-\text{COOH}$  group of glutamate.

Low coverage adsorption of (*S*)-GA at 350 K is in the anionic form. Subsequent adsorption of MAA at 300 K onto the chirally modified surface is almost exclusively in the enol tautomeric form. Jones and Baddeley propose that the enol species is adsorbed with the molecular plane perpendicular or at least slightly tilted with respect to the surface. If the former were to occur then the hydrogenation of the C=C bond required to form the chiral centre has an equal opportunity of occurring from either enantioface, producing a racemic mixture. In the catalytic system excesses of (*S*)-enantiomer is produced following modification at 350 K, taking this into account Jones and Baddeley propose that preferential tilting of the enol species induced by the interaction with adsorbed modifier leads to a preference of one enantiomeric product, which is in this case is (*S*)-GA.

Jones *et al.*, also investigated the adsorption from solution, (*S*)-GA as a function of modifier pH and temperature and the adsorption of MAA from solution onto (*S*)-GA pre-modified Ni{111}surfaces using PEM-RAIRS.<sup>[45]</sup> As previously mentioned, with (*S*)-GA, the dominant enantiomer produced in the methylacetoactate hydrogenation reaction is dependent upon the modification temperature. Modification at 273 K and pH 5 over nickel-based catalysts favours the production of the (*R*)-enantiomer. Conversely, modification at 350 K results in the formation of a racemic mixture of the (*R*)- and (*S*)-enantiomers. Increasing the temperature above 350 K results in an excess of the (*S*)-enantiomer.

Jones *et al.*, found that the modification of Ni{111} surfaces with (*S*)-GA is dependent upon the applied modification temperature and pH. At 300 K and a low pH, (*S*)-GA adsorbs in the cationic/zwitterionic form. As the pH increases, the adsorbed species

becomes progressively deprotonated. Modification at 350 K and a low pH, Jones *et al.*, report the formation of nickel glutamate. Increasing the pH results in the formation of nickel and sodium glutamate.<sup>[45]</sup>

The adsorption of MAA on (*S*)-GA pre-modified Ni{111} surfaces is also dependent upon modification temperature and pH. Jones *et al.*, report that with increasing modification temperature there is a greater tendency for enol formation. When (*S*)-GA modified nickel catalysts achieve the enantioselective production of (*R*)-MHB, MAA exists predominantly in the diketone form. In complete contrast, when (*S*)-GA modified nickel catalysts achieve the enantioselective production of (*S*)-MHB, MAA exists in the enol form. Jones *et al.*, postulate that the key to optimising enantioselectivity of the catalytic process may lie with control over the tautomeric form present on the surface.<sup>[45]</sup> This mirrors the aforementioned work of Jones *et al.*, examining (*R,R*)-TA on Ni{111} surfaces.<sup>[34]</sup>

## 1.7 OVERVIEW OF THESIS

This research project forms part of a larger project aimed at the creation of selective Au/Ni catalysts in relation to the nickel catalysed enantioselective hydrogenation of  $\beta$ -ketoesters. The nickel catalysed hydrogenation of  $\beta$ -ketoesters is one of the few successful examples of an enantioselective heterogeneous catalytic reaction. However, bare, unmodified nickel sites on the catalyst surface are known to catalyse a racemic reaction competitively with the enantioselective reaction thereby lowering the overall enantioselective yield.<sup>[10]</sup> In addition, modification of the nickel catalysts is a corrosive process and is susceptible to leaching of nickel into the modifying solution, thereby lowering the lifetime of the catalyst and consequently hindering the industrial scale-up of this enantioselective catalyst.

Due to gold's unique chemical and physical properties, it is increasingly used in a wide range of industrial reactions. These reactions include the oxidation of hydrocarbons, the water-gas shift reaction, the oxidation of ethene to vinyl acetate and conversion of vinyl ethyne to vinyl chloride, amongst others.<sup>[70]</sup> The first enantioselective homogeneous hydrogenation gold catalyst has also been discovered using a new neutral dimeric Au(I) complex bearing the 1,2-bis[(2R,5R)-2,5-dimethylphospholanebenzene] ligand for the asymmetric hydrogenation of alkenes and imines under mild reaction conditions with enantioselectivities of 95%. The catalytic activities and selectivities were comparable with those of platinum and iridium complexes derived from the same ligand.<sup>[71]</sup>

Traditionally, Au has been used in heterogeneous bimetallic catalysis to dilute the activity of the more active component and to alter the selectivity of the catalytic reaction.<sup>[72]</sup> The chemical industry requires large quantities of hydrogen for processes such as ammonia synthesis and fat hardening. The main route followed is the steam reforming of alkanes. This reaction is catalysed by supported nickel but parasitic reactions lead to the deposition of carbon with the resultant loss of activity. Ni/Au catalysts show enhanced resistance to carbon forming in the steam reforming process than monometallic nickel catalysts.<sup>[73,74]</sup> Gold is immiscible with bulk nickel so it is purely a surface phenomenon. The dissociative chemisorption of methane into methylene groups and their subsequent polymerisation to carbon requires an ensemble of several nickel atoms. Coating the nickel surface with gold reduces the probability of finding such groups. Some loss of activity is inevitable but the prolonged lifetime of the catalyst is preserved. Since gold has no activity of its own, this is a powerful demonstration of the modifying influence of gold on the surface of an active catalyst where the formation of a bulk alloy cannot occur.<sup>[73,74]</sup>

The overall objective of this thesis is to investigate the possibility of quenching the reactivity of the unmodified nickel sites by alloying with gold using a range of surface

science techniques. Alloying nickel with an inert metal such as gold, in theory, should dilute the reactivity of these unmodified sites and it is postulated result in reduced nickel leaching. It is predicted that the adsorption of the chiral modifier, (*S*)-GA, on the bimetallic Au/Ni surface will segregate nickel to the surface thereby creating active chirally modified nickel regions separated by inactive Au-rich unmodified regions. In the reverse system (Au/Ni{111}), Jones *et al.*, successfully demonstrated that the adsorption of (*R,R*)-TA onto Au/Ni{111} surfaces causes segregation of gold to the surface layer.<sup>[75]</sup> This process is referred to as adsorbate-induced segregation and is discussed in Chapter 4 of this thesis.

Chapter 2 of this thesis provides an overview of the characterisation techniques utilised in this research project while Chapter 3 examines the morphology, structure and composition of Au{111}/Ni bimetallic surfaces as a function of annealing temperature/nickel deposition temperature. The near surface structure and alloying behaviour of this system are examined using Scanning Tunnelling Microscopy and Medium Energy Ion Scattering.

Chapter 4 of this thesis examines the morphology, structure & composition, adsorption, and thermal stability of (*S*)-GA adsorbed onto Au{111}/Ni bimetallic surfaces as a function of annealing temperature/nickel deposition temperature using Scanning Tunnelling Microscopy, Reflection Absorption Infrared Spectroscopy and Temperature Programmed Desorption. The extent of adsorbate-induced segregation of nickel is estimated using Medium Energy Ion Scattering.

Chapter 5 of this thesis details the syntheses of enantioselective Au/Ni nanoparticles supported on mesoporous silica. These catalysts are modified by the adsorption of the chiral ligand, (*R,R*)-tartaric acid and tested for their activity and enantioselectivity with respect to methylacetoacetate hydrogenation. At each stage, the enantioselective catalysts

are characterised by a combination of Extended X-ray Absorption Fine Structure; Transmission Electron Microscopy; Energy Dispersive X-ray Spectrometry; Gas Chromatography and Atomic Absorption Spectroscopy. Overall conclusions of this research project and outlook is presented in Chapter 6.

**BIBLIOGRAPHY**

- [1] [www.nobel.se/chemistry/laureates/2001/chemadv.pdf](http://www.nobel.se/chemistry/laureates/2001/chemadv.pdf)
- [2] [www.ims-global.com/insight/news\\_story/0301/news\\_story\\_030116.htm](http://www.ims-global.com/insight/news_story/0301/news_story_030116.htm)
- [3] [www.pubs.acs.org/cen/coverstory/8118/8118chiral.html](http://www.pubs.acs.org/cen/coverstory/8118/8118chiral.html)
- [4] G. M. Schwab & L. Rudolph. *Naturwiss.* **20** (1932) 362.
- [5] H. U. Blaser; *Tetrahedron: Asymmetry*. **2** No. 9 (1991) 843.
- [6] C. F. McFadden, P. S. Cremer & A. J. Gellman. *Langmuir*. **12** (1996) 2483.
- [7] D. S. Sholl, A. Asthagiri & T. D. Power. *J. Phys. Chem. B* **105** (2001) 4771.
- [8] A. Ahmadi, G. Attard, J. Feliu & A. Rodes. *Langmuir*. **15** (1999) 2420.
- [9] A. J. Gellman, J. D. Horvath & M. T. Buelow. *J. Mol. Cat A: Chem.* **167**(2001) 3.
- [10] Y. Izumi. *Adv. Cat.* **32** (1983) 215.
- [11] A. Tai & T. Harada; *Tailored Metal Catalysts*. Y. Isawawa (ed.).  
D Reidel Publishing Company, (1986) 265.
- [12] A. Tai & T. Sugimura. *Chiral Catalyst Immobilisation & Recycling*.  
D.E De Vos (ed.) Wiley-VCH (2000) 173.
- [13] Y. Nitta, F. Sekine, T. Imanaka, & S. Teranishi. *Bull. Chem. Soc. Jpn.* **54** (1981) 980.
- [14] Y. Nitta, T. Imanaka, & S. Teranishi. *J. Catal.* **96** (1985) 429.
- [15] Y. Nitta & S. Teranishi. *Bull. Chem. Soc. Jpn.* **61** (1988) 295.

- [16] A. Hoek & W. M. H. Sachtler. *J. Catal.* **58** (1979) 276.
- [17] A. Groenewegen & W. M. H. Sachtler. *J. Catal.* **38** (1975) 501.
- [18] M. A. Keane & G Webb. *J. Chem. Soc. Chem. Commun.* **37** (1991) 1619.
- [19] G. Webb & P. B. Wells. *Cat. Today.* **12** (1992) 319.
- [20] M. A. Keane. *Catal. Lett.* **19** (1993) 197.
- [21] M. A. Keane. *Langmuir.* **13** (1997) 41.
- [22] M. A. Keane & G. Webb. *J. Molec. Cat.* **73** (1992) 91.
- [23] M. A. Keane. *Can. J. Chem.* **72** (1994) 372-381.
- [24] R. Raval. *Cat Tec.* **5** (2001) 12.
- [25] S. M. Barlow & R. Raval. *Surface Science Reports.* **50** (2003) 201.
- [26] M. O. Lorenzo, C. J. Baddeley, C. Muryn & R. Raval. *Nature.* **44** (2000) 376.
- [27] M. O. Lorenzo, S. Haq, T. Bertrams, P. Murray, R. Raval & C. J. Baddeley.  
*J. Phys. Chem: B.* **103** (1999) 10661.
- [28] R. Raval. *Current Opinion in Solid State and Materials Science.* **7** (2003) 67.
- [29] T. E. Jones & C. J. Baddeley. *J. Mol. Cat. A.* **216** (2004) 223.
- [30] T. E. Jones & C. J. Baddeley. *Langmuir.* **21** (2005) 9468.
- [31] T. E. Jones & C. J. Baddeley. *Surface Science.* **587** (2005) 69.
- [32] T. E. Jones & C. J. Baddeley. *Surface Science.* **519** (2002) 237.

- [33] T. E. Jones & C. J. Baddeley. *Langmuir*. **22** (2006) 148.
- [34] T. E. Jones & C. J. Baddeley. *J. Phys Chem C*. **111** (2007) 5500.
- [35] T. E. Jones & C. J. Baddeley. *Surface Science*. **513** (2002) 453.
- [36] P. Kukula & L. Cervený. *Applied Catalysis A: General*. **210** (2001) 237.
- [37] P. Kukula & L. Cervený. *Applied Catalysis A: General*. **185** (2002) 195.
- [38] P. Kukula & L. Cervený. *Applied Catalysis A: General*. **185** (2002) 195.
- [39] T. Osawa, T. Harada & A. Tai. *Catal. Today*. **37** (1997) 465.
- [40] T. Sugimura. *Catal. Surveys from Jpn*. **3** (1999) 37.
- [41] E. Klabunovskii, G. V. Smith & A. Zwigmond. *Heterogeneous Enantioselective Hydrogenation. Theory and Practice*. Catalysis by Metal Complexes. Springer. 2006
- [42] I. Sutterland, A. Ibbotson, R. Moyes & P. B. Wells. *J. Catal.* **125** (1990) 77.
- [43] S. M. Barlow, S. Louafi, D. Le Roux, J. Williams, C. Muryn, S. Haq & R. Raval. *Langmuir*. **20** (2004) 7171.
- [44] H. J. Yan, D. Wang, M. J. Han, L. J. Wan & C. L. Bai. *Langmuir*. **20** (2004) 7360.
- [45] D. Wang, H. J. Yan, Q. M. Xu, M. J. Han & L. J. Wan. *Topics Catal.* **35** (2005) 131.
- [46] V. Humblot, S. Haq, C. Muryn, W. Hofer & R. Raval. *J. Am Chem. Soc.* **124** (2002) 503.
- [47] X. Y. Zhao. *J. Am. Chem. Soc.* **122** (2000) 12584.
- [48] A. Kuhnle, T. R. Linderoth, B. Hammer & F. Besenbacher. *Nature*. **425** (2002) 891.

- [49] L. L. Atanasoska, J. C. Buchholz & G. A. Somorjai. *Surf. Sci.* **72** (1978) 189.
- [50] A. His, B. Liedberg, K. Uvdal, C. Tornkvist, P. Bodo & I. Lundstrom. *J. Colloid. Interf. Sci.* **140** (1990) 192.
- [51] S. M. Barlow, K. J. Kitching, S. Haq & N. V. Richardson. *Surf. Sci.* **401** (1998) 322.
- [52] J. Hasselstrom, O. Karis, M. Weinelt, N. Wassdahl, A. Nilsson, M. Nyberg, L. G. M. Pettersson, M. G. Samant & J. Stohr. *Surf. Sci.* **407** (1998) 221.
- [53] X. Y. Zhao, Z. Gai, R. G. Zhao, W. S. Yang & T. Sakurai. *Surf. Sci.* **424** (1999) L347.
- [54] V. Efstathiou & D. P. Woodruff. *Surf. Sci.* **531** (2003) 304.
- [55] R. B. Rankin & D. S. Sholl, *J. Phys. Chem. B.* **109** (2005) 16764.
- [56] C. Egawa, H. Iwai, M. Kabutoya & S. Oki. *Surf. Sci.* **532** (2003) 233.
- [57] I. Stensgaard. *Surf. Sci.* **545** (2003) L747
- [58] S. M. Barlow, S. Louafi, D. Le Roux, J. Williams, C. Muryn, S. Haq & R. Raval. *Langmuir.* **20** (2004) 7171.
- [59] D. I. Sayago, M. Polcik, G. Nisbet, C. L. A. Lamont & D. P. Woodruff. *Surf. Sci.* **590** (2005) 76.
- [60] S. M. Barlow, S. Louafi, D. Le Roux, J. Williams, C. Muryn, S. Haq & R. Raval. *Surf. Sci.* **590** (2005) 243.
- [61] B. Liedberg, I. Lundstrom, C. R. Wu & W. R. Salaneck. *J. Colloid. Interf. Sci.* **108** (1985) 123.

- [62] D. Holtkamp, M. Jirikowsky, M. Kempken & A. Benninghoven. *J. Vac. Sci. Technol. A*. **3** (1985) 1394.
- [63] X. Zhao, H. Yan, R. G. Zhao & W. S. Yang. *Langmuir*. **18** (2002) 3910.
- [64] W. Lange, M. Jirikowsky & A. Benninghoven. *Surf. Sci.* **136** (1984) 419.
- [65] S. Stewart & P. M. Fredericks. *Spectrochim. Acta A*. **55** (1999) 1641.
- [66] K. H. Ernst & K. Christmann. *Surf. Sci.* **224** (1989) 277.
- [67] P. Lofgren, A. Krozer, J. Lausmaa & B. Kasemo. *Surf. Sci.* **370** (1997) 277.
- [68] F. Gao, L. Zhenjun, Y. Wang, L. Burkholder & W. T. Tysoe. *J. Phys. Chem. C*. **111** (2007) 9981.
- [69] F. Gao, L. Zhenjun, Y. Wang, L. Burkholder & W. T. Tysoe. *Surf. Sci.* **601** (2007) 3276.
- [70] G. C. Bond, C. Louis & D. T. Thompson. *Catalysis by Gold. Catalytic Science Series- vol 6* (2006). Series Editor: G. J. Hutchings.
- [71] C. Gonzalez-Arellano, A. Corma, M. Iglesias & F. Sanchez. *Chem. Commun.* (2005) 3451.
- [72] G. C. Bond, C. Louis & D. T. Thompson. *Catalysis by Gold. Catalytic Science Series- vol 6* (2006). Series Editor: G. J. Hutchings.
- [73] F. Basenbacher, I. Chorkendorff, B. S. Clausen, B. Hammer, A. M. Molenbrok, J. K. Norskov & I. Stensgaard. *Science* **279** (1998) 1913.

- [74] A. M. Molenbrok & J. K. Norskov. *J. Phys. Chem.* **105** (2001) 5450.
- [75] T. E. Jones, T. C. Q. Noakes, P. Bailey & C. J. Baddeley. *J. Phys. Chem. B.* **108** (2004) 4759.

# Chapter 2

## *Experimental Techniques*

### **SYNOPSIS**

*In this chapter, a range of surface science techniques are outlined. These techniques are collectively capable of providing detailed information concerning the structure of a single crystal surface, its chemical composition, and its electronic structure. One generalisation that can be made in the study of surfaces by these techniques is that it is rarely satisfactory to use only one. For this reason, most surface science investigations utilise a multi-technique approach. In addition, a range catalytic characterisation techniques utilised in chapter five of this research project are detailed.*

## 2.1 INTRODUCTION

The aim of this chapter is to provide an overview of the surface science and catalytic characterisation techniques utilised in this research project. Heike Kamerlingh Onnes, the discoverer of superconductors, once said ‘*meten is weten*’ i.e. to measure is to know,<sup>[1]</sup> and the advent of such techniques has enabled the fascinating world of surface structure, composition and morphology to be scrutinised.

**Table 2-1** Overview of the techniques utilised in this research project.

Technique	Structure	Composition	Electronic structure	Molecular adsorption	Analytical separation
Low Energy Electron Diffraction ( <b>LEED</b> )	•				
Auger Electron Spectroscopy ( <b>AES</b> )		•			
Scanning Tunnelling Microscopy ( <b>STM</b> )	•		•		
Medium Energy Ion Scattering ( <b>MEIS</b> )	•	•			
Reflection Absorption Infrared Spectroscopy ( <b>RAIRS</b> )				•	
Temperature Programmed Desorption ( <b>TPD</b> )				•	
Transmission Electron Microscopy ( <b>TEM</b> )	•				
Energy Dispersive X-ray Spectroscopy ( <b>EDS</b> )		•			
Extended X-ray Absorption Fine Structure ( <b>EXAFS</b> )	• (local)	•			
Atomic Absorption Spectroscopy ( <b>AAS</b> )		•			
Gas Chromatography ( <b>GC</b> )					•

## 2.2 PREPARATION OF SINGLE CRYSTAL SURFACES

For structure determination, a surface must not be contaminated by adsorption of unwanted material as this could influence the applied surface science technique or even change the structure to be investigated. Therefore, it is essential that structural investigations be carried out under Ultra High Vacuum (UHV) conditions under pressures of the order of  $10^{-10}$  torr. This keeps the surface clean or in the state wanted at least for the time of the investigation. To achieve vacua in the low UHV region it is necessary to accelerate the rate at which gas molecules leave inner walls and instrument surfaces within the chamber. This is referred to as outgassing and involves raising the temperature of the entire chamber by baking. A standard bake out procedure would be 420-470 K for 12 hours. UHV ensures that gaseous species will not contaminate the sample surface during experiments. A further requirement of UHV systems is the ability to clean the sample i.e. to produce a surface that contains no more than a few percent of an atomic layer of species other than those that comprise the underlying bulk. The sample surface also needs to be well ordered to minimise defects. The main methods employed to achieve *in situ* cleaning are heating and argon ion bombardment.<sup>[2]</sup>

Heating a surface can lead to desorption of weakly bound adsorbed species particularly carbonaceous materials, oxides and water. In general, it is found that a combination of heating and argon ion bombardment is needed to obtain a completely clean surface. Argon ion bombardment typically removes several monolayers per minute by bombarding the surface with a beam of high energy argon ions (100-300 eV). Upon striking the surface, energy transfer from the argon ions to the substrate causes surface atoms to break their bonds with the substrate and desorb into the vacuum. This is referred to as sputtering.<sup>[2]</sup>

While heating will remove some impurities, it can also induce other others to appear at the surface by segregation from the bulk. Alternatively, sputtering is capable of removing the segregated impurities but tends to leave traces behind of carbon and oxygen when present as carbides or oxides. Repeated cycles of annealing and sputtering is generally required until segregants are depleted and removed from the bulk. In any case, use of single crystals requires annealing to eliminate the damage caused by argon ion bombardment and restore order.

## 2.3 AUGER ELECTRON SPECTROSCOPY

Auger Electron Spectroscopy (AES) is a surface specific technique exploiting the emission of low energy electrons via the Auger process. AES is one of the most widely used analytical techniques for compositional analysis of single crystal surfaces. The main advantage of this technique is its high sensitivity in the 5-20 Å region near the surface.<sup>[2,3]</sup>

When a beam of electrons of kinetic energy  $E_p$  is incident upon a sample surface; electrons can undergo backscattering without energy loss, termed elastic scattering. Alternatively, electrons can interact with the surface and lose energy, termed inelastic scattering. With inelastic scattering, as electrons move through the solid surface, energy loss occurs as a series of discrete events resulting in a broad spectrum of kinetic energies between zero and  $E_p$ . The energy loss follows an exponential first order decay law given by:<sup>[2,3]</sup>

$$I(d) = I_0 \exp(-d/\lambda(E)) \quad (2.1)$$

where  $I(d)$  is the measured intensity after the electron beam has travelled through the surface at distance  $d$ ;  $I_0$  is the initial beam intensity before interaction with the solid;  $\lambda$  is the inelastic mean free path for electrons of energy  $E$ .

The Inelastic Mean Free Path (IMFP)  $\lambda$ , is the distance an electron beam can travel before its intensity decays to  $1/e$  or  $(1/2.718)$  of its initial value. A small value of  $\lambda$  indicates a high probability for energy loss and the ability to travel only a short distance before being absorbed. Thus, electrons with a small IMFP are highly surface sensitive. The IMFP is only weakly dependent on the material it passes through but highly dependent on kinetic energy. Consequently, AES is a highly surface sensitive technique due to the limited free path of electrons with kinetic energies in the range of 20-1000 eV. This corresponds to 5-20 Å near the surface.<sup>[3]</sup>

AES is based upon a two step process. The first step involves formation of an electronically excited ion by exposing a sample to a beam of either x-rays or electrons. The emission of electrons creates core holes in atoms of the sample. The excited atom relaxes by filling the core hole with an electron from a higher shell (an electron level of lower binding energy) referred to as the down electron. Energy is liberated either as an x-ray photon or in an Auger transition by the emission of a second electron, the Auger electron that can escape into the vacuum as illustrated in figure 2-1.

The energy of the Auger electron is independent of the energy of the photon or electron that originally created the vacancy in the energy level and is representative of the binding energies of orbitals within the specific atoms. Their detection is used as a means of elemental analysis in AES.

Auger emissions are described in terms of the type of orbital transitions involved in the production of the Auger electron. For example, a  $KL_1L_{2,3}$  Auger transition involves an initial removal of a K electron followed by a transition of an  $L_1$  electron to the K orbital with the simultaneous ejection of a second  $L_{2,3}$  electron. Other common transitions are LMM and MNN.<sup>[2,3]</sup>

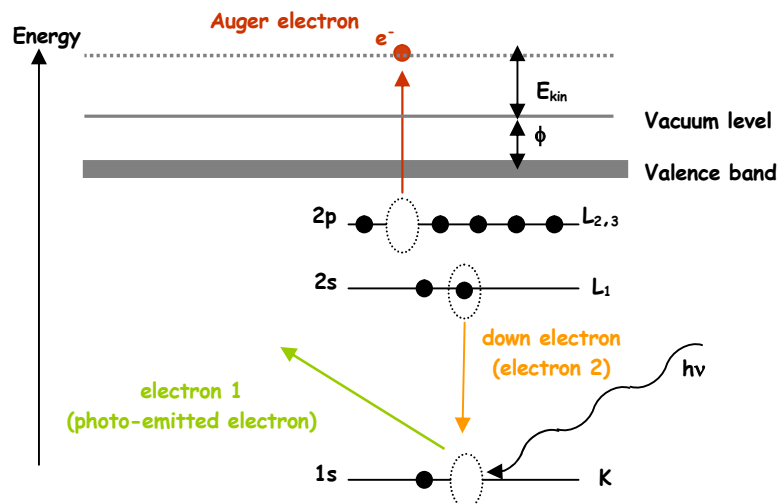


**Figure 2-1** An incident beam of x-rays/electrons causes photo-emission of a core electron. The core hole is filled by an electron transition from an electron level of lower binding energy. Consequently, energy is liberated either as a photon or in an Auger transition by the emission of an electron, the Auger electron that can escape into the vacuum with kinetic energy  $E_{kin}$ . Adapted from reference 3.

In AES, the sample is irradiated with electrons from an electron gun. The emitted secondary electrons are analysed for energy by an electron energy analyser and detected by an electron detector. The essential components of an Auger Electron Spectrometer are; an electron source, an electron energy analyser, and an electron detector.

Standard Auger electron spectra have been published for most elements of the periodic table. This way, the surface composition (quantitative Auger analysis) and cleanliness (for example, presence of the oxygen and carbon peaks) can be determined. Elements can be identified by recording the AES spectrum over a wide range generally 0-1000 eV. The kinetic energies of the intense peaks present in the spectrum are then compared with the elemental values.

Examination of atoms and molecules adsorbed onto the surface of single crystals is fundamental to surface science. In the analysis of adsorbates, the area under an Auger peak is directly proportional to surface concentration. Provided a point of reference is available i.e. a peak associated with a known surface coverage, AES may be used to

determine the amount of coverage of adsorbates. If the surface is covered with an adsorbate overlayer of thickness  $d$ , the intensity of adsorbate Auger peak  $I_s$  can be expressed as;<sup>[2,3]</sup>

$$I_s = I_o \exp(-d/\lambda \cos \theta) \quad (2.2)$$

where  $I_o$  is the intensity of the clean surface;  $\lambda$  is the IMFP of electrons;  $\theta$  is the angle between the detector and surface normal.

In this research project, the cleanliness of Au{111} surfaces was ascertained using AES i.e. ensuring that impurities such as carbon or sulphur had been removed from the single crystal surface by sufficient sputtering and annealing cleaning procedures. In addition, AES was used to estimate the coverage of nickel deposited on Au{111} surfaces. Monitoring the growth of the nickel Auger peak (61 eV & 848 eV) as a function of depositing time at constant flux enabled the estimation of nickel coverage by AES. AES experiments were carried out using an Omicron RFA Spectra LEED optics. The electron beam was produced by thermionic emission from a LaB<sub>6</sub> filament. The optics are interfaced to a PC and analysed using DAT 100 software.

## 2.4 LOW ENERGY ELECTRON DIFFRACTION

Low Energy Electron Diffraction (LEED) can reasonably claim to be the oldest of all modern surface science techniques, dating back to 1927.<sup>[4]</sup> LEED is one of the most important and commonly used techniques for determination of single crystal surfaces and structure of ordered adsorbate layers. A qualitative measurement entails recording a diffraction pattern. Analysis of the spot positions yields information on the size,

symmetry, and rotational alignment of the adsorbate unit cell with respect to the substrate unit cell.

LEED exploits electrons with energies between 20-300 eV. Electrons in this energy range possess de Broglie wavelengths ( $\lambda$ ) of 0.7-2-7 Å i.e. the same order of magnitude as lattice constants in solids. Electrons in this energy range have a small inelastic mean free path that are utilised in LEED and are highly surface sensitive.<sup>[5]</sup>

It is well known that light and electrons have both wavelike and particle-like characteristics. The relationship between their two characters is shown by Planck's equation,<sup>[5,6]</sup>

$$E = h c / \lambda \quad (2.3)$$

where E is the energy of the photon or particle; c is the velocity of light ( $\sim 3 \times 10^8 \text{ ms}^{-1}$ );  $\lambda$  represents wavelength;  $h = \text{Planck's Constant } (6.626 \times 10^{-34} \text{ J.s})$ .

A beam of monoenergetic low energy electrons falls on an ordered surface. Electrons are diffracted in all directions. The wavelength of the electrons depends on their velocity  $v$ , and consequently varies with the accelerating voltage, V, used. The relationship between the velocity and wavelength is given by the de Broglie relation;<sup>[5,6]</sup>

$$\lambda = h / m v \quad (2.4)$$

where  $m = \text{mass of an electron } (9.109 \times 10^{-31} \text{ Kg})$ ;  $h = \text{Planck's Constant } (6.626 \times 10^{-34} \text{ J.sec})$ .

The energy given to the electron is,<sup>[5,6]</sup>

$$eV = \frac{1}{2} m v^2 \quad (2.5)$$

where  $e$  is the electronic charge ( $1.6 \times 10^{-19}$  C);

Therefore the wavelength  $\lambda$  (Å) is:<sup>[5,6]</sup>

$$\lambda = h / (2 m e V)^{1/2} \quad (2.6)$$

This can be simplified to:<sup>[5,6]</sup>

$$\lambda = \left( \frac{150.6}{E(eV)} \right)^{1/2} \quad (2.7)$$

Application of equation 2.7 calculates de Broglie wavelengths in the range 2.74-0.388 Å for kinetic energies between 20-1000 eV. Therefore, electrons employed in LEED have wavelengths that are comparable with atomic spacing distances. This is the necessary condition for diffraction, enabling surface structure to be detected.

LEED experiments are conducted within a stainless steel UHV apparatus consisting of three main components; an electron gun, a sample holder for the single crystal and a detector. The detector is typically a fluorescent screen. The electrons are thermally emitted from a cathode of low work function, e.g. lanthanum hexaboride ( $\text{LaB}_6$ ) and are accelerated by a voltage variable according to the energy desired. A system of electrostatic lenses within the electron gun forms an almost parallel beam that is directed onto the sample. The sample must be an electrical conductor connected to earth to prevent charging.

Electrons are both elastically and inelastically scattered back from the surface whereby they are allowed to propagate in a field-free space between the sample and a transparent metallic grid. Before entering the detector, the elastically scattered i.e. diffracted electrons are separated from all others. This energy analysis is realised by a retarding field applied by

means of additional hemispherical grids. The first and last grids are earthed with the last grid followed by a fluorescent screen on which the diffracted electrons are post accelerated by a voltage of several kilovolts. The inner pair of grids serve as a cut off filter and are held at a negative potential. This ensures that only elastically scattered electrons reach the detector. The detector is biased at a high positive voltage (typically  $\sim 6$  keV) to accelerate the transmitted electrons to a sufficient kinetic energy to cause light emission from the fluorescent screen.

According to the direction of the beam, patterns of bright spots appear on the fluorescent screen. The LEED pattern is viewed by video camera from outside the LEED chamber. The data acquisition system is independent from the restrictions imposed by the UHV apparatus enabling the camera to be moved to any equipment as desired. The shape of the diffraction spots is determined by the type and degree of order on the surface. Consequently, spot profiles provide information about the surface order i.e. the presence and distribution of finite ordered islands or structural defects. When islands become smaller and smaller in lateral size the spots broaden more and more until eventually a diffuse distribution results on the screen. This is the case for disordered adsorption of atoms or molecules on a crystalline surface.

LEED experiments were carried out using an Omicron Spectra LEED optics with the electron beam produced by thermionic emission from an  $\text{LaB}_6$  filament. In this project, LEED was used to ensure a well-ordered  $\text{Au}\{111\}$  surface had been prepared after sputtering and annealing cleaning procedures.

## 2.5 SCANNING TUNNELLING MICROSCOPY

An important milestone in the history of surface science was the invention of the Scanning Tunnelling Microscope (STM). The STM has revolutionised the field of microscopy by stimulating an entire family of Scanning Probe Microscopes (SPM). Their unique capability to visualise surface topography and surface properties on the atomic scale has led to their application across a broad spectrum of scientific research, from solid-state physics to biological surface science.

In the scanning tunnelling microscope, a metallic tip is brought close to the surface (a few Ångstroms) and a potential difference is applied, with the consequence that a current begins to flow. This current is the tunnelling current, and it is monitored as the tip begins to scan across the surface. The direction of the current flow is determined by the polarity of the bias. If the sample is biased negative with respect to the tip, then electrons will flow from the surface to the tip. If the sample is biased positive with respect to the tip, then electrons will flow from the tip to the surface. This arises from the quantum mechanical tunnelling mechanism by which electrons can move between the tip and the sample. It permits particles to tunnel through a potential barrier, which according to classical laws of physics they could not surmount.<sup>[5,7]</sup>

The basis behind STM is the quantum mechanical phenomenon; quantum tunneling. Quantum tunneling arises where a particle is found outside a confining potential, despite it having insufficient energy to cross the barrier classically. Quantum tunneling involves the penetration of a potential barrier by an electron wave function. The potential barrier in the case of STM is a vacuum gap. In STM, as the distance between the probe tip and the sample to be analysed decreases to nanometer levels, electron wave functions of individual atoms at the base of the tip overlap locally with the atoms at the surface of the sample.

The electron wave functions at the Fermi level have a characteristic exponential inverse decay length  $K$  given by,<sup>[7]</sup>

$$K = \frac{\sqrt{2m\Phi}}{h} \quad (2.8)$$

where  $m$  is the mass of the electron ( $9.1 \times 10^{-28}$  g);  $\Phi$  is the local tunnelling barrier height (eV);  $h$  is Planck's Constant ( $6.626 \times 10^{-34}$  J . sec).

The magnitude of the tunnelling current is extremely sensitive to the gap distance between the tip and the sample, the local density of electronic states of the sample and the local barrier height. The tunnelling current decreases exponentially as the gap increases. This implies that a small change in tip to sample distance of 1 Å can cause the tunnelling current to vary by an order of magnitude or more, and this bestows a remarkable vertical sensitivity to the scanning tunnelling microscope.<sup>[5,7]</sup>

STM is a stylus type instrument. It consists of a sharp conducting probe typically called a tip, as it is literally a sharp metallic tip. The tip serves as a tunnel electrode and is scanned across a conducting sample surface by means of piezoelectric drives. The distance between the tip and the sample is approximately 1 nm ( $1 \text{ nm} = 10^{-9} \text{ m}$ ) enabling a tunnelling current to flow. This current depends exponentially on the distance between the tip and the sample and it is this exponential dependence, which allows for atomic resolution. Images obtained from STM effectively represent the surface topography. Topographical images are contours of constant surface charge densities. A lateral resolution of 0.1 Å and a vertical resolution of 0.01 Å are attainable with STM. Samples to be imaged with the STM must be electrically conductive.<sup>[5,7]</sup>

Atomic resolution in STM is infrequent and not guaranteed. Spontaneous switching of instrument resolution is a characteristic of the STM. Such switching indicates that changes

in the tip have occurred, which greatly affect the instrument's resolution; therefore tip structure plays a vital role in determining the nature of the STM image. Tips sharp enough to generate high-resolution images may be obtained straightforwardly - however, tip preparation is largely serendipitous. Tip preparation and characterisation is a significant hurdle in STM and the problem of obtaining reproducible tips with atomic resolution is not fully resolved. There are three basic requirements for tips. Firstly, short length, which reduces mechanical vibrations that will blur the image. Long tips cannot be used because of their mechanical instability during scanning. Secondly, high symmetry, which yields undistorted images. Thirdly, a sharp apex for achieving atomic resolution. Tips used are generally platinum-iridium (Pt-Ir) or tungsten (W). Pt-Ir is generally used for measurements in air due to their oxidation resistance; W is generally used in UHV because of the ease of etching, cleaning and mechanical stability.

There are two basic modes of operation with STM; constant current or constant height. Constant current mode involves a feedback loop system enabling the tip, via the piezoelectric drive, to be always at such a distance to the sample surface that the tunnelling current between the two remains constant. By recording the height of the tip, a topographical image can be obtained. The main disadvantage of the constant current mode, are the low scan speed required as crashing of the tip can occur with higher scan speeds. In constant height mode, the tip is rapidly scanned at a constant height over the sample surface while the feedback loop is turned off. The variations in tunnelling current are recorded as a function of topographic information. The main advantages to constant height mode are the increased scanning times and reduced image distortion such as thermal drifts. The main limitation to this mode of operation is that it is only applicable to atomically flat surfaces; otherwise the tip might crash into surface protrusions while scanning at high speed.<sup>[7]</sup>

STM was used in this research project to visualise the surface topography of Au{111}/Ni surfaces and of (S)-GA modified Au{111}/Ni surfaces. Experiments were carried out in constant current mode on an Omicron UHV system with an etched tungsten tip. The STM is interfaced to a PC and STM topographic images were analysed using Scala Pro 2.5 software. The base pressure of the UHV system is  $1 \times 10^{-10}$  torr.

## 2.6 MEDIUM ENERGY ION SCATTERING

Medium Energy Ion Scattering (MEIS) has the unique capability to provide a combination of both compositional and structural information within  $\sim 100$  Å of a single crystal surface. A collimated beam of hydrogen  $H^+$  or helium  $He^+$  ions is focused onto a single crystal surface along a known crystallographic direction. The energy of the positively charge ions used ranges from 50-500 keV. Scattering results as the ion beam interacts with the cores of atoms at the surface. The resultant energy and angle of the elastically scattered ions from the surface can be measured, enabling compositional and structural data to be determined. This is important in studies concerning alloy compositions. Alternatively, ions that are inelastically scattered below the surface lose energy that is proportional to the ions path length. A depth resolution of one atomic layer is feasible with MEIS.<sup>[8,9]</sup>

Two physical properties underline the MEIS technique; elastic scattering and inelastic scattering of the ion beam. The following description of scattering and inelastic scattering is adapted from references 8 and 9. Elastic scattering is based on energy and momentum conservation. If an incident ion of energy  $E_0$  and mass  $M_1$  strikes a stationary surface atom of mass  $M_2$ , it will consequently be scattered through angle  $\theta$ , with energy  $E_1$  as illustrated in figure 2-2.<sup>[8,9]</sup>

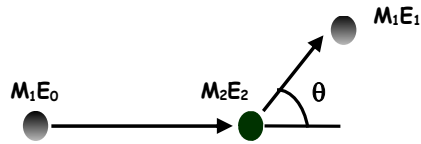


**Figure 2-2** The elastic collision between an incoming ion of mass  $M_1$  travelling with kinetic energy of  $E_0$  and the stationary atom,  $M_2$ . The energy of the incoming ion changes by a factor  $k^2$  upon collision with  $M_2$ .

The scattered ion of energy  $E_1$  equates to,<sup>[8,9]</sup>

$$E_1 = k^2 E_0 \quad (2.9)$$

$$k^2 = \left[ \frac{(M_2^2 - M_1^2 \sin^2 \theta)^{\frac{1}{2}} + M_1 \cos \theta}{M_2 + M_1} \right]^2$$

where  $E_0$  is the energy of an incident ion and  $k^2$  is the kinetic scattering factor.

The atom that is struck gains energy and recoils (assuming it was initially at rest) with energy  $E_2$  and mass  $M_2$ . The relationship between the scattered ion and surface atom is given by,<sup>[8,9]</sup>

$$E_0 = E_1 + E_2 \quad (2.10)$$

The kinetic scattering factor relates the energy of the scattered ion  $M_1 E_1$  to that of the incident ion  $M_1 E_0$ . The specific values of equation 2.9 depend upon the exact incident ion trajectory. Studies of scattered ions and their energies therefore provide a means of elemental compositional analysis. The mass of the scattering ion determines the energy of the backscattered ion and subsequently ion energy decreases with increasing scattering angle. For scattering angles of  $\theta = 90^\circ$  it is found that,<sup>[8,9]</sup>

$$k^2(90^\circ) = \frac{(M_2 - M_1)}{(M_2 + M_1)} \quad (2.11)$$

The probability density  $d\sigma / d\Omega$ , that an ion is scattered over a certain scattering angle is given by;<sup>[8,9]</sup>

$$\frac{d\sigma}{d\Omega} = F \left[ \frac{z_1 z_2 e^2}{4E \sin^2(\theta/2)} \right]^2 g(\theta, M_1, M_2) \quad (2.12)$$

where  $z_1$  and  $z_2$  are the atomic numbers of the incident ion and surface atom, respectively;  $\theta$  is the scattering angle;  $E$  is the energy applied (keV);  $e$  is the electronic charge ( $1.6 \times 10^{-19}$  Coulombs).

$F$  is a screening factor arising from the Moliere approximation that takes into account the screening of the nucleus by surrounding electrons;<sup>[8,9]</sup>

$$F = 1 - \left[ \frac{(0.0042 z_1 z_2)^{4/3}}{E} \right] \quad (2.13)$$

where  $g$  represents;<sup>[8]</sup>

$$g(\theta, M_1 M_2) \approx 1 - 2(M_1 / M_2)^2 \sin^4 \theta / 2 \quad \text{for } M_1 \ll M_2 \quad (2.14)$$

From equation 2.13 it arises that the cross section is proportional to the square of the atomic numbers  $z_1$  and  $z_2$ . Therefore, if the ion species is changed from  $H^+$  to  $He^+$  the scattering intensity increases fourfold. Secondly, the cross section is dependent upon the scattering angle  $\theta$ , and is proportional to;<sup>[8,9]</sup>

$$1 / \sin^4(\theta/2) \quad (2.15)$$

The scattering cross section for  $\theta = 90^\circ$  is four times larger than for  $\theta = 180^\circ$ . While smaller scattering angles are more advantageous than large scattering angles, mass separation in the energy spectrum is greater for larger scattering angles.

Ions as they move through a solid lose energy. The energy lost is attributed to interactions with electrons in the solid. This is referred to as stopping power. The stopping power depends upon the ion species, composition of the sample and the energy of the ion. MEIS experiments typically involve thin layers and inelastic energy losses that are sufficiently small such that the stopping power is given one constant value before the scattering process and another value after the scattering process.

Figure 2-3 represents an ion beam incoming at angle  $\theta_1$  and exiting at an angle  $\theta_2$ , relative to the sample normal. Assuming scattering occurs close to the surface and inelastic energy loss is small, the stopping power on approach  $(dE/dx)_{in}$  equals  $(dE/dx)_{E_0}$ . Similarly, the stopping power on exit  $(dE/dx)_{out}$  equals  $(dE/dx)_{k^2 E_0}$ .

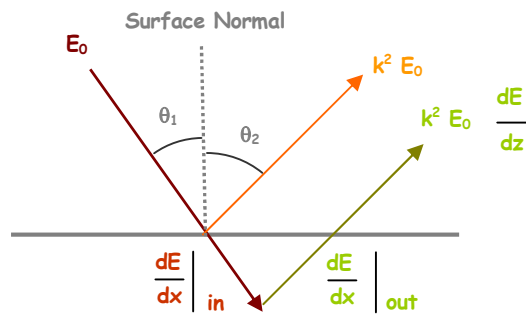


**Figure 2-3** Schematic representation of the inelastic energy loss of an ion beam beneath the surface.

The inelastic energy loss  $(dE/dz)$ , i.e. incoming path plus outgoing path per unit length measured along the surface normal can be expressed as;<sup>[8,9]</sup>

$$\frac{dE}{dz} = \frac{k^2}{\cos \theta_1} \left( \frac{dE}{dx} \right)_{E_0} + \frac{1}{\cos \theta_2} \left( \frac{dE}{dx} \right)_{k^2 E_0} \quad (2.16)$$

From this an ion scattered from a depth  $t$ , suffers an inelastic energy loss of;<sup>[8]</sup>

$$E_{loss} = \frac{dE}{dz} t \quad (2.17)$$

Energy losses in an inelastic collision depend upon the mass of the incident ion ( $M_1$ ) and the mass of the surface atom ( $M_2$ ). The energy scale is therefore a mass scale enabling elemental determination. At a given scattering angle,  $\theta$ , the ion will lose more energy in a collision with light target atoms than with heavier target atoms. As inelastic energy losses depend upon the length of the ion path in the solid, the energy scale is also a depth scale.

The determination of surface structure is achieved through shadowing, blocking and channelling effects. Aligning an incident ion beam along a low index crystallographic direction on a single crystal surface permits the top layer of atoms at the surface to be visible to the ion beam. Those atoms subsequently shadow atoms deeper into the surface as depicted in figure 2-4 (a). Only those atoms visible to the ion beam contribute to the backscattered yield. The shadow cone is a result of Coulombic interactions between the ion beam and the nucleus of the exposed atoms. The radius of the shadow cone  $R_s$ , is given by;<sup>[8,9]</sup>

$$R_s = 2(z_1 z_2 e^2 d / 4 \pi \epsilon_0 E)^{1/2} \quad (2.18)$$

where  $z_1$  and  $z_2$  are the atomic numbers of the incident ion and surface atoms respectively;  $e$  is the electronic charge ( $1.6 \times 10^{-19}$  Coulombs);  $d$  is the distance behind the atom visible to the ion beam;  $\epsilon_0$  vacuum permittivity constant;  $E$  is the beam energy (keV).

Surface layer relaxation, lattice vibrations, and adsorbate reconstructions can alter the shadow cone positions such that subsurface atoms may be illuminated by the ion beam thereby, contributing to the backscattered ion yield. Backscattering ions located beneath the surface region can be blocked from exiting the surface by other atoms. This is accomplished by aligning the detector along a low index blocking direction. This approach is referred to the use of double alignment geometry. The backscattering atom as illustrated

in figure 2-4 (b) can be considered as a point source of ions. Detecting ions across a range of scattering angles will show a range of blocking areas. With blocking, the top, top two and top three layers of atoms can contribute to the backscattered ion yield. MEIS is therefore a highly surface specific. The combining effects of shadowing and blocking enables the determination of surface structure.

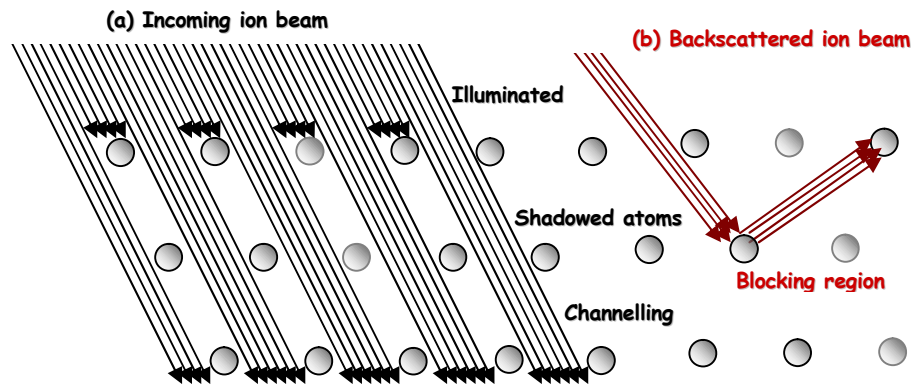


**Figure 2-4** (a) Channelling occurs when incident ions travel deep into the bulk thereby yielding information on bulk structure as the distance travelled by these ions is directly related to energy loss. With shadowing, the layer of atoms located at the surface visible to the ion beam cast a shadow cone over underlying atoms. (b) Backscattering ions located beneath the surface region can be blocked from exiting the surface by other atoms. This is referred to as blocking.

Because of small angle collisions with surface atoms, incident ions are deflected from the atomic rows into nearby channels. These non-backscattered ions can travel deep into the bulk without undergoing any hard collisions until they are either backscattered, neutralised or become heavily buried within the bulk. The backscattered ions that do reach the detector can yield information on bulk structure as the distance travelled by the ions is directly related to energy loss. This process is referred to as channelling and is illustrated in figure 2-4 (a).

MEIS experiments were carried out at the MEIS facility at Daresbury Laboratory. The facility consists of an ion source and accelerating lens (housed in a high voltage enclosure), a transfer beam line; and an experimental end station. Ions used for scattering are hydrogen  $H^+$  or helium  $He^+$  which are accelerated and focused at  $\sim 100$  keV onto the

sample. The experimental end station contains four interconnecting UHV chambers; a scattering chamber where the sample is placed, a storage chamber, a preparation chamber and a loading chamber.

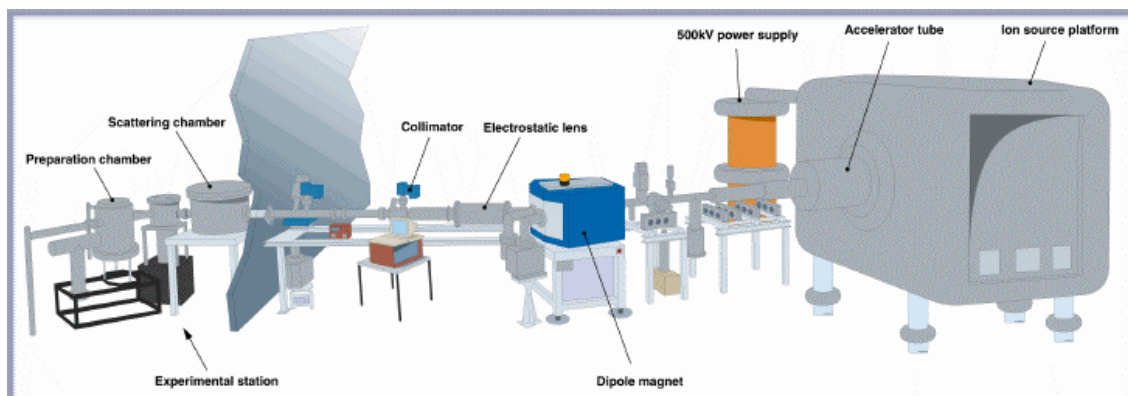


Figure 2-5 Experimental set-up of MEIS.

The ion source is a hot cathode duo-plasmatron source and is controlled from a computer console in the end station. Filament reliability is excellent with a lifetime of typically 500 hours. While the beam can be produced technically from any elemental gas, MEIS only requires  $H^+$  or  $He^+$ . The scattering chamber houses the sample goniometer, the toroidal electrostatic ion analyser, and beam current monitor. The chamber is UHV maintained at a pressure of  $10^{-10}$  torr.

A pneumatically operated gate valve connects the chamber to the beam line. The sample is fastened to a sample holder that is mounted on the sample goniometer. This is a high precision manipulator capable of lining up the sample with the beam by rotating, spinning and tilting the sample. Angular accuracies of  $\sim 0.1^\circ$  are achievable in all three directions. The storage chamber is connected via a sample transfer system to each of the other three end station chambers. Manually operated gate valves separate each end station. The sample holder can be stored on a carousel that rotates, located in the storage chamber.

The preparation chamber is a general-purpose two level chamber. The lower level is used for sample transfer and positioning; the upper level is used for sample cleaning,

preparation and characterisation (via LEED/AES). Samples are introduced into the system via a load lock chamber equipped with a sample heating stage that is used to outgas sample and holders and speed up their UHV compatibility.

The ion beam needs to be aligned along a known crystallographic direction of the Au{111} sample. Stereographic projections are used to visualise the crystallography of the different faces of the crystal. Alignment is achieved by scanning the three rotational axes of the goniometer. Each axis is scanned in turn thereby producing a plot of the integrated ion counts as a function of scattering angle. A minimum in the scan indicates where bulk alignment is optimised and the presence of channelling features.

The positions of the circles on the stereographic projection indicate the location of the channels for the Au{111} crystal. The size of the circles indicates the size and intensity of the channels. The [111] direction is the centre channel and lies parallel to the normal incident beam. Bulk alignment of the Au{111} crystal starts at this point. Adjusting the spin, rotation, and tilt and conducting a series of scans enables the required channel to be located along a specific azimuthal direction.



correct alignment of the beam and give an indication of surface layer relaxation. Energy versus ion intensity yields compositional information, useful for quantitative and qualitative elemental analysis. The analysis of the tiled data is further detailed in Chapter 3 of this thesis.

Structural information is obtained by superimposing polygons onto regions of surface/bulk on the tile and projecting the intensity contained within the polygon onto a plot of ion intensity *versus* scattering angle. Igor Pro software is used to create the polygons by calculating the energy loss the ion beam experiences as it travels through six atomic layers. This is achieved by taking into account the mass of the ion beam ( $\text{He}^+$ ) and target atoms (Au), the beam incident angle and the stopping power of the ion beam in the gold surface using the SRIM code.<sup>[10]</sup> The stopping power is constant for  $\text{He}^+$  in Au (284 eV/nm) and for nickel (338 eV/nm). The structural plots are then corrected for energy, angle dependency by application of the  $k^2$  correction. The plot is used to ensure correct alignment of the ion beam and comparison of the surface and bulk blocking channels can also give an indication of reconstruction of the surface upon deposition of adsorbates onto the Au{111} surface. The analysis of the tiled data is further detailed in Chapter 3 of this thesis.

Each layered geometry can yield quantitative and qualitative elemental data by analysis of the 2D tiled spectra. The summation of ion intensity over a narrow angular range at the base of each blocking channel renders a plot of ion intensity versus energy of the scattered ions. Essentially the plot represents the number of Au/Ni atoms illuminated in each layer geometry. Calculation of peak areas is feasible via background subtraction and integration. To compare the number of gold and nickel atoms illuminated in each layer geometry, it is necessary to normalize the background subtraction peak areas. The number of gold and

nickel atoms illuminated by the ion beam then can be directly compared between the layer geometries. The correction is achieved by:

1. Dividing by  $z^2$ .  $z$  is the atomic number of the surface atom (Au 79 Ni 28).
2. Multiplying by  $\sin^4\theta/2$ . The scattering angle,  $\theta$  dependence of the scattering cross-section.
3. The value for  $F$  is calculated in equation 12. This is the probability density that an ion is scattered over a certain scattering angle and is given by:

$$\frac{d\sigma}{d\Omega} = F \left[ \frac{z_1 z_2 e^2}{4E \sin^2(\theta/2)} \right]^2 g(\theta, M_1, M_2) \quad (2.18)$$

All MEIS experiments used a 100 keV He<sup>+</sup> beam with  $F=0.92$  for nickel and  $F=0.72$  for gold. In addition,  $g(\theta, M_1, M_2)$  has a value close to 1 and was therefore ignored in the calculations.

## 2.7 REFLECTION ABSORPTION INFRARED SPECTROSCOPY

Reflection absorption infrared spectroscopy (RAIRS) is a non-destructive technique for the analysis of molecular species adsorbed onto single crystal metallic surfaces. It fingerprints, and in particular, identifies the type of bonds present in a molecule adsorbed onto metallic surfaces.

With RAIRS, an infrared beam is focused through a transparent alkali halide window onto the metallic surface at grazing incidence ( $\sim 4^\circ$ ). The infrared beam is polarized prior to focusing. The reflected beam is focused through a second alkali halide window where it is recollimated onto a mercury cadmium telluride (MCD) detector (detection range 5000-800

$\text{cm}^{-1}$ ). The path of the IR beam is purged with dry nitrogen to minimise interferences from gas phase absorption bands associated with atmospheric  $\text{H}_2\text{O}$  and  $\text{CO}_2$ .<sup>[3]</sup>

There are two distinguishing features of RAIRS. Firstly, the infrared beam enters at the grazing angle – almost parallel to the metallic surface (figure 2-7 (a)) and secondly, only molecular vibrations that give rise to dipole components perpendicular to the surface yield infrared absorption (figure 2-7 (b)).

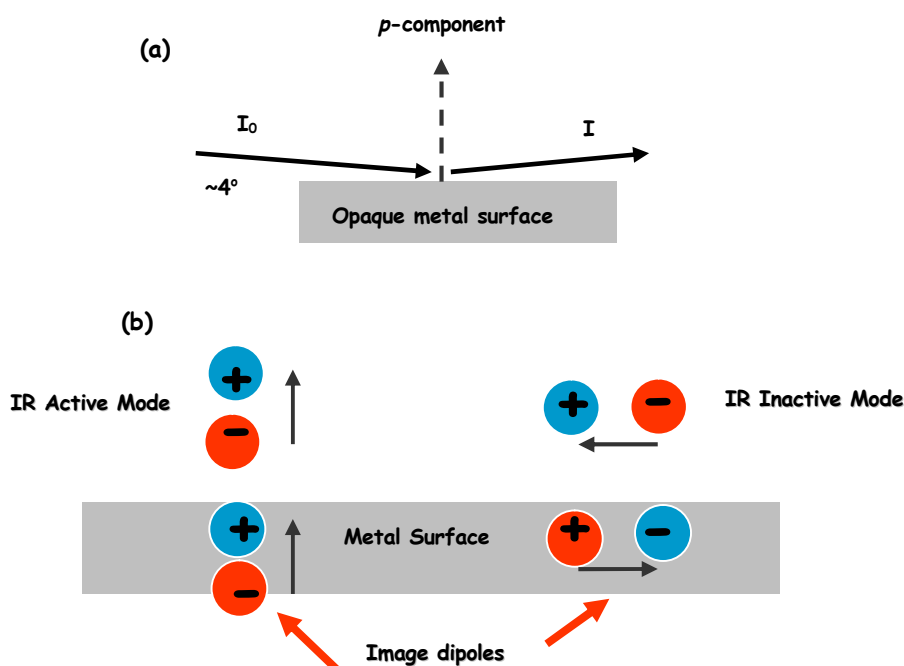


**Figure 2-7** (a) Illustration of the incident IR beam at grazing angle of  $\sim 3\text{-}8^\circ$  (b) Illustration of surface selection rule for observation of RAIRS in terms of image dipoles.

Sensitivity is an issue with RAIRS and sampling area's of *ca.*  $1\text{ cm}^2$  are typical. This corresponds to adsorbate coverage of  $\sim 10^{15}$  molecules ( $\sim 1$  nanomole). Consequently, the experiment is performed in a grazing incident to maximise surface sensitivity. This results in an increased the IR path length which in turn increases the sensitivity of thin films of adsorbates on metallic surfaces.<sup>[3]</sup>

For molecular vibrations to be infrared active, an accompanying change in the electric dipole moment must occur. During reflection, the  $p$ -component of infrared light excites

those molecular vibrations of the adsorbed molecule for which the component of the dipole moment perpendicular to the surface changes. Changes in dipole moment parallel to the surface (*s*-component) will cancel out the actual dipole and the molecular vibration will not be observed.<sup>[11]</sup>

RAIRS was used in this research project to ascertain the molecular orientation and adsorption properties of (*S*)-GA dosed onto bimetallic Au/Ni surfaces. A Nicolet Nexus 860 FTIR spectrometer was used to acquire RAIRS data (512 scans at a resolution of 4 cm<sup>-1</sup>) using an N<sub>2</sub>(l) cooled mercury cadmium telluride (MCT) detector. A background spectrum was taken of the Au{111}/Ni surface prior to exposure to (*S*)-GA. RAIRS data were taken as a function of (*S*)-GA exposure at a sample temperature of 300 K under UHV conditions.

## 2.8 TEMPERATURE PROGRAMMED DESORPTION

Temperature Programmed Desorption (TPD) is an extremely useful surface science technique examining the desorption of gases from single crystal metallic surfaces under vacuum. Specific information relating to the strength of interaction between the metallic surface and the adsorbed species is given.<sup>[3]</sup>

With TPD experiments; a linear temperature ramp is applied to the metal surface and the rate of desorption of the adsorbed species is monitored as a function of temperature and pressure. Typically, a computer controlled quadrupole mass spectrometer is used to detect the desorbing species. Because the adsorbed molecules can decompose into a range of products of differing mass, the quadrupole mass spectrometer simultaneously monitors several masses. In present case, the decomposition of (*S*)-GA on Au{111}/Ni surfaces is

investigated via TPD monitoring the mass of the parent ion (*S*)-GA, and other fragments such as H<sub>2</sub>, CO, CO and H<sub>2</sub>O.

With increasing temperature, the thermal energy available becomes sufficient to overcome the desorption activation barrier with the consequence that the adsorbate-surface bond breaks and desorption is observed.<sup>[3]</sup> Analysis of the desorption peak and the temperature at which the maximum desorption occurs is achieved via the Redhead method in which the activation energy of desorption,  $E_{des}$  is given by:<sup>[11]</sup>

$$E_{des} = RT_{max} \left[ \ln \left( \frac{\nu T_{max}}{\beta} \right) - 3.46 \right] \quad (2.19)$$

where  $R$  is the gas constant,  $T_{max}$  is the peak maximum temperature,  $\nu$  is the pre-exponential factor and  $\beta$  is the heating rate ( $dT/dt$ ).

This equation is approximately correct for first-order desorption in that the temperature of  $T_{max}$  is independent of coverage.

TPD was used in Chapter 4 of this thesis to examine the thermal stability of (*S*)-GA modified Au{111}/Ni surfaces as a function of nickel coverage and annealing temperature. All TPD experiments were carried out with a temperature ramp of  $\sim 5 \text{ Ks}^{-1}$  and the desorbing (*S*)-GA species monitored using a Spectra Microvision Plus Mass Spectrometer interfaced to a PC and analysed using Spectra RGA software for windows.

## 2.9 TRANSMISSION ELECTRON MICROSCOPY

Transmission Electron Spectroscopy (TEM) is a very powerful and versatile instrument capable of characterising the internal structure of a wide variety of materials, particularly when used in high resolution mode. This characterisation includes not only the imaging of

microstructure directly, but also the identification of the phases present in a specimen by either electron diffraction or spectroscopic chemical analysis techniques. The primary strength of the TEM is that it can provide characterisation at high resolution; hundreds of microns to Ångstroms.<sup>[6]</sup>

In an electron microscope with an accelerating voltage of 200 keV, the electron wavelength is 0.0251 Å, which is much shorter than the wavelength of X-rays used in conventional diffraction experiments. Resolution of 0.194 nm can be achieved with magnifications of up to 1,500,000 times giving high resolution.<sup>[6]</sup>

An electron microscope primarily contains an electron source and a group of electromagnetic lenses. The electron source provides a beam of electrons typically via thermionic emission. Due to the charged nature of these electrons, the beam can then be manipulated and focused by magnetic fields to produce diffraction and structural images of materials. The electron sources employed can include tungsten wire or a lanthanum hexaboride crystal. The electrons are accelerated by a potential difference of 200 keV. These fast moving electrons possess wavelengths much smaller than the interatomic distances in a crystal structure. Consequently, they are diffracted by the atoms when the electron beam interacts with a crystal. Due to relativistic effects of the electrons, caused by the acceleration by a large potential difference, the precise wavelength of the electrons is given by;<sup>[6]</sup>

$$\lambda = \frac{h(1 - \beta^2)^{\frac{1}{4}}}{(2m_e e_0 E)^{\frac{1}{2}}} \quad (2.20)$$

where  $h$  is Planck's constant;  $m_e$  is the rest mass of the electron;  $e_0$  is the electronic charge;  $E$  is the accelerating voltage (eV);  $\beta = v/c$ , where  $v$  is the velocity of the electron and  $c$  is the speed of light in a vacuum.

A TEM microscope consists of the following: (i) condenser lenses to focus the electron beam onto the sample, (ii) an objective lens to form the diffraction in the back focal plane and the image of the sample in the image plane and (iii) intermediate lenses to magnify the image or diffraction pattern on the screen. The electrons are first focused to form an approximately parallel beam by the condenser lenses. This beam then strikes the sample. Some of the electrons will be diffracted by the sample imparting structural information to the beam. The diffracted beam and the undiffracted or primary beam emerge through the sample and are recombined by the objective lens. The electron beam can be focused to a point that lies on a plane, normal to the straight-through beam, which is the back of the focal plane of the objective lens. This produces an electron diffraction pattern. In effect, the objective lenses complete an inverse Fourier transform to give a structural image. By alteration of the projector lens either the structural image or electron diffraction pattern can be propagated down the microscope and be recorded on a fluorescent screen or captured by CCD camera.

Au/Ni catalysts were prepared for TEM analysis as follows; a small amount of sample was ground in a pestle and mortar and acetone was added. As the sample consists of nanomaterial that may aggregate together, the suspension was sonicated. A few drops of the suspension were added to a copper grid. The solvent was allowed to evaporate thereby, depositing the sample on the grid. TEM images for the were attained by Ross Blackley of the electron microscopy facility run by Dr. Wuzong Zhou, University of St-Andrews. The transmission electron microscope was a Jeol JEM-2011 HRTEM.

## **2.10 ENERGY DISPERSIVE X-RAY SPECTROSCOPY**

Energy Dispersive X-Ray Spectroscopy (EDS) was used to obtain chemical compositions, elemental ratios and to detect impurities that may be present due to insufficient washing

of the Au/Ni supported colloids. X-rays are generated by bombarding the sample with a beam of high-energy electrons. When these electrons strike an atom, two processes can occur, elastic and inelastic scattering. Inelastically scattered electrons are used in EDS whereby, energy is either gained or lost by the incoming electrons. Electrons are accelerated through 200 keV and contain enough energy to ionise atoms by removing an electron from one of the core shells, before continuing on with reduced energy. If the electron is ejected from an inner shell then an electron from an outer shell will fall to remove the vacancy thus stabilising the atom. As this electron drops from a higher energy shell to a lower energy shell, energy is lost. This energy can be lost either as the emission of a second electron (an Auger electron) or an X-ray photon. The energy of this photon or Auger electron is characteristic of the energy level separation, which is unique to each element and can be used as a fingerprint to identify the elements present within the sample. In EDS, X-ray photons are detected rather than Auger electrons. The energies of the emitted X-rays are characterised according to which shells are involved. The standard terminology for describing the transition is:<sup>[6]</sup>

$K\alpha$  corresponds to an L to K transition.

$K\beta$  corresponds to an M to K transition.

## **2.11 EXTENDED X-RAY ABSORPTION FINE STRUCTURE**

X-ray Absorption Spectroscopy refers to how x-rays are absorbed by an atom at energies near and above the core-level binding energy of that atom and is subdivided into two regions. These regions contain information from the edge region (X-ray Absorption Near Edge Spectroscopy- XANES) and information from the post edge region (Extended x-ray Absorption Fine Structure- EXAFS).<sup>[11,12]</sup> The edge region contains information on the formal oxidation state and coordination chemistry of the absorbing atom. Whereas, the

oscillations above the post edge region or EXAFS yields information regarding the environment surrounding the absorbing atom like, for example, the type and distances of atoms neighbouring the absorbing atom in question. Essentially, EXAFS can be used to investigate the local environment around selected elements in a sample and is especially useful in bimetallic catalysis, quantitatively deciphering the role played by metal nanoparticles.<sup>[11,12]</sup>

X-ray absorption spectroscopy is a measurement of the absorbance near a particular edge as a function of photon energy. The initial decreasing part of an X-ray Absorption Spectroscopy spectrum is due to the interaction of x-ray photons with outer shell electrons. When the x-ray energy is equal to or greater than binding energy of a particular core level, the bound electron is ejected to the continuum due to the photo-electric effect and a sharp increase in the absorption spectrum is observed. This is the absorption edge and its position is characteristic for any type of absorbing atom, hence, EXAFS is element-specific.<sup>[11,12]</sup>

When discussing x-ray absorption, we are primarily concerned with the absorption coefficient  $\mu$ , which is determined by measuring the intensity of the photon beam before and after passing through the sample in transmission or fluorescence mode according to Beer's Law:

$$I = I_0 e^{-\mu t} \quad (2.21)$$

where  $I_0$  is the intensity of the incident beam;  $t$  is the sample thickness and  $I$  is the intensity of the transmitted beam.

The underlying physical process leading to the oscillations in the EXAFS region is the backscattering of the ejected photon-electron by neighbouring atoms as illustrated in

figure 2-8. From a quantum mechanical perspective, the ejected photonelectron can be seen as a spherical outgoing wave. The wavelength of this ejected photonelectron wave is dependent upon its energy and energy of the absorbing atom. The backscattered photon-electron interferes constructively or destructively with the outgoing wave at different wavelengths causing oscillations in the absorption spectrum.<sup>[11,12]</sup>

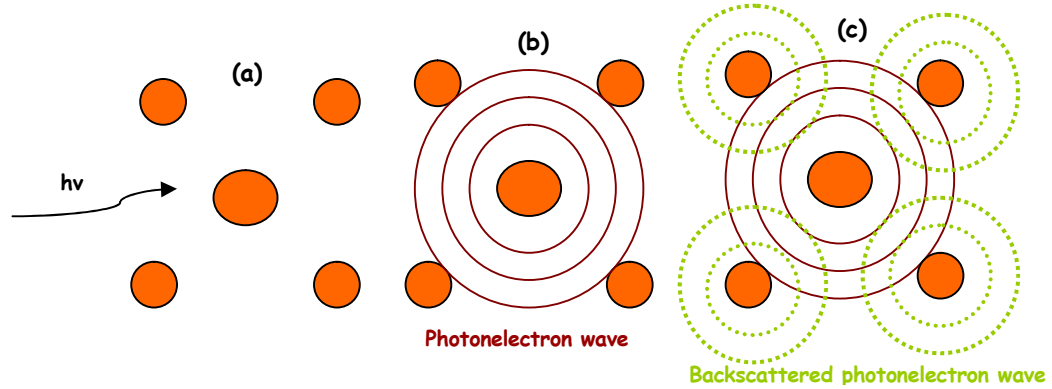


Figure 2-8 Illustration of the photon-electron backscattering process.

With EXAFS, one is interested in the oscillations above the absorption edge and the EXAFS fine structure  $\chi(E)$  can be defined as:

$$\chi(E) = \frac{\mu(E) - \mu_0(E)}{\mu_0(E)} \quad (2.22)$$

where  $\mu(E)$  is the measured absorption coefficient at energy  $E$  and  $\mu_0(E)$  is a theoretical absorption coefficient of an isolated atom i.e. no backscattering.

To extract structural information from the EXAFS fine structure, the x-ray energy is converted to  $k$ , the wave number of the photo-electron.  $\chi(k)$  is often shown weighted by  $k^2$  or  $k^3$  to amplify the oscillations.  $k$  is defined as:

$$k = \sqrt{\frac{2m(E - E_0)}{h^2}} \quad (2.23)$$

where  $E_0$  is the absorption edge energy;  $E$  is the absorption energy;  $m$  is the electron mass and  $h$  is Planck's constant.

For quantitative analysis, the EXAFS can be described by the following equation for a single scattering event:<sup>[11,12]</sup>

$$\chi(k) = \sum_j \frac{N_j S_0^2 f_j(k) e^{-2R_j/\lambda(k)} e^{-2k^2\sigma_j^2}}{kR_j^2} \sin\{2kR_j + \delta_j(k)\} \quad (2.24)$$

where  $\chi(k)$  is the EXAFS oscillations as a function of photo-electron wave number;  $N_j$  is the number of scattering atoms of type  $j$ ;  $S_0^2$  is the amplitude reduction factor. This parameter stems from the relaxation of the system in response to the creation of a core-hole;  $R_j$  is the distance from the central atom to a scattering atom of type  $j$ ;  $k$  is the wave vector associated with the photoelectron of energy  $E$ ;  $e^{-2k^2\sigma_j^2}$  is the Debye-Waller factor which accounts for thermal and static disorder in a solid with  $\sigma_j^2$  defined as the mean-square disorder of neighbour distance;  $e^{-2R_j/\lambda(k)}$  is a term accounting for the fact the photo-electron is elastically scattered a short distance in solids. This is a dampening factor depending on the ratio of the distance travelled,  $2R$ , to the electron mean free path,  $\lambda(k)$ ;  $\sin(2kR_j)$  relates the dependence of the EXAFS oscillatory structure on interatomic distance and energy;  $f_j(k)$  and  $\delta_j(k)$  are the scattering amplitude at atom  $j$  and phase-shift of the photo-electron wave during backscattering from a backscattering atom  $j$ , respectively.<sup>[19-21]</sup>

$f_j(k)$  and  $\delta_j(k)$  are the photon-electron scattering properties of the neighbouring atom and are dependent upon the atomic number  $Z$  of the scattering atom. Knowing these properties enables the determination of  $R$  the distance to the neighbouring atom;  $N$  the

number of scattering atoms i.e. coordination number and  $\sigma_j^2$ , the mean-square disorder of neighbour distance.

The analysis of EXAFS data involves the two major stages: reduction of the measured absorption spectra to EXAFS (i.e. application of equation 2.23) and the analysis of the  $\chi(k)$  data to obtain the structural parameters  $R$ ,  $N$ ,  $\sigma_j^2$  (i.e. application of equation 2.24).

This is achieved using the programs EXSPINE and EXCURV98.

Data reduction entails converting the raw data into an absorption spectrum by application of Beer's Law as described by equation 2.21 thereby converting the measured intensities to  $\mu(E)$  and removal of glitches and spikes. The  $\mu(E)$  data is then normalised, that is, the edge jump is scaled to one. The data now represents the absorption of one x-ray.  $\mu_0(E)$ , the theoretical absorption coefficient of an isolated atom cannot be measured but is approximated using a polynomial spline fitted to the EXAFS region. This also removes any residual background absorption associated with the windows or tape which the sample is attached to. Optimising the spline is the most subjective part of EXAFS data analysis as it can result in errors in the structural information. Poor background subtractions can result in changes to the frequency and amplitude of the data leading to erroneous determinations of distances and coordination numbers.

To extract structural information from the EXAFS data, the x-ray energy is converted to  $k$  by application of equation 2.23. Due to dampening of the signal at high  $k$ -values,  $\chi(k)$  is then weighted by  $k^2$  or  $k^3$  to amplify the oscillations. A better visualisation of data is obtained by Fourier transforming the weighted  $\chi(k)$  oscillation which is used for qualitative purposes. The x-axis units are  $R$  measured in angstroms and relate to interatomic distances. The peaks represent the signal from different backscattering shells.

The next stage of data analysis involves modeling the scattering amplitude  $f_j(k)$  and phase shift  $\delta_j(k)$  in the EXAFS equation to determine the structural parameters  $R$ ,  $N$  and  $\sigma_j^2$ , allowing  $E_0$  to change until a close match to the EXAFS data is achieved. The simulation program EXCURV98 is used and involves building a model environment, then calculating the theoretical EXAFS spectrum for that model. This is refined by comparing the theoretical spectrum to the real spectrum until the simulated theoretical spectrum matches the real experimental data. A best-fit approach is adopted.

Ni K-edge X-ray absorption spectra were collected on Station 7.1 at the Synchrotron Radiation Source, Daresbury. The storage ring operates at 2 GeV with a typical beam current of 100 mA. A double crystal Si(111) monochromator was utilised, de-tuned to 70 % of maximum intensity, for harmonic rejection. The Ni K absorption edge was calibrated by measuring K-edge from a Ni foil at  $E_0 = 8,333$  eV. Spectra were recorded at ambient temperature in transmission mode using ion detectors filled with Ar, 4 % absorbing  $I_0$  and 12 % absorbing  $I_t$ , backfilled to 1000 mbar with He. Catalyst preparation involved grinding each sample into a fine pellet with no pinholes. Two data sets were acquired per sample over the energy range of 7.4 to 8.4 keV. Background subtraction and theoretical analysis was carried out by Dr. C. J. Baddeley of the University of St-Andrews.

## 2.12 ATOMIC ABSORPTION SPECTROSCOPY

Atomic absorption spectroscopy (AAS) is a widely used analytical technique that measures the concentrations of metals using the absorption of light with detection limits in the range of 0.001 to 0.020 ppm. In their elemental form, metals will absorb ultraviolet light when they are excited by heat. All elements have a unique electronic structure and the wavelength of light absorbed is a unique property of each element. Measurement of the

intensity of light absorbed enables the concentration of the metals to be determined using a working curve after calibration with standards of known concentration.<sup>[13]</sup> The experimental set-up is illustrated in figure 2-9.

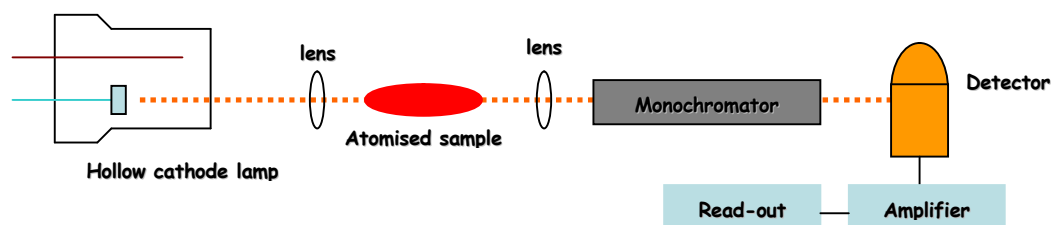


Figure 2-9 Experimental set-up of an Atomic Absorption Spectrometer.

AAS requires the metal atoms to be in the gas phase. This process is referred to as atomisation and involves the three stages of nebulisation, desolvation and vaporisation of the sample in a high-temperature source such as a flame. A solution of sample is converted to a mist of finely divided droplets by a jet of compressed gas (nebulisation). This flow of gas carries the sample into a flame where atomisation occurs. Atomisation occurs at temperatures between 1,980-3,450 K. The sample is evaporated to produce a finely divided solid molecular aerosol (desolvation). Dissociation of molecules then leads to an atomic gas (vaporisation). The atoms in turn can then dissociate into ions and electrons.<sup>[13]</sup>

The most common source of atomic absorption measurement is the hollow-cathode lamp. The lamp consists of a tungsten anode and a cylindrical metal cathode sealed in a glass tube that is filled with neon or argon at a pressure of 1-5 torr. The cathode is constructed from the metal to be analysed. When a high voltage is applied across the anode and cathode, the metal atoms in the cathode are excited into producing light with a certain emission spectra.

The electrons in the flame are then promoted to higher orbitals by absorbing a set quantity of energy. The amount of energy is specific to a particular electron transition in a

particular element. As the quantity of energy in the flame is known, the quantity remaining at the detector can be measured. Application of Beer's Law enables the calculation how many of transitions took place thus acquiring a signal that is proportional to the concentration of the element being measured.

AAS use monochromators and detectors for ultraviolet & visible light. The main purpose of the monochromator is to isolate the absorption line from background light due to interferences. Photomultiplier tubes are the most common detectors for AAS.

Atomic Absorption Spectroscopy was used in this research project to quantitatively determine the extent of nickel leaching during the catalytic modification process. AAS analysis was carried out by Mrs. Sylvia Williamson of the Thermal and Elemental Analysis facility, University of St-Andrews using a Pye Unicam AAS spectrometer.

## **2.13 GAS CHROMATOGRAPHY**

Gas Chromatography (GC) is an analytical technique that separates closely related components in a mixture. A micro-syringe is used to inject a liquid sample through a rubber septum into a flash vaporizer port located at the head of the column. The sample port is typically 323 K above the boiling point of the least volatile component of the sample. The liquid sample is dissolved in a gas carrier supply. This is typically a chemically inert gas like helium, argon, nitrogen or hydrogen. The carrier gas supply is also referred to as a mobile phase. The mobile phase is forced through an immiscible stationary phase, which is fixed in place in a column. The mobile phase does not interact with the sample components; its only function is to transport the sample through the column.<sup>[13]</sup>

The function of a stationary phase is to separate out the components in the sample. The components of a sample distribute themselves between mobile and stationary phases to varying degrees. Those components that are strongly retained by the stationary phase

move slowly with the flow of the mobile phase to the detector. In contrast, components that are weakly held by the stationary phase travel rapidly. As a consequence of these differences in mobility, sample components separate into discrete bands that can be analysed qualitatively or quantitatively. The Flame Ionization Detector (FID) is one of the most widely used and generally applicable detectors for GC. An FID is an ion detector using an air-hydrogen flame to produce ions. The ions propagate an electric current which is measured by the FID detector.<sup>[13]</sup>

A gas chromatograph Agilent 6850 GC was used in this research project. A flame ionised detector (FID) with a Restek Rt- $\gamma$ DEXsa chiral capillary column were fitted for the chiral separation of R- and S-MHB. Helium was introduced as a carrier gas and the oven temperature programmed from 313 K to 473 K at a ramp rate of 4 Ks<sup>-1</sup>. The stationary phase in the column consists of 14% cyanopropylphenyl and 86% dimethyl polysiloxane that is doped with 2,3-di-acetoxy-6-*O*-tert-butyl dimethylsilyl gamma cyclodextrin.

## BIBLIOGRAPHY

- [1] <http://nvl.nist.gov/pub/nistpubs/jres/107/3/j73lae.pdf>
- [2] D. P. Woodruff & T. A. Delchar. *Modern Techniques of Surface Science*. Second Edition. Cambridge University Press. 1994. ISBN 0-521-42498-4.
- [3] G. Attard & C. J. Barnes. *Surfaces*. Oxford University Primers – 59, Oxford Science Publications, 1998.
- [4] C. Davisson and L. H. Germer. *Phys. Rev.* **30** (1927) 705.
- [5] S. J. Garrett. CEm924 Course Notes, Michigan State University.  
<http://www.cem.msu.edu>
- [6] D. B. Williams & C. Barry Carter. *Transmission Electron Microscopy. A textbook for Materials Science*. Springer. 1996. ISBN 0-306-45324-x
- [7] R. Wiesendanger. *Scanning Probe Microscopy and Spectroscopy. Methods and Analysis*. Cambridge University Press. 1998. ISBN 0-521-42847-5.
- [8] R. M. Tromp. *Practical Surface Analysis. Vol II: Ion and Neutron Spectroscopy*. D. Briggs & M. Seath (Eds). John Wiley & Sons. 1973. ISBN 0-864-78645-x.
- [9] J. W. M. Frenken, R. M. Tromp & J. F. van der Veen, *Nuclear Instruments and Methods B* **17** (1986) 334.
- [10] [www.dl.ac.uk/MEIS/stereographs/sp.fcc.111.html](http://www.dl.ac.uk/MEIS/stereographs/sp.fcc.111.html)
- [11] J. W. Niemantsverdriet. *Spectroscopy in Catalysis; An Introduction*. Wiley-VCH. 2006. ISBN 978-3-527-31651-9.

- [12] J. M. Thomas & W. J. Thomas. *Principals and Practice of Heterogeneous Catalysis*. VCH. 1997. ISBN 3-527-29239.
- [13] H. H. Willard, L. L. Merritt, J. A. Dean & F. A. Settle. *Instrumental Methods of Analysis*. 1998. ISBN 0-534-08142-8.

# Chapter 3

## *Structural & Compositional Analysis of Au{111}/Ni Bimetallic Surfaces*

### **SYNOPSIS**

*This chapter details the characterisation of bimetallic Au{111}/Ni surfaces. The morphology, structure and composition of the bimetallic surface as a function of annealing temperature and nickel coverage is presented using Scanning Tunnelling Microscopy and Medium Energy Ion Scattering.*

## 3.1 INTRODUCTION

The importance of surface composition has been recognized for some time.

*‘When a plate of gold shall be bonded with a plate of silver or joined thereto, it is necessary to beware of three things, of dust, of wind and of moisture; for if any come between the gold and silver they may not be joined together’.* De Proprietatibus Rerum (The Properties of Things) AD 1250.<sup>[1]</sup>

The advent of surface science techniques has enabled the realm of metal surfaces to be investigated leading to a better understanding of catalytic systems. Significantly, Besenbacher *et al.*,<sup>[2]</sup> suggested correctly from STM studies that gold alloyed into a surface layer of a nickel catalyst would increase the effectiveness of the catalyst in steam reforming.<sup>[3]</sup> This was one of the very first examples of the design of a bimetallic catalyst from surface science studies.

Bimetallic systems are not constrained to metals that are miscible in the bulk but also to those that are immiscible in the bulk where surface alloys can be formed. The use of bimetallic systems is important in the development of selective catalysts where they have been shown to exhibit enhanced catalytic reaction rates and selectivities compared to their monometallic counterparts.<sup>[2-3]</sup>

### 3.1.1 SURFACE ALLOYING OF IMMISCIBLE METALS

When two metals are miscible in the bulk, intermixing and alloy formation at the surface is energetically favourable as demonstrated by a number of surface science studies for systems such as Cu-Au,<sup>[4]</sup> Fe-Cu<sup>[5]</sup> and Pd-Cu.<sup>[6]</sup> When two metals are immiscible in the bulk and do not form stable alloys, one would expect the deposited metal to simply grow on top of the surface of the other. Traditionally, metal-on-metal growth is characterised by three growth modes. In the Frank-van der Merwe growth mechanism, the deposited

metal grows layer by layer. The growth of a new layer does not begin until the preceding layer is complete. In the Stranski-Krastanov growth mechanism, the deposited metal grows initially in a layer by layer fashion followed by growth in the form of 3D islands. In the Volmer-Weber growth mechanism, the deposited metals grows via the formation of 3D islands.<sup>[7]</sup> However, STM studies have confirmed intermixing and alloy formation for metals that are immiscible in the bulk.<sup>[9-14]</sup> This is a promising avenue to design surfaces with unique physical and chemical properties that are applicable in many fields such as heterogeneous catalysis.

The growth of gold on nickel surfaces is an example of the latter class of system. Both gold and nickel have face centred cubic (fcc) bulk crystal structures; but there is a large lattice mismatch of 15.7 % (the lattice parameters of bulk Au and Ni are 4.079 Å and 3.524 Å respectively).<sup>[8]</sup> Consequently, it is energetically unfavourable for gold to form a pseudomorphic monolayer on nickel since there would be considerable compressive strain produced at the interface.

The growth of gold on Ni{110} has been examined in detail by Pleth Nielsen *et al.*,<sup>[9]</sup> who reported that gold atoms squeeze out nickel atoms at the surface and adopt their positions. The number of alloyed gold atoms in the surface layer increases with increasing gold coverage. The displaced nickel atoms nucleate into nickel islands that grow preferentially along the  $[1\bar{1}0]$  direction. While alloyed gold atoms are imaged as depressions  $\sim 0.2$  Å deep; nickel atoms that are next nearest neighbours to gold atoms appear brighter in the STM topographs. This is a powerful demonstration of the formation of a surface alloy where the two metals are immiscible in the bulk. Conversely, for Ni{111} surfaces, Au/Ni alloy formation is activated after deposition of gold at elevated temperatures greater than 423 K.<sup>[10]</sup> This is attributed to the fact that the energy necessary to alloy gold atoms into the nickel surface is higher for {111} surfaces; since the

nickel atoms in the {111} surface are in a higher coordination environment than other crystal planes.<sup>[10]</sup> Beyond a certain coverage where gold atoms are substituted into the Ni{110} surface layer, a transition from alloying to dealloying occurs.<sup>[9-10]</sup> A fraction of the gold atoms are displaced from the alloyed surface and nucleate into a new structure consisting of gold [001] oriented chains of alternating dimers and trimers. These vacancies arise due to surface strain induced by the substituted gold. Such alloying-dealloying phenomena have also been observed for the growth of lead on Cu{111}.<sup>[11]</sup>

For metal-on-metal growth, the interface between the deposited metal and the metal substrate is strained due to a lattice mismatch. Strain relief is achieved through misfit dislocations as postulated in 1949 by Frank and van der Merwe.<sup>[12]</sup> An example of such a system is gold on Ni{111}.<sup>[12]</sup> Gold does not grow pseudomorphically on Ni{111} with the result that lattice strain is relieved through misfit dislocations in the form of Moiré and triangular structures.<sup>[12]</sup> The origin of these misfit dislocations is related to the large lattice mismatch and the strong Au-Ni interactions at the interface.

Deposition of gold on Ni{111} at 170 K and annealing to room temperature produces a Moiré overlayer structure. Moiré structures are the result of one lattice growing on top of another with differing dimensions. Consequently, the overlayer periodically goes in and out of registry with the substrate. In this instance, eight surface gold atoms are present for every nine nickel atoms with gold varying periodically from three-fold sites to energetically unfavourable on-top sites. Strain relief is achieved through misfit dislocations where annealing of the aforementioned surface to ~400 K or deposition of gold on Ni{111} at room temperature leads to the formation of triangular structures. These structures are ascribed to the restructuring of the surface to accommodate the gold overlayer. The misfit dislocations are triangular in shape because the surface has a three-fold symmetry.<sup>[12]</sup>

Similar behaviour has been observed in the growth of silver on Cu{111}<sup>[13]</sup> and silver on Ni{111}<sup>[14]</sup> surfaces.

### 3.1.2 AU{111} RECONSTRUCTED SURFACES FOR METAL-ON-METAL GROWTH

It has been recognised for some time that the deposition of metals on the Au{111} herringbone reconstruction leads to organised growth for a wide variety of metals such as nickel,<sup>[15]</sup> iron,<sup>[16]</sup> cobalt,<sup>[17]</sup> palladium<sup>[18]</sup> and rhodium.<sup>[19]</sup>

Gold is unique in that it is the only fcc metal whose close packed surface reconstructs at room temperature. Clean Au{111} surfaces exhibit a surface reconstruction in UHV, air and electrochemical environments where the registry of surface gold atoms varies between regions of fcc and hexagonal-close packed (hcp) stacking. Where the two differing structures meet, buckling occurs. This is more commonly referred to as the herringbone reconstruction.<sup>[20]</sup>

The basis of the reconstruction has been studied in detail by STM.<sup>[20]</sup> Briefly, the distribution of 23 atoms among 22 bulk sites within the surface unit cell is responsible for the buckling. To reduce strain, a 60°/120° zig-zag pattern is adopted giving rise to the characteristic herringbone reconstruction. The transition between fcc and hcp regions are clearly visible and appear as a set of ridges to the STM. Enclosed within these ridges are regions of hcp stacking. Each set of ridges are separated by regions of fcc stacking. At the bending points (also referred to as elbows) of the reconstruction; initial growth of metals like iron, cobalt, and nickel is favored, while other metals like copper<sup>[26]</sup> and silver<sup>[22]</sup> preferentially grow on the step edges of the gold surface.

Chambliss and co-workers illustrated with STM that nickel preferentially grows in the elbows of the Au{111} herringbone reconstruction.<sup>[15]</sup> Regular arrays of nickel islands with uniform spacing were imaged. The average size of the nickel islands varied in proportion with nickel coverage. The ordered nucleation of nickel at these sites was attributed to the influence of the herringbone reconstruction on nickel atom diffusion. Chambliss and co-workers suggested the elbows of the herringbone reconstruction generate potential dips that trap diffusing nickel atoms. Monte-Carlo simulations showed that small trapping probabilities at the elbows may be sufficient to cause the observed alignment and growth of nickel islands.<sup>[15]</sup>

However, Meyer *et al.* ascribe these effects to a site selective place exchange of nickel atoms with gold surface atoms located at the elbows.<sup>[23]</sup> The substituted nickel atoms then act as nucleation sites for diffusing nickel atoms. Meyer *et al.*, postulate the exchange mechanism occurs at the elbows because the close-packed atomic row terminates there; giving rise to gold atoms with reduced lateral coordination that are more susceptible to the exchange process rather than those residing on the terraces.

Metal growth at the elbows of the herringbone reconstruction was also observed for iron<sup>[16]</sup>, cobalt,<sup>[17]</sup> palladium<sup>[18]</sup> and rhodium.<sup>[19]</sup> Meyer *et al.*, proposes this occurrence is due to these elements having a larger surface free energy and heat of sublimation than gold.<sup>[23]</sup> Accordingly, for elements with lower values of these quantities like silver<sup>[22]</sup> and copper<sup>[26]</sup>; no ordering was observed. However, aluminium is an exception to this energetic argument as aluminium grows preferentially in the elbows of the herringbone reconstruction.<sup>[21]</sup>

### 3.1.3 AIM OF RESEARCH

This study investigates the growth of nickel on Au{111} and subsequent annealing to produce a bimetallic system. The near surface structure and alloying behaviour of this system are examined using STM and MEIS.

STM and MEIS proved to be a powerful combination providing a detailed picture of the morphology, structure and composition of this system. To investigate the growth mode of nickel on Au{111} surfaces; STM was used to visualise the surface topography of this system on the atomic scale. MEIS was utilised in this research project because it is a surface sensitive technique capable of distinguishing between atom types enabling elemental identification and quantification of alloy compositions, which is essential in the examination of bimetallic systems.

This study forms part of a larger project aimed at the creation of selective Au/Ni catalysts in relation to the nickel catalysed enantioselective hydrogenation of  $\beta$ -ketoesters. The aim of this Chapter is to examine the compositional and structural influence of gold in this bimetallic system and to assess its potential use in the aforementioned enantioselective hydrogenation reaction.

## 3.2 EXPERIMENTAL

Two UHV systems were used in this study. The first was an Omicron variable temperature STM with a base pressure of  $1 \times 10^{-10}$  mbar consisting of two separate chambers for sample preparation and characterisation and STM measurements located at the University of St Andrews. The second UHV system for MEIS experiments is located at the UK National MEIS facility at STFC Daresbury Laboratory. This UHV system consists of a scattering chamber, a sample preparation and characterisation

chamber, a storage chamber and a fast entry load lock. A detailed description of these surface science techniques is given in Chapter 2.

### 3.2.1 STM EXPERIMENTS

The Au{111} sample was cleaned by cycles of ion sputtering ( $\text{Ar}^+$ , 0.9 kV,  $i_{\text{sample}} \sim 6 \mu\text{A}$ ) annealing to 873 K until a sharp (1 x 1) LEED pattern was attained and STM indicated that a clean Au{111} reconstructed surface had been produced. Nickel was evaporated onto the Au{111} surface at room temperature by means of a resistively heated tungsten filament around which nickel wire had been wound. The nickel deposition rate was calibrated via STM by monitoring the size of the nickel islands which nucleate into the elbows of the Au{111} herringbone reconstruction. STM topographic images were acquired in constant current mode using an electrochemically etched tungsten tip. Nickel growth was examined as a function of deposition and annealing temperature ranging from 300-650 K.

### 3.2.2 MEIS EXPERIMENTS

The Au{111} sample was cleaned by cycles of ion sputtering ( $\text{Ar}^+$ , 0.9 kV,  $i_{\text{sample}} \sim 6 \mu\text{A}$ ) and annealing to 873 K until a sharp (1 x 1) LEED pattern was observed and no impurities such as carbon or sulphur were detected by AES. This resulted in a well-ordered clean surface. The experiment involved depositing  $\sim 8$  ML of nickel at room temperature and annealing to progressively higher temperatures to investigate possible alloy formation and diffusion of nickel into the bulk. Nickel deposition was achieved by means of a resistively heated tungsten filament around which nickel wire had been wound. AES was used to estimate the coverage of nickel. Monitoring the growth of the nickel Auger peaks (61 eV & 848 eV) as a function of depositing time at constant flux enabled the estimation of nickel coverage. The Au{111}/Ni surface was then annealed to a series

of temperatures ranging from 300-630 K. Following each annealing temperature, LEED and AES analysis were performed.

The MEIS experiments described in this chapter use layer specific geometries as shown in figure 3-1. A beam of 100 keV He<sup>+</sup> ions was employed for all experiments. Surface structure is determined using the phenomenon of blocking. The ion beam was aligned at an angle of 35.26 ° with respect to the sample normal along the  $[\bar{1}\bar{1}\bar{4}]$  azimuthal direction. At this alignment, 1-, 2- and 3-atomic layer illumination can be attained by selecting appropriate outgoing blocking directions. This corresponds to the top, top two and top three surface layers respectively. These atoms shadow atoms deeper into the surface. Only those atoms visible to the ion beam contribute to the backscattered ion yield. 1-layer illumination (i.e. top surface layer) is achieved by aligning the ion beam along the  $[\bar{1}\bar{1}\bar{4}]$  crystallographic direction with the detector fixed at a scattering angle of 109.5 ° to enable detection of scattered ions along the [110] exit direction. 2-layer illumination (i.e. top two surface layers) is achieved by aligning the ion beam along the  $[\bar{1}\bar{1}\bar{4}]$  crystallographic direction with the detector fixed at a scattering angle of 90 ° to enable detection of scattered ions along the  $[\bar{2}21]$  exit direction. 3-layer illumination (i.e. top three surface layers) is achieved by aligning the ion beam along the  $[\bar{1}\bar{1}\bar{4}]$  crystallographic direction with the detector fixed at a scattering angle of 84.24 ° to enable detection of scattered ions along the  $[\bar{3}32]$  exit direction.

In the three exit directions, [110],  $[\bar{2}21]$  and  $[\bar{3}32]$  illustrated in figure 3-1 (a-c); ions scattered from subsurface atoms are prevented from reaching the detector by the presence of atoms in higher lying layers i.e. blocking. At these scattering directions, the detector

identifies regions of low ion counts, commonly referred to as blocking channels in the spectrum of ion intensity *versus* scattering angle. This is summarised in table 3-1.

Concurrently, ions that are deflected from the atomic rows into nearby channels can travel deep into the bulk without undergoing any collisions until they are either backscattered, neutralised or become heavily buried within the bulk. The backscattered ions that do reach the detector can yield information on bulk structure as energy loss is directly proportional to the distance travelled by the ions within a given sample. This process is referred to as channelling. This combination of shadowing, blocking and channelling provides a detailed picture of surface and subsurface atomic structure.

Table 3-1: Summary of the incident and exit directions and corresponding scattering angles used in the following set of MEIS experiments.

<b>Geometry</b>	<b>Surface layers illuminated</b>	<b>Incident</b>	<b>Exit</b>	<b>Scattering Angle</b>
1-layer	Top layer	$[\bar{1}\bar{1}\bar{4}]$	[110]	109.5°
2-layer	Top two layers	$[\bar{1}\bar{1}\bar{4}]$	$[\bar{2}2\bar{1}]$	90°
3-layer	Top three layers	$[\bar{1}\bar{1}\bar{4}]$	$[\bar{3}3\bar{2}]$	84.24°

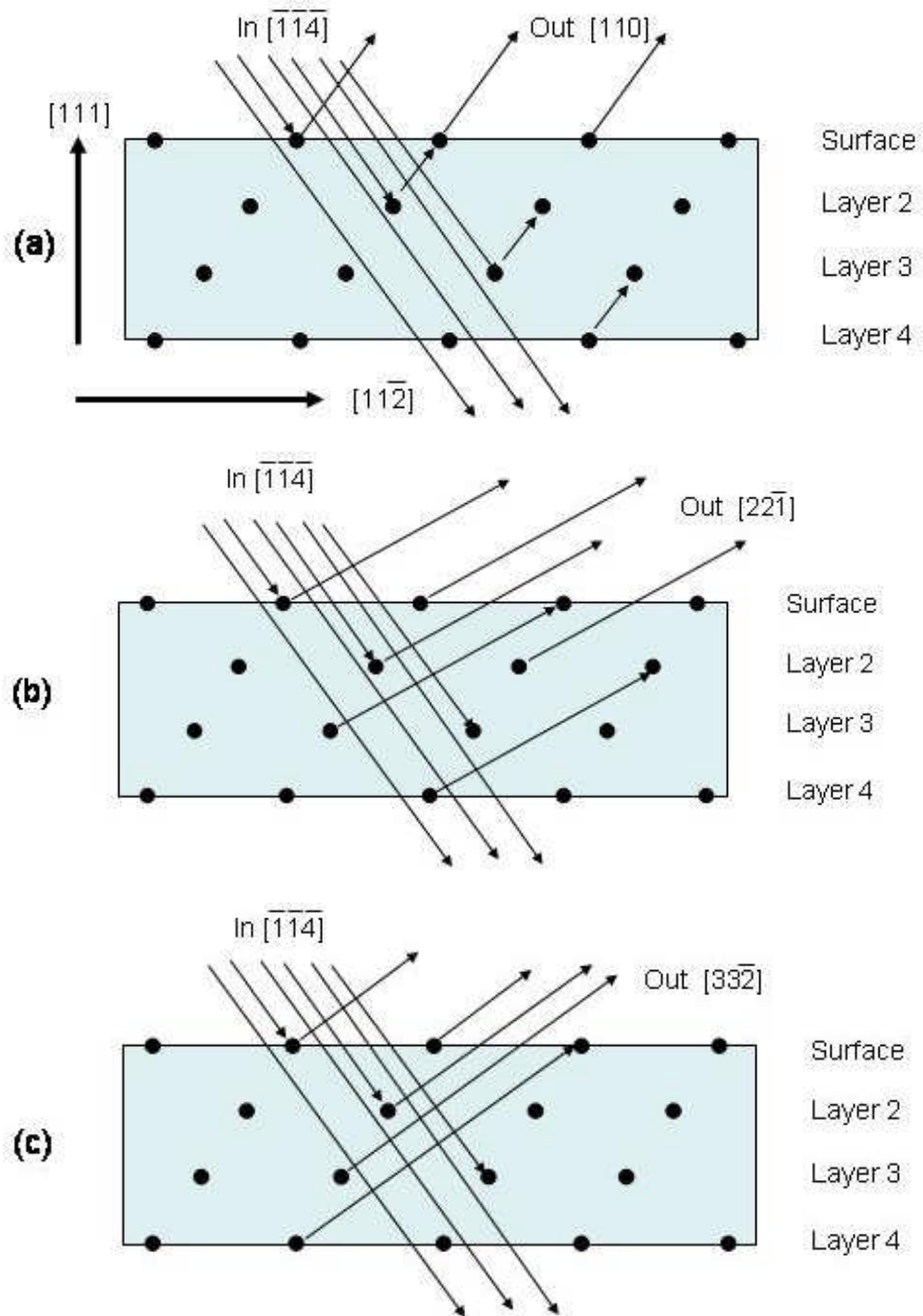


**Figure 3-1** Schematic diagrams showing the ion beam trajectories utilised to achieve (a) 1-, (b) 2- and (c) 3-layer specific alignments in the azimuth of the fcc {111} surface. The arrows represent ion trajectories and show, for example, how the 1<sup>st</sup>, 2<sup>nd</sup> and 3<sup>rd</sup> layer atoms are visible to the incident beam while, by contrast, the 4<sup>th</sup> layer atoms are shadowed. Similarly, outgoing trajectories show how the phenomenon of blocking can be utilised to achieve layer specific information.

Reproduced from reference 28.

Raw data is collected in the form of 2D tiles of ion count intensity as functions of energy and scattering angle. A complete data set is constructed electronically from several 2D tiles of different angles and energies producing a full 2D profile of the surface and subsurface regions. Each tile gives a complete picture of the scattering behaviour. Figure 3-2 presents a tiled raw data set. From this tile, both structural and compositional data may be derived for each applied annealing temperature. Structural data were obtained by superimposing polygons specific to a number of layers (i.e. cuts) onto regions of the tile and projecting the intensity contained within the polygon into a plot of ion intensity *versus* scattering angle. The cuts taken are illustrated by the grey arrows (a-d). Quantitative compositional analysis can be achieved by analysis of the 2D tiled spectra. The summation of ion intensity over a narrow angular range at the base of each blocking channel (illustrated by the brown arrows (e-g)) produces a plot of ion intensity *versus* energy of the scattered ions. Essentially these plots allow the calculation of the number of gold and nickel atoms illuminated in each experimental geometry.

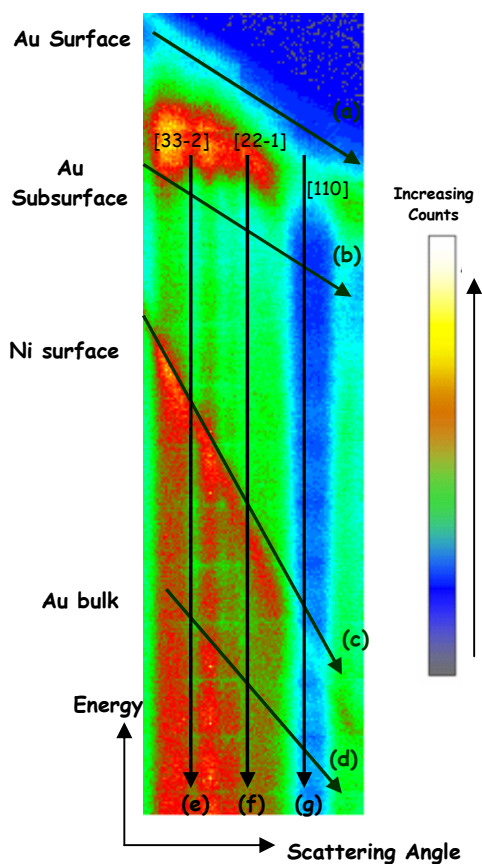


**Figure 3-2** A typical raw MEIS data.

Cuts taken across the tile (represented by the grey arrows) correspond to ion intensity *versus* scattering angle plots. Cuts taken down the blocking channels (represented by the brown arrows) correspond to ion intensity *versus* energy plots.

### 3.3 RESULTS

#### 3.3.1 STM STUDIES

The herringbone reconstruction is sensitive to impurities, consequently when it is observed one can be confident that a flat clean Au{111} surface has been successfully prepared. Figure 3-3 (a-d) are STM images of clean Au{111} exhibiting the herringbone reconstruction. Figure 3-4 (a-f) are a set of topographic STM images illustrating the changes in morphology as a function of coverage for deposition at room temperature of nickel on Au{111} at a nickel evaporation rate of  $0.1 \text{ ML min}^{-1}$ . Upon deposition, nickel resides in the elbows of the herringbone reconstruction. This is in good agreement with previous studies.<sup>[15,23]</sup> The nickel islands are ordered and uniformly spaced with a morphology ranging from circular, hexagonal to triangular depending on the coverage of nickel. In general, a low coverage of nickel results in circular islands while conversely

higher coverages of nickel results in triangular to hexagonally faceted islands. It is postulated each nickel island once residing in the elbows of the herringbone reconstruction acts as a nucleation site for further growth of the island.<sup>[15,23]</sup> With increasing nickel coverage, the nickel islands elongate and join forming monolayer ribbons. Increasing the coverage of nickel to 1.2 ML results in a flattened nickel overlayer with areas of exposed gold surface present.

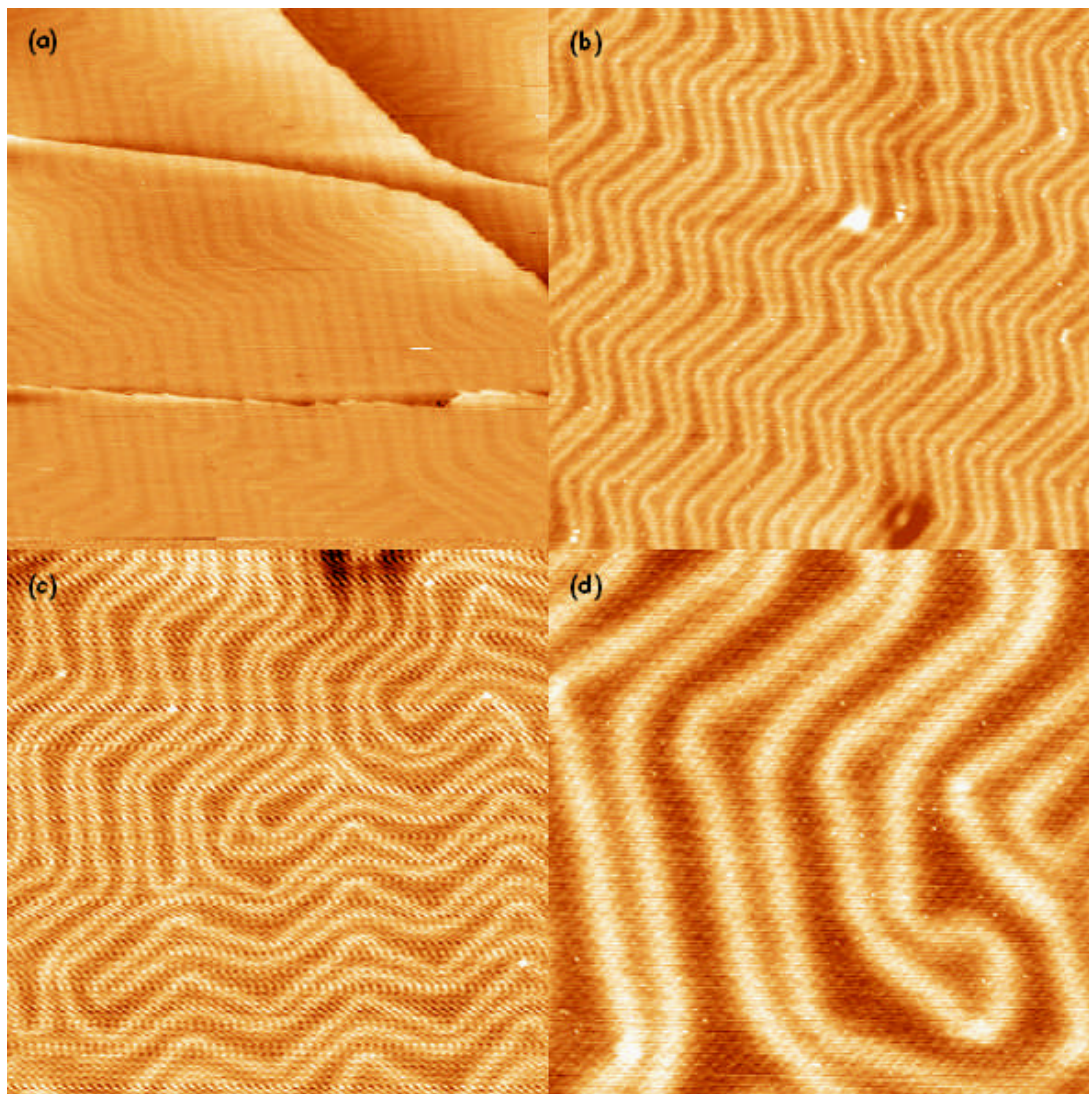


**Figure 3-3** STM topographic images of reconstructed Au{111} at room temperature. **(a)** 110 nm x 110 nm ( $V = +0.30$  V,  $I = 0.94$  nA). **(b)** 99 nm x 99 nm ( $V = -0.68$  V,  $I = 0.90$  nA). **(c)** 71 nm x 71 nm ( $V = +0.31$  V,  $I = 0.64$  nA). **(d)** 29 nm x 29 nm ( $V = +0.45$  V,  $I = 0.64$  nA).

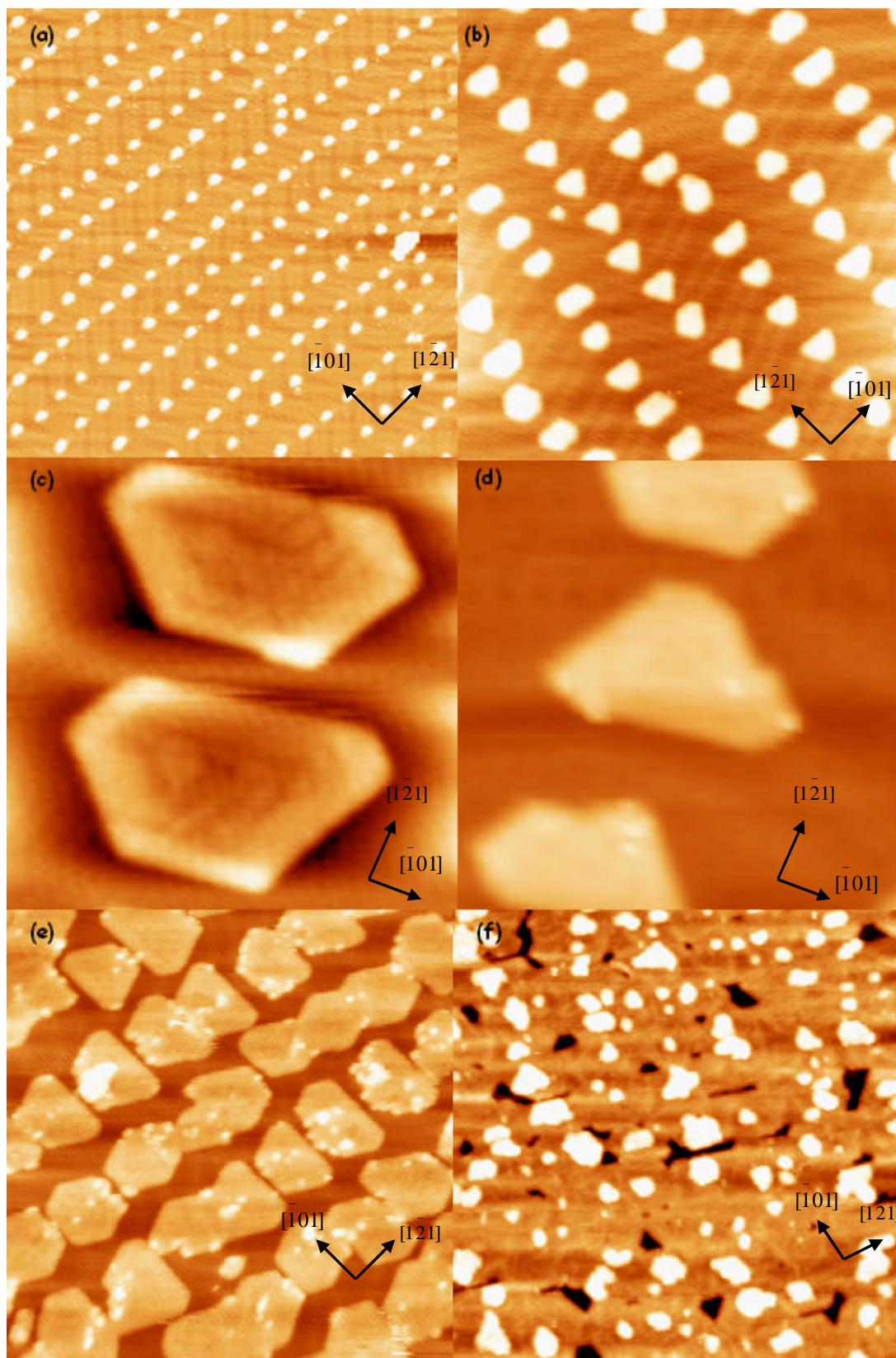


**Figure 3-4** (a) 0.05 ML Ni/Au{111}. STM image 140 nm x 140 nm ( $V = -0.85$  V,  $I = 2.13$  nA). (b) 0.5 ML Ni/Au{111}. STM image 66 nm x 58 nm ( $V = -0.82$  V,  $I = 1.5$  nA). (c) Nickel islands 11 nm x 11 nm. ( $V = -0.2$  V,  $I = 2.0$  nA) (d) Nickel islands 13 nm x 13 nm. ( $V = -0.2$  V,  $I = 2.0$  nA). (e) 0.8 ML Ni/Au{111}. STM image 53 nm x 53 nm. ( $V = -0.8$  V,  $I = 1.5$  nA). (f) 1.1 ML Ni/Au{111}. STM image 62 nm x 62 nm. ( $V = -0.8$  V,  $I = 1.8$  nA).

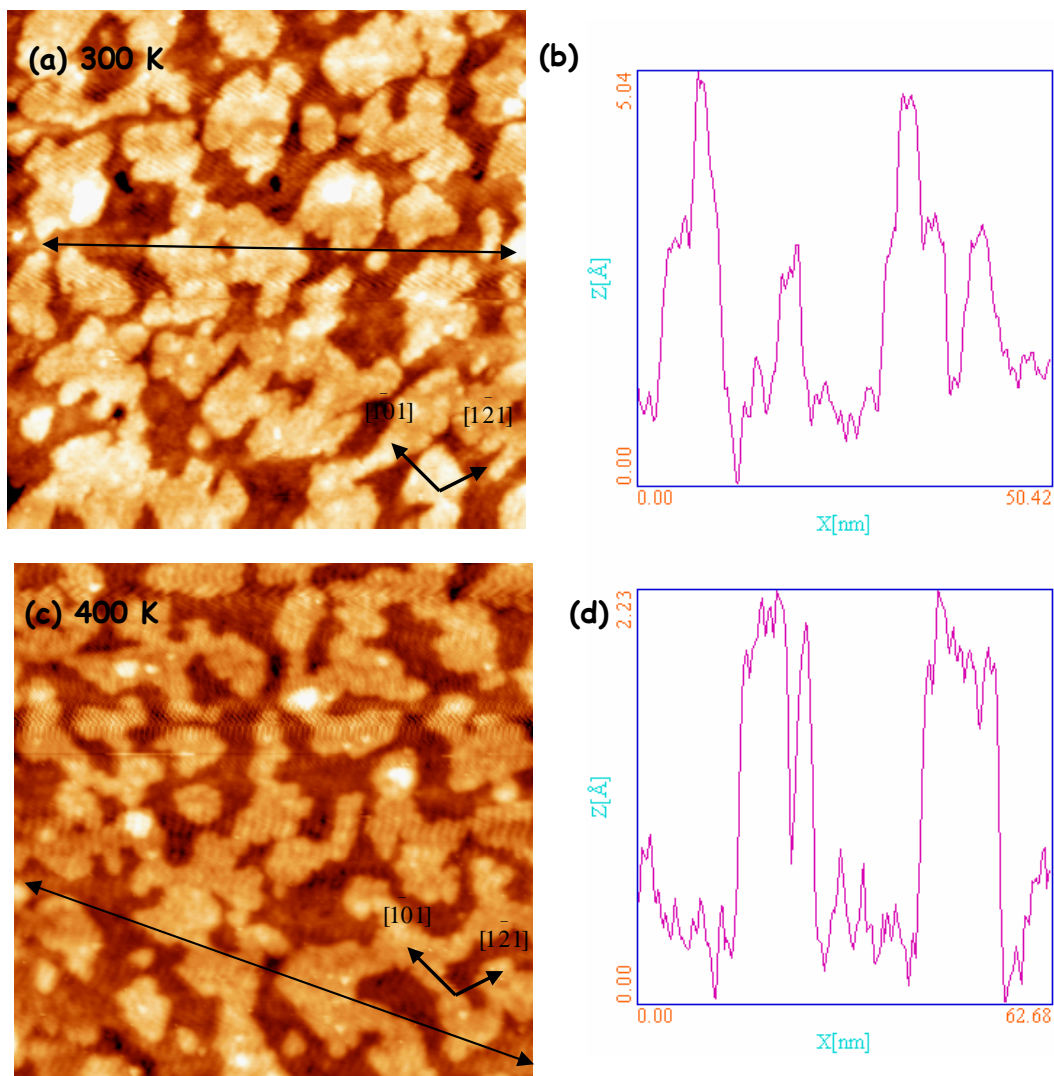
Figure 3-4 (a) is a topographic image captured at 140 nm x 140 nm of 0.05 ML of nickel deposited on Au{111}. The image shows 2D nickel islands residing in the herringbone elbows. On average, each nickel island is 1.8 Å in height, ~5 nm in diameter and circular in shape. The herringbone reconstruction is clearly visible. The average spacing is ~3.5 nm between the nickel islands in a row along the  $[1\bar{2}1]$  direction and ~7-7.5 nm between rows of the herringbone reconstruction along the  $[\bar{1}01]$  direction. Figure 3-4 (b) illustrates the further growth of ~0.2 ML nickel in the herringbone elbows. The presented topographic image is 66 nm x 58 nm. Each nickel island is ~5.5 nm in diameter and ~1.7 Å in height. The morphology of the nickel islands vary from triangular to hexagonal. The former tend to orient in opposite directions to the hexagonal islands. Whether the elbows of the reconstruction ‘pinches in’ or ‘pinches out’, seems to dictate the shape of the nickel islands. Triangular islands reside in the pinched in elbows and conversely hexagonal islands reside in the pinched out elbows of the reconstruction. This is in good agreement with the work of First and co-workers.<sup>[24]</sup> The average spacing is ~2.9 nm between the nickel islands in a row along the  $[1\bar{2}1]$  direction and ~6-7.5 nm between rows of the herringbone reconstruction along the  $[\bar{1}01]$  direction.

Figure 3-4 (c) is a topographic image of well defined hexagonally faceted nickel islands captured at 11 nm x 11 nm. The islands are ~1.8 Å in height and ~9.2 nm in diameter. Figure 3-4 (d) is a topographic image of well defined triangular nickel islands captured at 13 nm x 13 nm. The islands are ~1.9 Å in height and ~5.4 nm in diameter. Figure 3-4 (e) is 0.8 ML of nickel on Au{111}. The islands are hexagonal in shape. Each nickel island is ~1.9 Å in height and ~9.5 nm in diameter. The nickel islands coalesce into monolayer ribbons. Figure 3-4 (f) is 1.2 ML of nickel deposited on Au{111}. Nickel grows in a layer-by-layer fashion followed by growth of 3D clusters indicating the growth mechanism is

that of Stranski-Krastanov. However, growth of the second layer of nickel occurs prior to completion of the first layer. Areas of exposed gold surface are clearly visible.

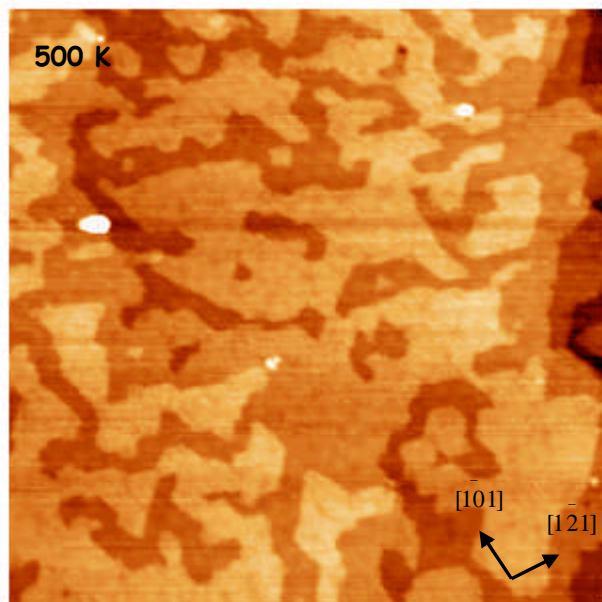
The following set of topographic STM images examines the change in morphology when  $\sim 4$  ML of nickel is deposited on Au{111} as a function of annealing temperature. The thermal treatment ranges from 300-650 K. Nickel was evaporated at a rate of  $0.1 \text{ ML min}^{-1}$  at room temperature. Annealing of the Au/Ni surface to 400-500 K results in progressive flattening of the large nickel islands. Further annealing to 550 K and to 600 K exhibits a Moiré structure and triangular misfit dislocations respectively. At 650 K, the surface resembles that of clean gold with a disordered herringbone reconstruction visible.

Figure 3-5 (a-b) is a 52 nm x 52 nm topographic STM image of  $\sim 4$  ML of nickel on Au{111} and corresponding line profile. Typically, the nickel islands measured  $\sim 5 \text{ \AA}$  in height. Figure 3-5 (c) is the aforementioned surface annealed to 400 K. The nickel islands have begun to flatten out and measure approximately  $\sim 2.2 \text{ \AA}$  in height.



**Figure 3-5** (a-b) STM image of  $\sim 4$  ML Ni deposited on Au{111} at room temperature and corresponding line profile. STM image taken at  $52 \text{ nm} \times 52 \text{ nm}$ . ( $V = -0.90$ ,  $I = 1.04 \text{ nA}$ ). (c-d) STM image and corresponding line profile of  $\sim 4$  ML of nickel deposited on Au{111} at room temperature and annealed to 400 K. STM image taken at  $66 \text{ nm} \times 66 \text{ nm}$ . ( $V = 0.59 \text{ V}$ ,  $I = 0.20 \text{ nA}$ ).

Figure 3-6 is an topographic image of  $\sim 4$  ML nickel on Au{111} and annealed to 500 K. A large terrace is visible displaying flattened nickel islands. Examining the topographic image, a hint of a Moiré structure is present however; this could not be clearly resolved.



**Figure 3-6** STM image of  $\sim 4$  ML of Ni deposited at room temperature on Au{111} and annealed to 500 K STM image taken at 180 nm x 180 nm. ( $V= 0.9$  V,  $I= 0.1$  nA).

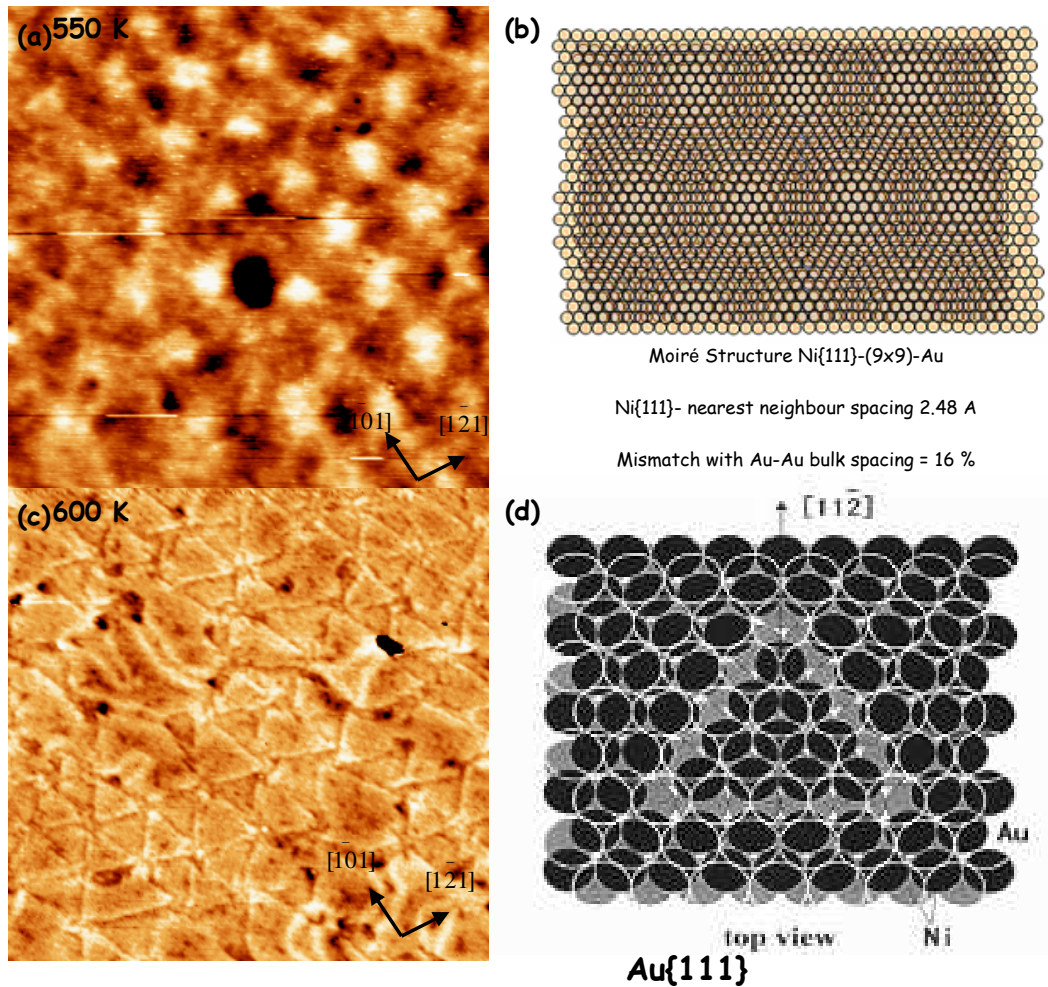
Annealing of the bimetallic Au/Ni surface to 550 K reveals a well-resolved Moiré structure as presented in figure 3-7 (a). Further annealing of the bimetallic surface to 600 K reveals triangular misfit dislocations as presented in figure 3-7 (b). These structures are a form of stress relief due to the large lattice misfit and the strong Au-Ni interactions at the interface.<sup>[12]</sup> The presence of a Moiré structure is indicative of a nickel overlayer or, more likely, the formation of a near-surface alloy. The triangular structures can be attributed to a restructuring of the Au{111} surface to accommodate the nickel overlayer and are triangular because the surface has three-fold symmetry.<sup>[25-26]</sup>

Figure 3-7 (b) is a diagrammatic representation of a Moiré structure of the reverse system, gold on Ni{111}. The periodicity in the diagram is  $\sim 22$  Å for this structure whereas it is  $\sim 80$  Å for the nickel (or Ni/Au) overlayer on Au{111} but the origins of this effect are similar. In the present case, the Au-Au spacing is thought to be contracted with respect to

the nickel bulk such that 29 Au-Au spacings are equivalent to 28 Ni-Ni spacings. This gives a lattice spacing of  $80/29 = 2.76 \text{ \AA}$ , which is between the nearest neighbour atomic distances of gold (2.884  $\text{\AA}$ ) and nickel (2.491  $\text{\AA}$ ). Assuming a linear variation of lattice parameter with Au/Ni composition, one may predict a Au:Ni ratio of  $\sim 69:31$  or approximately 2:1.

Figure 3-7 (d) is a diagrammatic representation of triangular misfit dislocations reproduced from reference 27 of the reverse system (gold on Ni{111}) but the origins of this effect are similar. In the case of Au/Ni{111}, these triangular misfit dislocations are attributed to a reconstruction of an underlying nickel layer to accommodate the preference of gold atoms to adopt three-fold sites. The underlying nickel layer reconstructs such that nickel atoms alter from fcc to hcp sites. Above these hcp nickel sites; gold atoms occupy three-fold adsorption sites giving rise to the triangular misfit dislocations.<sup>[12, 27]</sup>

The distance between two triangles of same angular orientation was measured to be  $\sim 90 \text{ \AA}$  in figure 3-7 (c) corresponding to  $\sim 31$  Au-Au spacings. As will be shown later, the annealing treatment required to produce this structure is sufficient to induce significant Au segregation to the surface. It is difficult, on the basis of STM alone, to explain the origin of the triangular misfit structure, but it may have a similar origin to that observed in the reverse system.<sup>[9]</sup>



**Figure 3-7** (a) STM image of 4 ML of Ni deposited at room temperature on Au{111} and annealed to 550 K STM image taken at 47 nm x 47 nm. ( $V = 0.92$  V,  $I = 0.16$  nA). (b) Schematic illustrating Au on Ni{111} forming a Moiré structure due to a 16 % lattice mismatch causing the two metals to go in and out of registry. (c) STM image of 4 ML of Ni deposited at room temperature on Au{111} and annealed to 600 K. STM image taken at 70 nm x 70 nm. ( $V = 0.79$  V,  $I = 2.0$  nA). (d) Schematic illustrating Au on Ni{111} forming a triangular structures. *Reproduced from reference 27.* An underlying nickel layer reconstructs such that nickel atoms alter from fcc to hcp sites. Above these hcp nickel sites; gold atoms occupy three-fold adsorption sites giving rise to the triangular misfit dislocations.

Further annealing to 650 K results in the reappearance of the herringbone reconstruction.

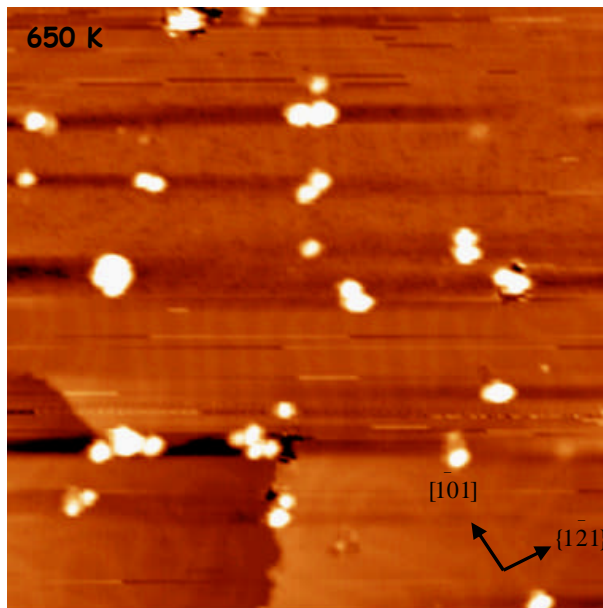


**Figure 3-8** STM image of  $\sim 4$  ML of Ni deposited at room temperature on Au{111} and annealed to 650 K. The herringbone reconstruction is visible. STM image taken at 74 nm x 74 nm. ( $V=0.9$  V,  $I=0.1$  nA).

The main conclusions drawn from the STM studies examining the deposition of nickel on Au{111} as a function of annealing are as follows:

1. Initial growth of nickel on Au{111} occurs in the elbows of the herringbone reconstruction. This site then acts as a nuclei for further aggregation of nickel island growth.
2. Nickel grows in a Stranski-Krastanov manner, whereby nickel grows initially in a layer-by-layer fashion followed by growth in the form of 3D islands. However, in this instance second layer growth occurs prior to the completion of the first layer with areas of exposed gold surface clearly visible.
3. Deposition of  $\sim 4$  ML of nickel on Au{111} as a function of annealing temperature produces a range of differing structures. Annealing of the bimetallic Au/Ni surface from 300 K to 500 K results in flattening of the large nickel islands. Further annealing to 550 K and to 600 K exhibits a Moiré

structure and triangular misfit dislocations respectively. At 650 K, the surface resembles that of clean gold with a disordered herringbone reconstruction visible.

## **3.3.2 MEIS STUDIES**

### **3.3.2.1 SURFACE & SUB-SURFACE COMPOSITION**

The surface and subsurface composition is obtained by taking cuts down the blocking channels as shown in figure 3-9. The blocking channels are regions of low ion counts due to the phenomenon of blocking as illustrated by the blue/green colour in the ion intensity. The arrows (a-c) in figure 3-9 represent the 3-, 2- and 1-layer blocking geometries respectively. The summation of ion intensity over a narrow angular range at the base of each blocking channel produces a plot of ion intensity *versus* energy of the scattered ions. Each plot presents the number of gold and nickel atoms illuminated in each experimental geometry.

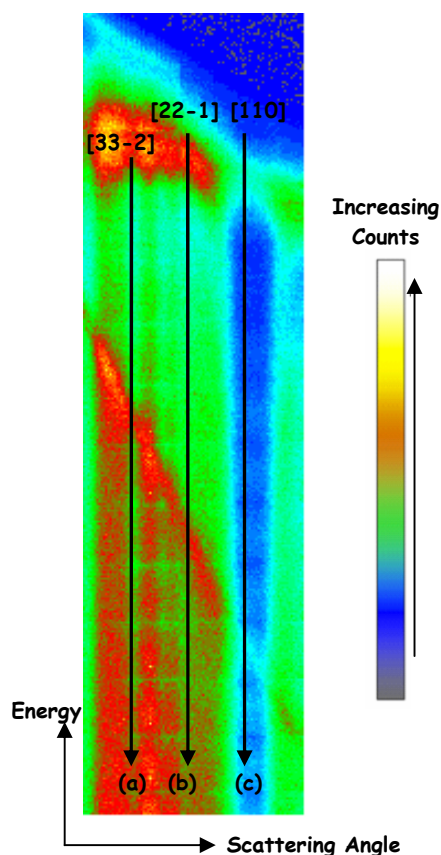


**Figure 3-9** Raw MEIS tile. Arrows (a-c) represent cuts taken down each blocking channel corresponding to the 3-, 2- and 1- layer blocking geometries respectively. The summation of ion intensity over a narrow angular range at the base of each blocking channel produces a plot of ion intensity *versus* energy of the scattered ions.

Figures 3-10 (a-c) are ion intensity *versus* energy plots as a function of annealing temperature for the 1-, 2-, and 3-layer geometries. This corresponds to the top, top two, and top three surface layers respectively. These plots show the variation in position and intensity of the gold related features.

The room temperature deposition of  $\sim 8$  ML of nickel on Au{111} results in three peaks:

1. A nickel peak of low intensity ranging from 84-90 keV (not shown for clarity purposes). Problems with the correction file for tiling the individual scans in Daresbury resulted in substantial background noise in the data with the consequence that the nickel intensity peak could not be used for quantitative measurements. This was due to the installation of a new data acquisition electronics system. The MEIS station scientists overestimated the maximum count rate possible for ion detection with the result that each individual 2D data

set was slightly distorted. When the data are tiled together, the distortion is manifested as a series of oscillations in the background that made analysis of the weak nickel signal difficult.

2. A broad gold subsurface peak ranging from 94-97 keV in figures 3-10 (a-c).
3. A gold surface peak of low intensity at a slightly higher energy than the subsurface peak ranging from 96-98 keV in figures 3-10 (a-c).

As the sample is progressively annealed to higher temperatures, the nickel peak loses intensity and by 600 K disappears.

From 300-410 K, the surface gold peak decreases in intensity. From 410-630 K, the surface gold peak re-emerges and steadily increases in intensity. At 630 K, the gold related feature resembles that of clean gold in both intensity and position.

With progressive annealing of the sample, three shifts of the gold subsurface peak occur. At 460 K, the subsurface peak shifts to lower energy – i.e. away from the gold surface peak. At 510 K the gold subsurface peak shifts back to a higher energy by  $\sim 1$  keV. From 510-570 K, the gold subsurface peak shifts to a lower energy and broadens. From 570-630 K, the gold subsurface peak gradually decreases in intensity and broadens until eventually disappearing at 630 K.

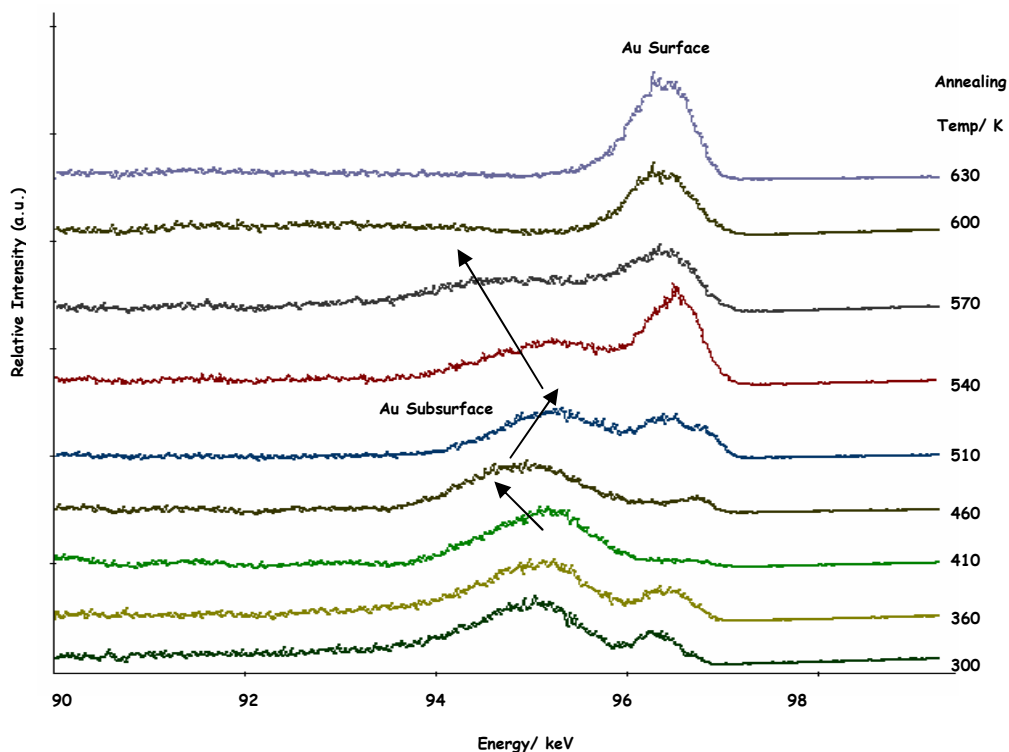


Figure 3-10 (a) Ion intensity *versus* energy plots for the 1-layer illumination geometry. This corresponds to an exit direction of [110]. ~ 8 ML of nickel deposited on Au{111} at room temperature as a function of annealing temperature.

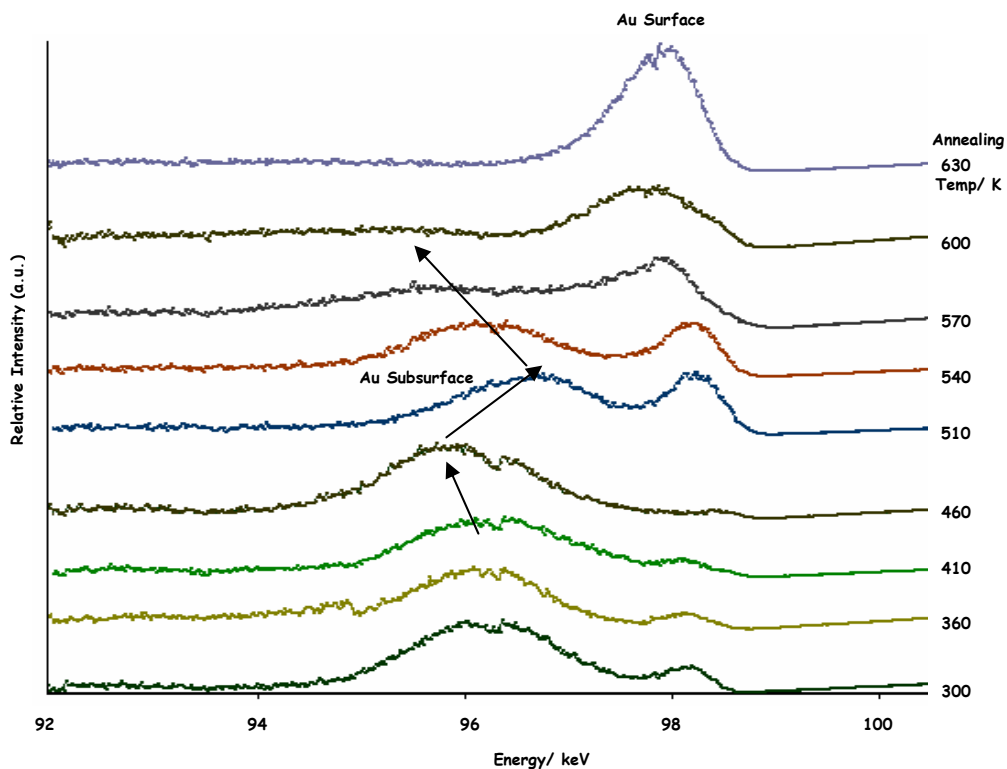
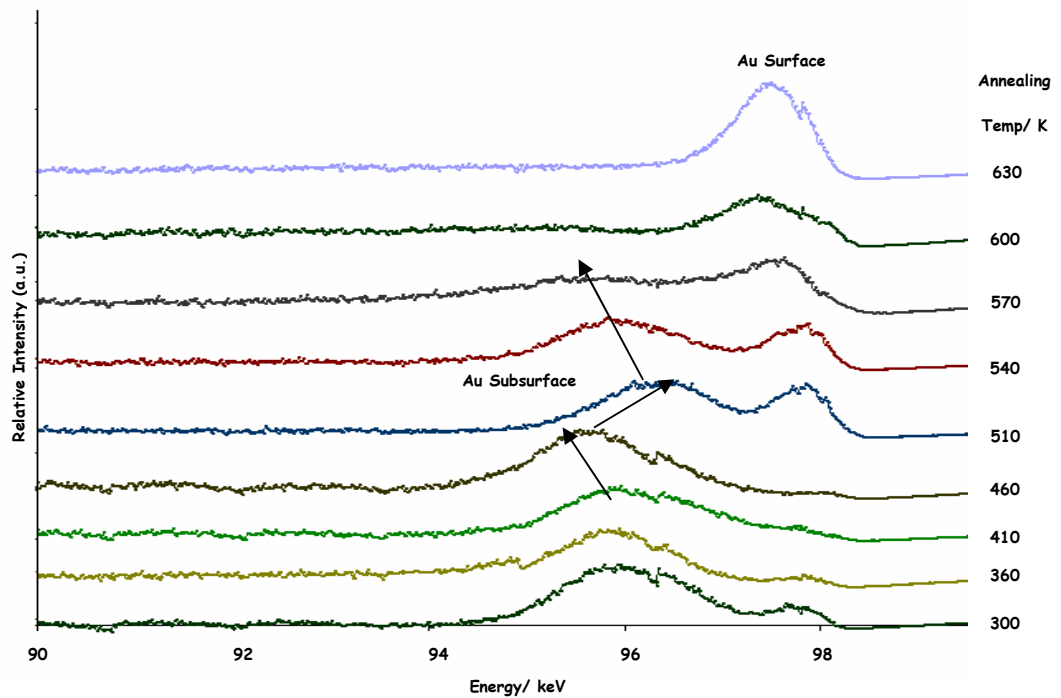


Figure 3-10 (b) Ion intensity *versus* energy plots for the 2-layer illumination geometry. This corresponds to an exit direction of [221]. ~ 8 ML of Ni was deposited on Au{111} at room temperature as a function of annealing temperature.



**Figure 3-10 (c)** Ion intensity *versus* energy plots of the 3-layer illumination geometry. This corresponds to an exit direction of  $[3\bar{3}2]$ .  $\sim 8$  ML of nickel deposited on Au{111} at room temperature as a function of annealing temperature.

The difference in energy (keV) between the gold surface and gold subsurface peaks gives an indication of the thickness of the nickel overlayer, which directly relates to the energy loss the ion beam undergoes when travelling through the sample. The actual thickness of the nickel overlayer was estimated, utilising the stopping power of  $\text{He}^+$  in gold (284 eV/nm) and the pathlength of the scattered ions. Taking into account the lattice parameter of gold and the number of layers illuminated, an average of 8 ML of nickel was estimated to be deposition on the Au{111} surface for the 1-, 2- and 3-layer illumination geometries.

Examining the compositional graphs of ion intensity *versus* energy in figures 3-10 (a-c); the energy scale (keV) can be viewed as a mass scale enabling elemental determination. At a given scattering angle,  $\theta$ , ions will lose more energy in a collision with light target atoms than with heavier target atoms. Energy losses for inelastic collisions depend upon the

mass of the incident ions ( $\text{He}^+ / 4$ ) and the mass of the surface atoms (Au 197/Ni 59) and the relative positions of the Au/Ni related features in figures 3-10 (a-c) are indicative of this. Hence, the nickel peak occurs at a substantially lower energy than the gold subsurface and surface peaks. The gold subsurface peak is at a slightly lower energy than the gold surface peak because as the ion beam moves through the sample, it undergoes inelastic losses and its energy decreases.

The presence of a broad subsurface gold peak upon deposition of nickel on Au{111} is indicative of a contribution from gold atoms buried beneath a thick nickel overlayer or the possible formation of a subsurface alloy. The former is more likely as indicated by a shift of the gold subsurface peak closer to the gold surface peak at 510 K.

The growth of nickel on Au{111} will result in a strained nickel overlayer. This can be attributed to a large difference in the nearest neighbour distance of gold (2.884 Å) and nickel (2.491 Å). As ions lose energy proportional to the distance travelled within the sample, gold subsurface atoms could be visible. This is a direct result of ineffective shadowing of the gold atoms by the strained nickel overlayer. Surface layer relaxation, lattice vibrations, and adsorbate reconstructions can also alter the shadow cone positions such that subsurface atoms may be illuminated by the ion beam thereby, contributing to the backscattered ion yield. However, in this instance, the surface layer relaxation is not thought to a major contributing factor, as this would have been verified by a shift in the blocking dips (the reader is referred to the following section 3.3.2.3). Consequently, the presence of the gold subsurface feature is most likely a result of a large lattice mismatch where the thick nickel overlayer ineffectively shadows the underlying gold atoms.

The presence of a gold surface feature in the ion intensity *versus* energy compositional graphs suggests the nickel deposit does not grow pseudomorphically. The fact that a small

surface Au peak is observed in the MEIS data suggest that, upon deposition, nickel segregates into islands with areas of gold surface still exposed to the incoming ion beam, hence contributing to the back scattered ion yield.

The growth of 3D crystallites of nickel prior to the completion of the first monolayer is validated by the STM topographic image presented in figure 3-4 (e-f). Nickel islands are clearly visible separated by regions which are consistent with being exposed Au surface. The nickel islands are several Ångstroms in height and preferentially growing in the herringbone elbows, followed by further growth of these islands into monolayer ribbons. Second layer growth begins before the first layer is completed with areas of exposed gold clearly visible. Consequently, the presence of a gold surface feature in the compositional data is ascribed to the growth mechanism of nickel via 3D island formation with areas of gold surface still exposed to the incoming beam, thereby contributing to the backscattered yield.

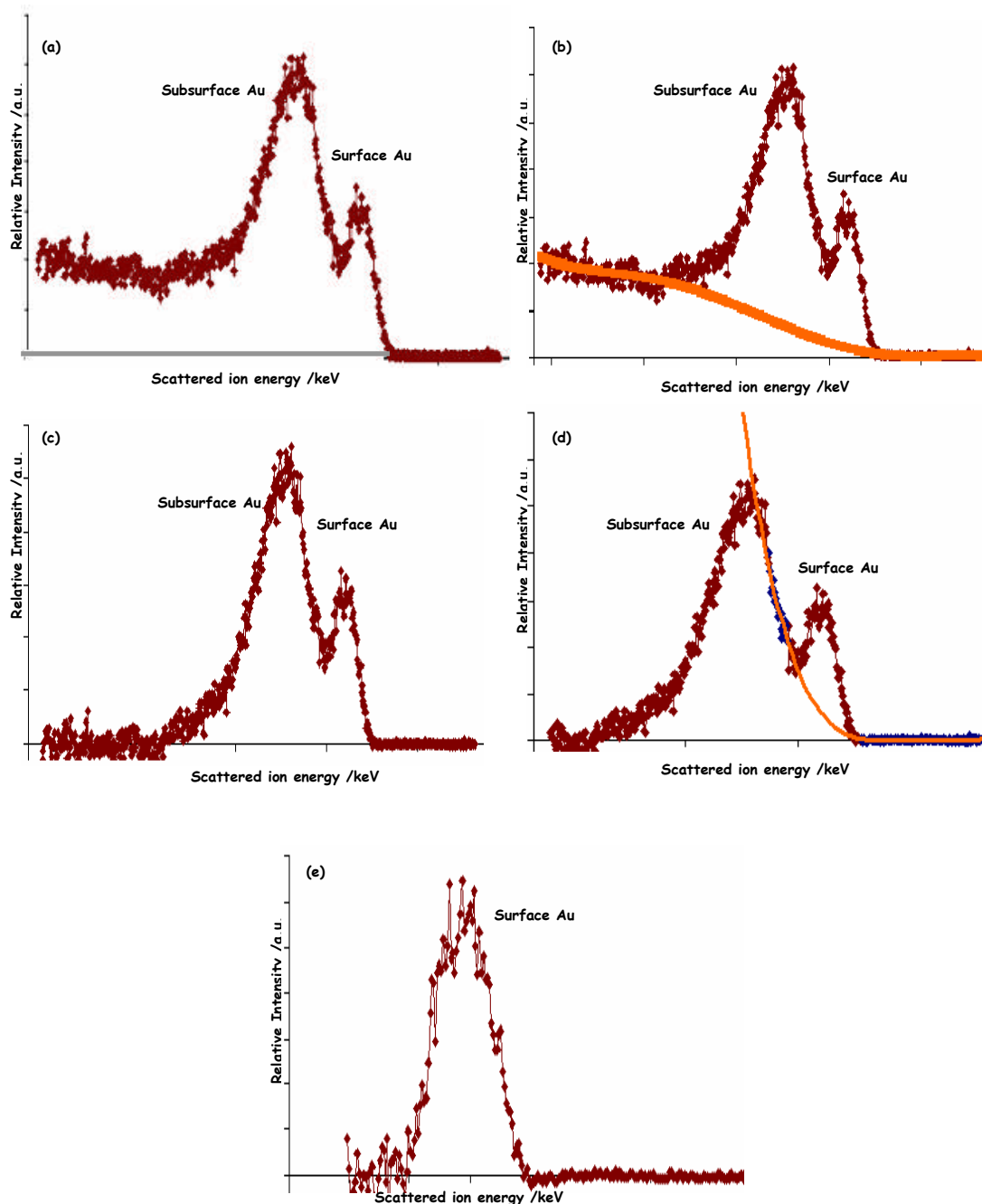
While Au/Ni alloy formation at room temperature is thermodynamically favourable at certain coverages,<sup>[8]</sup> in this occasion, the thick nickel overlayer consisting of 3D islands does not flatten out until an annealing temperature of 410-460 K. This is indicated by the decrease in intensity of the surface gold peak, which is consistent with the flattening of the nickel overlayer covering exposed gold thereby blocking a back contribution of scattered ions. As the nickel overlayer flattens upon annealing to 460 K, the gold subsurface peak broadens and shifts to a slightly lower energy. This shift cannot simply be explained by a flattening of the Ni overlayer since one would expect the sub-surface peak to become sharper and closer<sup>[8]</sup> to the surface peak in energy. The observed behaviour is best explained by a flattening of the overlayer and the onset of dissolution of Ni into Au producing a relatively thick film whose structure does not have the lattice parameter of Au, hence pushing the subsurface Au peak to lower energy.

At 510 K, an abrupt change in the spectra is observed. The subsurface gold peak shifts closer to that of the gold surface peak while concurrently the gold surface peak increases. This is attributed to the inter-diffusion of gold to the surface forming a bimetallic Au/Ni surface. Further annealing to 540-600 K results in the enhancement of the Au surface peak and the broadening and shifting to lower energy of the subsurface Au peak. With progressive annealing, the nickel diffuses into the bulk and by 630 K; the gold feature resembles that of clean gold in both intensity and position. The behaviour of the subsurface peak in the 510-630 K annealing range is consistent with the formation of a relatively thick Ni/Au alloy of varying composition. A relatively thin Ni rich alloy would be relatively ineffective at shadowing the underlying material. This would result in a subsurface Au signal peaking at an energy close to that of the surface Au peak. A gold rich Au/Ni alloy would have a lattice parameter close to that of Au, so to a first approximation aligning the beam in a 3-layer trajectory for bulk Au{111} would be close to an aligned beam for the alloy overlayer. However, since there is a small discrepancy in the lattice parameters, the shadowing of alloy atoms will become less and less effective with depth below the surface. Hence the subsurface signal will shift to deeper energies with increasing Au content in the alloy. Once the Ni has diffused completely into the bulk, the lattice parameter of the surface returns to that of Au and only a surface peak is observed as is typical for a 3-layer incident geometry.

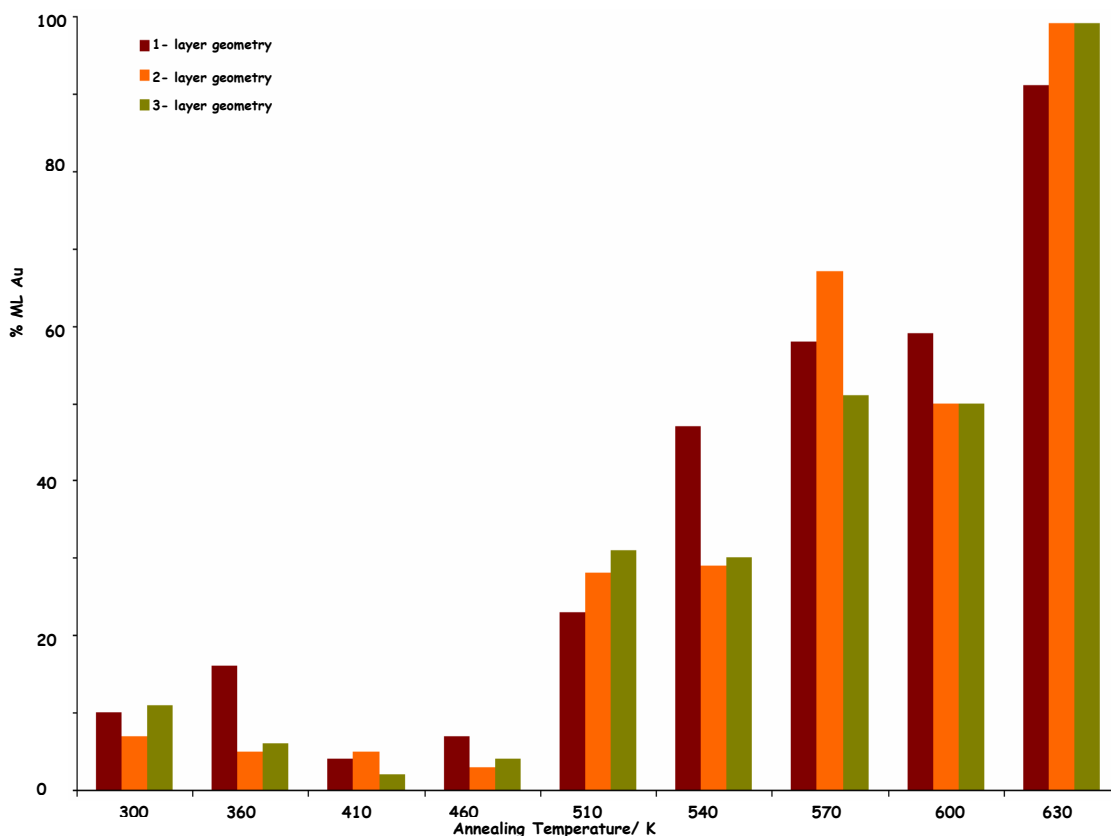
From figures 3-10 (a-c) it is evident that the gold surface and gold subsurface peaks are not well-resolved and with peak overlap occurring. Consequently, it proved difficult to extract accurately from the MEIS ion intensity *versus* energy plots, the gold intensity per layer geometry. A series of background subtraction fits were utilised to remove the subsurface gold contribution from the data. An example of the analysis is given in figure 3-11.

Figure 3-11 (a) presents the raw data. Fitting a 6<sup>th</sup> order polynomial to the background signal to the low energy side of the subsurface peak and the high energy side of the surface peak (figure 3-11(b)) effectively ‘flattens’ the data by subtracting the intensity contained within the polynomial from the raw data (figure 3-11(c)). A second background subtraction is taken to remove the contribution of the gold subsurface from the gold surface using a 6<sup>th</sup> order polynomial (figure 3-11(d)) resulting in a gold surface peak whose intensity can be measured. All MEIS intensity *versus* energy plots presented in this thesis were analysed in this manner.

Figure 3-12 is a bar chart representation of the percentage monolayer of gold as a function of annealing temperature contained in the 1-, 2-, and 3- layer geometries. A smooth increase in % ML of gold is evident with thermal treatment. This trend indicates nickel is diffusing through to the gold bulk forming surface structures upon annealing.



**Figure 3-11** A series of background subtractions which were used to remove the subsurface gold contribution from the surface gold data. **(a)** Intensity *versus* energy plot of the raw data. **(b)** Fitting of a 6<sup>th</sup> order polynomial to the raw data. **(c)** Flattening of the raw data by subtracting the intensity contained within the polynomial from the raw data. **(d)** Background subtraction of gold subsurface from the gold surface using a 6<sup>th</sup> order polynomial. **(e)** Surface gold peak.



**Figure 3-12** Bar chart representation of the monolayer percentage of gold contained in the 1-, 2-, 3-layer geometries as a function of annealing temperature. This corresponds to the top, top two, and top three surface layers respectively.

By measuring the surface Au peak intensity and normalising it to the clean Au surface for the 1-, 2- and 3-layer geometries, it is possible to gain a reliable estimate of the composition of the top few layers of the surface. Examining the 1-layer geometry (top surface layer) in figure 3-12; the room temperature deposition of nickel ( $\sim 8$  ML) on Au{111} results in 0.11 ML of gold exposed at the surface. Annealing of the surface to 360 K does not alter the composition of gold greatly. Thermal treatment to 410 K reduces the composition of gold to 0.04 ML. This can be explained by the flattening of the thick nickel 3D islands thereby covering the exposed gold surface areas. Annealing to 460 K results in a similar composition of 0.07 ML Au.

Annealing to 510 K increases the composition of gold in the 1-layer geometry to 0.23 ML of Au as gold diffuses to the surface. Similarly, the 2- and 3-layer geometries have 27 and

31% gold respectively. The fact that relatively little difference is observed between the composition of the top, top 2 and top 3 layers suggests that an alloy film, several layers thick is formed under these conditions. Annealing to 540 K further increases the gold composition at the top surface layer to 0.47 ML Au as nickel begins to diffuse to the gold bulk. The 2- and 3-layer geometries have similar compositions indicating a bimetallic Au/Ni structure is present in the top, top two and top three surface layers.

Thermal treatment to 570-600 K results in similar compositions of approximately 0.60 ML Au in the 1-layer geometry. By 630 K, no nickel is present at the surface region. A diagrammatic illustration of the aforementioned is presented in figure 3-13.

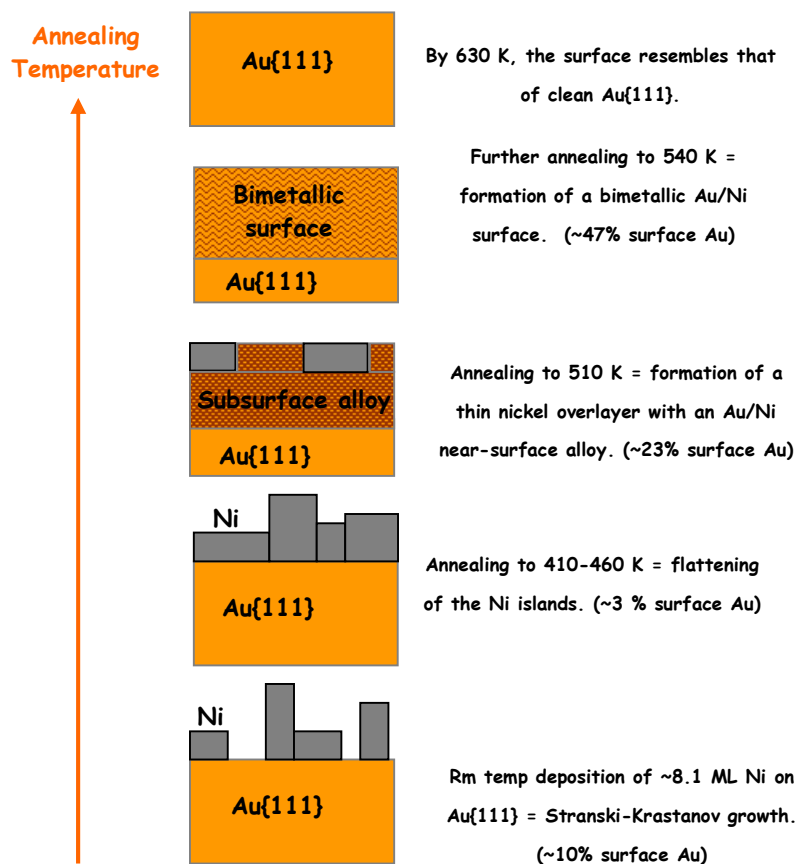


**Figure 3-13** Schematic illustration of alloy formation when ~8 ML of nickel is deposition on Au{111} at 300 K as a function of annealing temperature.

The main conclusions drawn from the MEIS compositional analysis include:

1. Nickel does not grow pseudomorphically on Au{111} at room temperature. Upon nickel deposition, the nickel agglomerates into 3D islands with areas of gold surface still exposed. Second layer growth occurs prior to the completion of the first layer with areas of exposed gold surface clearly visible. STM topographic images have verified this. Flattening of these thick nickel 3D islands occurs at an annealing temperature of 410-460 K.
2. A subsurface Au/Ni alloy is formed upon annealing to 510 K with a gold composition of 0.23 ML. Annealing to 540 K results in a bimetallic Au/Ni surface with a gold composition of 0.47 ML.
3. Annealing to 570 K initiates further inter-diffusion of gold to the top surface layer with a composition estimated to be  $\sim 0.60$  ML Au. This is in good agreement with STM where a Moiré structure was observed whose lattice parameter is consistent with a Au:Ni ratio of approximately 2:1.
4. By 630 K, nickel has diffused to the bulk and the Au{111} surface is restored to that of clean gold.

### 3.3.2.3 SURFACE AND SUB-SURFACE STRUCTURE

Information on the structure of the surface and sub-surface of a single crystal sample are attained by taking polygons specific to a number of layers (also referred to as ‘cuts’) across regions of the gold surface, gold subsurface, nickel surface and gold bulk in the raw tiled data and projecting the intensity contained within the cuts into ion intensity *versus* scattering angle plots. This is illustrated in figure 3-14.

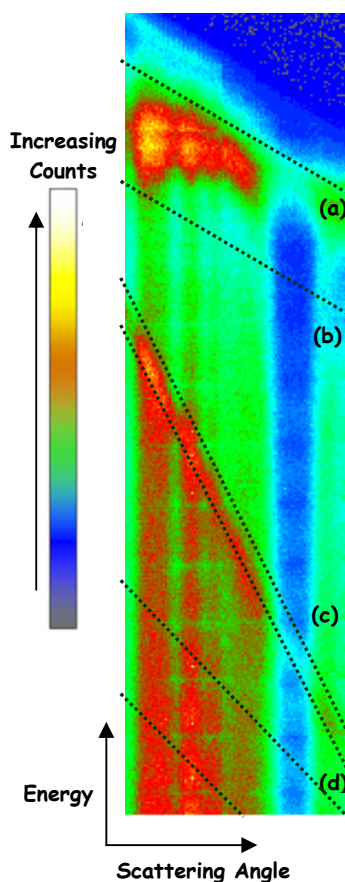


**Figure 3-14** Raw MEIS tile illustrating the position of the relative Au/Ni related features and the associated ‘cuts’ taken with polygons. The intensity contained within the cuts is projected into ion intensity *versus* scattering angle plots.

**(a) Au Surface**—Polygon cuts were taken across the tile specific to 2-, 4- and 6-layers.

**(b) Au Subsurface**- superimposed onto Au surface at a lower energy due the pathlength dependent inelastic energy loss of the ion beam. 12-layer polygon cuts were taken across the tile. The relative intensity contained within the cut (i.e. of 12-layers) was then subtracted from the gold surface 6-layer data.

**(c) Ni Surface**-superimposed onto Au Bulk due to mass of nickel atoms. 6-layer cuts were taken and the relative intensity contained within the cut (i.e. of 6-layers) was then subtracted from the gold bulk data.

**(d) Au Bulk**-scattered ions are at a low energy due to the distance the ions have travelled ( $\sim$  several nm) into the bulk before being detected. Polygon cuts were taken across the tile specific to 6-layers.

The gold surface data were attained by taking cuts representative of the top 2-, 4- and 6-layers across the tiled raw data and projecting the intensity contained within the cuts into ion intensity *versus* scattering angle plots. Similarly, the gold subsurface blocking spectra were attained by taking a 12-layer cut across the tiled raw data (this equates to gold surface & subsurface) and projecting the intensity contained within the cuts into ion intensity *versus* scattering angle plots. The 6-layer gold surface data were then subtracted from the 12-layer data giving the subsurface structural data.

Similar to the gold surface and subsurface plots, the nickel data were extracted by taking a 6-layer cut across the tiled raw data and projecting the intensity contained within the cuts into ion intensity *versus* scattering angle plots. The nickel surface data are derived from a similar energy to information from the Au bulk. Since the scattering cross section is proportional to  $z^2$ , the nickel surface data are superimposed on a sizeable background

derived from the bulk Au signal. Extracting the nickel surface structural data involves calculating the energy loss the ion beam experiences as it travels through 6-layers of (a) the gold bulk containing the nickel surface feature and (b) the gold bulk itself. Subtraction of the relative intensities of (b) from (a) other yields the nickel surface data.

Figure 3-15 displays gold bulk ion intensity *versus* scattering angle plot as a function of annealing temperature. As would be expected, the gold bulk data do not change upon deposition of nickel or with progressive annealing of the sample.

Figures 3-16, 17 and 18 are the 2-, 4- and 6-layer gold surface ion intensity *versus* scattering angle plots as a function of annealing temperature respectively. No difference in gold structure between the 2-, 4- and 6-layers was observed.

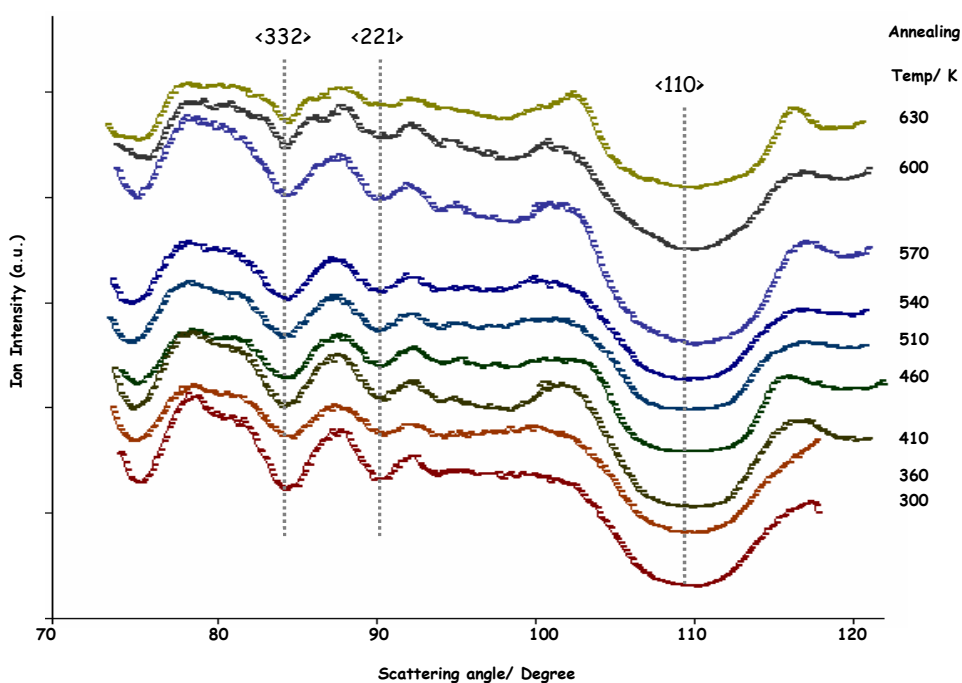


Figure 3-15 Gold bulk 6-layer ion intensity *versus* scattering angle plot as a function of annealing temperature.

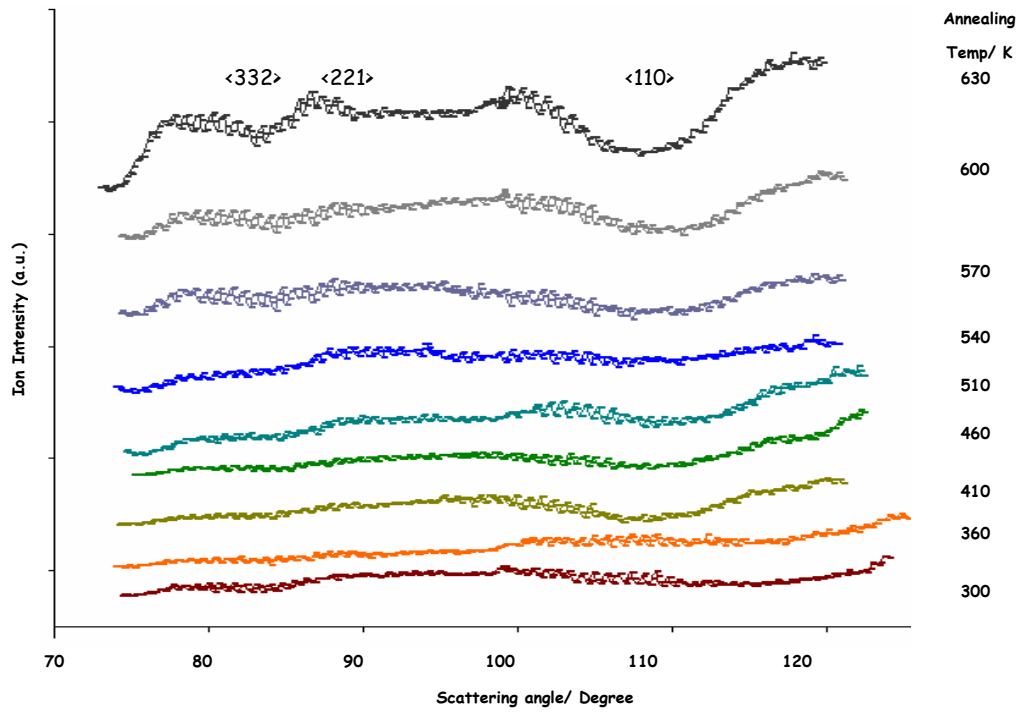


Figure 3-16 Gold surface 2-layer ion intensity *versus* scattering angle plot as a function of annealing temperature.

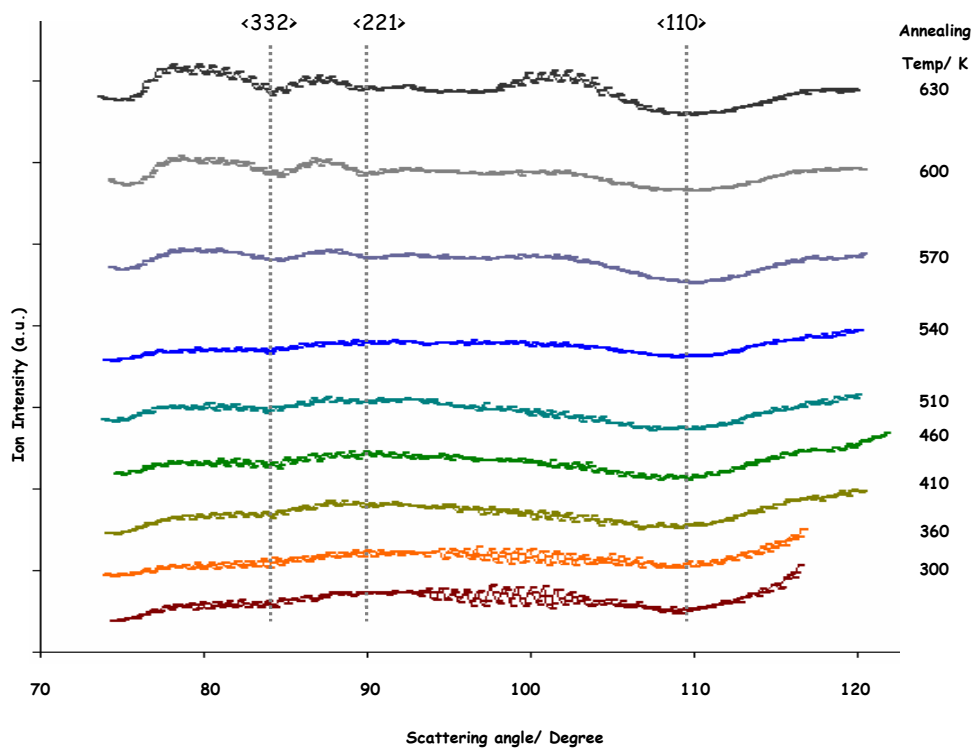


Figure 3-17 Gold surface 4-layer ion intensity *versus* scattering angle plot as a function of annealing temperature.

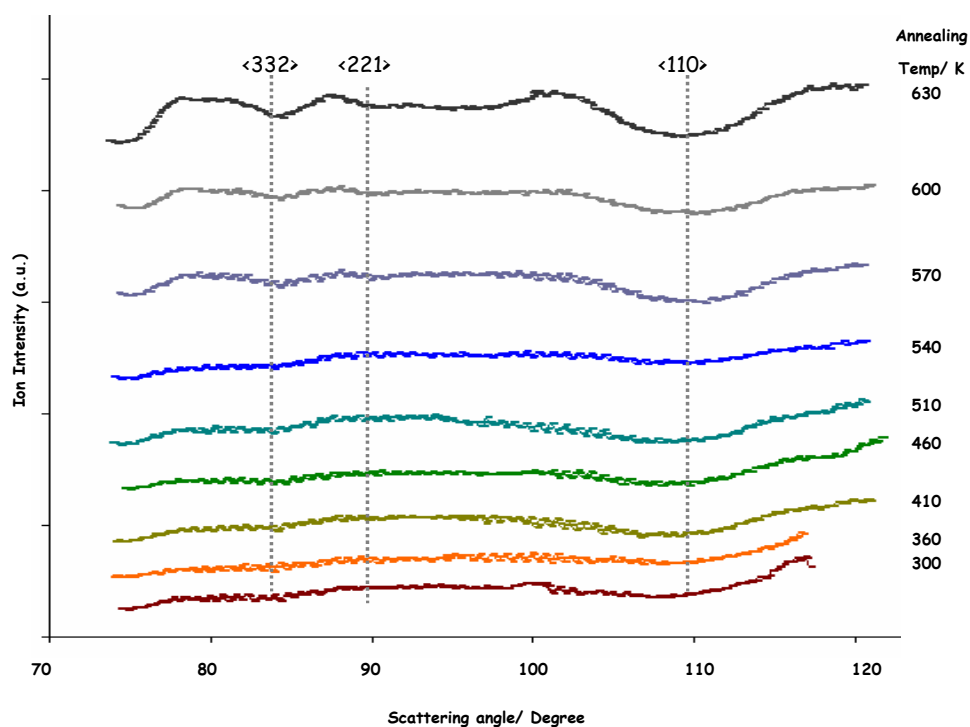


Figure 3-18 Gold surface 6-layer ion intensity *versus* scattering angle plot as a function of annealing temperature.

The blocking spectrum for the gold surface region is featureless upon deposition of  $\sim 8$  ML of nickel at room temperature. With progressive annealing of surface, gold regains its surface structure as nickel diffuses into the bulk. The lack of gold surface features upon deposition of nickel at room temperature is an indication that nickel is not growing pseudomorphically.

With progressive annealing of the surface, gold begins to regain its structure as nickel diffuses into the bulk thereby exposing the gold surface. However, at an annealing temperature of 540 K, the blocking features decrease slightly in intensity. This can be attributed to Au/Ni alloy formation. This correlates well with the compositional data and indicates the Au/Ni alloy possesses a different structure to that of surface gold.

With further annealing to 570 K, the gold surface blocking features increase in intensity and depth and by 630 K resemble the gold bulk.

Figure 3-19 is a 6-layer gold subsurface ion intensity *versus* scattering angle plot as a function of annealing temperature. The blocking features of the gold subsurface closely resemble those observed in the gold bulk spectra. Initially at room temperature, the blocking features are deep and well-defined. With progressive annealing, the blocking features broaden and decrease in depth. This suggests that considerable intermixing of the Au/Ni alloy has occurred.

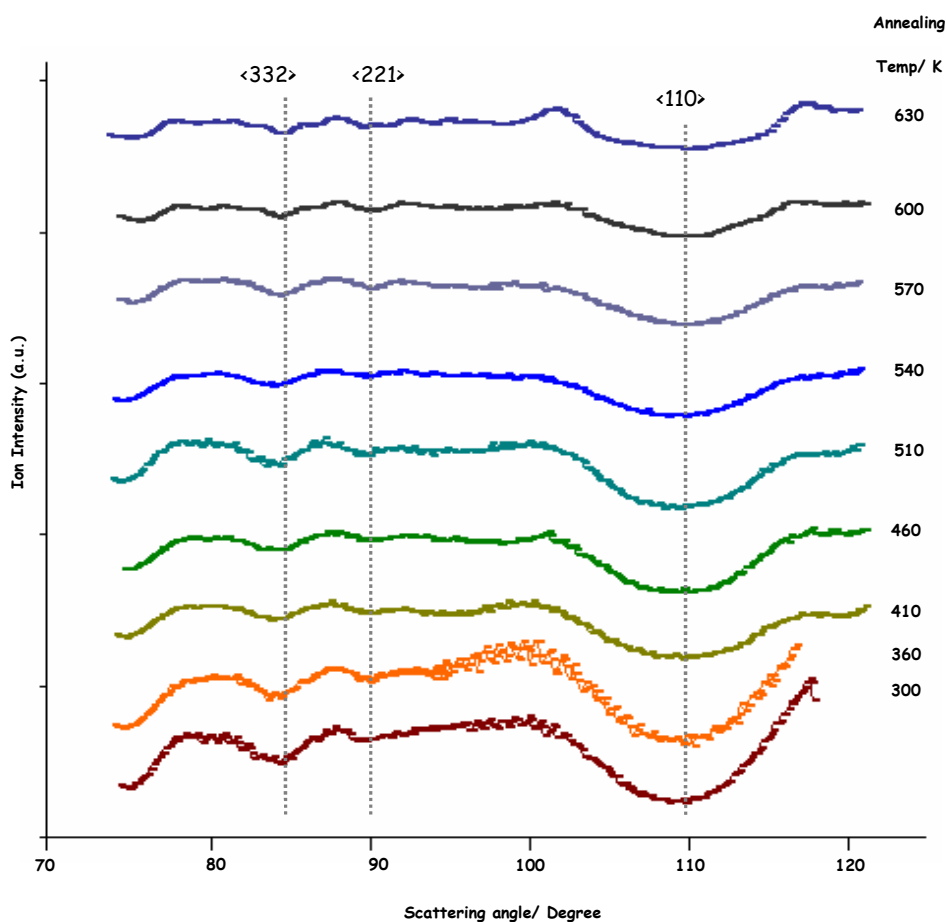


**Figure 3-19** Gold subsurface – 6 layer, ion intensity *versus* scattering angle plot as a function of annealing temperature.

Figure 3-20 is a 6-layer nickel surface ion intensity *versus* scattering angle plot as a function of annealing temperature. ~8 ML of nickel was deposited on the Au{111} surface at room temperature. The structure adopted by the nickel is not significantly different to that of the gold bulk. Progressive annealing results in the loss of blocking features as nickel diffuses into the bulk.

The presence of nickel on Au{111} will result in strain at the surface due to a large lattice mismatch of 15.7 %.<sup>[8]</sup> This in theory should be discernible by a shift in the nickel overlayer in relation to the gold bulk. However, no dramatic changes in the position of the blocking features for the nickel surface data were observed which implies the nickel overlayer and the Au/Ni bimetallic surface have a similar structure to Au{111} and that considerable intermixing of the two elements has occurred. However, a more realistic explanation of this affect can be attributed to a contribution from the gold bulk data. The nickel surface data are superimposed on the Au bulk data. Since the scattering cross section varies as  $z^2$ , the contribution from Au is significant. Subtraction of the relative intensities of the gold bulk data from the aforementioned equates to the nickel surface data. It is probable the presented nickel surface data in figure 3-20 contains considerable contribution from the gold bulk data. In conjunction to this, problems with the correction file for tiling the individual scans arose in Daresbury resulting in substantial background noise in the nickel data.

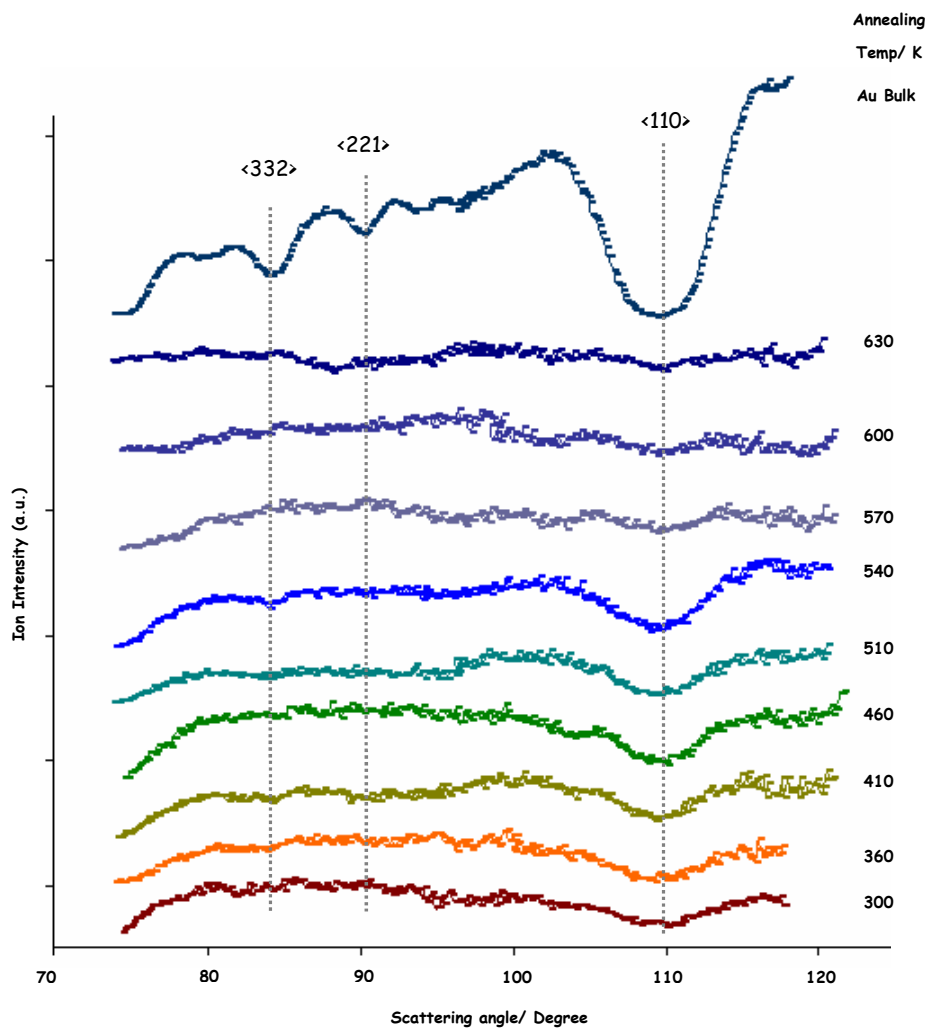


Figure 3-20 Nickel surface 6-layer ion intensity *versus* scattering angle plot as a function of annealing temperature.

The following set of graphs in figure 3-21 (a-i) present the 6-layer ion intensity *versus* scattering angle plots for all four regimes namely; gold bulk, gold surface, gold subsurface and nickel surface as a function of annealing temperature.

As should be expected, room temperature deposition of  $\sim 8$  ML Ni on Au{111} does not affect the gold bulk data as indicated by the presence of well-defined blocking dips. This remains the case throughout thermal treatment.

While, no obvious shift in the gold surface blocking features with thermal treatment were evident; there were subtle changes in the shape and intensity. With progressive annealing,

the blocking features increase in intensity with the exception of annealing to 540 K where the blocking features decrease in intensity. This decrease indicates a change in the gold surface structure. From 570 K the blocking features steadily increase in depth and intensity and resemble the gold bulk data by 630 K.

At room temperature, the gold subsurface blocking features are well-defined and bear a resemblance to the gold bulk data. This is consistent with an incommensurate nickel overlayer that does not alter the gold surface blocking features. Upon annealing to 410 K and 460 K, the gold subsurface blocking features shift slightly to a higher scattering angle. This correlates well with the compositional data in that at this temperature regime, the thick nickel 3D islands flatten. It is probable that the thick nickel overlayer produces considerable strain at the interface i.e. the lattice parameter of the surface region is altered with respect to that of the bulk. This is manifested in a slight shift of the blocking features to a higher scattering angle.

Further annealing to 510 K and 540 K shifts the gold subsurface blocking features back to their original scattering angle position. This can be attributed to a reduction of nickel at the surface as it diffuses to the subsurface regions. Annealing to 570-600 K decreases the intensity of the subsurface blocking features as nickel diffuses to the bulk. By 630 K, the gold subsurface blocking features resemble the gold bulk data but with decreased intensity.

In the reverse system, 4 ML Au/Ni{111}, Baddeley and co-workers observed substantial differences in the position of the blocking features for gold when compared to the nickel surface and nickel bulk data.<sup>[8]</sup> Similarly, Baddeley and co-workers also observed featureless structural data for the nickel surface despite the fact that 4 ML of gold was deposited on the Ni{111} surface. They attributed this occurrence to a contracted gold

overlayer where each gold atom along a given azimuthal direction is in a slightly different adsorption site with respect to the nickel beneath. They postulate each nickel atom will have blocking features at different scattering angles due to the contracted overlying gold atoms; resulting in blocking features at scattering angles typical of Ni{111} but with reduced depth's i.e. featureless. It is probable that a similar effect is occurring in the present case Ni/Au{111} with regard to the gold surface structural data.

Initially, at room temperature, the nickel surface blocking dips are featureless and with progressive annealing up to 540 K, the nickel blocking features increase in intensity adopting a gold bulk-like structure. From 570-600 K the nickel blocking features decrease in intensity and by 630 K, the structural data indicates no nickel is present in the system.

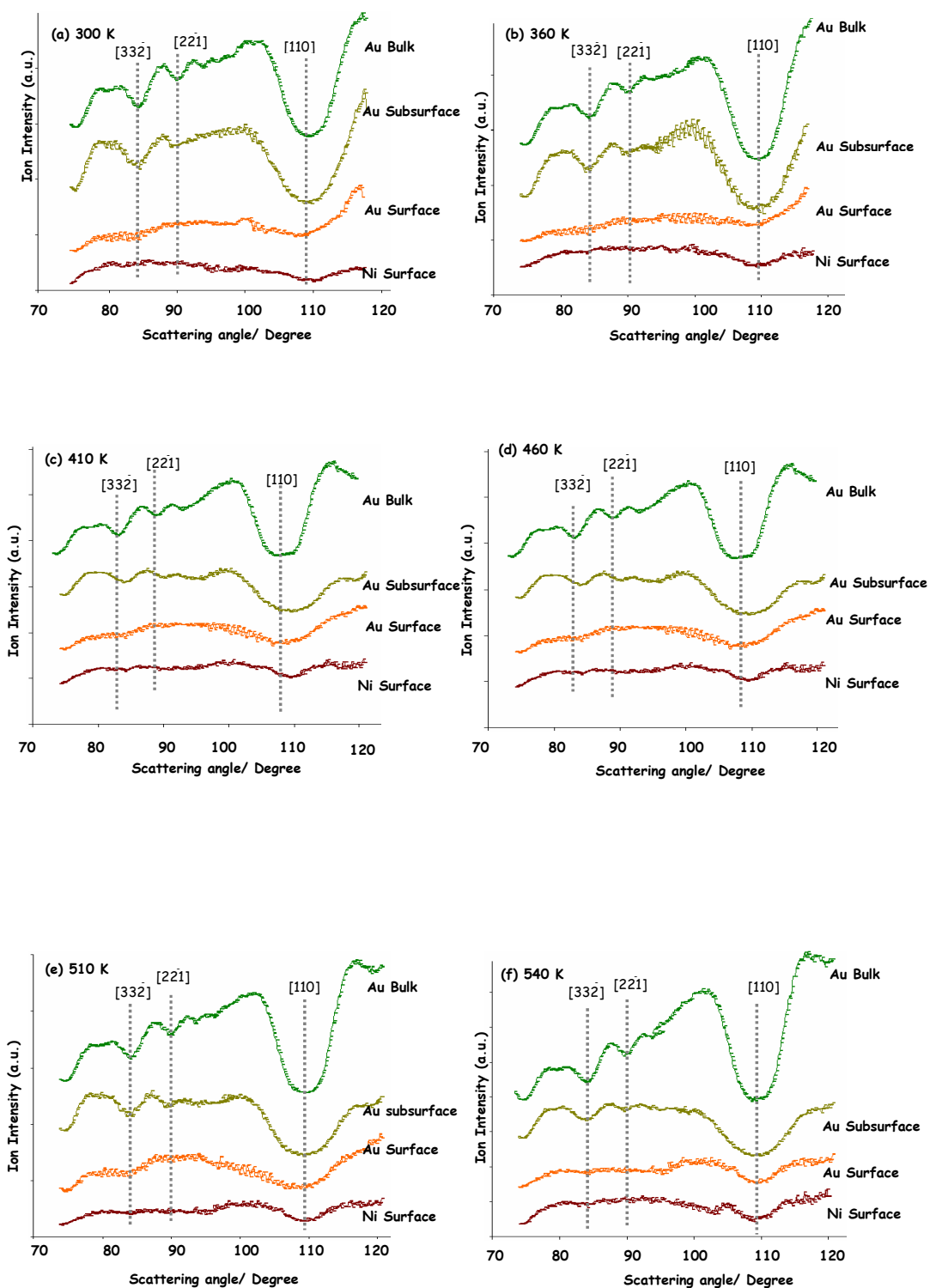


**Figure 3-21** Scattering angle *versus* ion intensity plots (6-layer) for all four regimes; gold bulk, gold surface, gold subsurface and nickel surface as a function of annealing temperature. (a) 300 K (b) 360 K (c) 410 K (d) 460 K (e) 510 K (f) 540 K.

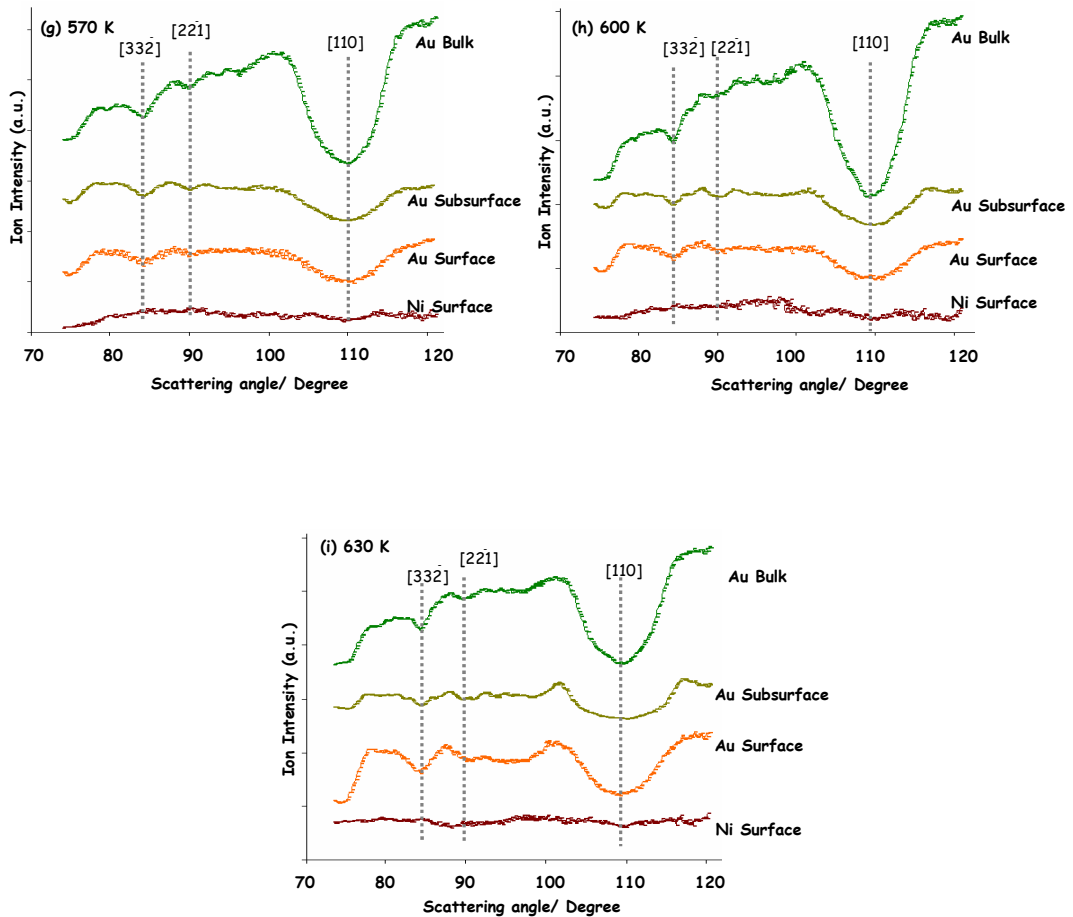


**Figure 3-21** Scattering angle *versus* ion intensity plots (6-layer) for all four regimes; gold bulk, gold surface, gold subsurface and nickel surface as a function of annealing temperature. **(g)** 570 K **(h)** 600 K **(i)** 630 K.

The main conclusions drawn from the MEIS structural data include:

1. The deposition of nickel on Au{111} has no effect on the gold bulk blocking features. This remains the case throughout thermal treatment.
2. Nickel does not grow pseudomorphically on Au{111} as indicated with the lack of gold surface structure after deposition of  $\sim 8$  ML of nickel at room temperature. With progressive annealing of surface, gold regains its structure as nickel diffuses into the bulk.

3. The gold subsurface blocking features resemble the gold bulk at room temperature in both position and intensity. Annealing to 410-460 K initiates a shift of these features to a higher scattering angle. This is analogous with the flattening of the nickel 3D islands; thereby producing strain at the interface. This is manifested in a slight shift of the blocking features to a higher scattering angle. Further annealing to 510 K and 540 K shifts the gold subsurface blocking features back to their original scattering angle position as nickel diffuses to the bulk. By 630 K, the gold subsurface blocking features resemble the gold bulk data but with decreased intensity.
4. The nickel blocking features were of low intensity after the room temperature deposited of nickel onto Au {111}. This implies that the nickel overlayer is not pseudomorphic. This is in contrast to the work of Jones *et al.*, on the reverse system, Ni{111}/ Au whereby the Au surface blocking spectra were dramatically different from the structure of the Ni bulk. This was explained by two symmetry-related growth modes for Au on Ni{111}.<sup>[8]</sup>
5. With progressive annealing, nickel diffuses to the gold bulk. By 630 K, the nickel data is featureless indicating negligible nickel in the system.

## 3.4 DISCUSSION

### 3.4.1 MORPHOLOGY OF AU{111}/NI SURFACES

The growth of nickel on Au{111} has been investigated with STM as a function of nickel coverage and annealing behaviour. Upon deposition at room temperature, nickel nucleates at the elbows of the Au{111} herringbone reconstruction. Regular arrays of nickel islands were observed; the location and spacing of which are determined by the herringbone

reconstruction. The size of the nickel islands increases with increasing nickel coverage. It has been previously disclosed that the nucleation and growth of nickel at these sites is initiated by an exchange process of gold atoms with nickel atoms.<sup>[23]</sup>

Initial deposition of nickel in the herringbone reconstruction produces circular islands. These islands then act a nucleus for further growth.<sup>[15,23-24]</sup> Increasing the coverage of nickel leads to growth of these circular islands to hexagonally faceted and triangular islands. Of interest, hexagonal and triangular islands tend to orient in opposing directions; the direction stipulated by the elbows of the herringbone reconstruction. Depending whether the elbow is 'pinched in' or 'pinched out' dictates the morphology of these islands. Hexagonal islands reside in the pinched out elbows of the reconstruction while conversely triangular islands reside in the pinched in elbows. With increasing coverage of nickel, these islands aggregate into monolayer ribbons. Nickel grows via Stranski-Krastanov growth mechanism i.e. layer-by-layer followed by growth of 3D islands. However, second layer growth begins prior to completion of the first layer; with areas of the gold surface still exposed. This proved important in deciphering the MEIS compositional data.

Deposition of ~4 ML of nickel on Au{111} and subsequent annealing produces an array of surface structures. Progressive annealing of the surface to 350-500 K results in flattening of the nickel islands. Further annealing to 550 K and to 600 K exhibits a Moiré structure and triangular misfit dislocations respectively. These structures are a form of stress relief due to a large lattice mismatch and strong Au-Ni at the interface. At 650 K, the surface resembles that of clean gold with a disordered herringbone reconstruction visible.

The periodicity of the Moiré structure was estimated to be  $\sim 80$  Å for the nickel (or Ni/Au) overlayer on Au{111}. This gives a lattice spacing for the bimetallic surface of  $\sim 2.76$  Å. Assuming a linear variation of lattice parameter with Au/Ni composition, a Au:Ni ratio of  $\sim 2:1$  was calculated. This is validated by the MEIS compositional analysis. The triangular misfit dislocations are attributed to a reconstruction of an underlying gold layer to accommodate the preference of nickel atoms to adopt three-fold sites. The distance between two triangles of same angular orientation was estimated to be  $\sim 90$  Å which indicates a substantial lattice mismatch between the Ni/Au near-surface alloy and the substrate Au{111}.

### 3.4.2 COMPOSITION OF AU{111}/NI SURFACES

Nickel does not grow pseudomorphically on Au{111} when deposited at room temperature due to a 15.9 % lattice mismatch. The compositional data for the 1-, 2- and 3-layer geometries show three features; a nickel surface feature, a gold subsurface feature and a gold surface feature. The energetic positions of these features can be determined because as ions scatter from deep lying atoms they undergo inelastic energy losses proportional to the path length within the sample, enabling a compositional depth profile to be attained.

The presence of these features is rationalised as follows. After Ni deposition at 300 K, the gold subsurface feature is ascribed to a contribution from gold atoms under a thick nickel overlayer. The nickel atoms are unable to effectively shadow the underlying gold atoms due the large lattice mismatch. The gold surface feature either derives from segregation of gold to the surface at 300 K or from areas of exposed gold surface that contribute to the backscattered ion yield. STM topographic images support the latter theory and the fact that the surface Au signal initially attenuates on annealing in the MEIS experiment indicates a wetting of the surface by Ni.

At room temperature, a composition of 10 % ML Au was determined for the 1-layer geometry i.e. the top surface layer. Annealing of the surface to 410-460 K flattens the nickel 3D islands and the gold composition reduces to ~3 % ML Au. Concurrently, the surface gold feature decreases in intensity as the nickel overlayer covers the exposed areas of gold surface thereby preventing a back contribution of scattered ions. The gold subsurface feature broadens to a lower energy as a result.

Further annealing of this surface to 510 K results in an increase in the visible mole fraction of gold to 0.23 in the 1-layer geometry. Similar values are obtained in each of the three aligned geometries. This indicates that an Au/Ni alloy with a relatively uniform composition exists in the top three layers. The peak in the subsurface gold feature shifts, by 1 keV, closer to the surface gold feature. This is indicative of a flat alloy surface with a relatively sharp interface with the underlying Au – in contrast to the initially deposited film.

In the temperature region where the Moiré structure is observed most clearly, the MEIS data indicate a ~2:1 Au:Ni ratio. This Moiré structure is also visible, though less clear, at lower annealing temperatures. At the lower temperature, it may be the case that the alloy of this composition is present along with pure Ni regions. In the STM, prior to the reappearance of the herringbone reconstruction, a surface structure exhibiting triangular misfit dislocations is observed. A similar structure is observed in the reverse system Au/Ni{111} albeit with a much shorter periodicity.

## BIBLIOGRAPHY

- [1] J. M. Walls; *Methods of Surface Analysis*. Cambridge University Press.  
ISBN 0-521-38690-x. 1
- [2] F. Besenbacher, I. Chorkendorff, B. S. Clausen, B. Hammer, A. M. Molenbroek, J. K. Norskov & I. Stensgaard. *Science*. **279** (1998) 1913.
- [3] A. M. Molenbroek & J. K. Norskov. *J. Phys Chem B*. **105** (2001) 5450.
- [4] D. D. Chambliss & S. Chiang. *Surf. Sci. Lett.* **263** (1992) L187.
- [5] D. D. Chambliss, K. E. Johnson, R. J. Wilson & S. Chiang. *J. Magnetism & Magnetic Mat.* **121** (1993) 1.
- [6] P. W. Murray, I. Stensgaard, E. Laegsgaard & F. Besenbacher. *Phys. Rev. B*. **52** (1995) R14404.
- [7] J. A. Rodriguez. *Surf. Sci. Rep.* **24** (1996) 223.
- [8] T. E. Jones, T. C. Q. Noakes, P. Bailey & C. J. Baddeley. *Surf. Sci.* **600** (2006) 2129.
- [9] L. Pleth Nielsen, F. Besenbacher, I. Stensgaard, E. Laegsgaard, C. Engdahl, P. Stoltze, K. W. Jacobsen & J. K. Norskov. *Phys. Rev. Lett.* **71** (1993) 754.
- [10] L. Pleth Nielsen, F. Besenbacher, I. Stensgaard, E. Laegsgaard, C. Engdahl, P. Stoltze & J. K. Norskov. *Phys. Rev. Lett.* **74** (1995) 1159.
- [11] C. Nagal, O. Haller, E. Platzgummer, M. Scidmid & P. Varga. *Surf. Sci.* **321** (1994) 237.

- [12] J. Jacobsen, L. Pleth Nielsen, F. Besenbacher, I. Stensgaard, E. Laegsgaard, T. Rasmussen, K.W. Jacobsen & J. K. Norskov. *Phys. Rev. Lett.* **75** (1995) 489.
- [13] K. Umezawa, S. Nakanishi, M. Yoshimura, K. Ojima, K. Ueda & W. M. Gibson. *Phys Rev. B.* **63** (2001). 035402.
- [14] K. Umezawa, T. Ito, S. Nakanishi & W. M. Gibson. *App. Surf. Sci.* **219** (2003) 102.
- [15] D. D. Chambliss, R. J Wilson & S. Chiang. *Phys. Rev. Lett.* **66** (1991) 1721.
- [16] B. Voigtlander, G. Meyer & N. M. Amer. *Surf. Sci.* **255** (1991) L529.
- [17] B. Voigtlander, G. Meyer & N. M. Amer. *Phys. Rev. B.* **44** (1991) 10353.
- [18] A. W. Stephensen, C. J. Baddeley, M. S. Tikov & R. M. Lambert. *Surf. Sci.* **398** (1998) 172.
- [19] E. I. Altman & R. J. Colton. *Surf. Sci.* **304** (1994) L400.
- [20] J. V. Barth, H. Brune, G. Ertl & R. J. Behm. *Phys. Rev. B.* **42** (1990) 9307.
- [21] B. Fischer, J. V. Barth, A. Fricke, L. Nedelmann & K. Kern. *Surf. Sci.* **389** (1997) 366.
- [22] D. D. Chambliss & R. J Wilson. *J. Vac. Sci. Technol. B.* **9** (1991) 928.
- [23] J. A. Meyer, I. D. Baikie, E. Kopatzki & R. J. Behm. *Surf. Sci. Lett.* **365** (1996) L647.
- [24] W. G Cullen & P. N. First. *Surf. Sci.* **420** (1999) 53.
- [25] F. Besenbacher. *Rep. Prog. Phys.* **59** (1996) 1737.
- [26] H. Brune. *Surf. Sci. Rep.* **31** (1998) 121.

- [27] K. Umezawa, S. Nakanishi & W. M. Gibson. *Surf. Sci.* **426** (1999) 225.
- [28] T. G. Owens, T. E. Jones, T. C. Q. Naokes, P. Bailey & C. J. Baddeley. *J. Phys Chem B* **110** (2006) 21152.

# Chapter 4

## *Characterisation of (S)-GA modified Au{111}/Ni Bimetallic Surfaces*

### **SYNOPSIS**

*This chapter details the characterisation of (S)-glutamic acid modified Au{111}/Ni bimetallic surfaces. The morphology of the bimetallic surface as a function of annealing temperature and nickel coverage is presented using Scanning Tunnelling Microscopy. Medium Energy Ion Scattering is used to probe adsorbate-induced segregation, while the adsorption and thermal stability (S)-GA on Au/Ni surfaces is examined using Reflection Adsorption Infrared Spectroscopy and Temperature Programmed Desorption.*

## 4.1 INTRODUCTION

In 1959, Richard P. Feynman pointed out that there is ‘*plenty of room at the bottom*’.<sup>[1]</sup> He predicted an exciting era of controlled nano-scaled fabrication of molecular architectures on substrates that had the potential to revolutionise science and technology. Such materials have many applications notably in the development of nano-scale devices, sensors and tools. There are two approaches to creating such nano-scale devices on substrates; these being the ‘top-down’ and ‘bottom-up’ techniques. The former use sophisticated tools such as electron beam writing and lithographic techniques allowing precision down to the sub-nanometre range. Essentially, ‘top-down’ techniques impose a structure or pattern on a substrate surface. In contrast, the ‘bottom-up’ approach aims to guide the assembly of atoms and molecules into well-ordered surface nanostructures and is based upon growth phenomena.<sup>[2]</sup> This approach aims to create nanostructures with controlled shape and composition through process such as adsorption, surface diffusion, nucleation and so forth. The advent of STM has enabled the imaging and manipulation of such atoms and molecules, enabling a better understanding of their self-organised and self-assembly processes.<sup>[3]</sup>

### 4.1.1 METAL-ORGANIC COORDINATION NETWORKS

Metal-directed self-assembly of functional molecules provides a new strategy for highly organised and controllable supermolecular architectures on surfaces. This approach involves self-organised metal-on-metal growth followed by the deposition of self-assembling functional molecules. The preferred nucleation of metal clusters such as nickel,<sup>[4]</sup> iron,<sup>[5]</sup> cobalt,<sup>[6]</sup> palladium<sup>[7]</sup> and rhodium<sup>[8]</sup> in the elbows of the Au{111} herringbone reconstruction are ideal substrates. For example, Clair *et al.*, have

demonstrated that cobalt<sup>[9]</sup> and iron<sup>[10]</sup> clusters grown on Au{111} in this manner can be corrosively oxidised by the adsorption of terephthalic acid (TPA).

The engineering of metal-organic coordination networks has received much attention as these novel materials potentially provide a pathway to porous materials for catalysis, gas storage and molecular recognition.<sup>[11-12]</sup> Transition metal carboxylates are also widely used as the building blocks for such supramolecular architectures with the aim to develop nanoporous networks with well-defined functionalisation. At the forefront of this research area are Kern, Barth and their co-workers. They have developed a successful approach in the production of 2D metal-organic networks.<sup>[13-18]</sup> In particular, the co-deposition of iron with carboxylic acid functionalised molecules such as terephthalic acid, trimesic acid and other aromatic acids on Cu{100} has led to extremely well-defined surface structures which have been characterised by STM. In addition, the formation of chiral 2D networks was reported using trimellitic acid, a close analogue of trimesic acid, has also been reported.<sup>[19]</sup> Such surfaces with controlled chirality have great potential for use in the development of enantioselective heterogeneous catalysts.

#### **4.1.2 ADSORBATE INDUCED SEGREGATION AT BIMETALLIC SURFACES**

There are many examples where bimetallic catalysts can outperform their monometallic counterparts in terms of both activity and selectivity.<sup>[20]</sup> Some of these systems have achieved industrial application, for example, platinum/iridium<sup>[21]</sup> and platinum/rhenium<sup>[22]</sup> combinations in petroleum reforming. Bimetallic catalysts containing gold show activity that is superior to that of either component separately in the synthesis of hydrogen peroxide, of vinyl acetate and in a number of other selective oxidation reactions.<sup>[23]</sup>

Ensemble (structural) effects and electronic (ligand) effects have traditionally been used to explain the enhanced properties of bimetallic catalysts. Ensemble effects relate to the number of surface atoms needed for a catalytic process to occur. For example, modification of an active group VIII transition metal with a IB metal greatly suppresses the catalytic activity for hydrocarbon reactions, which require a large number of neighbouring surface atoms. On the other hand, a reaction which needs one metal adsorption site is not affected. This means that the ensemble size effect is defined by the dilution of the active ensemble with an inert second metal.<sup>[20]</sup>

Ligand effects refer to modifications in catalytic activity or selectivity that is the direct result of electronic interactions between the two components of the bimetallic system. The electronic properties of one element can be modified by the presence of another element thereby altering the chemisorption and reaction properties of adsorbates. However, differentiation between ensemble and electronic effects is not obvious and in many cases, there is contribution from both effects.<sup>[20]</sup>

In many bimetallic systems, surface segregation can occur under a reactive gas environment where the more reactive metal segregates to the surface. For an alloy AB, a range of parameters controls segregation including the differences in bond strengths of A-A, B-B and A-B, atomic size, enthalpies of sublimation and surface energies, temperature, the exposed crystal plane, and metal particle size. Segregation generally occurs with the metal of lower heat of sublimation i.e. metal-metal bond strength. However, if there is a substantial difference in atom radius ( $> 10\%$ ) of the two metals in the lattice; there is a tendency for the metal of lower surface energy per unit area to segregate preferentially to the surface thereby reducing strain.<sup>[20]</sup>

The phenomenon of adsorbate-induced segregation is typically difficult to measure and MEIS is one of the few techniques capable of quantifying the layer-by-layer composition

of bimetallic surfaces under the influence of an adsorbate. In a reactive gas environment and the presence of an adsorbate, the surface composition will alter such that the more reactive metal will segregate to the surface. In the following study, we examine the effect of (S)-glutamic acid adsorbed onto bimetallic Au/Ni surfaces examining the change in surface composition with MEIS. Several groups have examined this phenomenon using MEIS; Deckers *et al.*, investigated oxidation induced segregation in the Ni{111}/Pt system.<sup>[24]</sup> Baddeley and co-workers examined Ni{111}/Au surfaces<sup>[25]</sup> and (R,R)-tartaric acid modified Ni{111}/Au surfaces<sup>[26]</sup> and the influence of Au on the adsorption of methylacetoacetate on Ni{111}.<sup>[27]</sup> More recently, Baddeley and co-workers have also examined the Pd{111}/Au/AcOH system.<sup>[28]</sup>

### 4.1.3 AIM OF RESEARCH

The nickel catalysed liquid phase hydrogenation of  $\beta$ -ketoesters is one of the most successful examples of enantioselective heterogeneous catalysis.<sup>[29]</sup> When nickel catalysts are modified by the adsorption from solution of  $\alpha$ -amino acids or  $\alpha$ -hydroxy acids; the hydrogenation of  $\beta$ -ketoesters occurs enantioselectively. However, bare, unmodified nickel sites on the catalyst surface are achiral, and therefore catalyse a racemic reaction competitively with the enantioselective reaction. This lowers the overall enantioselective yield. Merely saturating the nickel surface with the chiral modifier is ineffective as this results in less available metal sites for  $\beta$ -ketoester adsorption.<sup>[30]</sup>

The objective of this research is to quench the reactivity of these unmodified nickel sites by alloying with gold. The deposition of nickel on Au{111} surfaces and subsequent annealing will result in an Au{111}/Ni bimetallic overlayer as described in Chapter 3 of this thesis. It is postulated that the adsorption of the chiral modifier (S)-glutamic acid (figure 4-1) onto the bimetallic surface will preferentially segregate nickel to the surface, thereby creating active chirally modified nickel regions separated by inactive Au/Ni

bimetallic unmodified regions. The use of gold is well-known in heterogeneous catalysis and has been previously used to dilute the activity of other elements and to alter the selectivity of catalytic reactions.<sup>[20]</sup> It is also acknowledged that gold will interact weakly with the adsorbed chiral modifiers.

This study investigates the deposition of nickel on Au{111} and subsequent annealing to produce a bimetallic system, followed by exposure of the bimetallic surface to the chiral amino acid, (S)-glutamic (herein denoted (S)-GA). (S)-GA is an interesting modifier as the dominant enantiomer produced in the reaction is dependent upon the modification temperature; modification below 353 K gives (R)-MHB whereas, modification above 353 K gives (S)-MHB.<sup>[31]</sup> STM was used in these experiments to examine the morphology of the Au/Ni dosed (S)-GA surfaces, while MEIS was used as a quantitative probe of adsorbate induced segregation. The chemical form of the amino acid, (S)-GA varies, in solution, from cationic to zwitterionic to anionic to di-anionic as a function of pH. This was illustrated in figure 1-13 of this thesis. Consequently, RAIRS was used in this project to investigate the molecular conformation of (S)-GA in the aforementioned system while TPD was used to assess the thermal stability of the (S)-GA adlayers.

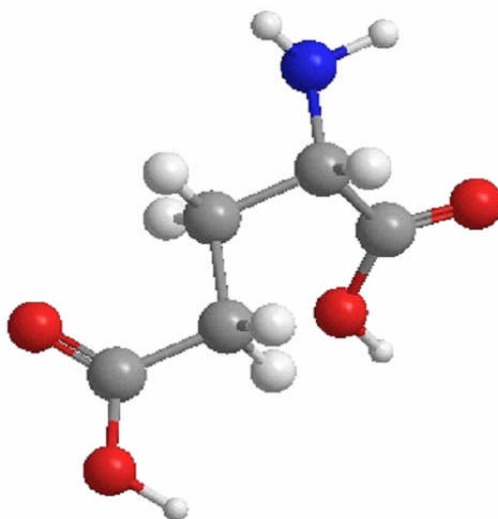


**Figure 4-1** Molecular structure of the chiral molecule, (S)-glutamic acid in the non-zwitterionic form.

## 4.2 EXPERIMENTAL

Three UHV systems were used in this study. The first was an Omicron variable STM & RAIRS UHV system with a base pressure of  $1 \times 10^{-10}$  mbar, consisting of three separate chambers for sample preparation & characterisation, STM, and RAIRS measurements located at the University of St Andrews. The second UHV system is located at the UK National MEIS facility at STFC Daresbury Laboratory. This MEIS chamber consists of a scattering chamber, a sample preparation & characterisation chamber, a sample transfer chamber and a fast entry load lock. The third chamber located at the University of St Andrews, has a base pressure of  $3 \times 10^{-10}$  mbar and was built by PSP Vacuum Technology Ltd. This chamber has facilities for AES, LEED, mass spectrometry and TPD experiments. A detailed description of these techniques was presented in Chapter 2.

### 4.2.1 STM & RAIRS EXPERIMENTS

The Au{111} single crystal was cleaned by cycles of ion sputtering ( $\text{Ar}^+$ , 0.9 kV,  $i_{\text{sample}} \sim 6 \mu\text{A}$ ) and annealing to 873 K until a sharp (1 x 1) LEED pattern was attained and STM indicated that a clean Au{111} reconstructed surface had been produced. STM topographic images were attained in constant current mode using an electrochemically etched tungsten tip.

Nickel was evaporated onto the Au{111} surface at room temperature by means of a resistively heated tungsten filament around which nickel wire had been wound. The nickel deposition rate was calibrated via STM by monitoring the size of the nickel islands which nucleate into the elbows of the Au{111} herringbone reconstruction. For these experiments 0.1-4 ML of nickel was deposited onto Au{111} at an evaporation rate of approximately  $0.1 \text{ Ni ML min}^{-1}$ . The prepared Au{111}/Ni surfaces (as a function of varying nickel coverage) were then exposed to (S)-GA (Fluka,  $\geq 99.5\%$ ). (S)-GA was sublimed from a differentially pumped solid doser with line of sight exposure to the

Au{111} single crystal. The temperature of (S)-GA was monitored by a thermocouple and was maintained at 403 K for all experiments. Prior to dosing, the (S)-GA was degassed for several hours at 360 K.

A Nicolet Nexus 860 FTIR spectrometer was used to acquire RAIR data (512 scans at a resolution of  $4\text{ cm}^{-1}$ ) using an N<sub>2</sub>(l) cooled mercury cadmium telluride (MCT) detector. A background spectrum was taken of the Au{111}/Ni surface prior to exposure to (S)-GA. RAIRS data were taken as a function of (S)-GA exposure at a crystal temperature of 300 K.

## 4.2.2 TPD EXPERIMENTS

The Au{111} single crystal was cleaned by cycles of ion sputtering (Ar<sup>+</sup>, 0.9 kV,  $i_{\text{sample}} \sim 6\ \mu\text{A}$ ) and annealing to 873 K until a sharp (1 x 1) LEED pattern was observed and no impurities such as carbon or sulphur were detected by AES. This resulted in a well-ordered clean surface. TPD experiments involved depositing nickel onto Au{111} at 300 K and annealing to progressively higher temperatures (300-600 K) to produce a bimetallic overlayer. Nickel was deposited at an evaporation rate of approximately  $0.1\ \text{ML}\ \text{min}^{-1}$  which was achieved by means of a resistively heated tungsten filament around which nickel wire had been wound. AES was used to estimate the coverage of nickel. Monitoring the growth of the nickel Auger peak (61 eV & 848 eV) and the attenuation of the Au (69 eV) peak as a function of depositing time at constant flux enabled the estimation of nickel monolayer coverage.

The prepared Au{111}/Ni bimetallic surface was then exposed to a saturated dose of (S)-GA via sublimation from a solid doser. The temperature of (S)-GA was monitored via a thermocouple and was maintained at 403 K for all experiments. Following the preparation of the Au{111}/Ni/(S)-GA surface, TPD experiments were carried out as a function of nickel coverage ranging from 0.1-8 ML of nickel and thermal treatment.

### 4.2.3 MEIS EXPERIMENTS

For all MEIS experiments, the Au{111}/Ni/(S)-GA surface was prepared in an identical manner to the TPD experiments. The following set of MEIS experiments involved the deposition of nickel at 300 K onto Au{111} and annealing (300-630 K) to produce a bimetallic surface. Following a saturated exposure of (S)-GA, the prepared surface was further annealed to monitor possible adsorbate induced segregation of nickel to the surface. In addition, nickel was deposited at varying temperatures ranging from 400 K to 500 K. At each stage, MEIS measurements were taken.

The MEIS experiments described in this Chapter use layer specific geometries identical to those used for Chapter 3. A summary is presented in table 4-1. An ion beam of 100 keV He<sup>+</sup> ions was employed for all experiments. Surface structure and composition was determined using the phenomenon of blocking, shadowing, and channelling. The ion beam was aligned 35.26 ° with respect to the sample normal along the  $[\bar{1}\bar{1}4]$  azimuthal direction. At this alignment, 1-, 2- and 3-layer illumination can be attained by selecting appropriate outgoing blocking directions. This corresponds to the top, top two and top three surface layers respectively.

Table 4-1: Summary of the incident and exit directions and corresponding scattering angles used in the following set of MEIS experiments.

<b>Geometry</b>	<b>Surface layers illuminated</b>	<b>Incident</b>	<b>Exit</b>	<b>Scattering Angle</b>
1-layer	Top layer	$[\bar{1}\bar{1}4]$	[110]	109.5 °
2-layer	Top two layers	$[\bar{1}\bar{1}4]$	$[\bar{2}21]$	90 °
3-layer	Top three layers	$[\bar{1}\bar{1}4]$	$[\bar{3}32]$	84.24 °

## 4.3 RESULTS

### 4.3.1 SUBMONOLAYER DEPOSITION OF NICKEL ONTO AU{111} SURFACES

#### 4.3.1.1 STM STUDIES

The morphology of Au{111}/Ni/(S)-GA surfaces were topographically imaged using STM. The following experiment illustrates the change in morphology of the Au{111}/Ni surface following the adsorption of (S)-GA. This change in morphology is dependent upon the initial size of the nickel islands deposited within the Au{111} herringbone reconstruction.

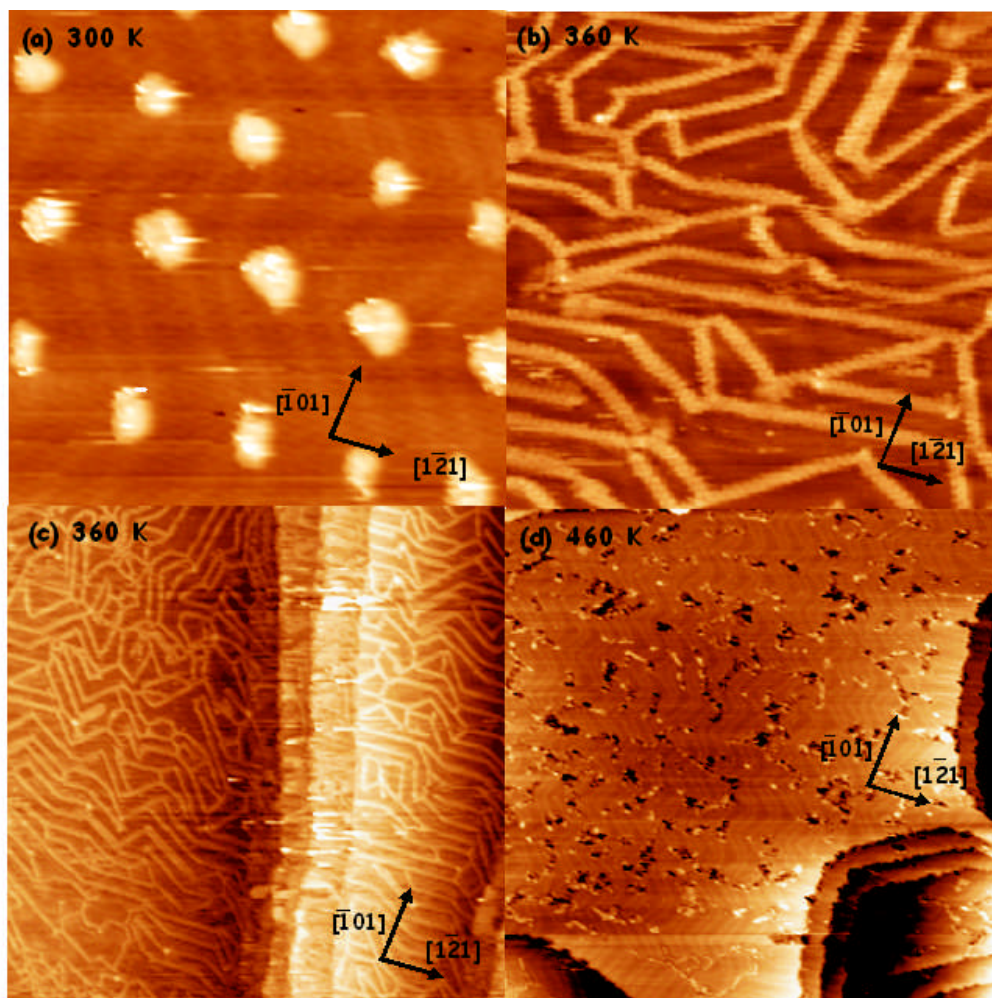
Figure 4-2 (a) is an STM topographic image of 0.1 ML of nickel deposited on Au{111} at room temperature. Initial growth of nickel involves nucleation into 2D islands at the elbows of the herringbone reconstruction as previously reported by Chambliss and co-workers.<sup>[4]</sup> The nickel islands are ~3 nm in diameter. Exposure of this surface to a saturated coverage of (S)-GA results in the disappearance of the nickel islands on the Au{111} surface. Annealing to 350 K presents an entirely new structure as depicted in Figure 4-2 (b). The Au{111} surface is covered with a network of interconnected chains of molecular features. A larger scale STM topographic image (140 nm x 110 nm) of the molecular features is presented in figure 4-2 (c). Further annealing of the surface to 450 K results in decomposition of the molecular features. This is illustrated in figure 4-2 (d).

Examining figure 4-2 (b), the molecular chains are aligned approximately along both  $\langle 101 \rangle$  and  $\langle 112 \rangle$  type azimuthal directions on the surface in comparable numbers. Predominantly, the molecular chains are 1D and straight. Parallel chains are separated by 3-4 nm. Neighbouring repeating features within a given chain are separated by ~7-8 Å.

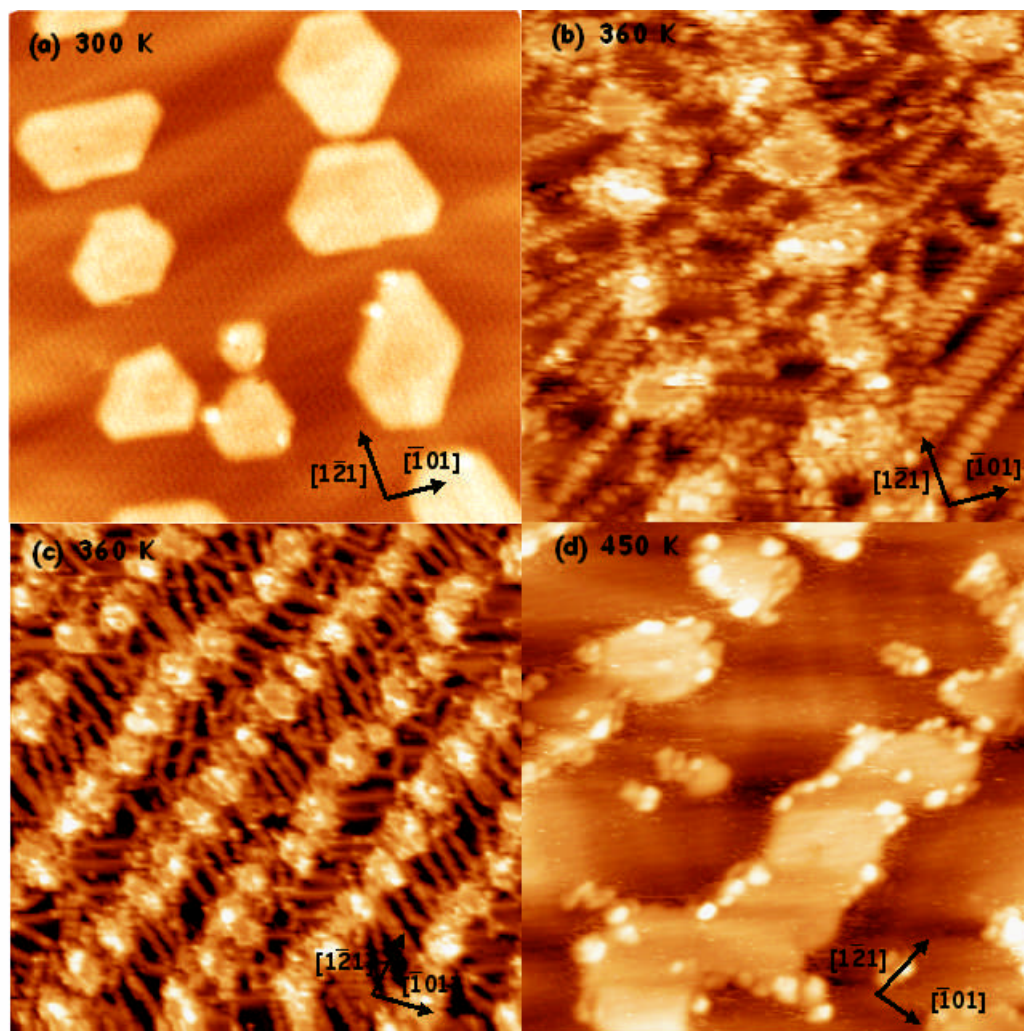
This periodicity appears to be approximately independent of the growth direction of the chain.

Figure 4-3 (a) is an STM topographic image of  $\sim 0.25$  ML of nickel on Au{111} deposited at 300 K. The 2D nickel islands are hexagonal in shape with well-defined straight edges ranging in size from approximately 5-6 nm in diameter. The nickel islands are aligned in parallel rows along the  $[\bar{1}\bar{2}1]$  direction within the herringbone reconstruction. Following exposure of this surface to (S)-GA at 300 K and annealing to 350 K (figure 4-3 (b)), the nickel islands are still visible, but their edges are corroded and less well-defined. In addition, the nickel islands are connected via 1D chains of molecular features. The molecular chains connecting the nickel islands grow preferentially in two directions. The first is aligned at an angle of  $\sim 80 \pm 5^\circ$  with respect to the  $[\bar{1}\bar{2}1]$  direction. At this growth direction, the molecular features have a measured periodicity of  $\sim 7.3 \pm 0.3$  Å. The second growth direction is aligned an angle of  $57 \pm 5^\circ$  with respect to the  $[\bar{1}\bar{2}1]$  direction. With this growth direction, the molecular features have a measured periodicity of  $6.3 \pm 0.3$  Å. The majority of the molecular chains exist in single rows although there are examples of double rows of features. The molecular chains link two nickel islands however chain growth in a number of cases is terminated by collision with another chain.

Figure 4-3 (c) shows a larger scale image of the aforementioned surface. The preferred growth direction of the 1D molecular chains zig-zags from one row of nickel islands to the next in an analogous manner to the herringbone reconstruction. Annealing of this surface to 450 K results in decomposition of the molecular features as shown in figure 4-3 (d). The nickel islands have coalesced in ribbons.



**Figure 4-2** (a) STM topographic image (30 nm x 30 nm) following deposition of 0.1 ML of nickel on Au{111} at 300 K ( $V = -0.80$  V,  $I = 0.19$  nA). (b) STM topographic image (30 nm x 30 nm) of figure 4-1 (a) following exposure of Au{111}/0.1 ML nickel to (S)-GA and annealing to 360 K ( $V = -0.92$  V,  $I = 0.14$  nA). (c) STM topographic image of figure 4-1 (b) captured at 140 x 110 nm ( $V = -0.92$  V,  $I = 0.14$  nA). (d) STM topographic image of the aforementioned surface (150 nm x 100 nm) flashed annealed to 450 K. The herringbone reconstruction is clearly visible ( $V = -0.92$  V,  $I = 0.14$  nA) and the molecular features have decomposed.



**Figure 4-3** (a) STM topographic image (30 nm x 30 nm) following the growth of 0.25 ML nickel on Au{111} at 300 K ( $V = -0.90$  V,  $I = 2.0$  nA). (b) STM topographic image (30 nm x 30 nm) of figure 4-4 (a) following exposure to a saturated coverage of (S)-GA dosed at 300 K and subsequently annealed to 360 K ( $V = -0.90$  V,  $I = 0.16$  nA). (c) Larger scale STM topographic image 70 nm x 70 nm of the aforementioned surface ( $V = -0.90$  V,  $I = 0.16$  nA). (d) Further annealing to 450 K, results in the decomposition of the molecular features. The nickel islands have coalesced into ribbons. The STM topographic image was captured at 30 nm x 30 nm ( $V = -0.92$  V,  $I = 0.14$  nA).

Main conclusions drawn from STM studies of Au{111}/Ni/(S)-GA surfaces include:

1. 0.1 ML of nickel deposited on Au{111} grows within the herringbone reconstruction. The diameter of the nickel islands is  $\sim 3$  nm. The adsorption of (S)-GA onto this surface results in the complete disappearance of the nickel islands. Flash annealing of this surface to 360 K presents an entirely new structure of interconnecting 1D chains of molecular features. Further annealing of this surface to 450 K initiates the decomposition of molecular features.
2. 0.25 ML of nickel deposited on Au{111} grows within the herringbone reconstruction. The diameter of the nickel islands ranges from 5-6 nm. The adsorption of (S)-GA onto this surface results in corrosion of the nickel islands. Flash annealing of this surface to 360 K presents a new structure whereby each nickel island is connected via 1D chains of molecular features. Further annealing of this surface to 450 K results in decomposition of the molecular chains.

#### 4.3.1.2 RAIRS STUDIES

RAIR data were acquired as a function of (S)-GA exposure on a range of Au{111}/Ni surfaces with varying nickel coverage (0.1-0.6 ML) and annealing temperature. It should be noted that no adsorption of (S)-glutamic acid was detected on the clean Au{111} surface at 300 K. Figure 4-4 shows the RAIR spectra acquired following exposure of Au{111}/0.1 ML Ni to (S)-GA at a crystal temperature of 300 K. At low exposures, a relatively intense band is observed at  $1647\text{ cm}^{-1}$  accompanied by less intense bands at 2991, 2947, 1516, 1421, 1295, 1247, and  $917\text{ cm}^{-1}$ . As (S)-GA coverage increases, an additional band is observed at  $1756\text{ cm}^{-1}$ . At the highest exposure of (S)-GA, this becomes the most intense band.

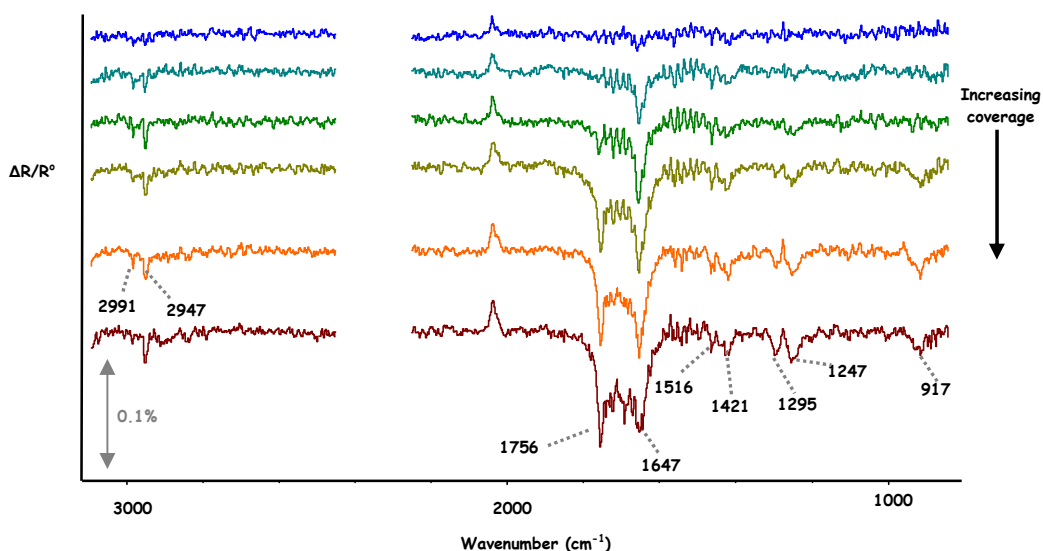


Figure 4-4 RAIR spectra following a saturated (40 L) dose of (S)-GA on Au{111}/0.1 ML Ni at a single crystal temperature of 300 K.

Figure 4-5 shows the RAIR spectra acquired following exposure of Au{111}/0.25 ML Ni to (S)-GA at 300 K. Bands in similar positions to those observed for the 0.1 ML nickel film are present but with different relative intensities. For example, the 1643  $\text{cm}^{-1}$  and the 1421  $\text{cm}^{-1}$  bands are more intense and the former band is always more intense than the 1747  $\text{cm}^{-1}$  band even at the highest (S)-GA exposure.

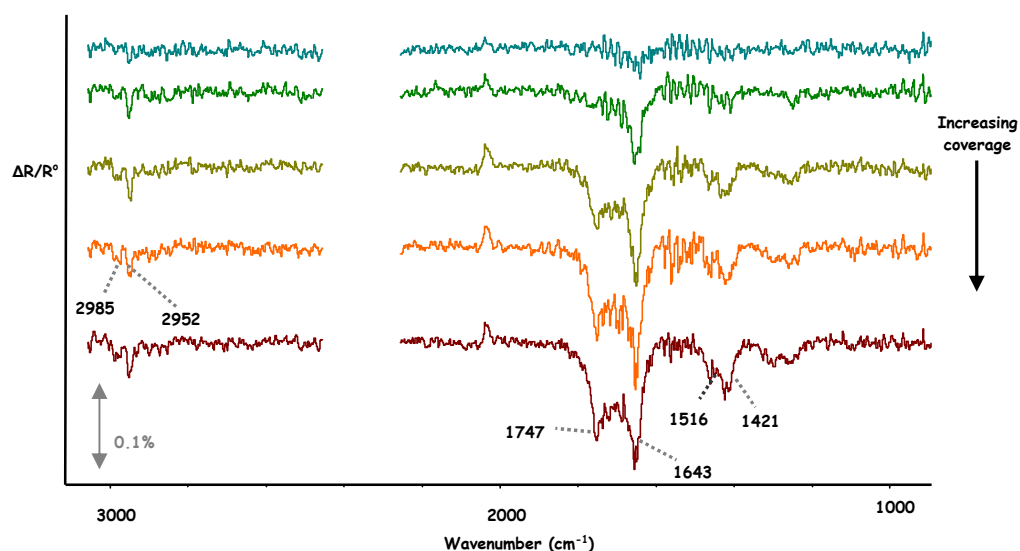
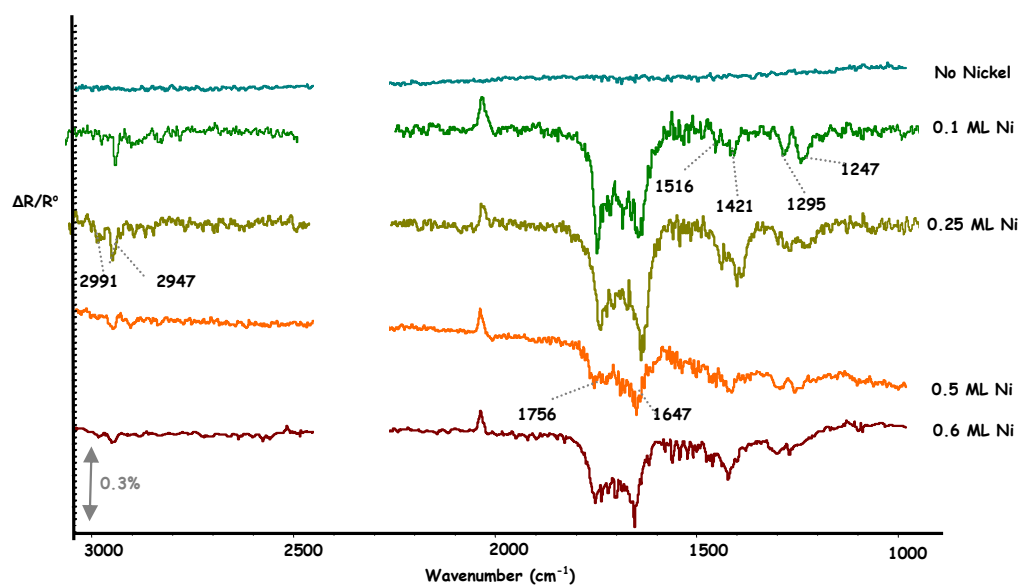


Figure 4-5 RAIR spectra following a saturated (40 L) dose of (S)-GA on Au{111}/0.25 ML Ni at a single crystal temperature of 300 K.

Figure 4-6 shows the RAIR spectra following a 40 L dose of (S)-GA on Au{111} surfaces as a function of nickel coverage. The lowest coverage of nickel  $\sim 0.1$  ML results in a relatively intense bands at 1647 and 1756  $\text{cm}^{-1}$  accompanied by less intense bands at 2947, 1516, 1421, 1295, and 1247  $\text{cm}^{-1}$ . Of all the bands, 1756  $\text{cm}^{-1}$  is the most intense.

Increasing the coverage of nickel to 0.25-0.6 ML results in bands in similar positions to those observed for the 0.1 ML nickel film but with different relative intensities. The dominating bands are located at 1747, 1643 and 1421  $\text{cm}^{-1}$ . The 1643  $\text{cm}^{-1}$  band is always more intense than the 1747  $\text{cm}^{-1}$  band. This is in contrast to the 0.1 ML Ni film on Au{111}.



**Figure 4-6** RAIR spectra following a saturated (40 L) dose of (S)-GA on Au{111} at a single crystal temperature of 300 K as a function of nickel coverage (0.1-0.6 ML Ni). Following each deposition of nickel on Au{111} and exposure to (S)-GA, the Au{111} crystal was re-prepared.

#### 4.3.1.2 TPD STUDIES

Figure 4-7 (a-c) presents TPD data acquired following a  $\sim 40$  L dose of (S)-GA adsorbed onto Au{111}/Ni surfaces as a function of nickel coverage at 300 K. Ni was deposited at 300 K and Ni coverage was varied between 0 and 4 ML. The primary desorption products observed in the following set of TPD experiments occurred at masses 2 ( $\text{H}_2$ ), 28 ( $\text{CO}$ ) and

44 (CO<sub>2</sub>) as measured with a quadrupole mass spectrometer. Molecular (S)-GA (mass 150) was not observed to desorb from the Au{111}/Ni surfaces, indicating that adsorbed (S)-GA decomposes into fragments on the surface as the temperature is ramped. In addition, a blank experiment of (S)-GA dosed onto a clean gold surface was conducted. No desorption pattern was detected and this is indicative that (S)-GA does not stick to the gold surface at 300 K. Figure 4-7 (a) presents the TPD spectra of mass 2 (H<sub>2</sub>) for Au/Ni surfaces dosed with a saturated coverage of (S)-GA, as a function of nickel coverage. On thinner films of nickel (0.25-2 ML Ni), two desorption maxima are observed. The first is a low-temperature desorption with T<sub>max</sub> values ranging from 356-374 K, and the second is a high-temperature desorption with T<sub>max</sub> values ranging from 495-522 K. The latter increases from 495 to 522 K with increasing nickel coverage from 0.5 to 2 ML.

With increasing coverage of nickel, the shape of the desorption features also changes. Lower coverages of nickel (0.25-1ML) results in relatively broad features; while increasing the nickel coverage from 2 to 4 ML results in well-resolved asymmetric features. A nickel coverage of 4 ML gives a single asymmetric feature with a desorption T<sub>max</sub> of ~531 K. This is approximately ~20 K higher than the high-temperature desorption feature of 0.25 ML Ni, suggesting that thicker coverages of nickel increases the stability of (S)-GA on the Au/Ni surface. Figure 4-7 (b) exhibits the TPD spectra of mass 44 (CO<sub>2</sub>). No low-temperature desorption is observed; instead a single well-resolved asymmetric desorption feature is observed at T<sub>max</sub> ranging from 495-531 K for nickel coverages of 0.25 to 4 ML on Au{111} surfaces dosed with (S)-GA. Figure 4-7 (c) shows the TPD spectra of mass 28 (CO). This closely resembles figure 4-7 (a), as low and high-temperature desorption features are present. The temperature regimes are very similar differing only by a few Kelvin. Common to all three TPD spectra is that the lowest coverage i.e. 0.25 ML of nickel always has a higher desorption T<sub>max</sub> than 0.5 ML of nickel by up to ~25 K.

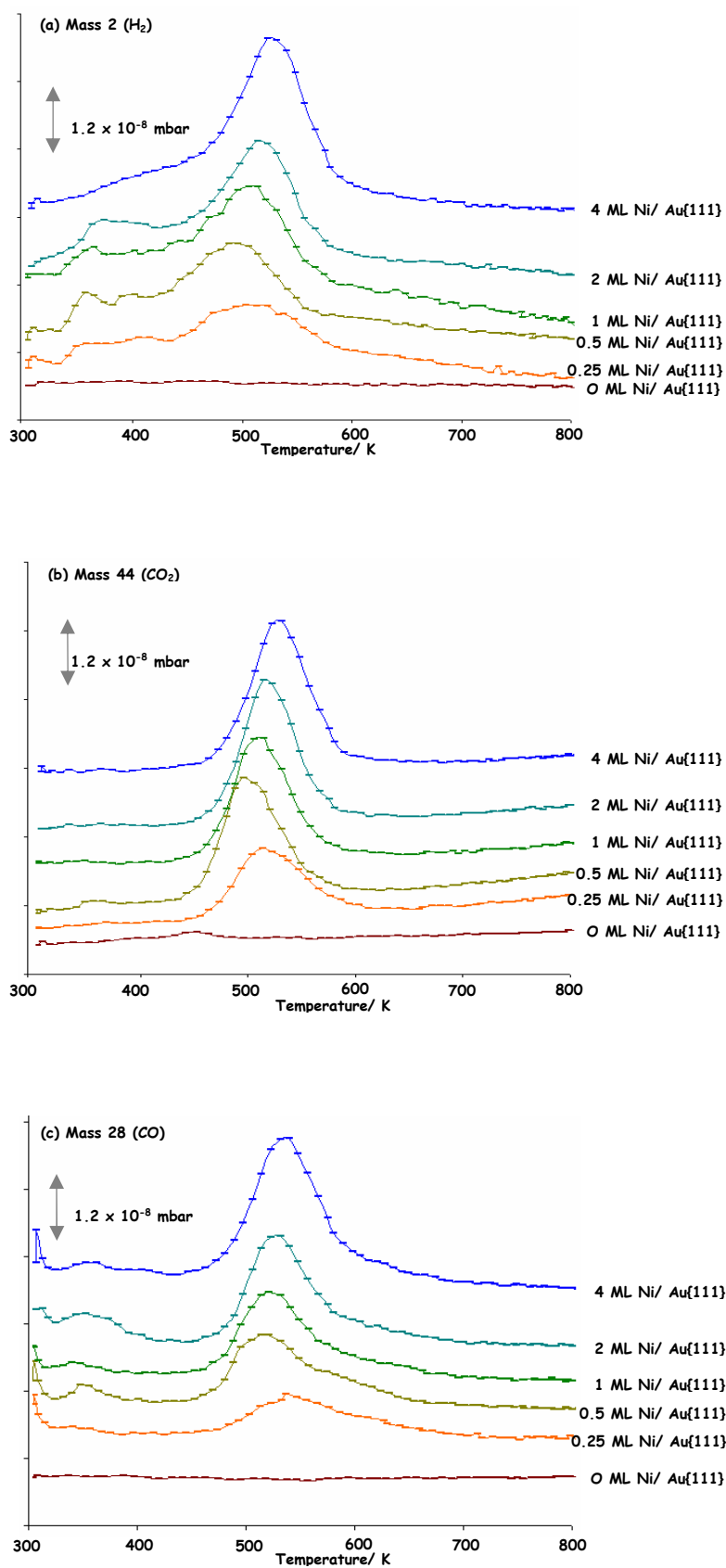


**Figure 4-8** TPD spectra following a saturated (40 L) dose of (S)-GA on Au{111}/Ni surfaces as a function of nickel coverage (0-4 ML Ni) on Au {111} with a single crystal temperature of 300 K. (a) Mass 2 ( $H_2$ ) (b) Mass 44 ( $CO_2$ ) (c) Mass 28 ( $CO$ ).

## 4.3.2 DEPOSITION OF ULTRATHIN NICKEL FILMS ONTO AU{111} SURFACES AS A FUNCTION OF ANNEALING TEMPERATURE

### 4.3.2.1 RAIRS STUDIES

Figure 4-8 shows the RAIR spectra following a 40 L dose of (S)-GA on Au{111}/4 ML nickel surfaces as a function of thermal treatment. (S)-GA dosed on Au{111}/4 ML Ni with no thermal treatment results in relatively intense bands at 1756, 1647, 1421 and 1295  $\text{cm}^{-1}$ . The band at 1756  $\text{cm}^{-1}$  is the most intense. Re-preparing the same surface and annealing to 360 K results in the same bands with similar relative intensities. Annealing an Au{111}/4 ML Ni sample to 410 K followed by exposure to (S)-GA at 300 K results in bands at 1756, 1647 and 1421  $\text{cm}^{-1}$  of low intensity. The band at 1647  $\text{cm}^{-1}$  is the most intense. Au{111}/4 ML Ni and annealing to 460 K, 510 K and 570 K prior to exposure to (S)-GA results in relatively intense bands, predominantly at 1756  $\text{cm}^{-1}$  and at 1295  $\text{cm}^{-1}$  of low intensity. The band at 1756  $\text{cm}^{-1}$  is the most intense.

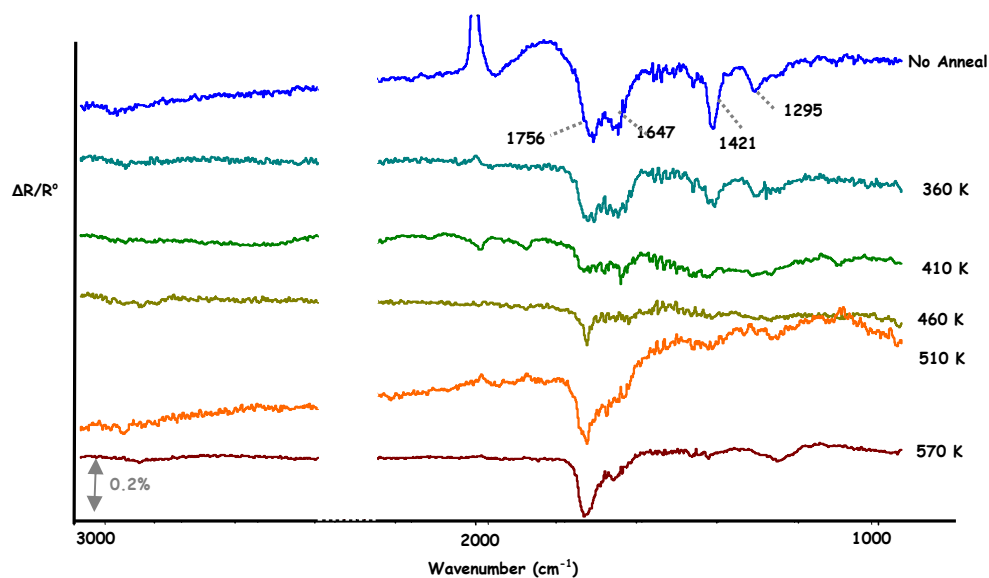


**Figure 4-8** RAIR spectra following a saturated (40 L) dose of (S)-GA on Au{111}/ 4 ML Ni as a function of annealing temperature. After each annealing temperature and exposure to (S)-GA, the Au{111} crystal was re-prepared.

#### 4.3.2.2 TPD STUDIES

Figure 4-9 (a-c) are TPD data acquired following a  $\sim 40$  L dose of (S)-GA adsorbed onto Au{111}/Ni surfaces as a function of thermal treatment (300-630 K). 8 ML of nickel was deposited on the Au{111} single crystal surface at room temperature. The primary desorption products observed occurred at masses 2 ( $H_2$ ), 28 (CO) and 44 ( $CO_2$ ) as measured with a quadrupole mass spectrometer. Molecular (S)-GA (mass 150) was not observed desorbing from the Au{111}/Ni surface.

The  $H_2$ ,  $CO_2$  and CO spectra shown in figure 4-9 (a-c) all follow a similar trend; the desorption features are well-resolved and asymmetric with a desorption  $T_{max}$  varying by a few Kelvin in each spectra. For all spectra,  $H_2$ ,  $CO_2$  and CO features at 300 K have a desorption  $T_{max}$  of  $\sim 483$  K. Annealing of the Au/Ni surface to 460 K increases the desorption  $T_{max}$  ranging from 518 to 525 K. Further annealing of this surface to 540 K, decreases the desorption  $T_{max}$  ranging from 503 to 513 K. Annealing to 600 and 630 K results in no desorption of  $H_2$ , CO and  $CO_2$ .

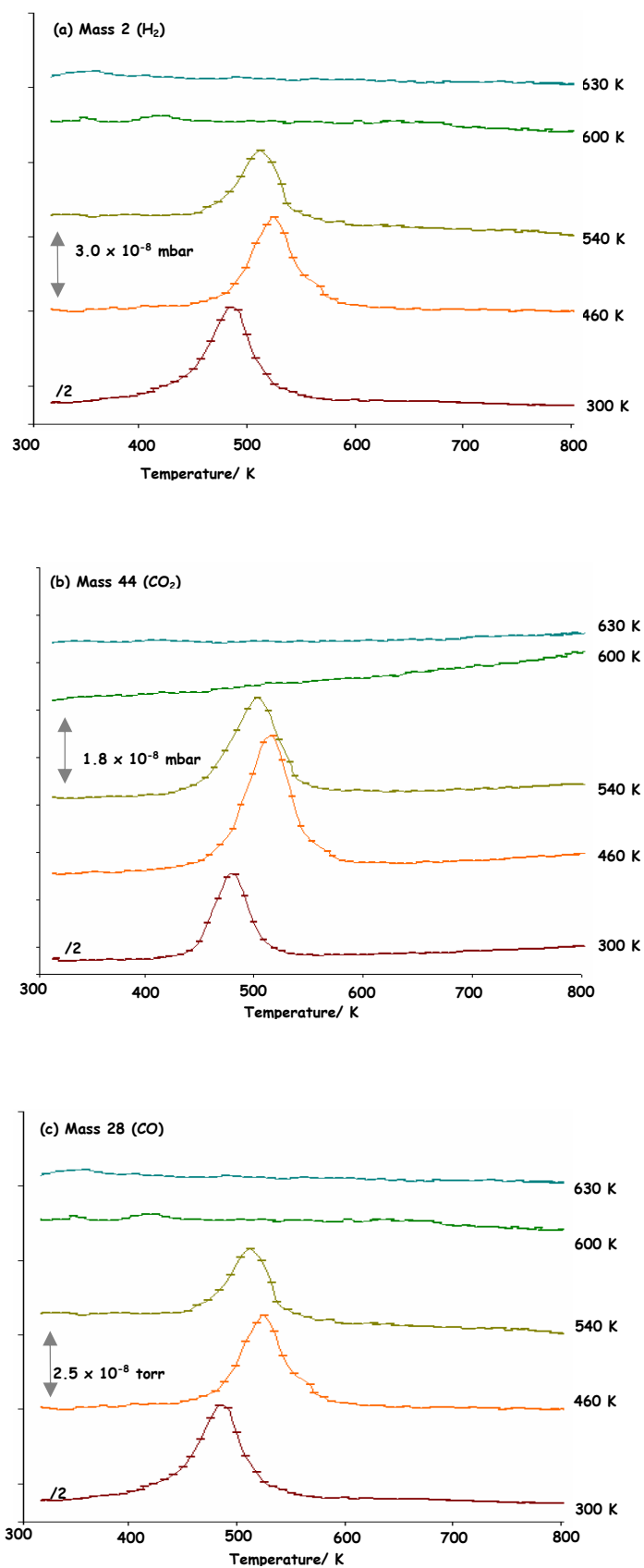


**Figure 4-9** TPD spectra following a saturated (40 L) dose of (S)-GA on Au{111}/Ni surfaces as a function of annealing temperature (300-630 K). 8 ML of nickel was deposited at 300 K. (a) Mass 2 ( $H_2$ ) (b) Mass 44 ( $CO_2$ ) (c) Mass 28 ( $CO$ ).

### 4.3.2.3 MEIS STUDIES

MEIS was used in this study to examine the composition of Au{111}/Ni surfaces as a function of thermal treatment and exposure to the chiral modifier, (S)-GA. The extent to which (S)-GA induces segregation of nickel to the bimetallic surface is assessed. The following experiments involve depositing nickel onto Au{111} at 300 K followed by thermal treatment to produce a bimetallic overlayer. The bimetallic surface is then exposed to a 40 L dose of (S)-GA. The adsorbate covered surface is further thermally treated to induce adsorbate induced segregation of nickel. At each stage MEIS measurements were taken.

In order to determine the influence of (S)-GA on the surface Ni/Au composition, we monitored the intensity of the Au surface peak in the intensity *versus* energy plots for the most surface sensitive (i.e. 1-layer) geometry. The Au peak area was normalised to the peak for the analogous clean surface spectrum. It should be noted that the number of visible layers is likely to slightly exceed 1.0 ML in this geometry due to the fact that the surface layer relaxation and the enhanced vibrations of surface atoms make a fraction of the second layer visible to the beam. Hence the stated compositions are likely to slightly under-estimate the absolute fraction of Au in the surface layer. It is possible in this case to measure the Ni peak. However, for a number of reasons, it is difficult to reliably quantify the surface composition of Ni. Firstly, since Ni does not form a pseudomorphic layer on Au, Ni layers are visible even in the 1-layer geometry. Secondly, the existence of two relatively abundant isotopes of Ni makes it difficult to perform a depth profile.

Table 4-2 presents the measured intensity of the gold surface feature in the ion intensity *versus* energy plots for the 1-layer geometry. This corresponds to the top surface layer. Segregation effects are less definite in the 2- and 3-layer geometries (i.e. top two and top three surface layers). This can be attributed to gold and nickel atoms being ‘swapped’

between the top two surface layers as (S)-GA under a reactive gas environment effectively pulls the nickel atoms to the surface layer. The extent of segregation is expressed in terms of monolayer Au depleted from the surface and was determined using a background subtraction analysis identical to that described in the previous Chapter. The reader is referred to Chapter 3, section 3.3.2.1 for further discussion of the analysis. In addition, the nickel to gold ratio is presented in brackets. This is the normalised Ni peak divided by the normalised Au peak. It should be noted that it became increasingly difficult to accurately measure the Ni peak at 600 K and consequently the ratios were not include.

**Table 4-2:** Composition of gold contained in the 1-, 2-, 3- layer geometry expressed in ML. Approximately 9 ML of nickel was deposited on Au{111} at 300 K. The Au/Ni surface was thermally treated to induce a bimetallic overlayer (360-600 K), followed by dosing of (S)-GA (40 L), at a single crystal temperature of 300 K. The aforementioned surface is then further annealed to 350 and 400 K, to induce segregation of nickel to the surface.

Deposition temperature of Ni /K	Annealing temp/ K	Composition of Au (expressed in ML) for the 1-layer Geometry (i.e. top surface layer). In brackets is the Ni to Au ratio.			
		Post- annealing	Post-adsorption of (S)-GA	Post- annealing to 350 K	Post- annealing to 400 K
300	360	0.21 (7)	0.22 (9)	0.09 (22)	0.20 (13)
300	460	0.24 (8)	0.25 (8)	0.11 (12)	0.28 (7)
300	540	0.47 (4)	0.26 (9)	0.23 (10)	0.30 (8)
300	600	0.62 (1)	0.65	0.48	0.65

Overall, following exposure of the Au/Ni surface to (S)-GA and annealing to 350 K, the composition of gold at the surface decreases substantially. This indicates (S)-GA induces segregation of nickel to the surface. For annealing temperature regimes of 360-540 K, the

composition of Au decreases by up to 50 % after exposure of the surface (S)-GA. However, this affect is less pronounced at the higher annealing temperature of 600 K.

Figure 4-10 (a-d) display the ion intensity *versus* energy plots of  $\sim 9$  ML film of nickel deposited onto Au{111} at 300 K. The prepared surfaces are annealed to a series of temperatures followed by exposure to (S)-GA and further annealing for the 1-layer illumination geometry. These plots show the relative position and intensity of the gold subsurface and gold surface related features located at 83 and 85 keV respectively. Deposition of nickel at 300 K and annealing of the Au/Ni surface to 360 K gives a composition of 0.21 ML Au. Interestingly, the adsorption of (S)-GA onto this surface does not modify the gold composition greatly. However, annealing of this surface to 350 K results in a substantially reduced composition of 0.09 ML Au as (S)-GA successfully segregates nickel to the surface region.

Examining figure 4-10 (a), a subtle decrease in the intensity of the gold surface related feature at  $\sim 85$  keV is evident after treatment of the Au/Ni surface to (S)-GA and annealing to 350 K. The gold peak increases in intensity with further annealing of the surface to 400 K. Examining 4-10 (b), the Au/Ni surface was annealed to 460 K with 0.24 ML of gold was estimated to be at the surface. Exposure of the Au/Ni surface to (S)-GA and annealing to 350 K reduces the gold composition to 0.11 ML as nickel is segregated to the surface. Annealing of the surface to 400 K increases the composition of gold at the surface to 0.28 ML. This trend is clearly manifested in the ion intensity plots. Annealing of the Au/Ni surface to 540 K gives a gold composition of 0.47 ML. The gold composition dramatically decreases to 0.26 ML upon adsorption of (S)-GA to the surface. Further annealing to 400 K increases the composition of gold at the surface to 0.30 ML. The segregation affects are less dramatic at the highest annealing temperature of 600 K (figure 4-10 (d)).

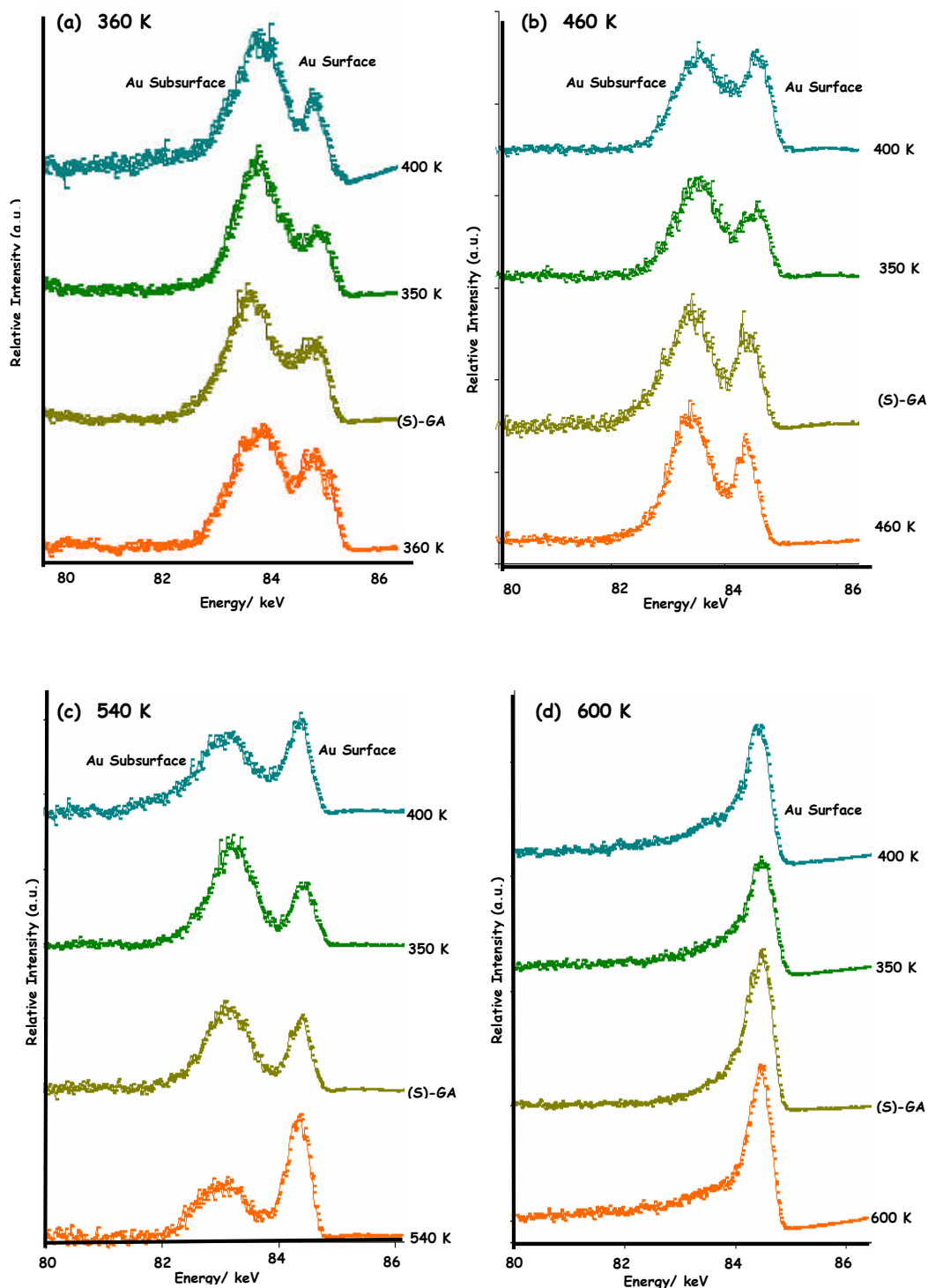


**Figure 4-10** Ion intensity *versus* energy plots for the 1-layer illumination geometry. Approximately 9 ML of nickel was deposited on Au{111} at room temperature and annealed to a series of temperatures. **(a)** Annealed to 360 K **(b)** Annealed to 460 K **(c)** Annealed to 540 K **(d)** Annealed to 600 K. The annealed Au{111}/Ni surfaces were subsequently exposed to (S)-GA and further annealed to 350-400 K.

### 4.3.3 DEPOSITION OF NICKEL ONTO AU{111} SURFACES AT ELEVATED TEMPERATURES

#### 4.3.3.1 TPD STUDIES

Figure 4-11 (a-c) present TPD data acquired following a  $\sim 40$  L dose of (S)-GA adsorbed onto Au{111}/Ni surfaces at a nickel deposition temperature at 300-550 K. 8 ML of nickel was deposited on the Au{111} single crystal surface at varying temperature. The primary desorption products observed occurred at masses 2 ( $H_2$ ), 28 (CO) and 44 ( $CO_2$ ) as measured with a quadrupole mass spectrometer. Molecular (S)-GA (mass 150) was not observed desorbing from the Au{111}/Ni surface.

The  $H_2$  and  $CO_2$  spectra shown in figure 4-11 (a-b) present features that are well-resolved and asymmetric with very similar desorption  $T_{max}$  (varying only by a few Kelvin) in each spectra. At 300 K,  $H_2$  and  $CO_2$  features have a desorption  $T_{max}$  of  $\sim 483$  K. Deposition of nickel at 400 K increases desorption to a  $T_{max}$  of  $\sim 510$  K. With increasing nickel deposition temperature of 450-550 K, desorption  $T_{max}$  decreases to  $\sim 487$ -496 K in both spectra. The CO spectra in figure 4-11 (c) presents analogous desorption temperatures to  $H_2$  and  $CO_2$ , differing only by the broadness of the desorption features.

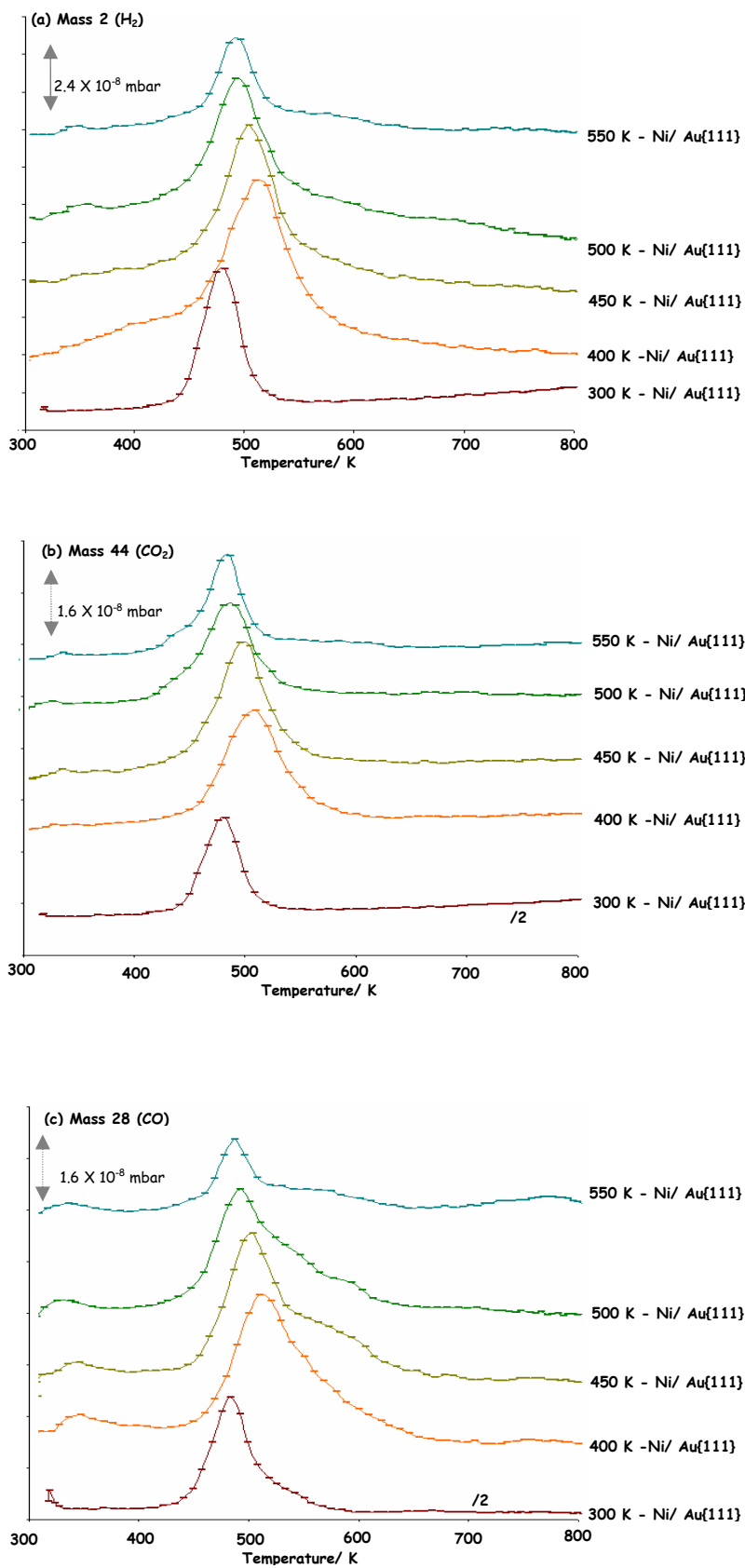


**Figure 4-11** TPD data acquired following  $\sim 40$  L of (S)-GA adsorbed onto Au{111}/Ni surfaces. The temperature of nickel deposition varied from 300 to 550 K. (a) Mass 2 ( $H_2$ ) (b) Mass 44 ( $CO_2$ ) and (c) Mass 28 ( $CO$ ).

### 4.3.3.2 MEIS STUDIES

#### 4.3.3.2.1 COMPOSITIONAL ANALYSIS

The following set of MEIS experiments involved depositing nickel onto Au{111} at 400 K, 450 K and 500 K. The prepared Au/Ni surface was then exposed to (S)-GA with the aim to induce segregation of nickel to the surface. Table 4-3 represents the composition of gold contained in 1-layer geometry. Examining table 4-3, there are no noticeable segregation effects when nickel is deposited at 400 and 500 K. Segregation is detected for the 450 K deposited film, though it is not clear why this data set should behave differently to the 400 and 500 K experiments. Figure 4-12 (a-c) presents the ion intensity *versus* energy plots for ~10 ML of nickel deposited onto Au{111} at 400, 450, and 500 K for the 1-layer geometry. The lack of adsorbate induced segregation is manifested in the plots.

**Table 4-3:** Atomic percentage of gold detected in the 1-layer geometry. This corresponds to the top surface layer respectively. Approximately 10 ML of nickel was deposited on Au{111} at 400 K, 450 K and 500 K. Ni to Au ratio is presented in brackets.

Nickel deposition temp/ K	Composition of Au (ML) in 1-layer geometry % Ni to Au ratio is presented in brackets.				
	Pre-adsorption of (S)-GA	Post-adsorption of (S)-GA	Post-annealing to 350 K	Post-annealing to 400 K	Post-annealing to 500 K
400	38 (10)	42 (11)	47 (11)	37(13)	n/a
450	75 (5)	71 (3)	n/a	32 (7)	75 (4)
500	X	61 (6)	n/a	48 (7)	66 (6)

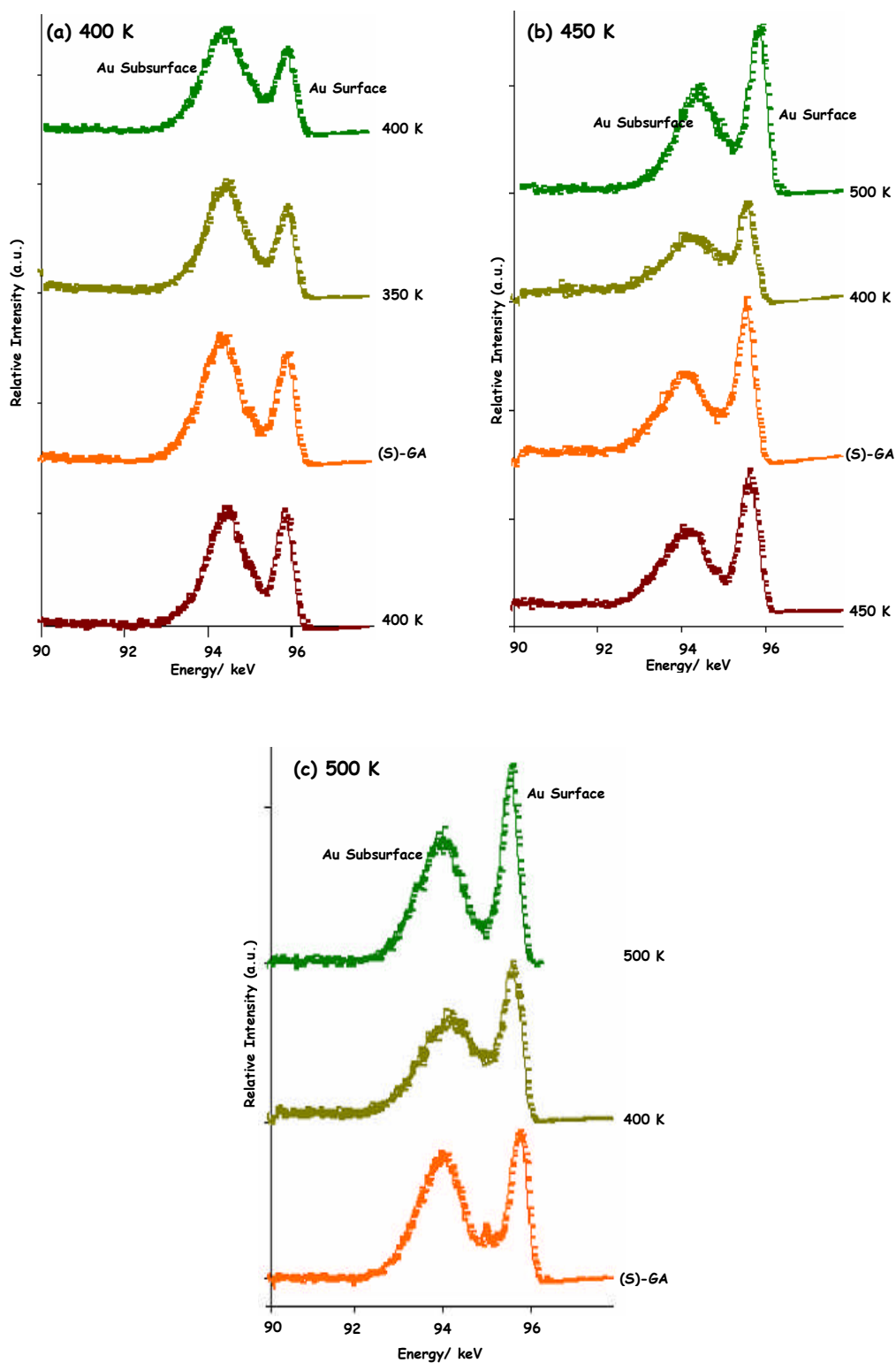


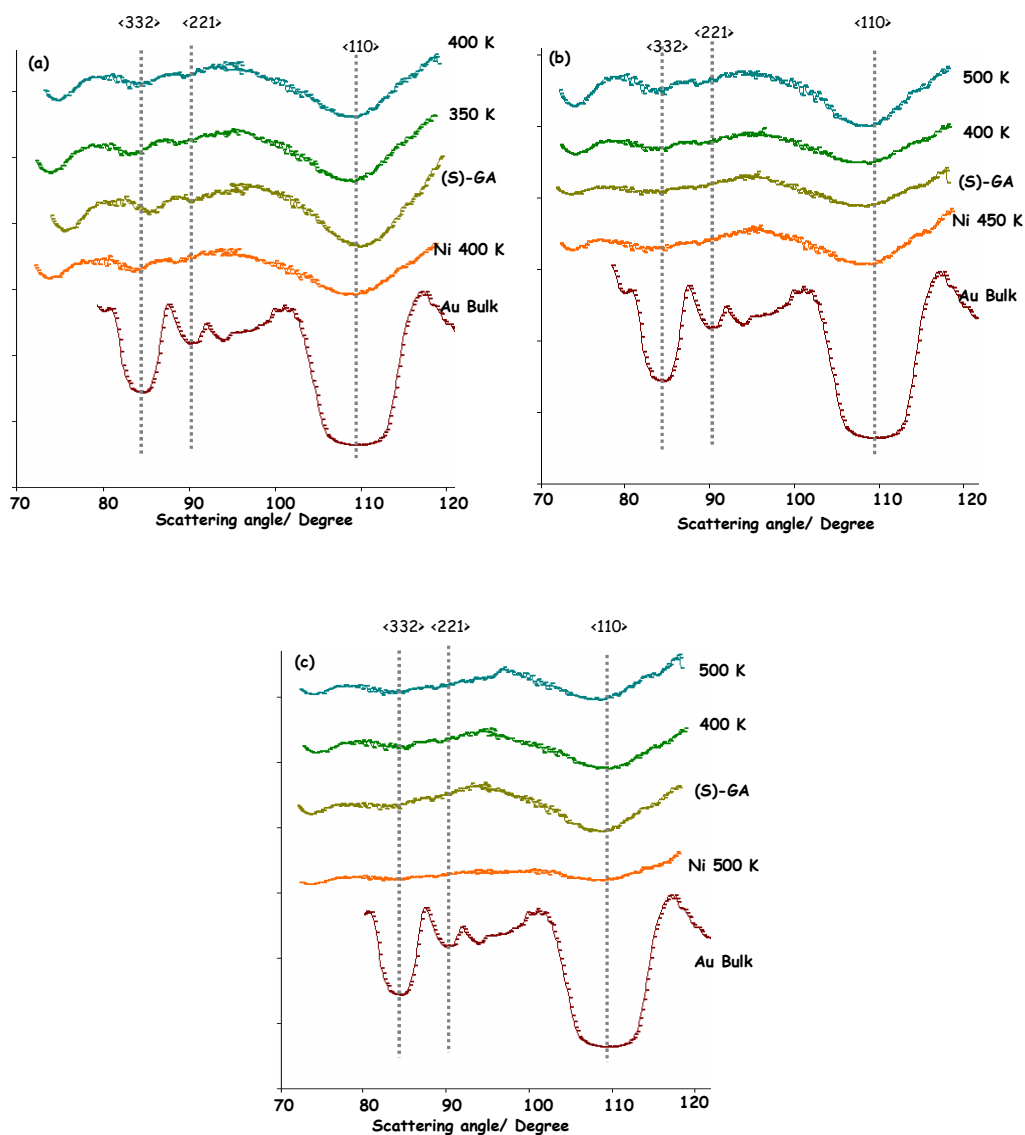
**Figure 4-12** Ion intensity *versus* energy plots for the 1-layer illumination geometry.  $\sim 10$  ML of nickel was deposited on Au{111} at (a) 400 K (b) 450 K and (c) 500 K. The Au{111}/Ni surfaces were subsequently exposed to (S)-GA and further annealed to 350-500 K.

#### 4.3.3.2.1 STRUCTURAL ANALYSIS

The adsorption of (S)-GA onto bimetallic Au{111}/Ni surfaces is expected to have a negligible effect on the structural data. This can be rationalised as follows; adsorbates like (S)-GA are composed of light C, H and O atoms, which are unlikely to adopt adsorption sites corresponding to a continuation of the underlying lattice. Hence, in the experimental geometries utilised in these experiments, the adsorbate atoms will be ineffective at both shadowing and blocking.<sup>[26]</sup> In addition, the shadow cone radius is proportional to the square root of the atomic number of the target atom and adsorbates such as C, H and O are relatively ineffective at shadowing underlying atoms. This has shown to be the case in a number of studies, such as in the adsorption of (R,R)-tartaric acid in the Ni{111}/Au system<sup>[26]</sup> and in the effect of chloroethene adsorption in the CuPd{110} system.<sup>[31]</sup>

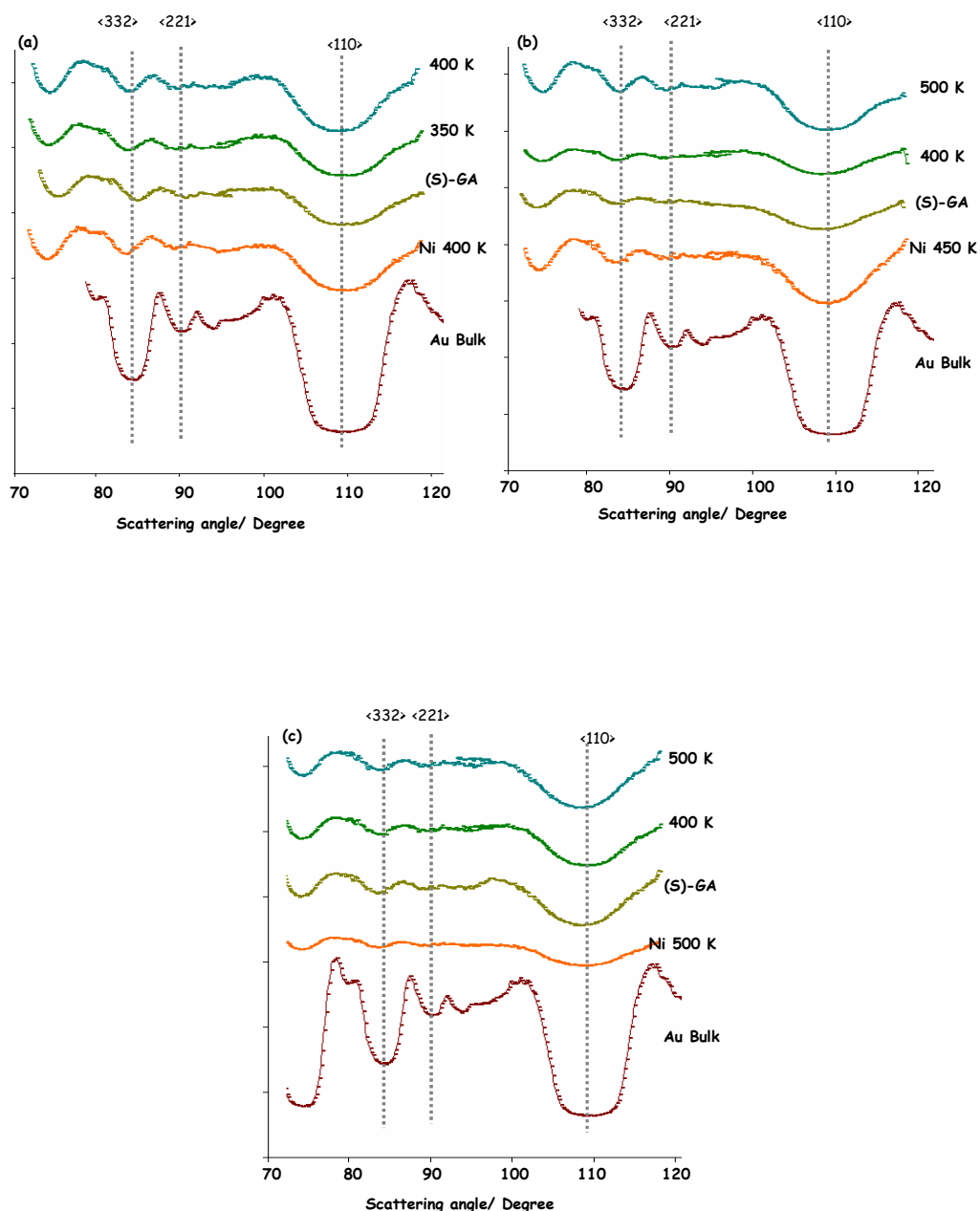
Nonetheless, the structural data is presented for a number of reasons. Firstly, as nickel is deposited onto Au{111} at varying temperatures of 400 K, 450 K and 500 K; it is postulated that nickel may adopt a different structure to that of when deposited onto Au{111} at room temperature. Secondly, as nickel segregates to the bimetallic Au/Ni surface due to the adsorption of (S)-GA (as confirmed by the compositional analysis); changes in structure at surface may be manifested by a subtle shift in the blocking features. Thirdly, it is important to confirm correct alignment of the beam which gives confidence in the quality of MEIS data. This is achieved through analysis of the gold bulk data. For comparison, the gold bulk data is included in each structural plot.

Figure 4-13 (a-c) displays gold surface (6 layers) ion intensity *versus* scattering angle plots as function of nickel deposition temperature. Nickel was deposited onto Au{111} at 400 K, 450 K and 500 K.



**Figure 4-13** Gold surface (6 layers) ion intensity *versus* scattering angle plots. ~9 ML of nickel was deposited on Au{111} at (a) 400 K (b) 450 K (c) 500 K and exposed to (S)-GA and further annealed to 350-500 K.

Figure 4-14 (a-c) displays gold subsurface (6 layers) ion intensity *versus* scattering angle plots as function of nickel deposition temperature. Nickel was deposited onto Au{111} at 400 K, 450 K and 500 K. The blocking features of the gold subsurface closely resemble those observed in the gold bulk spectra.



**Figure 4-14** Gold surface (6 layers) ion intensity *versus* scattering angle plots.  $\sim 9$  ML of nickel was deposited on Au{111} at (a) 400 K (b) 450 K (c) 500 K and exposed to (S)-GA and further annealed to 350-500 K.

Figure 4-15 displays the nickel surface (6 layers) ion intensity *versus* scattering angle plots.  $\sim 9$  ML of nickel as function of nickel deposition temperature at 400 K, 450 K and 500 K. The nickel structure differs dramatically from that of nickel deposited at room temperature. The blocking features are more intense and deep. It is difficult to ascertain if this is a real effect or merely a contribution from the gold bulk data. In contrast, Baddeley and co-workers examined the reverse system, Ni{111}/Au with MEIS and the deposition

of gold onto Ni{111} surfaces resulted in substantial shifting of gold related blocking features.<sup>[25]</sup>

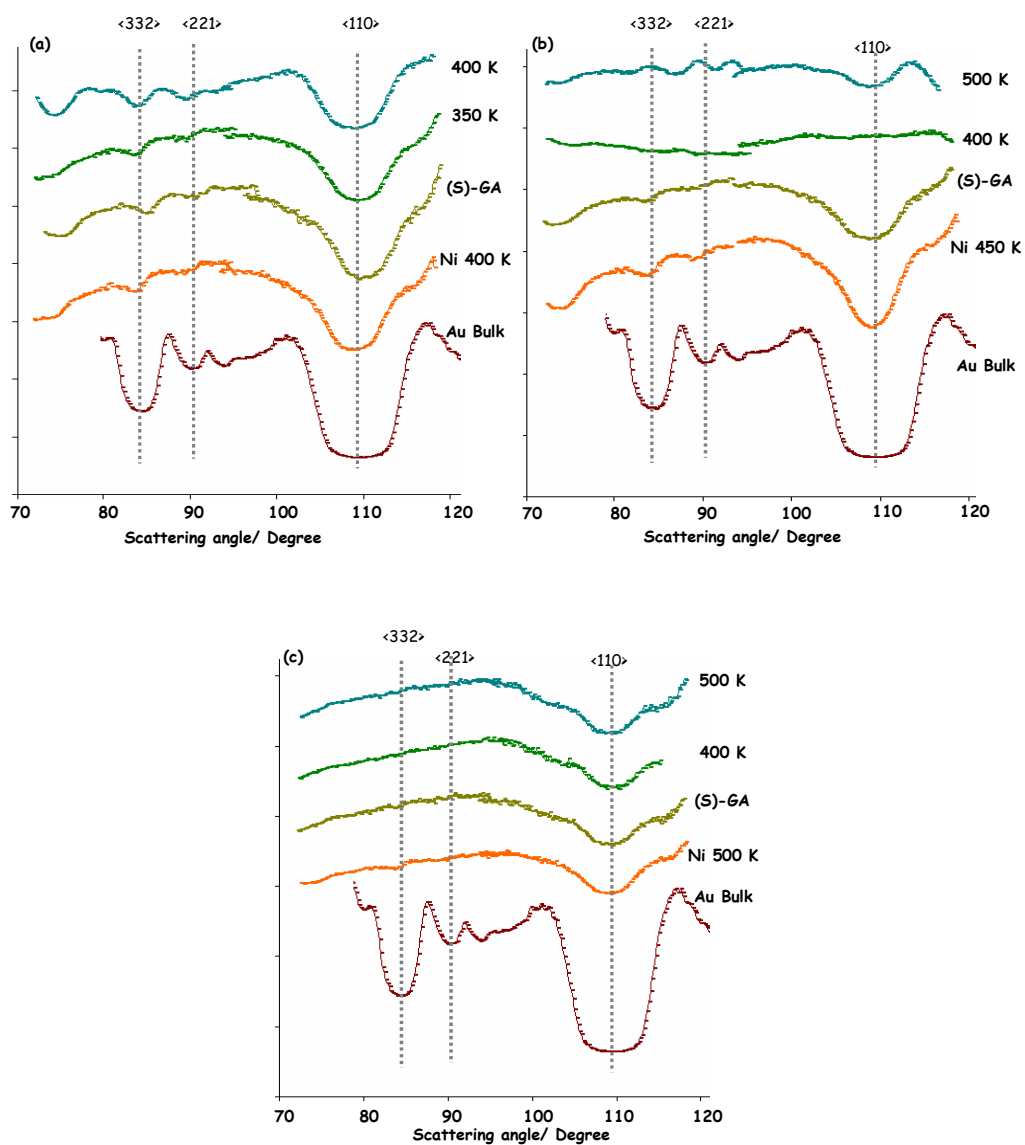


**Figure 4-15** Nickel surface 6 layers ion intensity *versus* scattering angle plots. 10.25 ML of nickel was deposited on Au{111} at (a) 400 K (b) 450 K (c) 500 K and exposed to (S)-GA and further annealed to 400 K and 500 K.

## 4.4 DISCUSSION

### 4.4.1 MORPHOLOGY & PROPOSED MODEL OF (S)-GA ON AU{111}/NI SURFACES (STM)

The morphology of submonolayer nickel islands on Au{111} exposed to (S)-GA was examined using STM. It was found that the changes in morphology were dependent upon the initial size of the nickel islands deposited within the Au{111} herringbone reconstruction. The disappearance of nickel islands (~3 nm in diameter) following adsorption of (S)-GA onto the Au{111}/0.1 ML Ni surface at 300 K is indicative of extensive corrosion. Annealing of this surface to 360 K presents a structure of interconnecting 1D chains of molecular features. (S)-GA is not stable on Au{111} at 300 K and consequently it can be concluded that the 1D molecular chains contain corroded nickel, most probably in the form of Ni<sup>2+</sup> ions.

When 0.25 ML of nickel is deposited on Au{111} at 300 K and the surface exposed to (S)-GA, extensive corrosion of the nickel islands (originally 5-6 nm in diameter) occurs. Annealing of this structure to 360 K results in 1D chains of molecular features. The growth direction of molecular chains zig-zag from one row of nickel islands to the next in an analogous manner to the herringbone reconstruction. Of particular importance is the presence of the molecular chains on the Au{111} surface considering (S)-GA does not adsorb onto gold. The adsorption of amino acids onto bimetallic surfaces has been examined by Zhao *et al.*, in relation to the Au{111}/Cu/glycine<sup>[32]</sup> and the Ag/Cu/glycine systems.<sup>[33]</sup> In the latter case, Zhao *et al.*, attributed molecular features on silver regions of the surface due to the spillover of glycine from the copper regions. This resulted in the formation of chemisorbed glycine on silver. Such chemisorbed features were not observed following the adsorption of glycine on a pure silver surface.<sup>[32]</sup> In the present study

Au{111}/Ni/(S)-GA, the appearance of molecular features on the gold regions of the surface between nickel islands indicates a similar process is possibly occurring.

In order to elucidate the structure of the 1D molecular chains, literature relating to the solid state structures of transition metal glutamates (determined using XRD) was examined.<sup>[34-36]</sup> In each case, the crystal structures contained water molecules. As the sublimation doser for (S)-GA was baked and outgassed for several hours prior to use and the Au{111}/Ni surface annealed to 360 K prior to STM topographic imaging, it is unlikely that any water is involved in the formation of the 1D molecular chains observed in this experiment.

In the crystal structure of copper (II) glutamate, the copper ions are surrounded by ligands in an approximately square planar geometry.<sup>[34-36]</sup> Each Cu<sup>2+</sup> ion is bonded to the aliphatic –COO group and the N and one O of the amino acid functionality of a different glutamate species. Many Ni(II) complexes are known with square planar geometries stabilised by the d<sup>8</sup> electron configuration.<sup>[37]</sup> If a similar geometry was adopted by the nickel ions with the aliphatic –COO- binding to the Ni<sup>2+</sup> in a bidentate arrangement and the amino acid functionality interacting with the metal ion via the N and one of the amino acid O atoms, it is possible to construct a model which reproduces the 1D of the metal organic chains. This is illustrated in figure 4-16 (a). It has been assumed that the Ni-O and Ni-N distances are approximately 2 Å in line with analogous 3D crystal structures.<sup>[38]</sup> If each glutamate molecule adopts an equivalent geometry with respect to the surface, the chains would be predicted to form an arc rather than straight chains as observed with STM. The curving of the chain can be avoided in the model by invoking an alternating geometry for neighbouring glutamate species. This is illustrated in figure 4-16 (b).

The schematic model presented in figure 4-16 (b) shows the carbon chain of glutamate in a geometry similar to that adopted in the crystal structure of e.g. copper (II) glutamate.

For the current study, the periodicity of the model is significantly too long to agree with the STM images (figure 4-3). The periodicity represented by the model in figure 4-16 (b) is similar to that observed in the crystal structure of copper (II) glutamate where chains of glutamate ions adopt a helical structure.

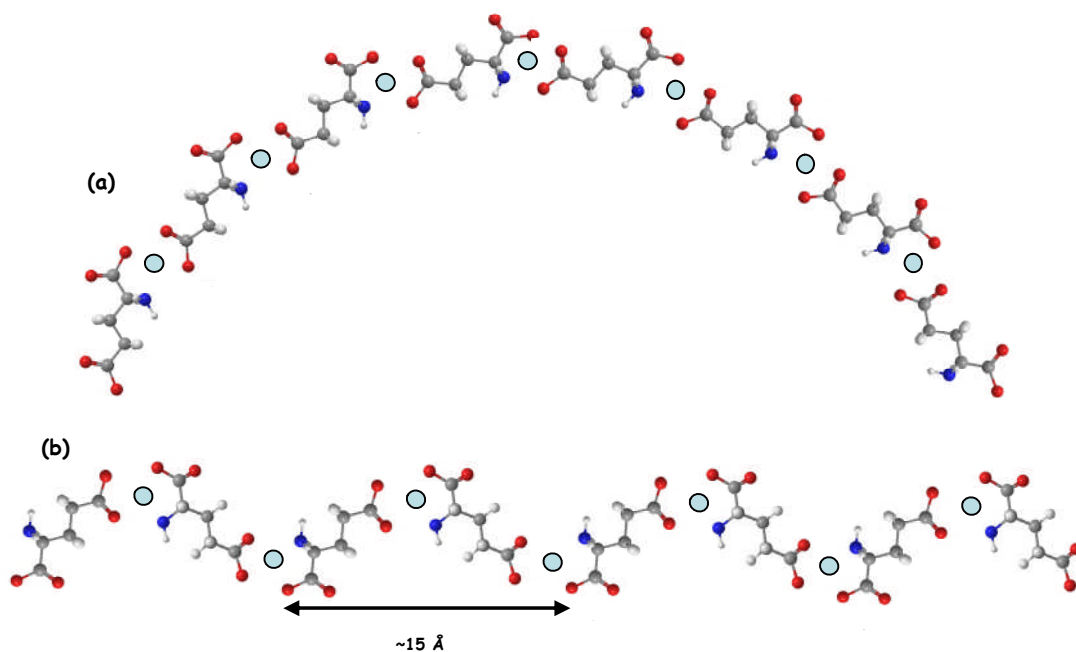


**Figure 4-16** (a) Schematic model illustrating the shape of 1D molecular chains of nickel (II) glutamate whereby each glutamate species adopts an *identical* geometry with respect to the underlying surface. (b) Schematic model illustrating the shape of 1D molecular chains of nickel (II) glutamate whereby each glutamate species adopts an *alternating* geometry with respect to the underlying surface.

A possible explanation for the shorter periodicity observed in STM is that the carbon backbone of each glutamate molecule is substantially curved giving the glutamate chains a tightly coiled helical structure. This is illustrated in figure 4-17. The greater curvature of the helices can be attributed to the lack of water in the glutamate chains produced under UHV conditions. It is feasible that the absence of water ligands in the crystal structure is compensated for by an interaction between the non-coordinating O atom of the amino acid functionality and a neighbouring Ni<sup>2+</sup> ion and/or an intramolecular H-bonding interaction with the –NH<sub>2</sub> functionality causing a coiling of the carbon backbone of

glutamate. Nevertheless, it is unlikely and energetically unfavourable for the glutamate backbone to coil up sufficiently to produce periodicities in the range of 6-8 Å. This is consistent with the molecular repeat measured in the STM images.

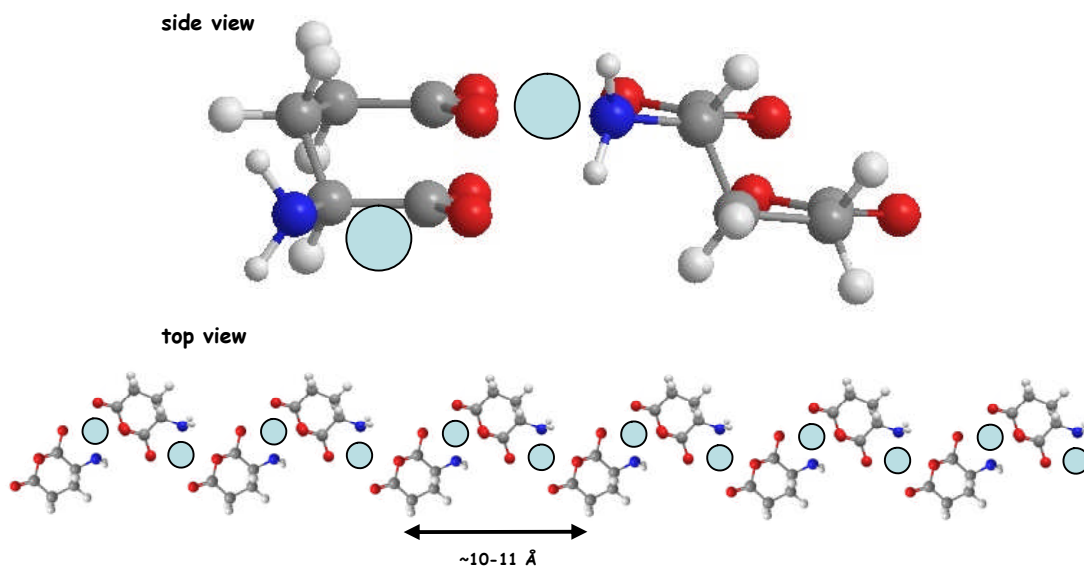


**Figure 4-17** Schematic illustration the side and top views of nickel (II) glutamate chains whereby the glutamate species adopts a helical geometry with a tight curvature.

Examining the thermal chemistry of glutamic acid and metal glutamates an alternative model for the 1D molecular chains can be proposed which is more consistent with the STM data. If solid glutamic acid is heated to a high temperature  $\sim 473$  K, the C-backbone undergoes a cyclisation process to produce pyroglutamic acid with the loss of a water molecule but with preservation of the stereochemistry at the chiral centre.<sup>[39]</sup> This is illustrated in figure 4-18 (a). Similarly, metal glutamate salts are known to convert to the pyroglutamate on heating.<sup>[40]</sup> It is possible that the glutamate species at the edges of the nickel islands are able to react, following gentle heating of the sample, under UHV conditions to produce nickel pyroglutamate  $\text{Ni}(\text{pyGlu})_2$ . This is illustrated in figure 4-18 (b).

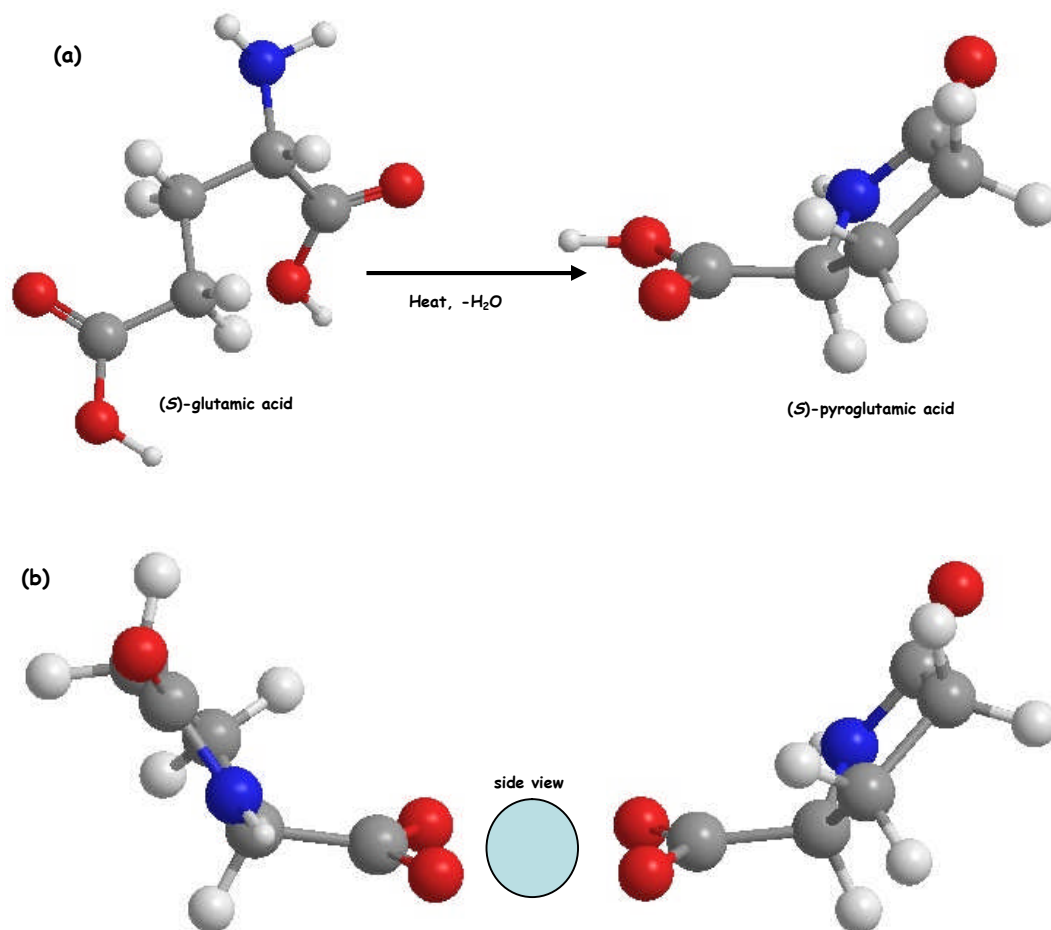


**Figure 4-18** (a) Reaction scheme for the conversion of (S)-glutamic acid into (S)-pyroglutamic acid. (b) Side view of a nickel (II) pyroglutamate complex.

Taking the aforementioned into consideration, it can be proposed that there are two means by which the nickel pyroglutamate units interact with neighbouring species to form 1D chains. By analogy with the crystal structure of zinc pyroglutamate,<sup>[41]</sup> it is possible that some of the molecular chains are composed of nickel pyroglutamate species stabilised via two intermolecular H-bonds between the N atoms in the 5-membered heterocyclic ring and an adjacent O atom of the carboxylate species attached to the Ni ion. Similar intermolecular interactions have been invoked in ordered structures of alanine<sup>[42-44]</sup> and glycine<sup>[45]</sup> on Cu{110}. The proposed structure is shown in figure 4-19 and matches the periodicity within the <101> oriented chains and the orientation of the molecular features in the STM image of Figure 4-3 (b).

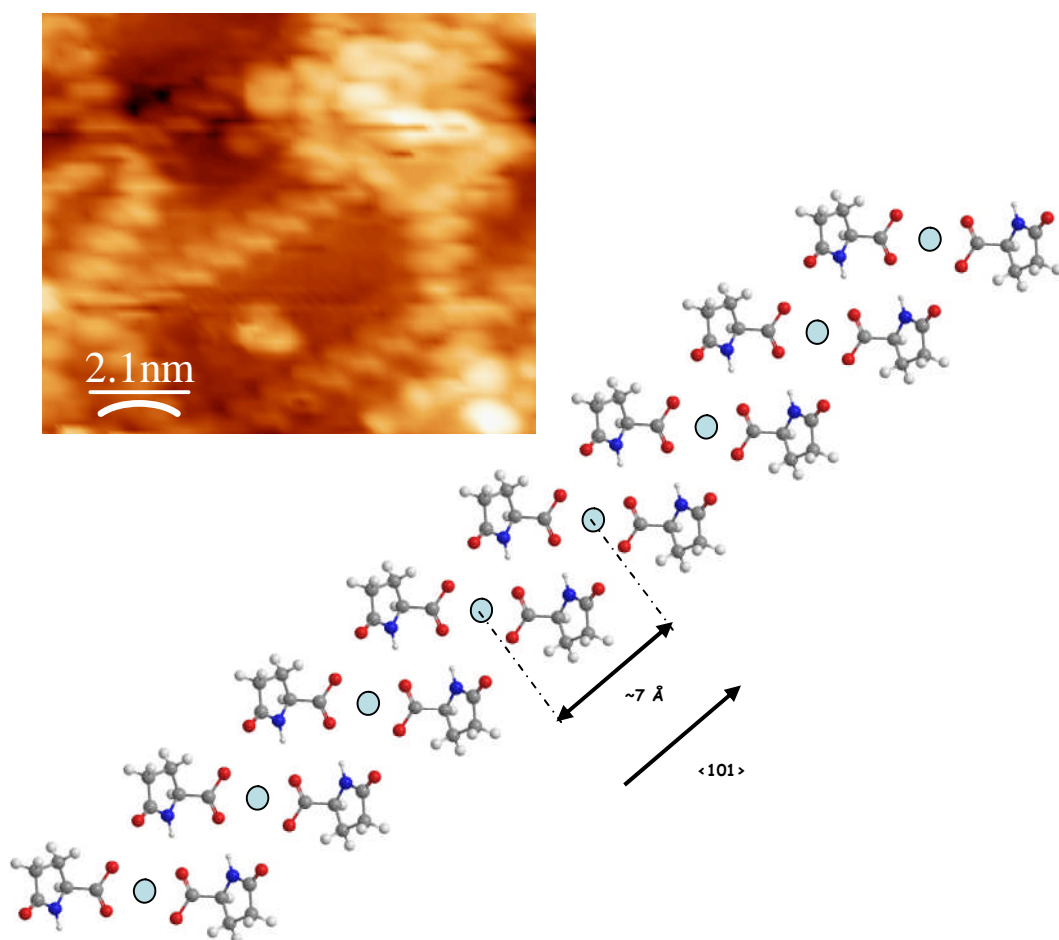


**Figure 4-19** Top view of the proposed H-bonded chain model (inset shows an STM topographic image of such a chain).

In addition, since the heterocycle on each pyroglutamate species is substantially tilted away from the surface (figure 4-18 (b)), the C=O group is unlikely to be in a favourable geometry to interact with neighbouring species. This may be the reason why 1D rows of molecules appear to be favoured. It is interesting to note that in the H-bonded chain, the chirality of the pyroglutamate ligands dictates the growth direction of the chains. In figure 4-3 (b), it is possible to identify the three rotationally equivalent growth directions of these chiral chains, but are unable to find any chains which grow with the mirror equivalent molecular orientation. The second type of 1D chain is oriented  $\sim 30^\circ$  from the H-bonded chains described above (i.e. along  $\langle 112 \rangle$ -type directions). In these chains the ‘molecular’ features imaged by STM are close to perpendicular to the propagation direction of the molecular chains. In addition, the molecular features are slightly closer together than the

H-bonded chains. Consequently, it is proposed that these chains also consist of nickel pyroglutamate species. However, instead of being H-bonded to a neighbouring species, it seems more feasible that neighbouring species are linked via ionic interactions between  $\text{Ni}^{2+}$  and carboxylate units (figure 4-20). Such behaviour is analogous to the bonding in the formation of metal organic coordination networks reported by Clair *et al.*, for cobalt terephthalate on Au{111}.<sup>[9]</sup>

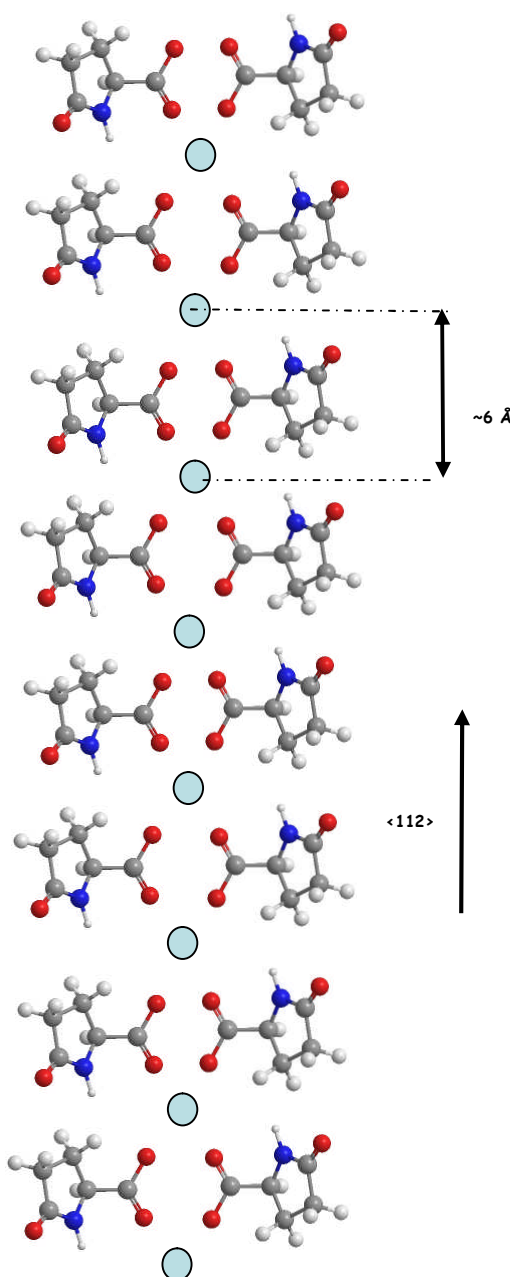


Figure 4-20 Top view of the proposed ionically bonded chain model.

In an attempt to identify the composition of the molecular features observed in the STM topographic images; the features in figure 4-2 (b) were counted and compared to the number of nickel atoms observed in a region of similar dimensions. ~500 features are observed in figure 4-2 (b) in a region with dimensions of 30 nm x 30 nm. In figure 4-2 (a), approximately 16 nickel islands occupy a similar area of the Au{111} surface. The edges of these islands are poorly resolved, but the particles are typically 2-3 nm in diameter (~3 to 7 nm<sup>2</sup> in area). Hence, in a typical area one may estimate that there are between 900 and 2000 Ni atoms. Since both models involve two glutamate species per repeating unit, we may estimate that there are ~1000 pyroglutamate species. In each of the nickel pyroglutamate models, one nickel ion is present per repeat unit (i.e. 500 Ni ions). This suggests that we cannot account for all the nickel in the initial islands. Extensive streaking was observed in the STM images implying that some surface species are mobile and therefore the chains do not account for all the material present on the surface.

Examining the STM images, it is interesting that the 1D molecular features have preferred alignments with respect to the underlying gold surface. In the large-scale image shown in Figure 4-3 (c), it appears that the lines of molecular features predominantly zigzag between rows of nickel islands. The initially deposited islands are close to hexagonal with each edge aligned along the <101> directions of the Au{111} substrate. It is not clear whether the molecular chains emanate from the sides or the corners of the hexagonal particles. The most likely explanation for the orientation of the molecular chains is that the dominant growth direction follows the soliton boundaries of the Au{111} herringbone reconstruction. The soliton boundaries separate the fcc and hcp regions of the Au{111} surface and this transition region may provide stronger adsorption sites to accommodate the adsorbate. It may be possible to argue that the underlying reconstruction creates an anisotropy in the properties of the (close to) hexagonal islands

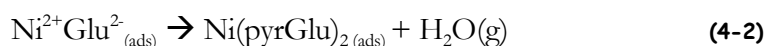
which make certain facet directions more reactive than others. This could also contribute to the zigzag effect of the molecular chains between rows of clusters.

In the 0.25 ML Ni experiment, the growth of chains often appears to be perpendicular to the close packed edges of the nickel islands. Chain growth appears to propagate until the chain collides with another chain or another cluster. It is likely that the termination of chain growth is a key factor in the survival of larger clusters, though it may also be the case that the larger clusters become passivated by the presence of adsorbed glutamate.

RAIR data taken at 300 K suggests that pyroglutamate is not formed by the initial adsorption process. Wagner and Baran reported the vibrational spectrum of a range of metal pyroglutamate complexes. None of the IR spectra displayed a carbonyl band above  $1700\text{ cm}^{-1}$ . The disappearance of the small clusters following exposure to (S)-glutamic acid at 300 K suggests that corrosion occurs at this temperature presumably leading to the formation of nickel (II) glutamate which is too mobile to image with STM. This can be described by the following reaction:



Annealing the surface to 350-360 K results in the formation of the pyroglutamate chains via the reaction shown schematically in figure 4-20 (a) and represented by the following equation:



#### 4.4.2 ADSORPTION & THERMAL STABILITY OF (S)-GA ON AU{111}/NI SURFACES (RAIRS/TPD)

This project investigated the exposure of (S)-GA to Au{111}/ Ni surfaces as a function of varying nickel coverage (0.1-4 ML) and annealing temperature with the objective to

ascertain the adsorption geometry of the amino acid on Au/Ni surfaces. The adsorption of (S)-GA on Ni{111} has been previously studied in detail using RAIRS by Jones *et al.*,<sup>[46]</sup> and the RAIR spectra reported in this project are similar to those observed for Ni{111} under similar adsorption conditions. Jones *et al.*, found that (S)-GA on Ni{111} surfaces at 300 K adsorbed in the zwitterionic form, while adsorption at higher temperatures occurs via the anionic or di-anionic form. (S)-GA adsorbed onto Ag{110}<sup>[47]</sup> at 300 K was found to predominantly occurred in the anionic form. Similarly, other amino acids on Cu<sup>[48-50]</sup> surfaces have a tendency to preferentially adsorb in the anionic form under UHV. Of interest, the main vibrational band associated with the anionic form of (S)-GA is the -NH<sub>2</sub> stretch located at 1550-1574 cm<sup>-1</sup>, which is shifted down from its gas phase value of ~1625 cm<sup>-1</sup>. Similar assignments have been made in the case of alanine,<sup>[48]</sup> glycine<sup>[49]</sup> and praline<sup>[50]</sup> on Cu{110}. In the current study, this band was never detected.

Examining the deposition of 0.1 ML of nickel on Au{111} at 300 K (figure 4-4), the vibrational bands present are characteristic of (S)-GA adsorbing in the zwitterionic form. Theoretical support for the assignments comes from Ramirez and Navarrete<sup>[51,52]</sup> who studied the vibrational spectrum of zwitterionic glutamic acid with force field and normal co-ordinate calculations. The band at 1516 cm<sup>-1</sup> is assigned to the symmetric bending mode of -NH<sub>3</sub><sup>+</sup> and the 1421 cm<sup>-1</sup> band is assigned to the symmetric stretch of the carboxylate group of the amino acid. With increasing coverages of (S)-GA an additional vibrational band at ~1750 cm<sup>-1</sup> is present and is assigned to the C=O stretch of the aliphatic carboxylic acid. At lower coverages of (S)-GA, this band is observed at ~1650 cm<sup>-1</sup>. The difference in frequency is attributed to the extent to which this functional group is involved in intermolecular interactions. At lower coverages, (S)-GA adsorbs in the zwitterionic form in the centre of the nickel islands. As the islands become filled, the glutamate species are forced to populate sites at the edge of islands (i.e. at the interface between nickel and gold). This causes the aliphatic carboxylic acid group to point away

from the islands unable to interact with other adsorbed species since no glutamate species are adsorbed on gold sites under these conditions.

Examining figure 4-6, (S)-GA adsorbed onto Au{111}/ Ni surfaces as a function of nickel coverage 0.1-0.6 ML; there is a reversal in the relative intensity of the 1650 and 1750  $\text{cm}^{-1}$  bands as the nickel coverage increases. This can be ascribed to a change in the ratio of edge sites to sites at the centre of the nickel islands; the latter (i.e. 1750  $\text{cm}^{-1}$  band) decreasing with increasing island size.

Examining figure 4-8, adsorption of (S)-GA onto 4 ML Ni/Au{111} as a function of annealing temperature is also similar to that observed on Ni{111} with bands observed that are characteristic of a zwitterionic species chemically bound to the nickel via the amino acid carboxylate functionality at 1421  $\text{cm}^{-1}$ . Annealing of the Au/Ni/(S)-GA surface to 410 K results in considerable intermixing and creation of an alloyed surface with a composition of ~23 % of a monolayer of gold at the surface (as determined by MEIS). Under these conditions, the intensity of the carboxylate feature located at 1647  $\text{cm}^{-1}$  is attenuated and the 1421  $\text{cm}^{-1}$  feature is completely absent. Further annealing to 510-570 K results in depletion of nickel from the surface and the gradual loss of the carboxylate feature. Under these conditions, RAIR spectra are consistent with the non-zwitterionic (S)-GA species.

Examining the TPD data, it is apparent that the pyroglutamate species (formed upon gentle annealing of the (S)-GA dosed Au/Ni surface to 473 K) is relatively stable up to ~500 K when it is likely that decomposition and desorption occurs – the STM images at higher annealing temperature are indicative of molecular/atomic deposits on the bimetallic surface. This is manifested by the  $\text{H}_2$ ,  $\text{CO}_2$ , CO features having similar desorption temperatures. In the present case, the TPD data is complementary to the MEIS data in that the desorption temperature of the  $\text{H}_2$ ,  $\text{CO}_2$ , CO features correlates to

the concentration of nickel on the Au{111} surface. Overall, it is evident that Ni- rich surfaces increase the stability of the pyroglutamate species by up to ~30 K. For example, examining figure 4-9 (a-c), deposition of nickel onto Au{111} at 300 K has a  $T_{\max}$  of ~483 K for the three features detected ( $H_2$ ,  $CO_2$ , CO). This increases to 518 K upon annealing of the aforementioned surface to 460 K. This analogous to the surface becoming more nickel- rich as the 3D nickel islands flatten. Further annealing to 540 K results in the desorption  $T_{\max}$  reduced by ~10 K. This is analogous to the surface becoming more gold- rich as nickel diffuses to the subsurface. This is an indication that nickel on gold is less reactive than pure nickel surfaces.

### 4.4.3 ADSORBATE-INDUCED SEGREGATION (MEIS)

MEIS proved to be an extremely effective technique for observing the effects of adsorbate-induced segregation. This chapter detailed the quantitative compositional changes observed following the adsorption of (S)-GA onto Au/Ni surfaces. This was achieved by measuring the relative intensities of the Au surface peaks before and after (S)-GA adsorption.

Thin films of nickel were deposited onto Au{111} as a function of thermal treatment and nickel deposition temperature. Deposition of nickel at 300 K and annealing to a series of temperatures ranging from 360-600 K showed remarkable segregation of nickel to the surface layer following the adsorption of (S)-GA; the composition of Au dropping by as much as 50 % in most cases following (S)-GA adsorption. Less segregation of nickel to the surface was observed at 600 K. This is attributed to the surface being extremely Au rich (~ 60 % Au) as disclosed in Chapter 3, with the consequence that less (S)-GA can adsorb onto the surface.

The lower tendency of adsorbate-induced segregation of nickel at elevated deposition temperatures of 400, 450 and 500 K is extremely interesting and points to the importance

of disorder on the surface. This can be rationalised as follows. The monolayer deposition of nickel at 300 K results in the growth of a thick nickel overlayer consisting of 3D islands. These nickel islands do not ‘flatten out’ until an annealing temperature of 410-460 K giving a disordered overlayer (as described in chapter 3). It is realistic to say that these 3D nickel islands and disordered overlayer would have numerous defect sites where it may be more facile to swap nickel atoms for gold atoms. In contrast, the deposition of nickel at elevated temperatures would result in a ‘flattened’ and relatively ordered nickel overlayer with less defect sites available making it thermodynamically more difficult to exchange nickel and gold atoms.

The fact that segregation is enhanced as a function of annealing treatment after exposure to (S)-glutamic acid has several possible causes. Segregation requires diffusion barriers to be overcome so, though it may be thermodynamically favoured at room temperature, the diffusion kinetics may prevent extensive segregation. However, as the sample is annealed, diffusion is enhanced and segregation becomes more facile. In addition, on more Au rich surfaces, the (S)-glutamic acid species adsorbed at 300 K are in the neutral non-zwitterionic form (RAIRS) and are likely to be essentially physisorbed on the surface. Unfortunately, we are unable to measure the RAIR spectra as a function of annealing temperature. However, it may be that deprotonation to the anionic form and/or conversion to pyroglutamate occurs on annealing the surface creating a molecular species which is able to interact more strongly with Ni atoms in the surface, thus facilitating segregation.

## 4.5 IMPLICATIONS FOR ENANTIOSELECTIVE CATALYSIS

The adsorption from solution of (S)-GA on nickel catalysts is known to create catalysts capable of the enantioselective hydrogenation of  $\beta$ -ketoesters. While, the formation of

pyroglutamate under UHV conditions has no relevance to the catalytic system, it indirectly highlights the importance of nickel crystallite size. From the results presented in this Chapter it has been shown that highly dispersed nickel nanoparticles (<3 nm) would be expected to be completely dissolved by modification with (S)-GA whereas, larger nickel particles will be corroded but would survive the modification process – perhaps stabilised by the adsorption of glutamate on the more Ni{111}-like regions of the particles. It is also possible that the etched nickel particles will possess chiral arrangements of nickel atoms that may be active sites for chiral hydrogenation chemistry. MEIS successfully demonstrated that (S)-GA can induce extensive segregation of nickel to the Au/Ni surface under a reactive gaseous environment. The use of gold in the nickel catalysed enantioselective hydrogenation of  $\beta$ -ketoesters is a very promising avenue in that it is selectively feasible to quench the racemic unmodified sites in this catalyst. Therefore, it should in theory, be possible to increase the overall enantioselectivity of this catalytic system if the unmodified (Au rich) sites on the surface are indeed inactive.

## 4.6 SUMMARY

The adsorption of (S)-GA on 2D nickel islands grown on Au{111} results in the formation of two distinct species – zwitterionic (S)-GA adsorbed on Ni-like sites and a similar species adsorbed at edge sites whose aliphatic –COOH group is unable to interact with neighbouring adsorbed species. Nickel particles with initial diameters <3 nm are completely destroyed by the adsorption of (S)-GA at 300 K. Larger nickel particles are modified in shape, but survive the adsorption process presumably becoming passivated by the adsorbed glutamate layer. Annealing (S)-GA coated surfaces to 360 K results in the corrosion of islands and the formation of 1D chains of molecular features. By analogy with the crystal structure of metal glutamates, it was concluded that the periodicity of the molecular features is too short to be consistent with the formation of nickel (II)

glutamate. Instead, it is believed that glutamate undergoes an internal cyclisation process – forming pyroglutamate with the liberation of a water molecule. Two types of chain are identified. We propose that one is formed by intermolecular H-bonding interactions between neighbouring pyroglutamate units. The second is more likely to be stabilised by ionic interactions between Ni<sup>2+</sup> and the carboxylate functionalities of pyroglutamate. Chains appear to nucleate on the soliton boundaries of the Au{111} herringbone reconstruction giving preferred growth directions between rows of clusters. MEIS quantitatively demonstrated that (S)-GA can successfully induce nickel segregation to the Au/Ni surface; the composition of gold reduced by 50 % in most cases. The extent of segregation is found to be greater if Ni films are deposited at 300 K and subsequently annealed than if Ni films are deposited at elevated temperature.

**BIBLIOGRAPHY**

- [1] R. P Feynman. *Eng. Sci.* **23** (1960) 22.
- [2] G. Binnig & H. Rohrer. *Rev. Mod. Phys.* **59** (1987) 615.
- [3] J. V. Barth, G. Costantini & K. Kern. *Nature* **437/29** (2005) 671.
- [4] D. D. Chambliss, R. J Wilson & S. Chiang. *Phys. Rev. Lett.* **66** (1991) 1721.
- [5] B. Voigtlander, G. Meyer & N. M. Amer. *Surf. Sci.* **255** (1991) L529.
- [6] B. Voigtlander, G. Meyer & N. M. Amer. *Phys. Rev. B.* **44** (1991) 10353.
- [7] A. W. Stephensen, C. J. Baddeley, M. S. Tikov & R. M. Lambert. *Surf. Sci.* **398** (1998) 172.
- [8] E. I. Altman & R. J. Colton. *Surf. Sci.* **304** (1994) L400.
- [9] S. Clair, S. Pons, S. Fabris, S. Baroni, H. Brune, K. Kern & J.V. Barth. *J. of Phys.Chem. B.* **110** (2006) 5627.
- [10] S. Clair, W. Pons, H. Brune, K. Kerns & J. V. Barth. *Angew. Chem Int. Ed.* **44** (2005) 7294.
- [11] A. Stein. *Advan.Mater.* **15** (2003) 763.
- [12] M. E. Davis. *Nature* **417** (2002) 813.
- [13] J. V. Barth, J. Weckesser, N. Lin, A. Dmitriev & K. Kern. *App. Physics Mater. Sci & Proces.* **76** (2003) 645.

- [14] A. Dmitriev, H. Spillmann, N. Lin, J. V. Barth & K. Kern. *Ang. Chem. Intern. Ed.* **42** (2003) 2670.
- [15] S. Stepanow, M. Lingenfelder, A. Dmitriev, H. Spillmann, E. Delvigne, N. Lin, X.B. Deng, C. Z. Cai, J. V. Barth & K. Kern. *Nature Mat.* **3** (2004) 229.
- [16] A. P. Seitsonen, M. Lingenfelder, H. Spillmann, A. Dmitriev, S. Stepanow, N. Lin, K. Kern & J. V. Barth, *J. Amer. Chem. Society.* **128** (2006) 5634.
- [17] T. Classen, G. Fratesi, G. Costantini, S. Fabris, F. L. Stadler, C. Kim, S. de Gironcoli, S. Baroni & K. Kern. *Angew. Chem. Intern. Ed.* **44** (2005) 6142.
- [18] N. Lin, S. Stepanow, F. Vidal, J. V. Barth & K. Kern. *Chem. Comm.* (2005) 1681.
- [19] A. Dmitriev, H. Spillmann, M. Lingenfelder, N. Lin, J. V. Barth & K. Kern. *Langmuir.* **20** (2004) 4799.
- [20] D. A King, D. P. Woodruff (Eds.). *The Chemical Physics of Solid Surfaces, Vol. 10. Surface Alloys & Alloyed Surfaces.* Amsterdam, Elsevier. 2000. Chapter 14.
- [21] J. H. Sinfelt & G. H. Via. *J. of Catal.* **56** (1979) 1.
- [22] K. C. Taylor. *Catal. Rev.* **35** (1993) 457.
- [23] G. C. Bond, C. Louis & D. T. Thompson. *Catalysis by Gold.* Catalytic Science Series- Vol. 6 (2006). Chapter 1.
- [24] S. Deckers, F. H. P. M. Habraken, W. F. van der Weg, A. W. Denier van der Gon, J. F. van der Veen & J. W. Genus. *Appl. Surf. Sci.* **45** (1990) 12.
- [25] T. E. Jones, T. C. Q. Noakes, P. Bailey & C. J. Baddeley. *Surf. Sci.* **600** (2006) 2129.

- [26] T. E. Jones, T. C. Q. Noakes, P. Bailey & C. J. Baddeley. *J. Phys. Chem. B.* **108** (2004) 4759.
- [27] T. E. Jones, T. C. Q. Noakes, P. Bailey & C. J. Baddeley. *Surf. Sci.* **569** (2004) 63.
- [28] T. E. Owens, T. E. Jones, T. C. Q. Noakes, P. Bailey & C. J. Baddeley. *J. Phys. Chem. B.* **110** (2006) 21152.
- [29] Y. Izumi. *Advan. Cat.* **32** (1983) 215.
- [30] T. E. Jones & C. J. Baddeley. *Surf. Sci.* **513** (2002) 453.
- [31] C. J. Baddeley, L. H. Bloxham, S. C. Laroze, R. Raval, T. C. Q. Noakes & P. Bailey. *J. Phys. Chem. B.* **105** (2001) 2766.
- [32] X. Y. Zhao & J. Rodriguez. *Surf. Sci.* **600** (2006) 2113.
- [33] X. Y. Zhao, H. Yan, X. W. Tu, R. G. Zhao & W. S. Yang. *Langmuir.* **19** (2003) 5542.
- [34] C. M. Gramaccioli & R. E. Marsh. *Acta Crystallogr.* **21** (1996) 594.
- [35] M. Mizutani, N. Maejima, K. Jitsukawa, H. Masuda & H. Einga. *Inorg. Chim. Acta.* **283** (1998) 105.
- [36] F. A. Cotton & G. Wilkinson. *Advanced Inorganic Chemistry.* 5<sup>th</sup> Edition. Wiley, New York. 1998.
- [37] N. Guillou, C. Livage, M. Drillon & G. Ferey. *Angew. Chem., Int. Ed.* **42** (2003) 5314.
- [38] C. Najera & M. Yus. *Tetrahedron Asymmetry.* **10** (1999) 245.
- [39] C. C. Wagner & E. J. J. Baran. *Raman Spectrosc.* **35** (2004) 395.

- [40] H. Schmidbaur, I. Bach, D. L. Wilkinson & G. Muller. *Chem. Ber.* **121** (1998) 1441.
- [41] R. B. Rankin & D. S. Sholl. *Surf. Sci.* **574** (2005) L1.
- [42] S. M. Barlow, S. Louafi, D. Le Roux, D. Williams, C. Muryn, S. Haq & R. Raval. *Surf. Sci.* **590** (2005) 243.
- [43] D. I. Sayago, M. Polcik, G. Nisbet, C. L. A. Lamont & D. P. Woodruff. *Surf. Sci.* **590** (2005) 76.
- [44] G. Jones, L. B. Jones, F. Thibault-Starzyk, E.A. Seddon, R. Ravel, S. J. Jenkins & G. Held. *Surf. Sci.* **600** (2006) 1924.
- [45] Q. Chen, D.J. Frankel & N. V. Richardson. *Surf. Sci.* **497** (2002) 37.
- [46] T.E. Jones, M. E. Urquhart & C. J. Baddeley. *Surf. Sci.* **587** (2005) 69.
- [47] T. E. Jones, C. J. Baddeley, A. Gerbi, L. Sevio, M. Rocca, L. Vattuone. *Langmuir.* **21** (2005) 9468.
- [48] J. Williams, S. Haq & R. Raval. *Surf. Sci.* **368** (1996) 303.
- [49] S. M. Barlow, K. J. Kitching, S. Haq & N. V. Richardson. *Surf. Sci.* **401** (1998) 322.
- [50] E. M. Marti, S. M. Barlow, S. Haq & R. Raval. *Surf. Sci.* **501** (2002) 191.
- [51] J. T. L. Navarrete, L. Bencivenni, F. Ramondo, V. Hernandez & F. J. Ramirez. *J. of Molec. Struc.-Theochem.* **330** (1995) 261.
- [52] F. J. Ramirez & J. T. L. Navarrete. *Spectrochimica Acta Part A -Molecular and Biomolecular Spectroscopy.* **52** (1995) 293.

# Chapter 5

## *Catalysis by Colloids*

### **SYNOPSIS**

*Colloidal preparative routes have been used in this project to synthesise bimetallic Au/Ni nanoparticles supported on ordered and disordered silica. The catalysts are then modified by the adsorption of the chiral ligand, (R,R)-tartaric acid and tested for their enantioselectivity with respect to methylacetoacetate hydrogenation. At each stage the catalysts are characterised by a combination of Extended X-ray Absorption Fine Structure (EXAFS), Transmission Electron Microscopy (TEM), Energy Dispersive X-ray Spectrometry (EDS), Gas Chromatography (GC) and Atomic Absorption Spectroscopy (AAS).*

## 5.1 INTRODUCTION

Particles suspended in a liquid are considered colloidal if their size ranges between 10 nm and 500 nm. Described by Wilhelm Ostwald as '*lying in the world of neglected dimensions*', colloids have a long history.<sup>[1]</sup> In the antiquity, the ancients prepared and used two important forms of colloidal gold, namely potable gold (supposedly the Elixir of life) and Purple of Cassius used to make ruby glass. The first scientific approach to synthesise gold particles dates back to the nineteenth century with Michael Faraday.<sup>[2]</sup>

Bimetallic colloids can exist as an alloy or as a layered structure and are of special interest as they serve as models for studying the formation of different alloys. Another attraction to the synthesis of bimetallic colloids is their core/shell layered structure whereby, a coat of one metal encapsulates a core consisting of the other. It possible to save precious metals like Pt and Pd by optimising the preparation conditions so that only a thin surface layer occurs.<sup>[3]</sup> Colloidal systems have received much attention of late due to their unusual catalytic properties as compared to those of the bulk metal. This is attributed to their extremely small size and large surface to volume ratio.<sup>[4-5]</sup>

The reduction of metal salts in solution is the method must often used to generate bimetallic colloids. The sizes of the particles depend upon the reducing agent and the preparation conditions such as concentration and temperature. Stabilisers such as linear polymers, ligands, surfactants or oxide supports are used to prevent coagulation of the colloidal nanoparticles. In academia, incorporation of colloids into silica supports is a topic of intense research since the discovery of mesoporous silica by Mobil scientists in 1992.<sup>[6-11]</sup> This encompasses a wide-field relating not only to catalysis but also to materials science.

### 5.1.1 MESOPOROUS SILICA SUPPORTS

Mesoporous silica supports have received much attention due to their large pore sizes (2-50 nm) compared with those of conventional microporous zeolites (<2 nm). The main advantage of using mesoporous supports in catalysis are the large pores that facilitate mass transfer of active species and the high surface area that enables a high concentration of active sites per mass of support material. Large substrates can be incorporated into a mesoporous support which is not possible with zeolites due to pore blockage.<sup>[12]</sup> Silicas have a rigid structure and do not swell in solvents enabling them to be used in high temperatures and high pressures making them ideal for enantioselective catalysis.

Mobil Corporation in 1992 first discovered ordered mesoporous solids with what became known as the M41S family of silica and aluminosilicates; hexagonal MCM-41, cubic MCM-48 and lamellar MCM-50 phases.<sup>[13-15]</sup> These mesoporous materials were prepared from ionic surfactants primarily cetyl trimethyl ammonium bromide (CTAB), as structure directing agents. The synthesis is carried out in basic conditions and follows an ionic mechanism of formation (denoted  $S^+ I^-$  where S=surfactant and I=inorganic species). Stucky and co-workers extended this mechanism to a whole different series of other electrostatic assembly mechanisms, namely the reversed  $S^- I^+$  mechanism and counter-ion mediated  $S^+ X^- I^+$  and  $S^- M^+ I^-$  pathways.<sup>[16-18]</sup>

Pinnavaia and co-workers synthesised two additional mesoporous solids (HSM and MSU) using non-ionic organic-inorganic interactions. Neutral surfactants such as primary amines and poly(ethylene oxides) and neutral silica precursors were used ( $S^0 I^0$ ).<sup>[19]</sup> Long-range hexagonal worm like structures were produced resembling MCM-41. However, these mesoporous structures had thicker pore walls, higher thermal stability and had the added advantage that the surfactant and template molecules (if incorporated e.g. ligands) could be recovered by simple extraction. This is of huge economical importance.

Following this, Stucky and co-workers introduced a new synthesis route (abbreviated SBA-*n* **S**anta-**B**arbara-*n*) using amphiphilic block copolymers as organic structure directing agents.<sup>[19]</sup> In particular, the triblock copolymer Pluronic P123 because of its mesostructural ordering properties, amphiphilic character, low cost commercial availability and biodegradability was used. Pluronic P123 consists of ethylene oxide/ propylene oxide/ ethylene oxide (PEO-PPO-PEO) of various quantities and ratios. SBA-15 is a long-range ordered mesoporous silica with two-dimensional hexagonal symmetry. It exhibits an extremely high surface area from 100 to 600 m<sup>2</sup>/g and consists of a hexagonal array of uniform one-dimensional cylindrical pores with pore diameters in the range of 5-30 nm.

Using aqueous acidic conditions pH ~1 and a dilute triblock polymer concentration, SBA-15 can be synthesised with a highly ordered mesostructure and thick uniform silica walls (31-64 Å) enhancing the thermal stability over previous mesoporous materials. The pore size and thickness of the walls can be varied by altering the heating temperatures (308-413 K) and time (11-72 hr) of SBA-15 in the reaction solution. Tetraethoxysilane (TEOS) is typically used as a silica source in the preparation of SBA-15. At pH values from 2 to 6, above the isoelectric point of silica, no precipitation or formation of silica gel occurs. At a neutral pH ~7, only disordered or amorphous silica is obtained.<sup>[19]</sup>

SBA-15 and SiO<sub>2</sub> are perfect hosts for metal nanoparticles because of their inert character which allows for a better understanding of possible alloying effects, particle morphology and size effects. In this project, Au/Ni nanoparticles are incorporated into these supports. It is anticipated that the long range periodicity and pore structure of SBA-15 will restrict the growth of the bimetallic nanoparticles producing small particles ranging from 5 to 30 nm. This is compared to SiO<sub>2</sub>. The size and morphology of the bimetallic nanoparticles,

leaching behaviour and sintering of these particles is examined as a function of reduction method.

### 5.1.2 BIMETALLIC AU/NI CATALYSIS

The application of bimetallic catalysis to industry has been extensive. These systems often exhibit enhanced catalytic reaction rates and selectivities compared to their monometallic counterparts. Gold catalysis is a topic of intense research since Haruta and Date's exciting discovery that well-dispersed gold nanoparticles are extremely active for CO oxidation.<sup>[20]</sup> Since then a plethora of literature has appeared on the synthesis of gold nanoparticles.<sup>[21]</sup>

In recent times, gold has been used in heterogeneous bimetallic catalysis to dilute the activity of the more active component and to alter the selectivity of the catalytic reaction. In 1998, Basenbacher *et al.*, predicted that Ni/Au catalysts would show enhanced resistance to carbon forming in the steam reforming process than monometallic nickel catalysts.<sup>[22-23]</sup> Gold is immiscible with bulk nickel at temperatures relevant to catalyst preparation conditions so this is purely a surface phenomenon. STM studies of gold deposited on Ni {100} by Pleth Nielsen *et al.*, verified Ni/Au alloy formation on the surface of the nickel single crystal.<sup>[24]</sup> More recently, Triantafyllopoulos and Neophytides also reported that the addition of a small quantity of gold to Ni/YSZ catalysts inhibits carbon formation in the steam reforming process.<sup>[25]</sup> Keane and co-workers have also been examining the potential of bimetallic Ni/Au in catalytic hydrodechlorination reactions.<sup>[26-27]</sup> The incorporation of gold to this nickel system resulted in higher activity; an effect they attributed to a surface Ni-Au synergism. Since bulk gold has no activity of its own, the aforementioned are powerful demonstrations of the modifying influence of gold on surfaces of active catalysts where the formation of a bulk alloy is not possible.

### 5.1.3 AIM OF RESEARCH

Enantioselective Au/Ni nanoparticles supported on SiO<sub>2</sub> and SBA-15 have been synthesised in this project. The catalysts are modified by the adsorption of the chiral ligand, (R,R)-tartaric acid and subsequently tested for their activity and enantioselectivity with respect to methylacetoacetate hydrogenation. The nickel catalysed hydrogenation of  $\beta$ -keto esters is one of the few successful examples of an enantioselective heterogeneous catalytic reaction. However, bare, unmodified nickel sites on the catalyst surface are known to catalyse a racemic reaction competitively with the enantioselective reaction thereby lowering the overall enantioselective yield.<sup>[28]</sup> In addition, modification of the nickel catalysts is a corrosive process and is susceptible to leaching of nickel into the modifying solution, thereby lowering the lifetime of the catalyst.

The aim of this chapter is to investigate the possibility of quenching the reactivity of unmodified nickel sites by alloying with gold. Alloying nickel with an inert metal such as gold, in theory, should dilute the reactivity of these unmodified sites and it is postulated to result in reduced nickel leaching. It is predicted that the adsorption of the chiral modifier, (R,R)-tartaric acid, on the bimetallic Au/Ni surface will segregate nickel to the surface thereby creating active chirally modified nickel regions separated by inactive Au-rich unmodified regions as detailed in Chapter 4 of this thesis. At each stage the enantioselective catalysts are characterised by a combination of Extended X-ray Absorption Fine Structure (EXAFS); Transmission Electron Microscopy (TEM), Energy Dispersive X-ray Spectrometry (EDS), Gas Chromatography (GC) and Atomic Absorption Spectroscopy (AAS). These characterisation techniques and experimental conditions are detailed in Chapter 2.

## 5.2 EXPERIMENTAL

Incorporation of metal nanoparticles into SiO<sub>2</sub> and SBA-15 supports was achieved by co-impregnation. Three methods were used to reduce the Au/Ni nanoparticles. The first, often referred to as the Turkevich method, derives its name from the work of Turkevich and Stevenson.<sup>[29]</sup> Solutions of Au/Ni metal precursors are reduced with trisodium citrate and hydroxylamine hydrochloride, stabilised by the modifier (R,R)-tartaric acid and brought into contact with the silica support. This method did not successfully reduce nickel and consequently alternative reduction methods were explored to reduce the bimetallic Au/Ni nanoparticles. Compared with noble metals, nickel nanoparticles are relatively difficult to prepare due to being easily oxidised. Copious procedures exist for the synthesis of gold nanoparticles however literature on the preparation of Ni nanoparticles is sparse. Hydrazine hydrate was used because recent studies by Bettahaer and co-workers showed that it is a good reducing agent in aqueous medium for nickel particles and does not form mixed oxides with silica.<sup>[30-33]</sup>

The metal precursors were co-impregnated with the silica support and reduced *in situ* by use of hydrazine hydrate with the use of a Schenk line. The third method reduced the Au/Ni nanoparticles via a 5 % H<sub>2</sub> in Ar mixture at 823 K in a furnace. Following this, the prepared Au/Ni colloids were modified with (R,R)-tartaric acid and tested in the enantioselective liquid phase hydrogenation of methylacetoacetate to (R)-methyl-3-hydroxybutyrate (herein denoted (R)-MHB).

### 5.2.1 PREPARATION OF SBA-15

SBA-15 was synthesised following the literature procedure by Stucky and co-workers.<sup>[16-17]</sup> 4.0 grams of triblock copolymer Plurionic P123 (BASF) was dissolved into a mixture of 138 grams of dH<sub>2</sub>O, 12.2 grams of 37 % concentrated hydrochloric acid (Fluka) and 8

grams of tetramethoxysilane (TEOS) (Aldrich). The resulting mixture was stirred at 313 K for 24 hours. The mixture was transferred to a Teflon bottle and then aged at 373 K for two days. The sample was recovered by filtration, washed with dH<sub>2</sub>O and air-dried overnight. The organic template was removed by calcination in N<sub>2</sub> at 823 K for 4 hours followed by further calcination in O<sub>2</sub> at 823 K for 4 hours. The mesoporous support was pre-treated in air at 823 K for 10 hours prior to use.

It should be noted that the silica supports were not fully characterised via x-ray diffraction (XRD) and N<sub>2</sub> isotherms as the aim of this study is to ascertain the alloy and/or core-shell behaviour of the Ni and Au nanoparticle inserted into these supports.

## **5.2.2 CO-IMPREGNATION & CO-REDUCTION OF AU/NI SUPPORTED COLLOIDS**

### **5.2.2.1 TURKEVICH METHOD**

To produce a 1 : 1 molar ratio of Au : Ni colloids, 16 mL of 2.04 x 10<sup>-4</sup> M gold (III) chloride trihydrate (Aldrich) and 80 mL of a 1 % solution of trisodium citrate (Fluka) were simultaneously added (very gradually) to 1600 mL of stirring boiling dH<sub>2</sub>O. Boiling and stirring were maintained for a further 1 hour yielding a ruby red solution. The solution was diluted to 8 L. Over a period of 2 hours, 40 mL of 2.04 x 10<sup>-4</sup> M nickel (II) nitrate hexahydrate (Aldrich) and 83 mL of 1 % hydroxylamine HCl (Sigma) were added simultaneously in a dropwise manner with constant stirring. After 48 hours of stirring at room temperature, 2 grams of (R,R)-tartaric acid (Fluka) was added to stabilise the particles. The solution was left stirring for 2 hours followed by the addition of 1 gram of SBA-15 mesoporous support. The solution was stirred for a further 12 hours, rotary evaporated and the resulting catalyst stored in a vacuum dessicator. The molar ratio of Au : Ni was varied between 1 : 2 and 1:8.

### 5.2.2.2 IMPREGNATION

1 gram of SBA-15/ SiO<sub>2</sub> (Fluka; fumed Surface Area 280 m<sup>2</sup>/g) was impregnated with 40 mL of aqueous nickel (II) nitrate hexahydrate and 40 mL of aqueous tetrachlorauric acid. Both metals were calculated to obtain the nominal composition of 1.0-8.0 wt. % Au and 5.0-10.0 wt. % Ni. The mixture was stirred for 16 hours at room temperature; rotary evaporated at 350 K and dried in a furnace for 16 hours at 373 K in air.

### 5.2.2.3 HYDRAZINE HYDRATE REDUCTION

The reduction of the Au/Ni nanoparticles particles was performed under argon atmosphere in a two necked reaction flask, dipping in an oil bath. The reduction was performed under reflux. The supported Au/Ni colloids were added to the reaction flask containing 50 mL of dH<sub>2</sub>O. The suspension was stirred for 20 minutes at room temperature under vacuum. Under an Ar atmosphere, 10 mL of hydrazine hydrate (Sigma) was added in excess. Aliquots of the mixture were taken and the pH was measured using litmus paper. The pH of the solution was 10-12 and should remain constant throughout the reduction process. The reaction mixture was slowly heated to 353 K and maintained at this temperature for 30 minutes. At this temperature the mixture turns black. The mixture was then filtered, washed with dH<sub>2</sub>O until a neutral pH was obtained, rotary evaporated at 333 K and stored in a vacuum desiccator until further use.

### 5.2.2.4 HYDROGEN REDUCTION

The impregnated nanoparticles were first treated at 823 K in air for 5 hours at a constant flow rate. The nanoparticles were allowed to cool to room temperature then reduced under a stream of hydrogen gas for 2 hours at 823 K. The reduced nanoparticles were slowly cooled and stored in a vacuum desiccator.

### 5.2.3 MODIFICATION OF AU/NI NANOPARTICLES

Modification was carried out in a round bottomed flask with a reflux condenser. The reduced catalysts were modified with 100 mL of a 270 mM solution of (R,R)-tartaric acid. 4 grams of sodium bromide was added to the reaction mixture and maintained at pH 5.1 with sodium hydroxide. The modification temperature was kept at 373 K and the reaction mixture stirred for an hour and a half. The modified catalysts were then filtered (filtrate was kept for AAS analysis to examine the extent of nickel leaching), washed to neutral pH with aliquots of dH<sub>2</sub>O and the hydrogenation solvent, THF.

### 5.2.4 CATALYTIC TESTING

The synthesised Au/Ni bimetallic colloids were tested in the enantioselective liquid phase hydrogenation of methylacetoacetate to (R)-methyl-3-hydroxybutyrate. The hydrogenation reaction was carried out in an autoclave (Parr 4842) and the reaction mixture subsequently analysed with gas chromatography using a chiral Restek Rt- $\gamma$ DEXs capillary column. The stationary phase in the column consists of 14% cyanopropylphenyl and 86% dimethyl polysiloxane which is doped with 2,3-di-acetoxy-6-0-tert-butyl dimethylsilyl gamma cyclodextrin.

2.5 grams of methylacetoacetate was hydrogenated at 353 K for 24 hours using 0.5 grams of catalyst in 20 mL of THF solvent. The pressure of hydrogen was 10 bar. The hydrogenated reaction mixture was then tested for its conversion of methylacetoacetate and tested for its enantioselectivity by gas chromatography. The enantiomeric excess (ee) was calculated from the following equation:

$$\% ee = \frac{[(R)\text{-MHB}] - [(S)\text{-MHB}]}{[(R)\text{-MHB}] + [(S)\text{-MHB}]} \times 100 \quad (1)$$

where (R)-MHB and (S)-MHB denote the concentrations of methyl (R)-3-hydroxybutyrate and methyl (S)-3-hydroxybutyrate, respectively.

## 5.3 RESULTS

### 5.3.1 TEM & EDS STUDIES

A valuable technique for examining the structure of nanoparticles is TEM. In the present study, it can be used in the high resolution mode to reveal the internal structure of nanoparticles. While it is difficult to fully ascertain whether or not the nanoparticles are located inside the pores of the silica supports with TEM solely; in this study, elongated metallic nanoparticles running parallel to the pore structure are assumed to do so. This proved important as one could image the leached nanoparticles after the modification and hydrogenation procedures. Lattice planes of the nanoparticles were used to confirm the identity of the nanoparticles. HRTEM analysis was carried out after reduction, modification and hydrogenation of selected supported bimetallic Au/Ni particles. High magnification TEM of the bimetallic nanoparticles is necessary to obtain information on the morphology of nanoparticles. Bimetallic colloids can exist as an alloy or as a core/shell layered structure whereby one metal encapsulates a core consisting of the other. It is not possible to deduce this information from low magnification TEM micrographs. In addition, EDS provided chemical compositions of the features present in selected catalysts.

#### 5.3.1.1 TURKEVICH METHOD

HRTEM micrographs of prepared SBA-15 mesoporous structures are presented in figure 5-1. The micrographs show an ordered hexagonal silicate structure. Figure 5-1 (a) is viewed with pores running perpendicular to the beam and figure 5-1 (b) is viewed with pores running parallel to the beam. It should be noted that the images taken are too under

focused for quantitative analysis i.e. the pores appear smaller than they really are and the dark, electron-rich region (silica walls) are enhanced and appear bigger than what they actually are. However, from the micrographs it is evident that the prepared SBA-15 is of good quality and well ordered indicating the synthesis method described by Stucky *et al.*<sup>[16-17]</sup> was accurately adhered to by the author.

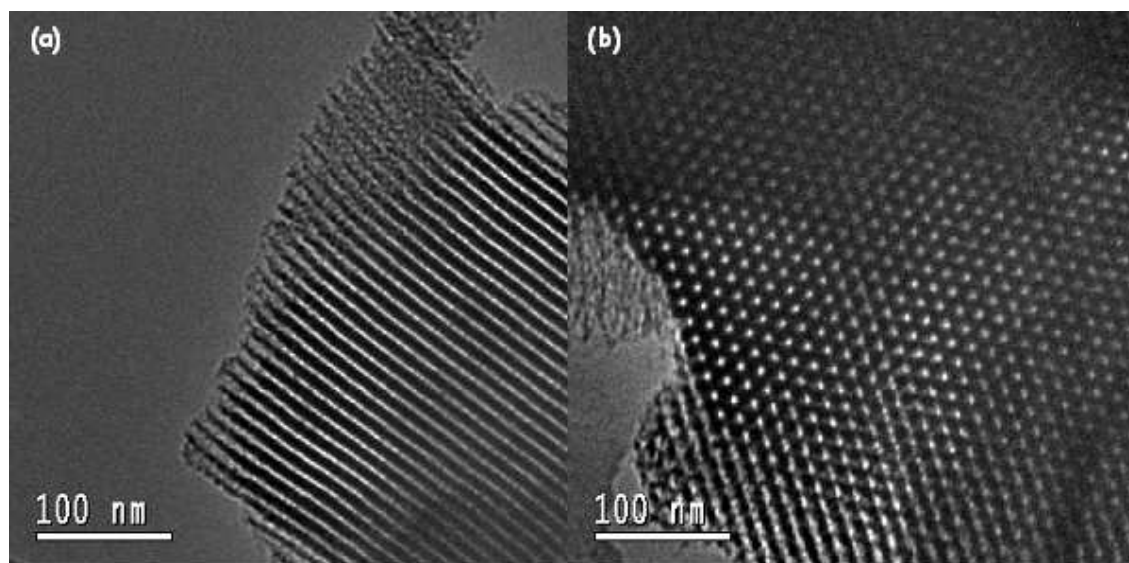


**Figure 5-1** HRTEM micrographs of SBA-15 illustrating pores running (a) perpendicular and (b) parallel to the beam. Images from PhD thesis of Dr. R. Hodgkins (with permission).<sup>[34]</sup>

Au/Ni bimetallic particles were prepared by co-reduction with trisodium citrate and hydroxylamine hydrochloride. This procedure was based upon bimetallic Au/Pd colloidal preparation methods.<sup>[29]</sup> Figure 5-2 (a-b) are TEM micrographs of Au/Ni colloids supported on SBA-15. The average particles size for both micrographs was ~30 nm. In figure 5-2 (b), the Au/Ni colloids were too large to enter the support and as a result congregated on the SBA-15 fringes. This result was anticipated. A unique feature of gold is the range of colours it displays.<sup>[21]</sup> A ruby-red colour is representative of large particles. Typically, suspensions of 1-3 nm particles are brown to dark orange-brown and 5 nm particles are purple-brown to purple-red. A ruby-red colour was formed upon reduction with sodium citrate. Various EDS spectra taken of the supported Au/Ni colloids found

no evidence for the presence of nickel. This suggests it was not sufficiently reduced. Figure 5-3 is an EDS spectrum taken of the Au/Ni colloids. The Cu peak at 8 keV originates from the copper sample grid.

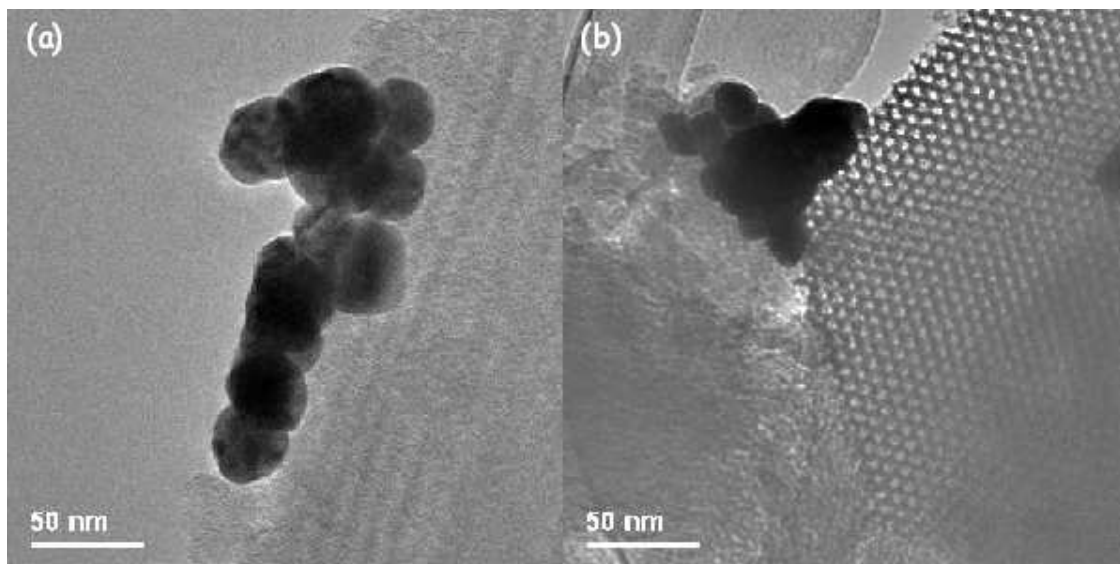


Figure 5-2 HRTEM micrographs of Au/Ni/SBA-15 supported colloids with a Au : Ni molar ratio of 1 : 8.

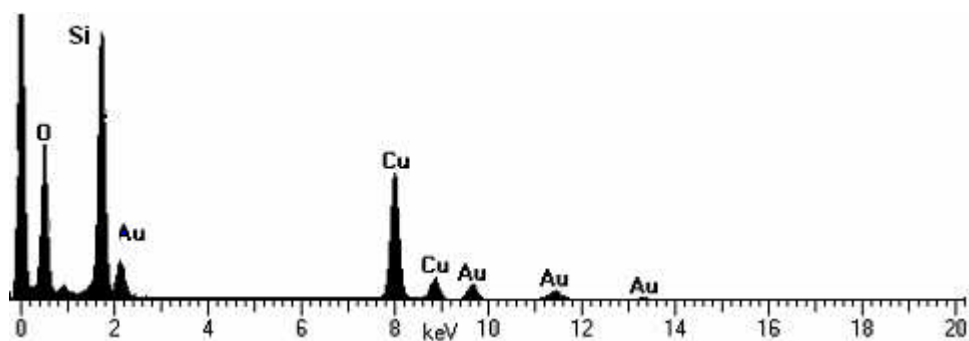


Figure 5-3 EDS spectrum of Au/Ni colloids with a molar ratio of 1 : 8. Colloids were reduced via the Turkevich method and supported on SBA-15. No presence of nickel was observed.

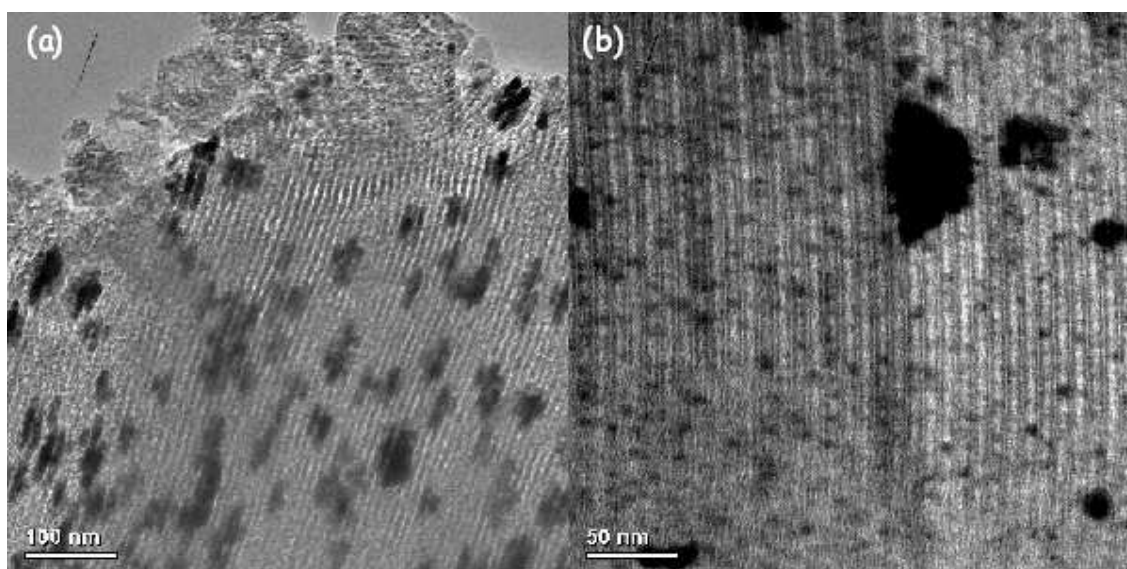
The main conclusions drawn from Au/Ni colloids prepared via the Turkevich method include; the average Au/Ni particle size was too large to enter the mesoporous support and consequently congregated on the fringes of the SBA-15 support. Reduced metallic nickel was not present, as determined by EDS.

### 5.3.1.2 HYDRAZINE HYDRATE REDUCTION

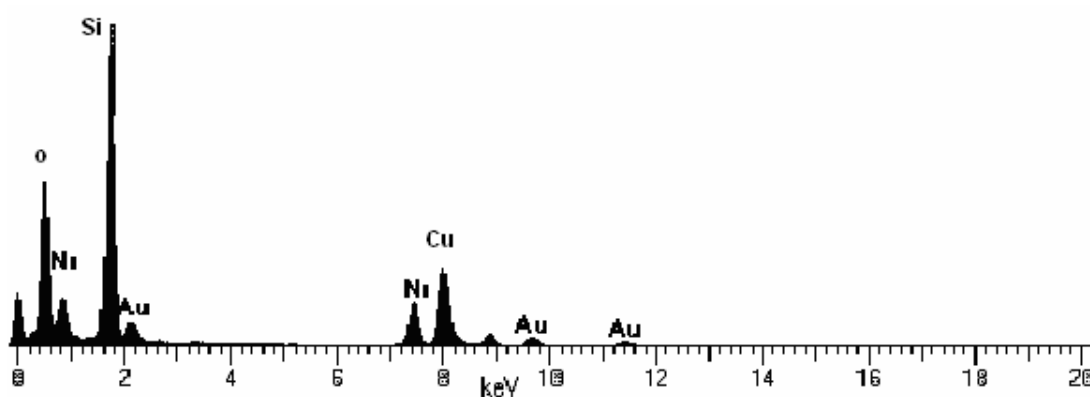
#### 5.3.1.2.1 SBA-15 SUPPORTED CATALYSTS

Figure 5-4 (a-b) are TEM micrographs of bimetallic 1 wt. % Au/0.5 wt. % Ni colloids reduced with hydrazine hydrate and supported on SBA-15. The micrographs were viewed with pores running perpendicular to the beam. In both micrographs, the bimetallic Au/Ni nanoparticles were present, as confirmed by EDS (figure 5-5). The bimetallic nanoparticles were found to be homogeneously dispersed within the support channels. On closer inspection, while some particles are spherical others cluster together in the channels with an average length of ~30-60 nm. Each nanoparticle had an approximate diameter of 6 nm. An important observation is that the prepared SBA-15 is of good quality and ordered with well defined channels.

The main conclusions drawn from bimetallic Au/Ni colloids prepared via the hydrazine hydrate reduction method and supported on SBA-15 include; nickel was successfully reduced and bimetallic Au/Ni/SBA-15 supported colloids were prepared. Average nanoparticle diameter ranges from ~6 nm. The bimetallic particles were successfully encapsulated in the support channels. Overall, the SBA-15 prepared was reproducibly of good quality and ordered with well defined channels.



**Figure 5-4** HRTEM micrographs of bimetallic 1 wt. % Au/ 0.5 wt. % Ni colloids reduced by hydrazine hydrate and supported on SBA-15.



**Figure 5-5** EDS spectrum of bimetallic 1 wt. % Au/ 0.5 wt. % Ni colloids reduced by hydrazine hydrate and supported on SBA-15.

These catalysts were then modified with (*R,R*)-tartaric acid and tested for their enantioselectivity in relation to methylacetoacetate hydrogenation. No enantioselectivity was observed. In light of this, the nickel concentration was increased from 0.5 wt. % to 5 wt. %. All HRTEM micrographs from this point forth contain 5 wt. % Ni unless otherwise stated. An important part of this study is to assess the leaching behaviour of the bimetallic catalysts after modification with (*R,R*)-tartaric acid. Figure 5-6 are TEM micrographs of post-reduction, -modification and -hydrogenation of a SBA-15 supported

4 wt. % Au/Ni catalyst reduced with hydrazine hydrate. Throughout the three stages, the mesoporous support remains in relatively good condition. Reduction with hydrazine hydrate occurs at pH 10-12 and such a high pH does not seem to be detrimental to the condition of the support. Figure 5-7 are the corresponding EDS spectra for the selected areas.

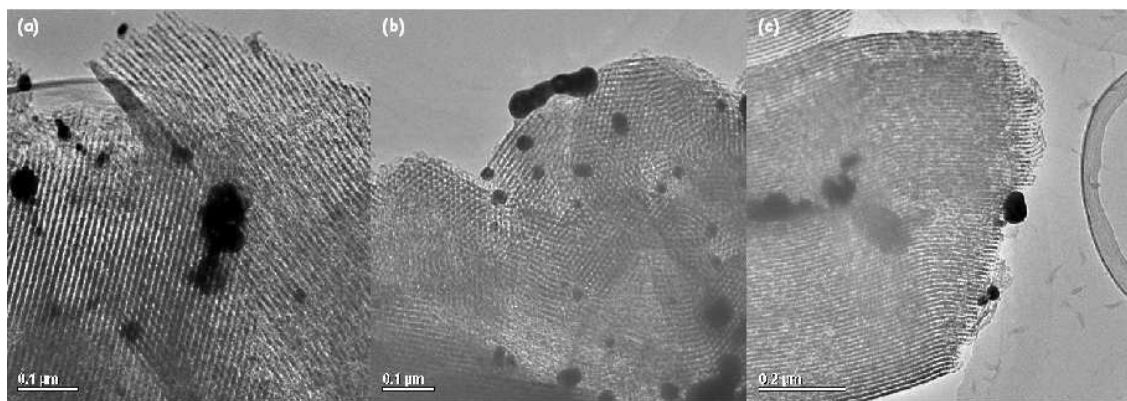


**Figure 5-6** HRTEM micrographs of 4 wt. % Au/5 wt % Ni supported on SBA-15 and reduced with hydrazine hydrate.

(a) Post-reduction. (b) Post-modification. (c) Post-hydrogenation.

Upon reduction of the Au/Ni bimetallic catalyst there is agglomeration of particles to the exterior of the support. This is an overall trend with hydrazine hydrate reduction which intensifies with increasing gold weight percentage. Modification of the nanoparticles resulted in leaching (as confirmed by AAS; section 5.3.3) and further agglomeration of particles. This does not increase further after the hydrogenation reaction. Examining the selected TEM micrographs and EDS spectra it is difficult to decipher exactly the extent of leaching. It may be the case that in this instance the particles to the exterior of the support in the post-modification TEM micrograph originated from the hydrazine hydrate reduction procedure. A calculation reported by Von Heimendahl estimated that all TEMs since their conception had only examined  $0.6 \text{ mm}^3$  of material!<sup>[35]</sup> Hence, TEM is not a sampling tool but rather provides an insight to selected areas. Examining the figure 5-7 (b) post-modification; the EDS spectrum shows a decrease in the intensity of the Ni peak at

7.8 keV due to leaching. Figure 5-7 (c) post-hydrogenation also shows a further decrease in nickel intensity at 0.9 keV, indicating the participation of nickel in the hydrogenation reaction.

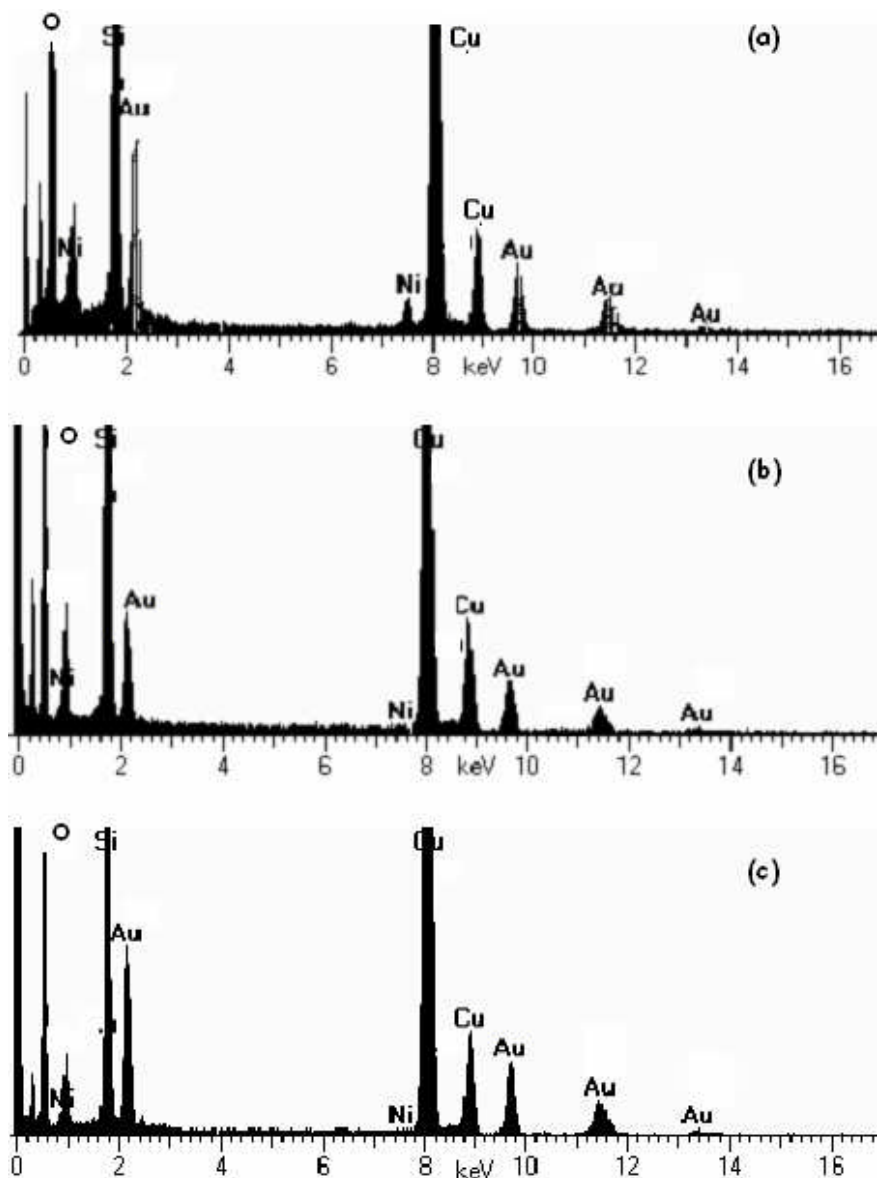
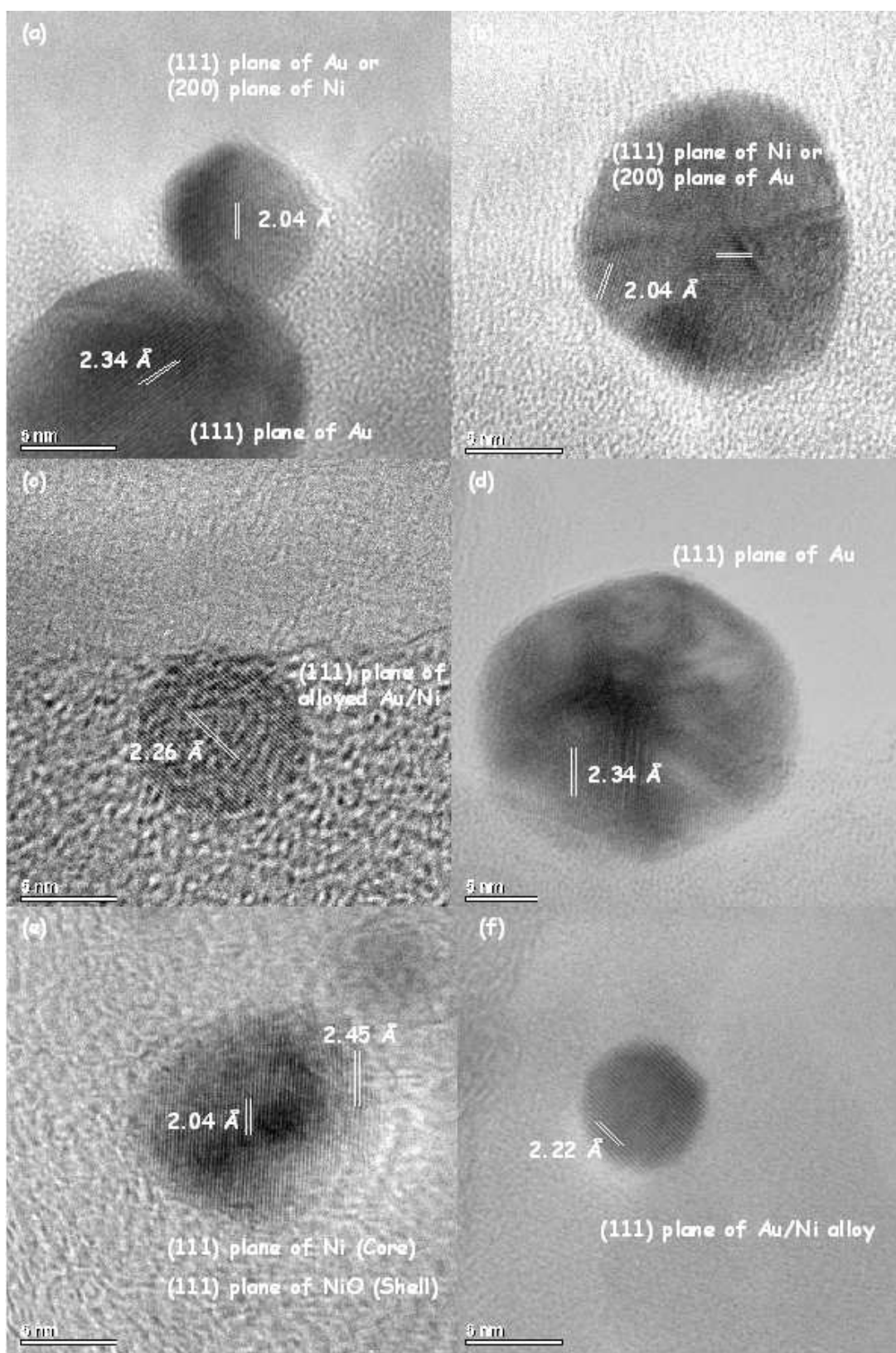


**Figure 5-7** EDS spectra of 4 wt. % Au/ 5 wt % Ni supported on SBA-15 and reduced with hydrazine hydrate. **(a)** Post-reduction. **(b)** Post-modification. **(c)** Post-hydrogenation

Reduction of SBA-15 supported 1-8 wt % Au/Ni nanoparticles with hydrazine hydrate produces an assortment of Ni, NiO, large faceted Au particles and alloyed Au/Ni nanoparticles. A substantial amount of nickel particles comprise of a Ni/NiO core/shell

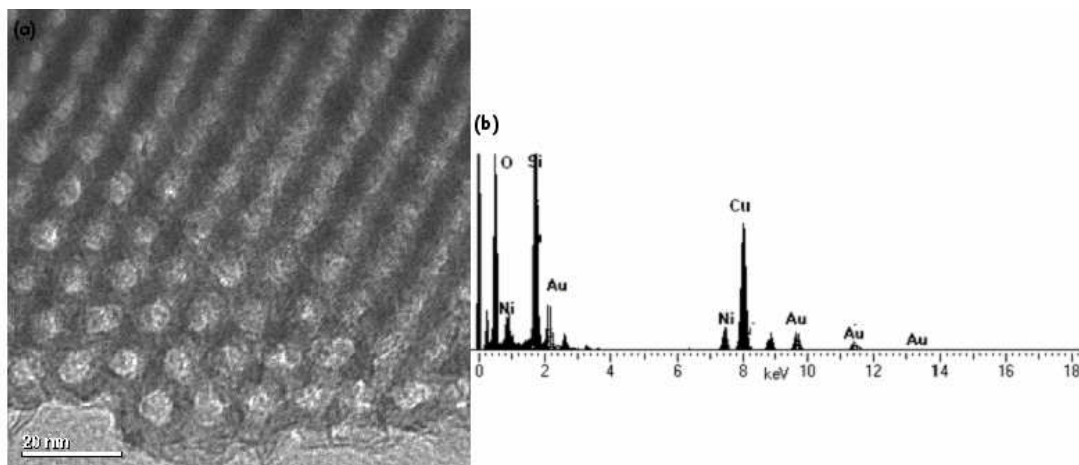
structure. A selection of HRTEM micrographs showing representative nanoparticles typical of hydrazine hydrate reduction is presented in figure 5-8 (a-f).

Figure 5-8 (a) consists of two particles. The larger spherical particle exhibits lattice fringes whose periodicity (2.34 Å) is consistent with the separation of (111) planes of gold. It has a measured diameter of 15 nm. The smaller particle directly above it has a measured lattice fringe of 2.04 Å and a diameter of 8 nm. This periodicity is consistent with the (111) planes of Ni or the (200) planes of Au. Figure 5-8 (b) similarly displays lattice fringes of 2.04 Å which are in agreement with the (111) planes of Ni or the (200) planes of Au. The particle is 15 nm in diameter. Figure 5-6 (c) has a measured lattice fringe of 2.26 Å and a diameter of 9 nm. This periodicity is between the (111) planes of Au 2.34 Å and the (111) planes of Ni 2.04 Å. The particle therefore provides evidence of alloy formation. Figure 5-8 (d) is a faceted 20 nm particle with a lattice fringe of 2.24 Å. This periodicity is consistent with separation of the (111) planes of Au. Gold particles of this size are plentiful with hydrazine hydrate reduction and are positioned directly on the surface of the mesoporous support. Figure 5-8 (e) is Ni/NiO core/shell structure with a diameter of 12 nm. The dark contrast (measuring ~9 nm) in the central part of the particle displays a lattice fringe of 2.04 Å which is consistent with the plane separation of (111) for Ni. The light contrast (measuring ~3 nm) on the periphery of the particle exhibits a lattice fringe of 2.45 Å. This periodicity is consistent with the separation of (111) planes for NiO. Figure 5-8 (f) is an alloyed Au/Ni particle with a diameter of 5-6 nm located within the SBA-15 channels. It has a measured lattice fringe of 2.15 Å. This periodicity is midway between the (111) planes of Au 2.34 Å and the (111) planes of Ni 2.04 Å. Alloyed Au/Ni particles are abundant with hydrazine reduction were generally located within the mesoporous channels.



**Figure 5-8** HRTEM micrographs of SBA-15 supported 1-8 wt % Au/5 wt % Ni nanoparticles reduced with hydrazine hydrate. **(a)** Larger particle shows the (111) plane of Au and smaller particle shows the (111) plane of Ni or (200) plane of Au. **(b)** Particle with (111) plane of Ni or (200) plane of Au. **(c)** Particle with (111) plane of Au/Ni alloy. **(d)** Particle with (111) plane of Au. **(e)** Ni/NiO core/shell structure. **(f)** (111) plane of Au/Ni alloy.

Figure 5-9 is a TEM micrograph of reduced 8 wt. % Au/Ni catalyst supported on SBA-15 and its corresponding EDS spectrum. While the EDS cannot confirm nor discount alloy formation it certainly shows a close proximity of gold and nickel within the SBA-15 support.



**Figure 5-9** (a) HRTEM micrograph of hydrazine hydrate reduced 8 wt. % Au/5 wt. % Ni supported on SBA-15. (b) Corresponding EDS spectrum of the selected area revealing the presence of gold and nickel in close vicinity to each other.

Reduction with hydrazine hydrate gives a wide range of particle sizes varying from 5 nm to 25 nm. Large particles 12-25 nm in diameter were found directly on the surface of the mesoporous support and consist mainly of large faceted Au particles. For those particles homogeneously dispersed within the SBA-15 pores, the particle size varied from ~5-9 nm in diameter. These particles are spherical and others are elongated and oriented along the channel axis of the SBA-15 channels. Spherical nickel and nickel oxide particles have typical diameters of ~8-12 nm. It is difficult to distinguish between Ni (111) and Au (200) planes due to the identical lattice fringe of 2.04 Å. A substantial portion of Ni particles display a NiO shell, a quantity which further increases upon modification of the nanoparticles. This is attributed to modification occurring in air and the characteristic oxidising nature of nickel. Alloyed Au/Ni particles tend to have a smaller diameter of ~5-9 nm on average and were more plentiful at lower gold loadings. The measured lattice

fringes varied from 2.15-2.25 Å. There is no supporting evidence for Au/Ni core/shell structures.

#### 5.3.1.2.2 SiO<sub>2</sub> SUPPORTED CATALYSTS

Figure 5-10 are TEM micrographs of a 4 wt. % Au/Ni catalyst (a) post-reduction (b) post-modification and (c) post-hydrogenation. Leaching of nanoparticles from the silica support is clearly evident after the chiral modification process. The particles seem to further agglomerate after hydrogenation. The corresponding EDS spectra are shown in figure 5-11. There is a substantial increase in the presence of gold in the spectra following modification and hydrogenation of the nanoparticles.

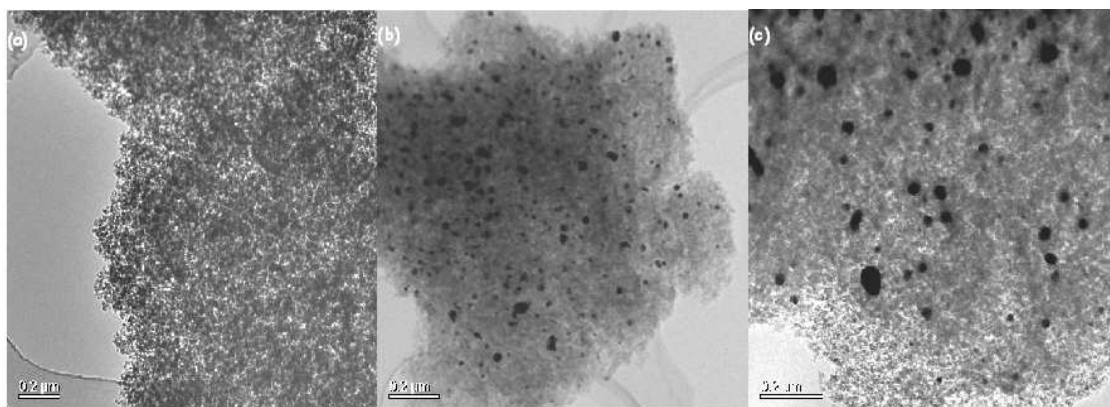


**Figure 5-10** HRTEM micrographs illustrating the leaching behaviour of 4 wt. % Au/ 5 wt. % Ni supported on SiO<sub>2</sub> and reduced with hydrazine hydrate. **(a)** Post-reduction. **(b)** Post-modification. **(c)** Post-hydrogenation.

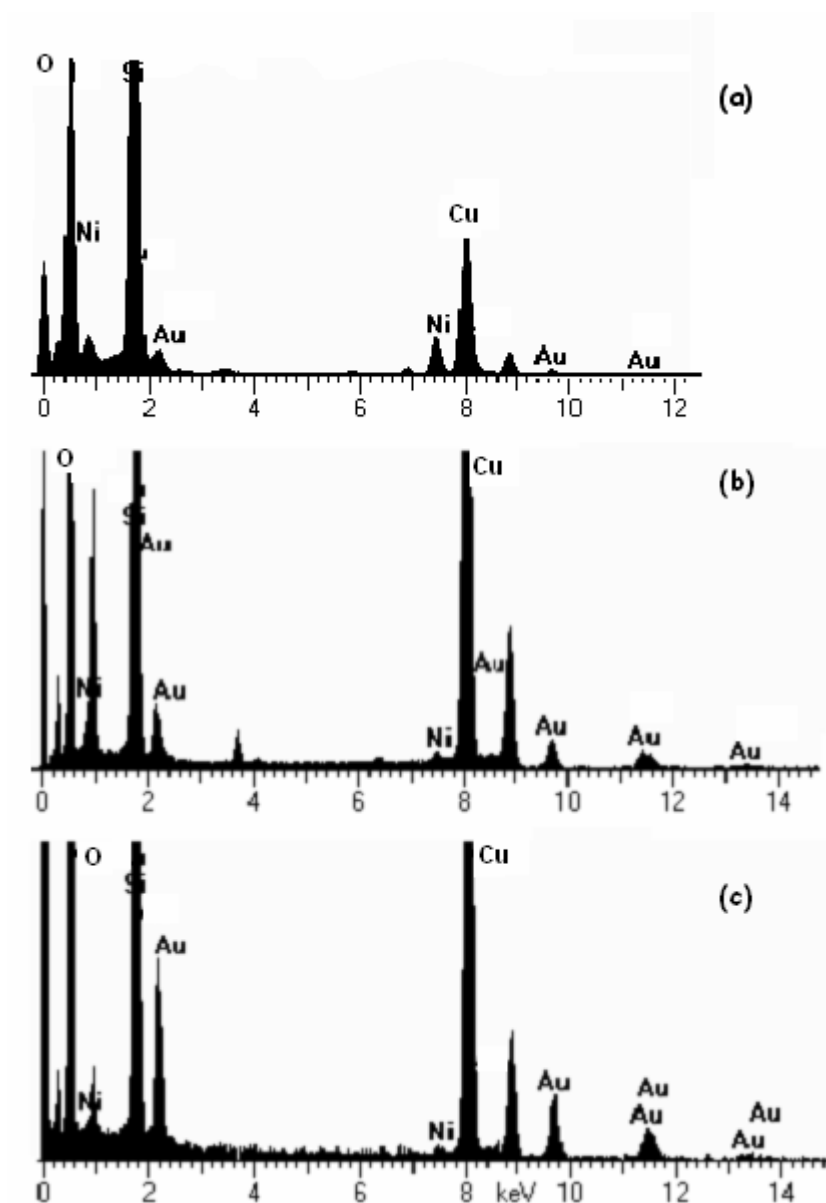


**Figure 5-11** EDS spectra of 4 wt. % Au/ 5 wt. % Ni supported on SiO<sub>2</sub> and reduced with hydrazine hydrate.

(a) Post-reduction. (b) Post-modification. (c) Post-hydrogenation.

Reduction of SiO<sub>2</sub> supported 1-8 wt. % Au/Ni nanoparticles with hydrazine hydrate produces an assortment of Ni, NiO and bimetallic Au/Ni nanoparticles and large faceted Au particles. A selection of TEM micrographs illustrating the various nanoparticles is shown in figure 5-12.

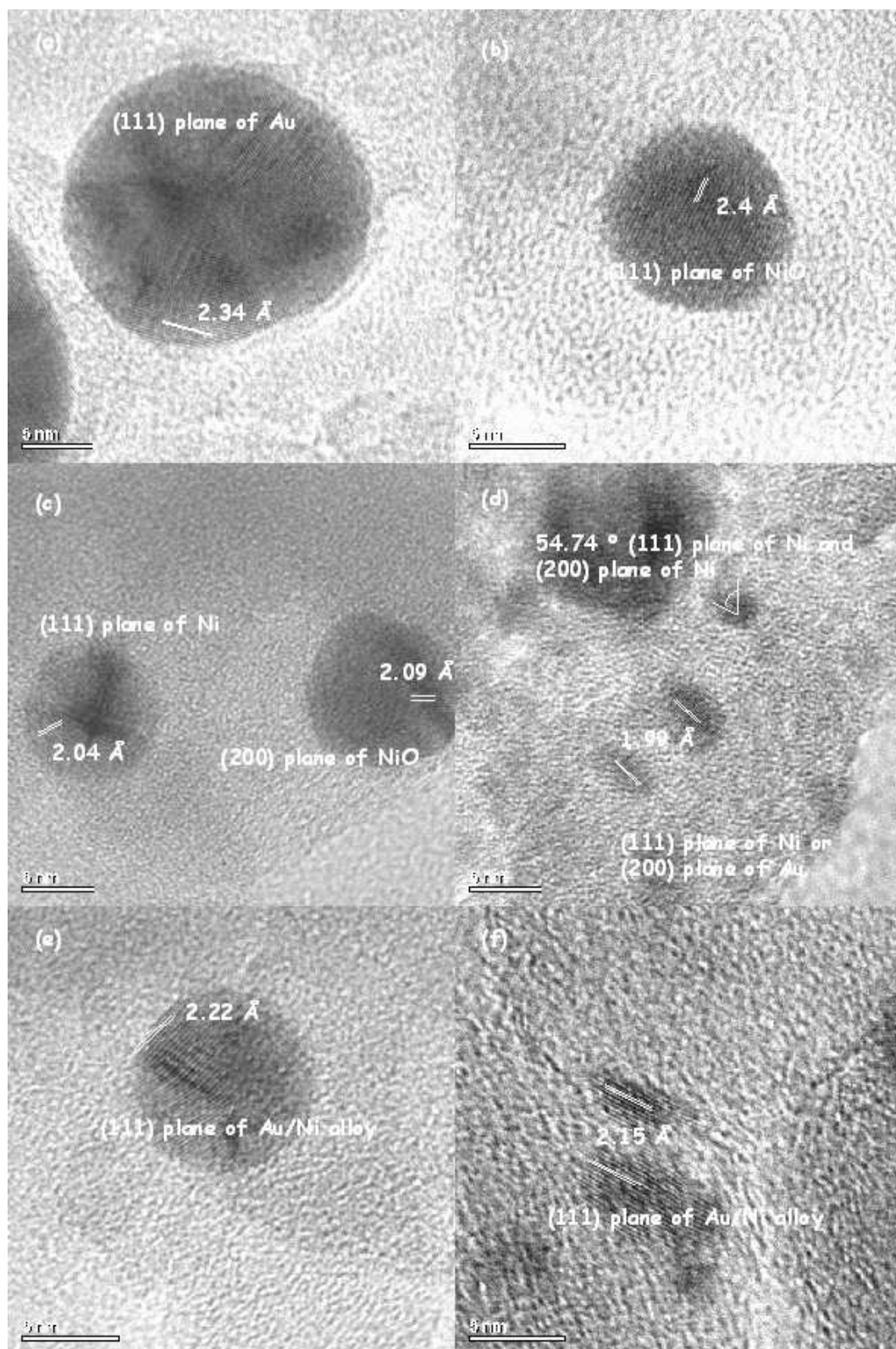


**Figure 5-12** HRTEM micrographs of  $\text{SiO}_2$  supported 4 wt. % Au/ 5 wt. % Ni nanoparticles reduced with hydrazine hydrate. **(a)** Particle with (111) plane of Au. **(b)** Particle with (111) plane of NiO. **(c)** Particle on left- (111) plane of Ni.

Particle on right- (200) plane of NiO. **(d)** Ni particle exhibiting the (111) and (200) planes. Also, a cluster of particles either exhibiting Ni (111) plane or Au (200) plane. **(e)** Au/Ni alloy with a lattice fringe of 2.22 Å. **(f)** Au/Ni alloy with a lattice fringe of 2.15 Å.

Figure 5-12 (a) shows a large faceted Au particle with a diameter of 13 nm and a lattice fringe of 2.34 Å consistent with (111) Au planes. Figure 5-12 (b) is a spherical NiO particle, 9 nm in diameter with a measured lattice fringe of 2.46 Å. This corresponds to the (111) plane of NiO. Figure 5-12 (c) comprises of two particles. The particle on the left has a lattice fringe of 2.04 Å and a diameter of 8.5 nm. This fringe spacing is consistent with either the (111) plane of Ni or the (200) plane of Au. The larger particle on the right is NiO exhibiting its (200) plane with a diameter of 9.6 nm. Figure 5-12 (d) consists of a cluster of three nanoparticles. Two nanoparticles have an identical lattice fringe of 1.9 Å and a diameter of 2.2 nm and 3.3 nm respectively. This fringe spacing is consistent with either the (111) plane of Ni or the (200) plane of Au. The third particle is nickel with (111) and (200) planes present at an angle of 54.74 °. It has a measured diameter of 2.6 nm. Figure 5-12 (e) is an alloyed Au/Ni particle with a lattice fringe of 2.22 Å with a diameter of 8.7 nm. Figure 5-12 (f) are alloyed Au/Ni nanoparticles exhibiting the (111) plane. The sizes of the particles are 1.7 nm and 3.7 nm respectively.

Reduction of Au/Ni catalysts supported on disordered SiO<sub>2</sub> gave varied particle sizes ranging from 3-25 nm in diameter. In general smaller particles less than 15 nm in diameter were spherical and larger particles greater than 15 nm in diameter hexagonal in shape. The latter were predominantly faceted Au. The average particle size upon reduction of 1, 2, 4 and 8 wt. % Au/Ni with hydrazine hydrate was approximately 5 nm, 9 nm, 10.5 nm and 15 nm respectively. The selected areas measured are presented in figure 5-13 and show the nanoparticles homogeneously dispersed within the support. Alloyed Au/Ni particles tended to have a smaller diameter of ~3-9 nm on average. There was no evidence of Au/Ni core/shell structures. While extensive leaching of the nanoparticles after chiral modification was clearly evident (figure 5-10) there was no obvious change in particle size or morphology for those nanoparticles still located within silica support.

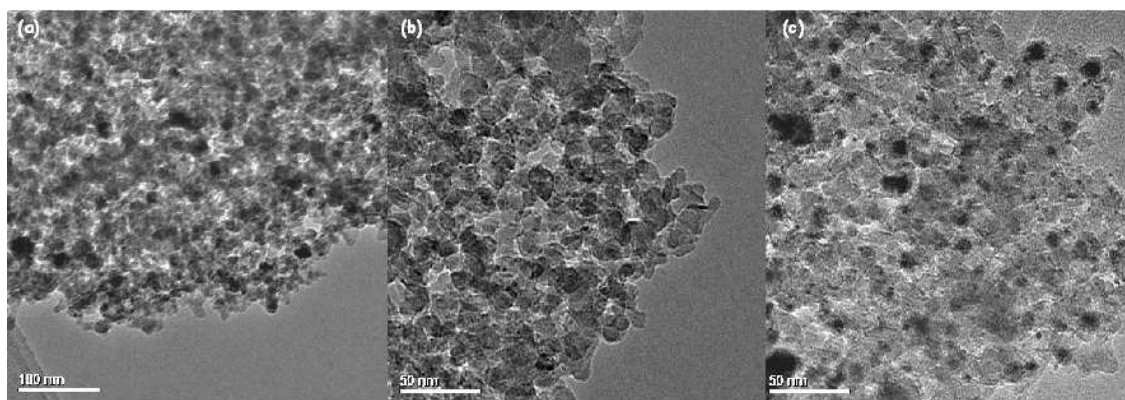


**Figure 5-13** 5 wt. % Ni with varying Au content. These catalysts were hydrazine hydrate reduced and supported on SiO<sub>2</sub>.

(a) 2 wt. % Au (b) 4 wt. % Au. (c) 8 wt. % Au.

The main conclusions from SBA-15/ SiO<sub>2</sub> supported hydrazine hydrate reduced catalysts include:

1. Ni, NiO, Au, Ni/NiO core/shell structures and Au/Ni alloyed particles were synthesised. These varied in morphology from spherical, hexagonal to large faceted particles. The latter was predominantly gold. Particle sizes ranged from 3-25 nm in diameter.
3. Particles successfully encapsulated within the mesoporous channels were spherical and/or elongated with the growth directed by the spatial restrictions of the channel walls of up to ~60 nm in length.
4. Leaching of nickel was evident after the chiral modification with (*R,R*)-tartaric acid.

### 5.3.1.3 HYDROGEN REDUCTION

#### 5.3.1.3.1 SBA-15 SUPPORTED CATALYSTS

Figure 5-14 (a-b) are HRTEM micrographs of monometallic 5 and 10 wt. % Ni catalysts respectively. The particle sizes and morphology differ greatly. Increasing the nickel loading results in larger particle sizes and a well -defined morphology. Figure 5-14 (a) is a cluster

of particles with a measured lattice fringe of 1.98 Å and 2.04 Å; consistent with the (111) plane of Ni. The particles are not well-defined and range in diameter from 2.7-3.7 nm. The 10 wt. % Ni catalyst contains Ni and NiO nanoparticles. The diameter of the particles varies from 5.1 to 7.5 nm.

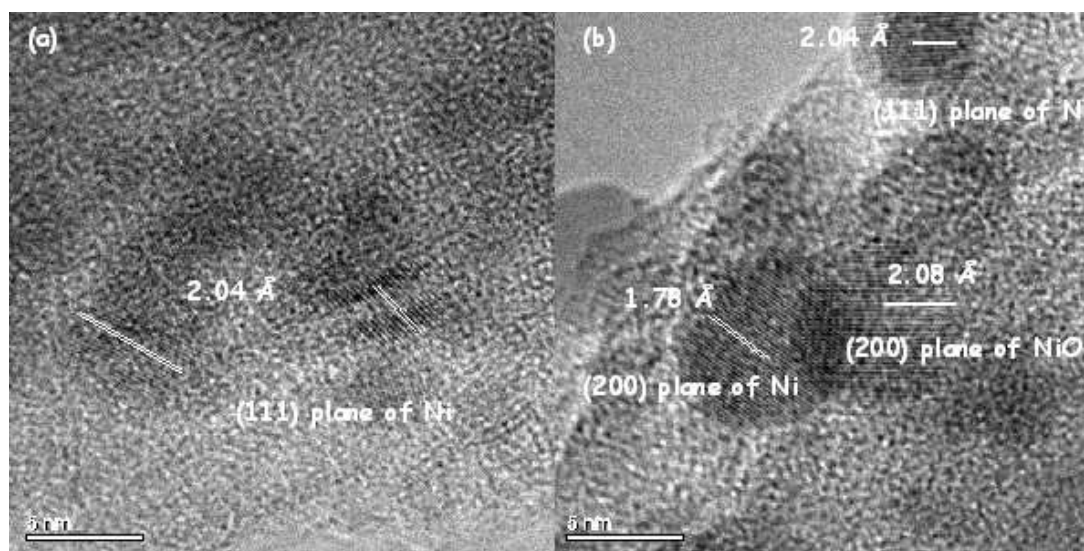


**Figure 5-14** HRTEM micrographs of Ni catalysts reduced with hydrogen and supported on mesoporous SBA-15. (a) 5 wt. % Ni. (b) 10 wt % Ni.

Figure 5-15 are HRTEM micrographs and corresponding EDS spectra for SBA-15 supported 4 wt. % Au/Ni nanoparticles reduced with hydrogen. Figure 5-15 (a) was taken after reduction of the nanoparticles and displays large clusters to the exterior of the SBA-15 support. The largest cluster is ~500 nm in diameter and is a nickel/gold mixture as determined by EDS. The large clusters may arise from the presence of chloride in the gold precursor which promotes mobility and agglomeration of the gold species during thermal treatment<sup>[21]</sup>. From figure 5-15 (a) calcination in air and reduction in hydrogen did not remove the residual chloride but instead induced sintering. Increasing the gold loading to 8 wt. % led to a substantial reduction of gold incorporated within the SBA-15 support with massive sintering and agglomeration of the gold to the exterior of the support. This was verified by EDS. Because of this, leaching of nanoparticles after modification was

difficult to assess. Figure 5-15 (b) is a HRTEM micrograph illustrating the excellent condition of the mesoporous support after hydrogenation.

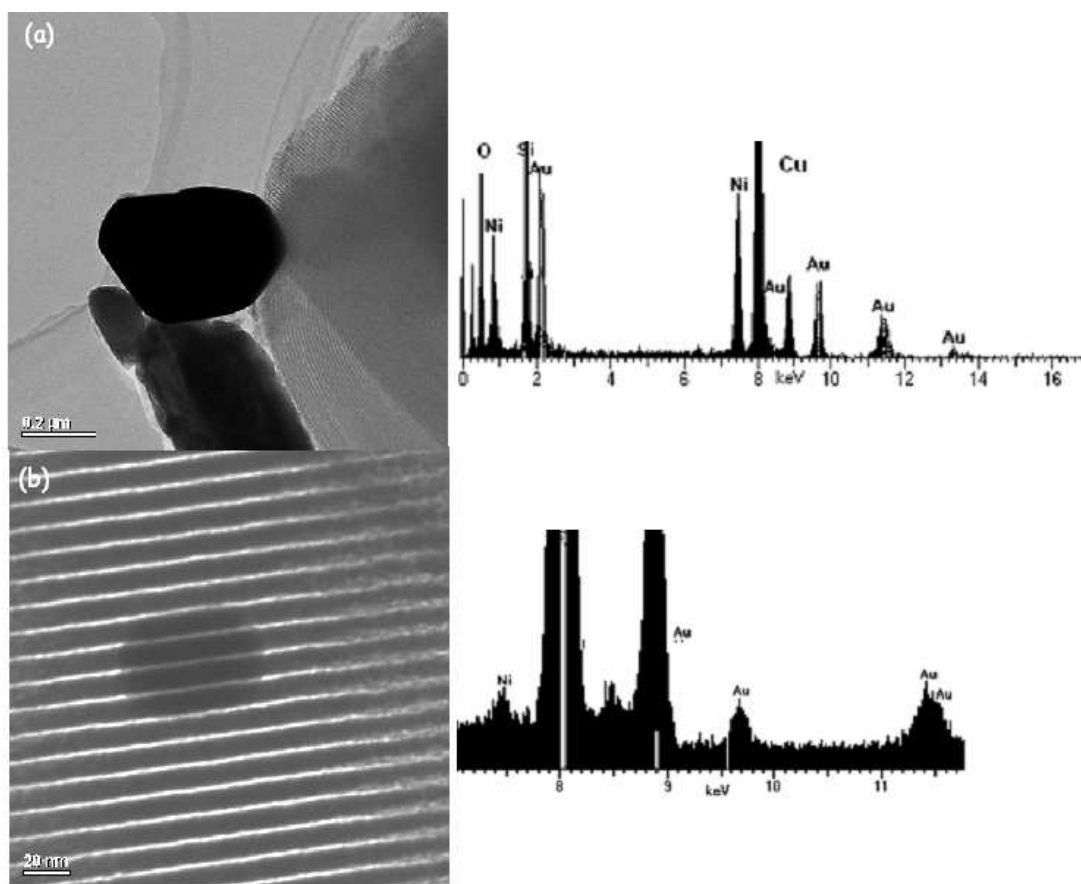


**Figure 5-15** TEM micrographs and corresponding EDS spectra of SBA-15 supported 4 wt. % Au/5 wt. % Ni nanoparticles reduced with hydrogen. **(a)** Large clusters ~ 500 nm in diameter after reduction. **(b)** HRTEM micrograph illustrating the excellent condition of the mesoporous support after hydrogenation.

Reduction of SBA-15 supported 1-8 wt. % Au/Ni catalysts with hydrogen produces a mixture of Ni, NiO, alloyed Au/Ni particles and large faceted Au particles. Figure 5-16 (a) is a representative Au/Ni catalysts with elongated particles. Larger particles are located on the surface of the mesoporous support. Some particles are spherical; others are clustering along the channel axis. Figure 5-16 (b) is a NiO particle, 13.1 nm in diameter. Figure 5-16 (c) is a group of NiO particles exhibiting the (200) plane. Particles like this are plentiful following chiral modification in air are typically ~3-8 nm in diameter. Figure 5-16

(d) has a measured lattice fringe of 2.15 Å and a diameter of 7.0 nm. This is a well-defined alloyed Au/Ni particle and such particles are abundant after hydrogen reduction.

Reduction of Au/Ni nanoparticles supported on SBA-15 with hydrogen differs greatly from the hydrazine hydrate method. Particle sizes range from 3-25 nm and clusters to the exterior of the support can range up to ~500 nm in diameter. A mixture of Ni, NiO and alloyed Au/Ni particles are predominantly located within the SBA-15 support. Some particles were spherical; others elongated, clustering along the mesoporous channels. The average pore size is ~9-10 nm. Typically Ni and NiO particles vary from 3-15 nm and alloyed Au/Ni particles ranged from 5-9 nm in diameter. For Au/Ni alloy formation; lower loadings of gold were preferable. This can be partially attributed to the elevated temperatures used in reduction. Fewer alloyed particles were observed at the higher gold loadings of 8 wt. %. This suggests that the higher the gold loading, the stronger the preference for gold to migrate together and less chance of it interacting with the support thereby producing larger particles which in turn agglomerate into larger clusters i.e. the Au particles to the exterior of the support act as nucleation sites promoting further Au growth. However, at lower loadings of gold, SBA-15 was able to contain the nanoparticles within the channels. The average particle size was 5-9 nm which is close to the pore size of SBA-15. It is thought the thick pore wall characteristic of SBA-15 was able to confine the nanoparticles within its channels. The extent of leaching after modification was difficult to determine due to the sintering of gold after reduction.

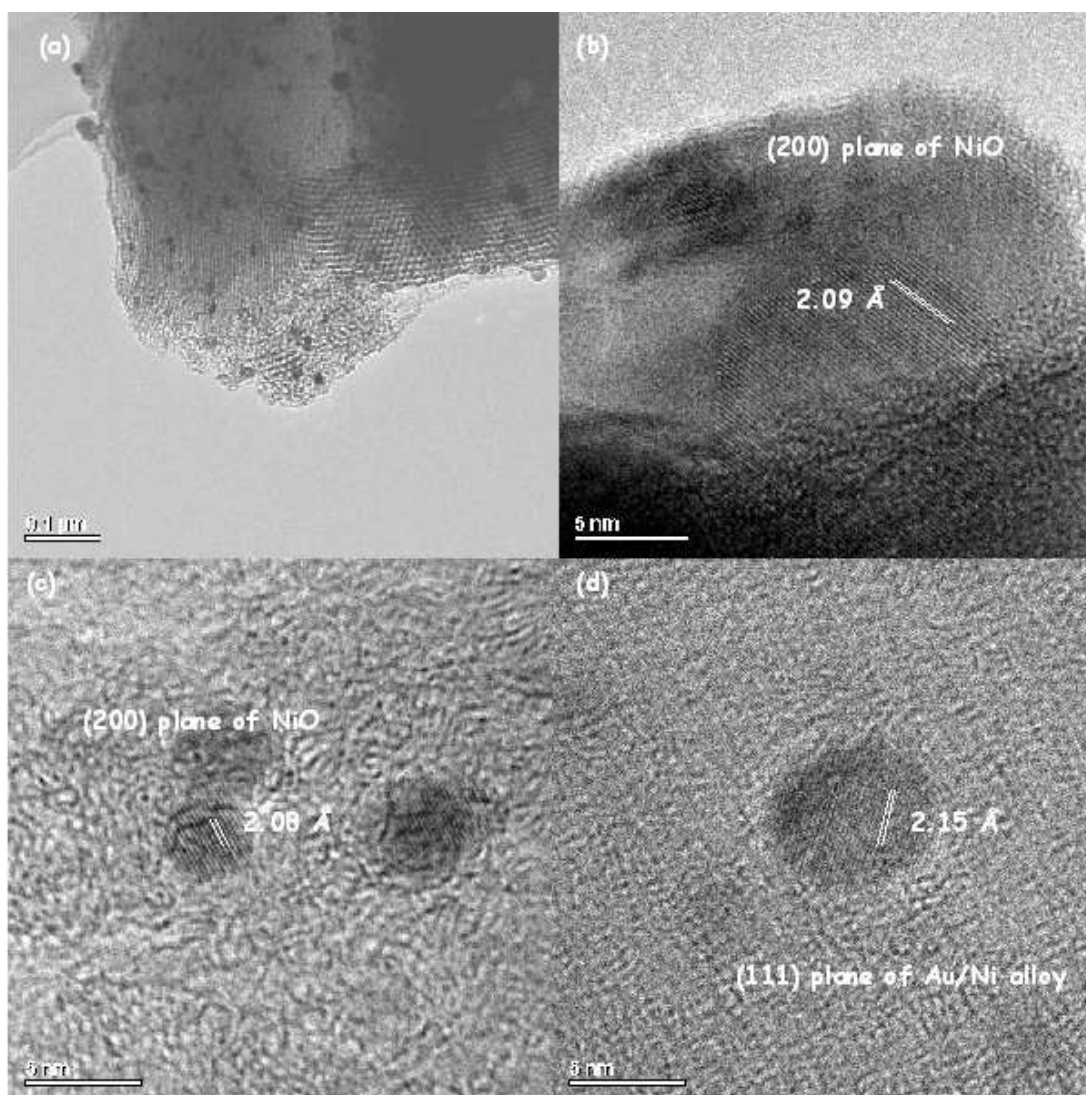
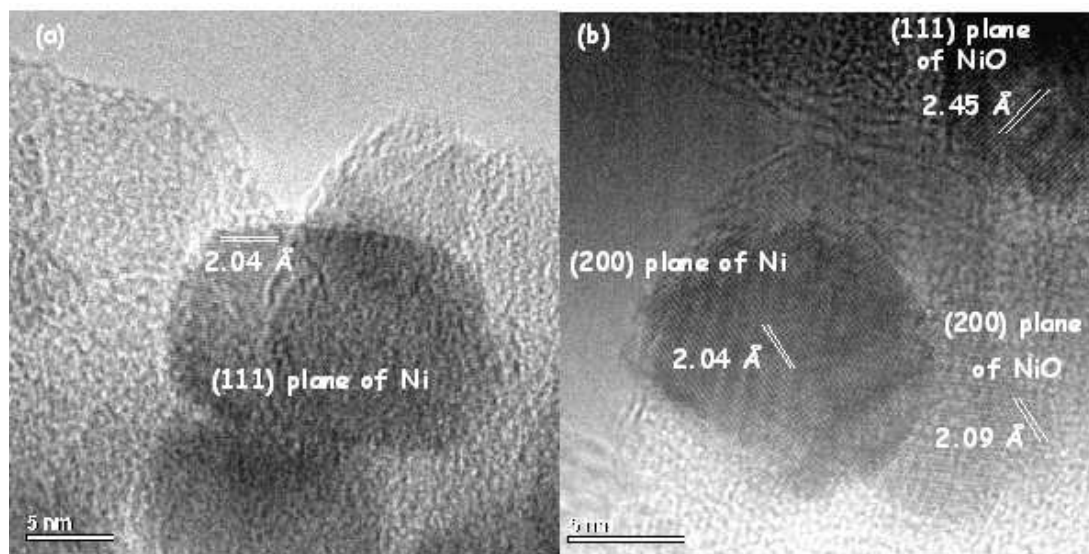


**Figure 5-16** TEM micrographs of SBA-15 supported Au/Ni nanoparticles reduced with hydrogen. **(a)** Au/Ni catalyst with elongated particles encapsulated in the SBA-15 support. **(b)** NiO particle exhibiting the (200) plane with a diameter of 13.1 nm. **(c)** Cluster of NiO particles. **(d)** (111) plane of Au/Ni alloy.

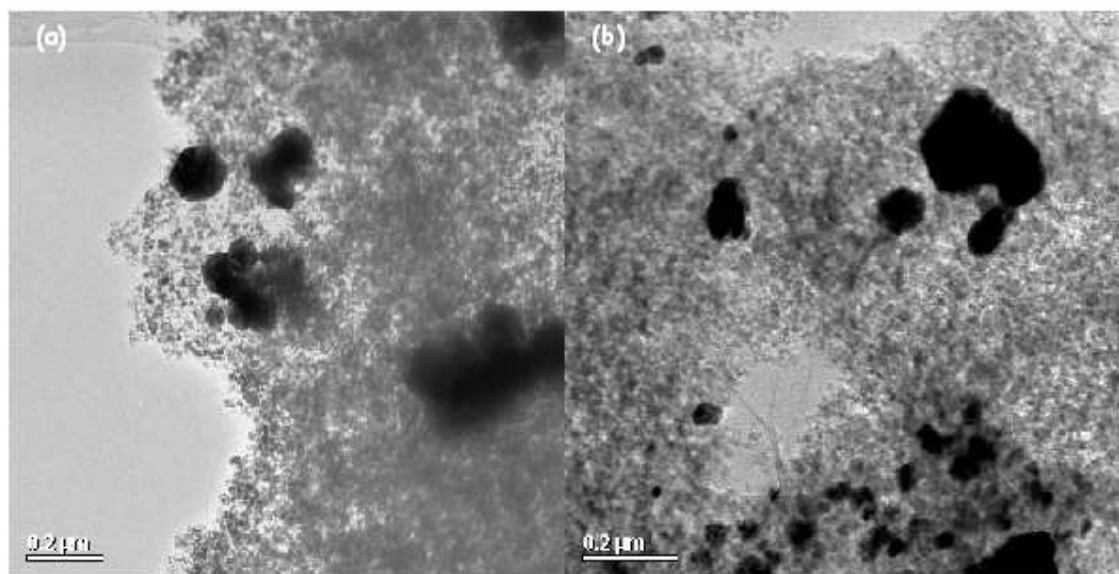
### 5.3.1.3.2 SiO<sub>2</sub> SUPPORTED CATALYSTS

Figure 5-17 are HRTEM micrographs of monometallic 10 wt. % Ni catalysts. This catalyst is SiO<sub>2</sub> supported and was hydrogen reduced at 853 K. Figure 5-17 (a) is a Ni particle exhibiting the (111) plane (2.04 Å) and a diameter of 17.4 nm. Figure 5-17 (b) are Ni and NiO particles. The latter exhibits the (111) and (200) planes. Moiré fringes are evident in the Ni particles indicating an overlay of the lattices of Ni and NiO. The diameter of the Ni particle is 11.1 nm. Calcination in air and reduction in hydrogen atmospheres at 823 K

of 1-8 wt. % Au/Ni/SiO<sub>2</sub> supported catalysts results in extensive sintering of gold as illustrated in figure 5-18 (a-b). This increases with higher gold loadings of 4-8 wt. %.



**Figure 5-17** HRTEM micrographs of 10 wt. % Ni **(a)** Ni particle with (111) plane. **(b)** Ni, NiO particles exhibiting the (200) and (111) plane respectively.



**Figure 5-18** HRTEM micrographs of Au/5 wt. % Ni/ SiO<sub>2</sub> supported nanoparticles reduced with hydrogen. **(a)** 4 wt. % Au. **(b)** 8 wt. % Au.

Au/Ni nanoparticles supported on SiO<sub>2</sub> and reduced with hydrogen produces a mixture of Ni, NiO, alloyed Au/Ni particles and large faceted gold particles. Particle sizes range from 5-65 nm with clusters to the exterior of the support as large as ~450 nm. Figure 5-19 (a) is an Au/Ni alloy, 8.9 nm in diameter, exhibiting fringes whose periodicity (1.9 Å) is consistent with the separation of the (200) planes of an Au/Ni alloy. Figure 5-19 (b) is a large faceted particle, 43.5 nm in diameter. Figure 5-18 (c) is collection of Ni and NiO particles. The latter is 9.2 nm in diameter. Figure 5-19 (d) is an Au/Ni alloy with a lattice fringe of 2.26 Å and a diameter of 11.5 nm. An outer shell is visible but not well-defined.

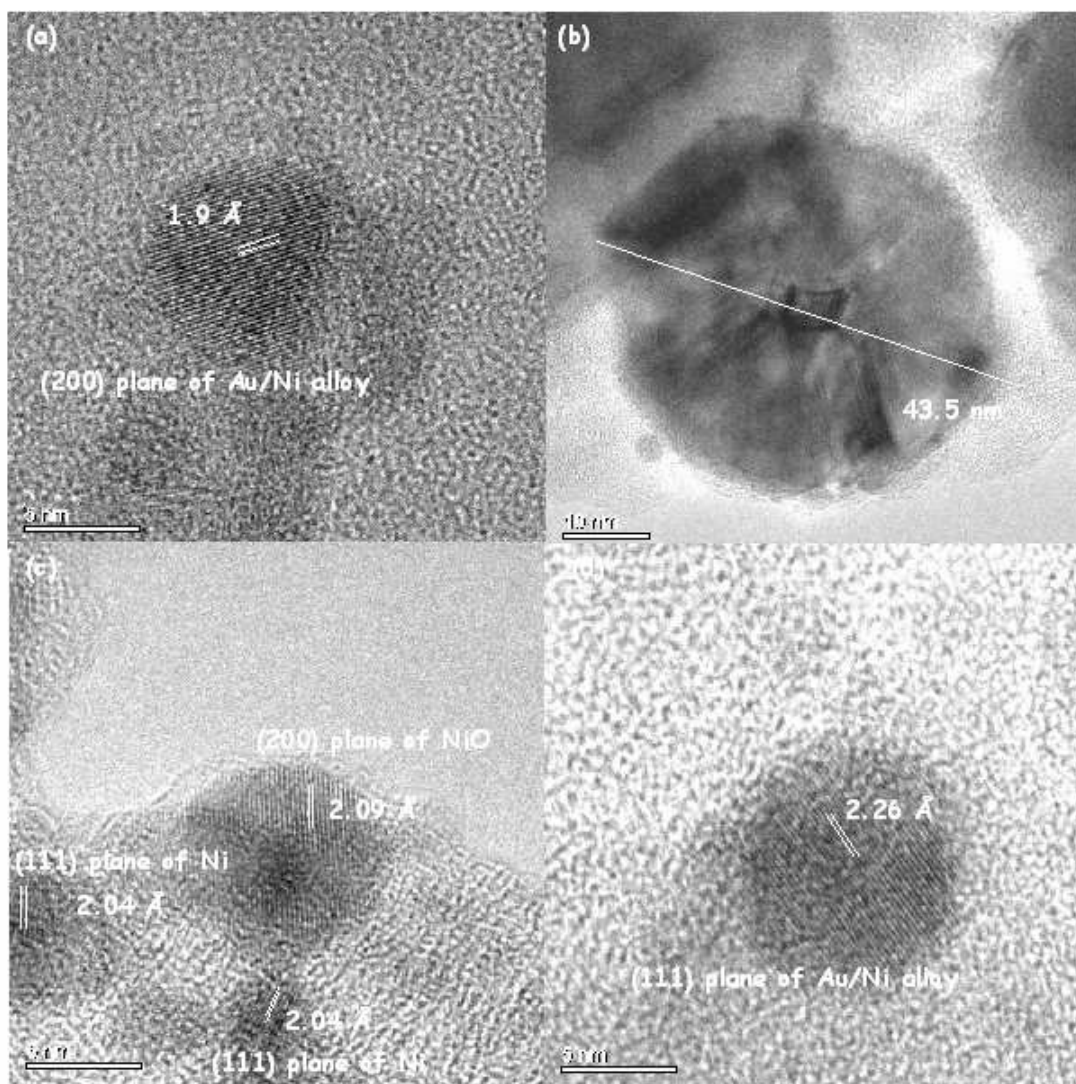


**Figure 5-19** HRTEM micrographs of Au/Ni SiO<sub>2</sub> supported nanoparticles reduced with hydrogen. **(a)** Au/Ni alloy with a lattice fringe of 1.9 Å, corresponding to the (200) plane. **(b)** Large faceted particle, 43.5 nm in diameter. **(c)** Collection of Ni and NiO particles. **(d)** Alloyed Au/Ni particle with a lattice fringe of 2.26 Å.

The main conclusions from SBA-15/ SiO<sub>2</sub> supported catalysts reduced with hydrogen include

1. Ni, NiO, Au and Au/Ni alloyed particles were synthesised varying in morphology from spherical, hexagonal to large faceted particles. Particle size varies from 3-500 nm. Au/Ni alloy formation is favoured at lower gold loadings.
2. Particles were spherical while others were elongated when located along the channel walls of the mesoporous support.
3. Sintering of gold particles was observed due to the presence of chloride in the gold precursor during thermal treatment.

### 5.3.2 EXAFS STUDIES

The primary objective of the following EXAFS study is to examine the average local environment of nickel atoms in the various bimetallic Au/Ni supported catalysts. An important aspect in bimetallic catalysis is whether or not an alloy is formed. Using EXAFS, valuable information on the number and kind of neighbouring atoms at a given distance and the structural disorder within the catalysts can be attained. The composition of these catalysts is deciphered with particular attention paid to the interaction of nickel and gold in the bimetallic system. Reduction methods are compared i.e. the use of hydrogen and hydrazine hydrate and their effect on the composition of the bimetallic system.

The  $\mu(E)$  normalized Ni K-edge EXAFS profiles for a series of supported Au/Ni catalysts are presented in figure 5-20. The catalysts range from 1-8 wt. % Au/ 5 wt. % Ni. The oscillatory structure results from the backscattering of the photoelectron from neighbouring atoms. The presence of gold in the supported bimetallic catalysts has a clear

impact and this is evident in the EXAFS oscillations which differ greatly from the 10 wt % Ni/ SBA-15 spectra. In addition, a variation between hydrogen (d-f) and hydrazine reduced SiO<sub>2</sub> catalysts (g-i) is evident. The normalized Ni K-edge spectra for hydrazine hydrate reduced SiO<sub>2</sub> bimetallic catalysts have less intensity in their EXAFS oscillations, an indication of variation in its local environment.

Figure 5-21 is the  $\chi(k) k^2$  weighted absorbance versus  $k$  spectra (left-hand-side) and the Fourier transform magnitude versus  $R$ , distance (right-hand-side) for SBA-15 Au/Ni supported catalysts. The Fourier transform spectra consist of peaks corresponding to the different shells of neighbouring atoms. Peak position corresponds to the frequency of the EXAFS wiggles which in turn is related to the average distance in the shell. The peak height corresponds to the amplitude of the EXAFS which in turn is related to the number of atoms in the shell i.e. coordination number and the disorder parameter  $\sigma^2$ . However, the Fourier transform spectra are purely for visualization purposes and is simply an intermediate step in the data processing. Detailed quantitative analysis is typically done in  $k$ -space. Results and structural parameters derived from curve-fitting  $\chi(k) k^2$ -weighted EXAFS absorbance are listed in table 5-1.

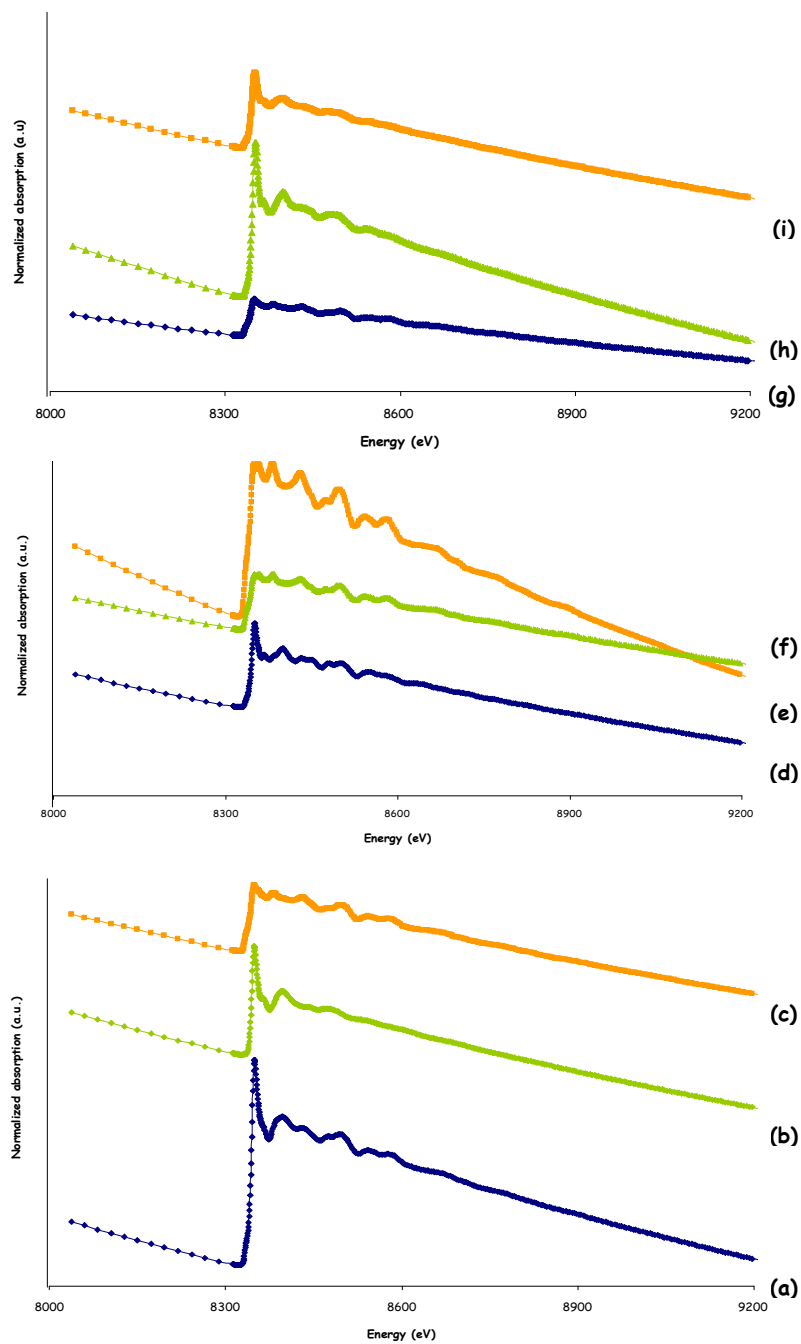


**Figure 5-20** Normalized Ni K-edge EXAFS spectra for **(a)** 10 wt. % Ni/ SBA-15/ hydrazine **(b)** 1 wt. % Au/ Ni/ SBA-15/ hydrazine **(c)** 2 wt. % Au/Ni/ SBA-15/ hydrogen **(d)** 2 wt. % Au/Ni/ SiO<sub>2</sub> / hydrogen **(e)** 4 wt. % Au/Ni/ SiO<sub>2</sub>/ hydrogen **(f)** 8 wt. % Au/Ni/ SiO<sub>2</sub> / hydrogen **(g)** 2 wt. % Au/Ni/ SiO<sub>2</sub>/ hydrazine **(h)** 4 wt. % Au/Ni/ SiO<sub>2</sub>/ hydrazine **(i)** 8 wt. % Au/Ni/ SiO<sub>2</sub>/ hydrazine.

Examining the Fourier transforms of (a) hydrazine reduced 10 wt. % Ni shows three major peaks at 2.0 Å, 2.4 Å and at 3.5 Å. The most intense peak at 2.4 Å is due to a Ni-Ni bond and is in the same position as that for Ni foil. This peak represents the first coordination shell of the central absorbing atom. The next nearest neighbor is a Ni bond with a peak position of 3.4 Å. The small peak at 2.0 Å is Ni-O. The latter is shifted to a slightly lower value of 1.8 in the FT spectrum due to application of the phase shift  $\delta(k)$ :  $\sin\{2kR + \delta(k)\}$ . A shift of -0.5 Å is typical.<sup>[36]</sup> All data presented in this EXAFS study are not phase-corrected.

Examining the Fourier transform spectra of (b) hydrazine reduced 1 wt. % Au/Ni exhibits three main peaks. Ni-O at 2.5 Å; first shell Ni-Ni at 2.4 Å and second shell Ni-Ni at 3.5 Å. Shouldering the latter is Ni-Ni of NiO at 3.0 Å. No nickel-gold interaction is evident.

The Fourier transform spectrum of (c) hydrogen reduced 2 wt. % Au/Ni spectra displays two primary peaks of importance. The first shell Ni-Ni at 2.4 Å and second shell Ni-Ni at 3.4 Å. Shouldering the first shell Ni-Ni at 2.9 Å is Ni-Ni of NiO. The curve-fitting analysis indicates an interaction between nickel-gold is present but in a tiny quantity with a coordination number of 0.38 (table 5-1). There is no obvious trend in the data at this early stage of analysis; however the similarity between all catalysts and the Ni foil data indicates that the Ni component in each sample is metallic in nature. For all three spectra the simulated data fits the experimental data well indicating good agreement of the structural parameters tabulated. Structural disorder is low for all three catalysts (averaging  $\sim 0.015$  Å). Typically  $\sigma^2$  ideally should be between 0.001-0.02 Å.

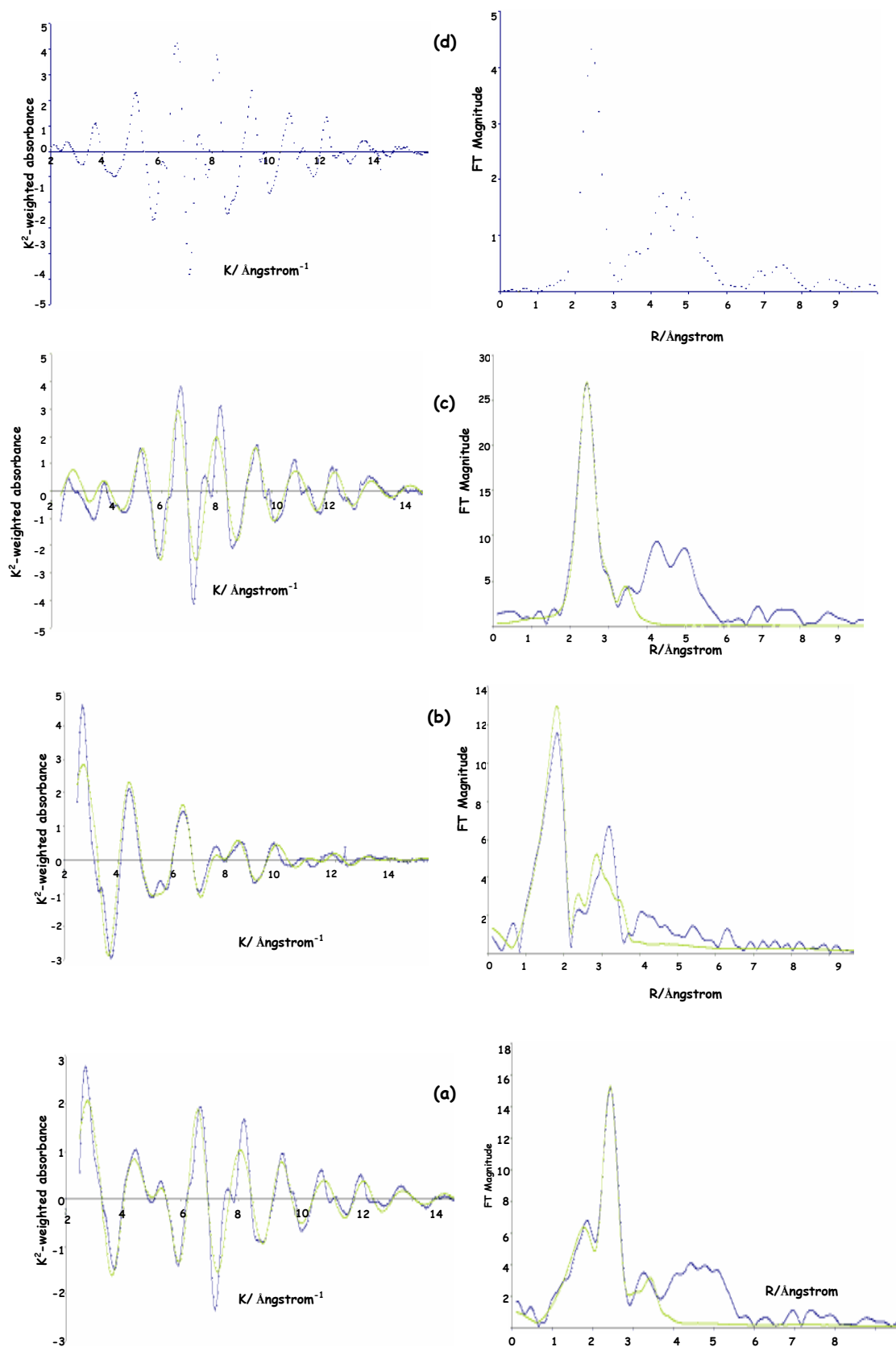


**Figure 5-21** EXAFS spectra for SBA-15 supported Au/ Ni catalysts. Spectra on the left are  $\chi(k) k^2$  weighted absorbance versus  $k$  and spectra on the right are the Fourier transform magnitude versus distance, R. Experimental data is represented in blue and curve-fitting analysis is represented in green. **(a)** 10 wt. % Ni/ hydrazine **(b)** 1 wt. % Au/ Ni/ hydrazine **(c)** 2 wt. % Au/Ni/ hydrogen **(d)** Ni foil.

**Table 5-1** Structural parameters derived from curve-fitting Ni K-edge  $k^2$  weighted  $\chi(k)$  EXAFS for various bimetallic Au/Ni supported catalysts.

Material	Reduction	A <sup>A</sup> -Bs <sup>B</sup>	N <sup>C</sup>	R <sup>D</sup> (Å)	( $\sigma^2$ ) <sup>E</sup> (Å <sup>2</sup> )
4 wt. % Au/ 5 wt. % Ni SiO <sub>2</sub>	Hydrazine	Ni-Ni	3.35	2.48	0.01
		Ni-Ni	2.27	3.49	0.01
		Ni-Ni (Ni Oxide)	5.11	3.01	0.01
		Ni-O (Ni Oxide)	5.85	2.04	0.01
		Ni-Au	3.32	2.86	0.01
8 wt. % Au/ 5 wt. % Ni SiO <sub>2</sub>	Hydrazine	Ni-Ni	3.69	2.48234	0.01
		Ni-Ni	0.56	3.52943	0.01
		Ni-Ni (Ni Oxide)	4.59	3.00096	0.01
		Ni-O (Ni Oxide)	5.36	2.05294	0.01
		Ni-Au	5.75	2.84407	0.02
2 wt. % Au/ 5 wt. % Ni SiO <sub>2</sub>	Hydrogen	Ni-Ni	4.49	2.48802	0.01
		Ni-Ni	2.71	3.52052	0.01
		Ni-Ni (Ni Oxide)	12.95	2.95541	0.01
		Ni-O (Ni Oxide)	4.99	2.07782	0.01
		Ni-Au	2.85	2.85020	0.02
4 wt. % Au/ 5 wt. % Ni SiO <sub>2</sub>	Hydrogen	Ni-Ni	11.45	2.48040	0.01
		Ni-Ni	6.63	3.48386	0.01
		Ni-Ni (Ni Oxide)	0.85	2.94713	0.01
		Ni-O (Ni Oxide)	0	2.07398	0.01
		Ni-Au	0	2.70217	0.02
8 wt. % Au/ 5 wt. % Ni SiO <sub>2</sub>	Hydrogen	Ni-Ni	11.62	2.48342	0.01
		Ni-Ni	6.17	3.48622	0.01
		Ni-Ni (Ni Oxide)	1.18	2.92494	0.01
		Ni-O (Ni Oxide)	0	2.08843	0.01
		Ni-Au	0	2.73479	0.02
1 wt. % Au/ 5 wt. % Ni SBA-15	Hydrazine	Ni-Ni	0.31	2.42541	0.01
		Ni-Ni	2.34	3.54182	0.01
		Ni-Ni (Ni Oxide)	4.22	3.04965	0.01
		Ni-O (Ni Oxide)	9.74	2.03870	0.01
		Ni-Au	0	2.7	0.02
2 wt. % Au/ 5 wt. % Ni SBA-15	Hydrogen	Ni-Ni	9.90	2.48262	0.01
		Ni-Ni	4.75	3.48978	0.01
		Ni-Ni (Ni Oxide)	3.27	2.93742	0.01
		Ni-O (Ni Oxide)	0.52	2.06734	0.01
		Ni-Au	0.38	2.74867	0.01

<sup>A</sup> Absorber atom

<sup>B</sup> Backscatter atom

<sup>C</sup> Coordination Number

<sup>D</sup> Bond Distance

<sup>E</sup> Debye-Waller factor

Figure 5-22 is the  $\chi(k)$   $k^2$  weighted absorbance versus  $k$  spectra (left-hand-side) and the Fourier transform magnitude versus  $R$ , distance (right-hand-side) for SiO<sub>2</sub> Au/Ni supported catalysts reduced with hydrogen.

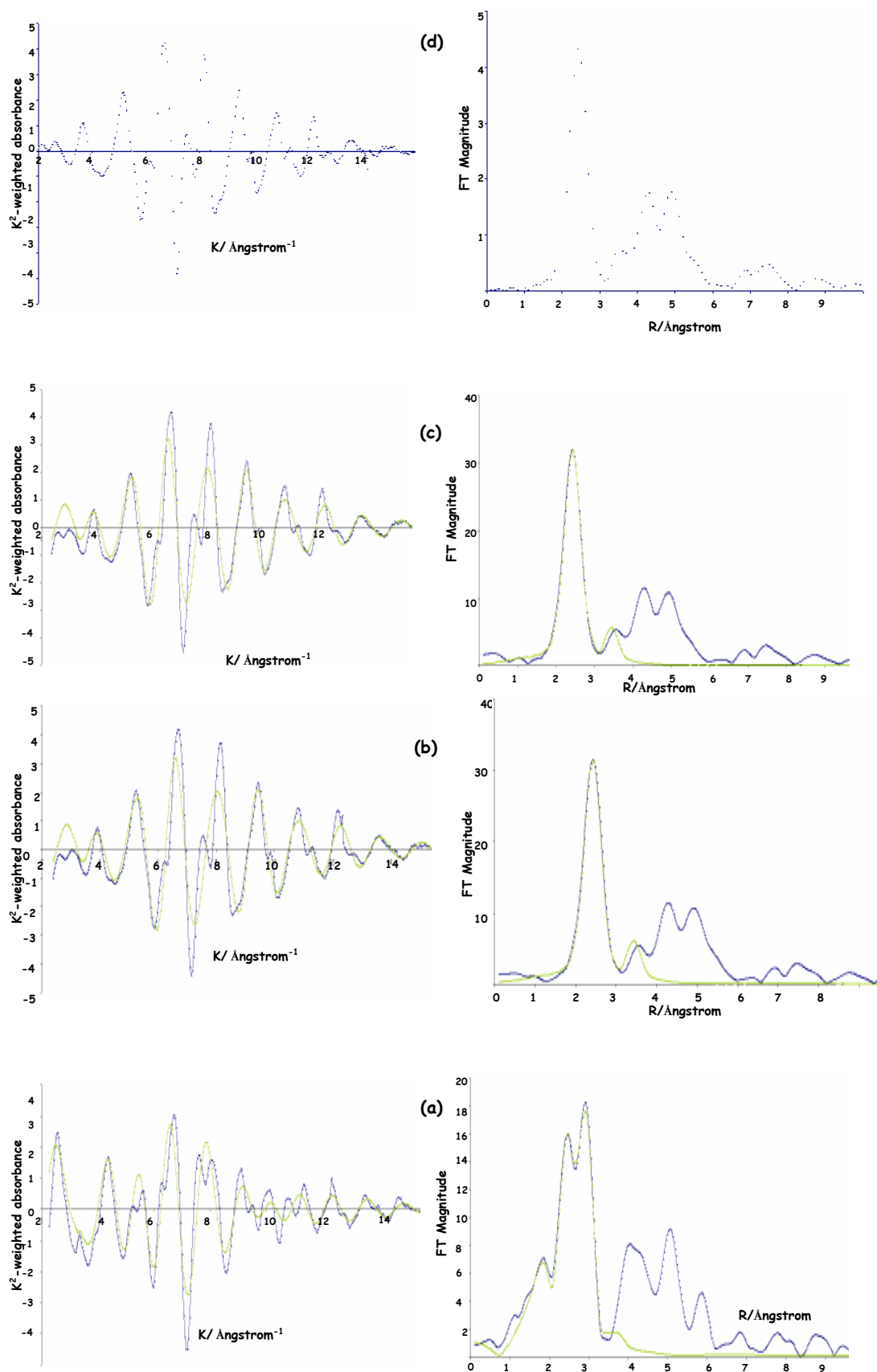


**Figure 5-22** EXAFS spectra for SiO<sub>2</sub> supported Au/Ni catalysts reduced with hydrogen. Spectra on the left are  $\chi(k)$   $k^2$  weighted absorbance versus  $k$  and spectra on the right are the Fourier transform magnitude versus distance,  $R$ . Experimental data is represented in blue and curve-fitting analysis is represented in green. **(a)** 2 wt. % Au/Ni **(b)** 4 wt. % Au/Ni **(c)** 8 wt. % Au/ 5 wt. % Ni **(d)** Ni foil.

Spectra 5-22 (a) 2 wt. % Au/Ni has three main peaks. Ni-O at 2.0 Å, first shell Ni-Ni at 2.4 Å and Ni-Ni (NiO) at 2.9 Å. The curve-fitting analysis indicates an interaction between Ni-Au with a coordination number of 2.85. This peak is not visible due to the Ni-Ni (NiO) peak. The spectra for 4 wt. % Au/Ni and 8 wt. % Au/Ni is very similar. There are two primary peaks; first shell Ni-Ni at 2.4 Å and second shell Ni-Ni at 3.4 Å. Structural parameters indicate there is no NiO or Ni-Au present. Structural disorder is low. These results support TEM evidence where there is little interaction of gold with the support at higher gold loadings. This is due to sintering of gold during thermal treatment.

Figure 5-23 is the  $\chi(k) k^2$  weighted EXAFS absorbance versus  $k$  spectra (left-hand-side) and the Fourier transform magnitude versus  $R$ , distance (right-hand-side) for SiO<sub>2</sub> Au/Ni supported catalysts reduced by hydrazine hydrate.

Both spectra (a-b) for 4 wt.% Au/Ni and 8 wt. % Au/Ni are very similar comprising mainly of Ni, NiO and an Au/Ni alloy. This supports TEM data. Ni-O is at a distance of 2.0 Å; first shell Ni-Ni at 2.4 Å and Ni-Ni (NiO) at 3.4 Å. Ni-Au is present in both catalysts at 2.8 Å, but due to the broadness of the Ni-Ni (NiO) peak cannot be distinguished clearly. A coordination number of 3.32 for 4 wt. % Au and 5.75 for 8 wt. % Au is assigned by the curve-fitting analysis. Structural disorder is low for both catalysts. There is good agreement between the experimental data and curve-fitting analysis.

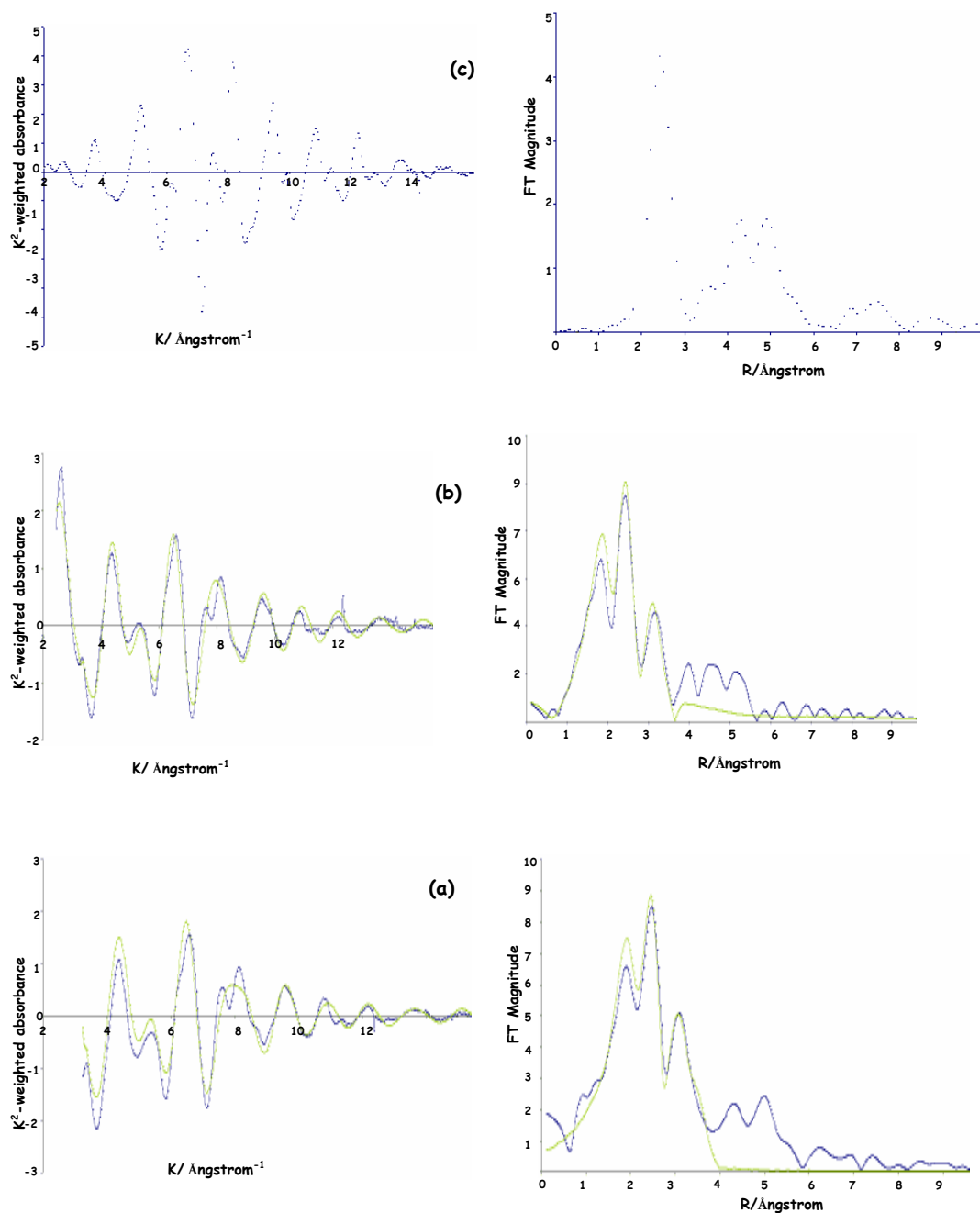


Figure 5-23 EXAFS spectra for SiO<sub>2</sub> supported Au/ Ni catalysts reduced with hydrazine hydrate. Spectra on the left are

$\chi(k)$   $k^2$  weighted absorbance versus  $k$  and spectra on the right are the Fourier transform magnitude versus

distance,  $R$ . Experimental data is represented in blue and curve-fitting analysis is represented in green. (a) 4 wt. % Au/Ni

(b) 8 wt. % Au/Ni (c) Ni foil.

Figure 5-24 is the experimental Fourier transform magnitude versus distance  $R$ , for all 1-8 wt. % Au/ 5 wt. % Ni supported catalysts. Ni foil data is also presented for comparison purposes.

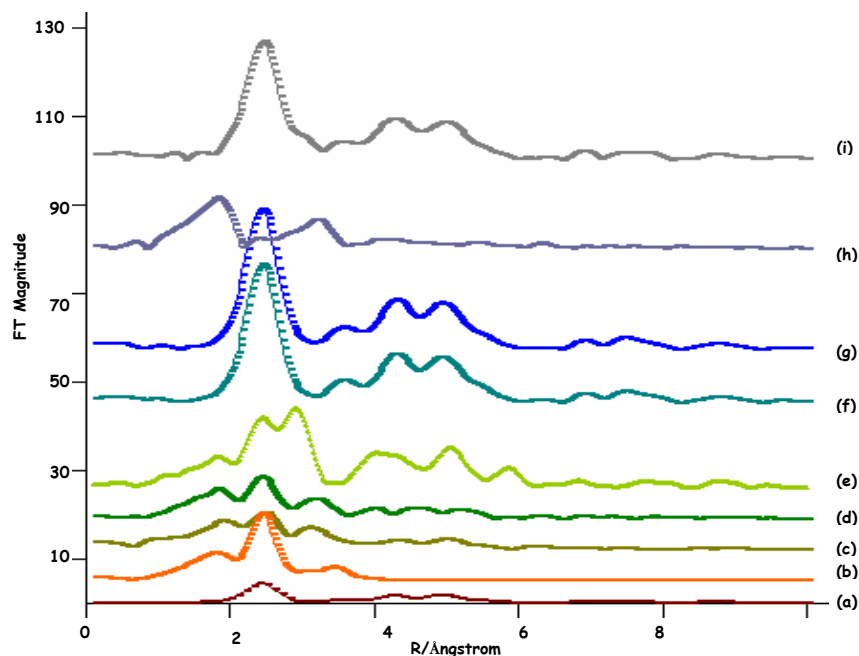


**Figure 5-24** Fourier transform magnitude Ni K-edge experimental EXAFS spectra for (a) Nickel foil (b) 10 wt. % Ni/ SBA-15/ hydrazine (c) 4 wt. % Au/Ni/ SiO<sub>2</sub>/ hydrazine (d) 8 wt. % Au/Ni/ SiO<sub>2</sub>/ hydrazine (e) 2 wt. % Au/Ni/ SiO<sub>2</sub>/ hydrogen (f) 4 wt. % Au/Ni/ SiO<sub>2</sub>/ hydrogen (g) 8 wt. % Au/Ni/ SiO<sub>2</sub>/ hydrogen (h) 1 wt. % Au/Ni/ SBA-15/ hydrogen (i) 2 wt. % Au/Ni/ SBA-15/ hydrogen.

The main conclusions drawn the EXAFS data includes:

1. There is good agreement between the EXAFS and TEM & EDS data.
2. NiO is present with hydrazine reduction and not with hydrogen reduction.
3. Reduction with hydrazine hydrate produces a Ni-Au interaction; reduction with hydrogen at low gold loadings produces a Ni-Au interaction and none at higher gold loadings. This can be attributed to sintering during thermal treatment.

### 5.3.3 AAS & GC STUDIES

Modification of the bimetallic catalysts with (R, R)-tartaric acid is a corrosive process and is characterised by the leaching of nickel into the modifying solution. Analysis of post-modification solutions as a function of gold loading in these bimetallic catalysts was investigated with atomic absorption spectroscopy. The corrosive nature of the modification process results in the extraction of nickel nanoparticles from the support and is detrimental to the enantioselective ability and lifetime of the catalyst. Leaching of nickel is evident as the colour of the modification solution changes from clear to olive green. Table 5-2 presents the extent of leached nickel (ppm) after modification and percentage enantioselectivities (ee) and conversion of MAA after hydrogenation of the bimetallic Au/Ni catalysts supported on SBA-15 and SiO<sub>2</sub> as a function of reduction method.

Examining disordered SiO<sub>2</sub> supported bimetallic catalysts reduced with hydrazine hydrate; a linear decrease in the amount of nickel leached as the gold loading is increased is evident. The 1 wt. % Au catalyst leached 602 ppm of nickel and gave an enantioselectivity of 2.1 %. An increase of gold content to 8 wt % reduced the quantity of nickel leached to approximately one third of the aforementioned value. Simultaneously, a substantial increase in enantioselectivity to 10.0 % was achieved. No quantity of leached nickel or enantioselectivity for pure nickel catalysts could be determined. These catalysts could not be reduced to a metallic state with hydrazine hydrate. This is attributed to the high surface area of the support and will be further discussed in section 5.4.4.

SBA-15 supported catalysts reduced with hydrazine hydrate exhibit a similar trend; with increased gold loading, leaching of nickel decreases and enantioselectivity increases. No quantity of leached nickel or enantioselectivity for monometallic nickel catalysts could be determined. These catalysts could not be reduced with hydrazine hydrate. This will be further discussed in section 5.4.4. An addition of 1 wt. % Au to monometallic 5 wt. % Ni

leached 443 ppm of nickel giving a corresponding ee of 2.5 %. Further increasing the gold loading to 4 and 8 wt. % gave an ee of 8.1 % and 5.9 % respectively. The amount of leached nickel is similar for both catalysts, approximately 200 ppm. It is postulated that increasing the amount of gold present in SBA-15 catalysts to 8 wt. % may have caused pore blockage as the gold particles elongate along the channel axis. This is detrimental to the catalytic activity as the chiral molecules cannot access the nanoparticles.

SiO<sub>2</sub> supported bimetallic Au/Ni catalysts reduced with hydrogen at 823 K gave comparable ee's to its counterpart; hydrazine hydrate. Monometallic nickel catalysts were successfully reduced via hydrogen and leached 959 ppm for 10 wt % Ni and 593 ppm for 5 wt % Ni catalysts. Upon addition of 1 wt. % gold to the latter catalyst leaching was substantially reduced to 194 ppm with a corresponding enantioselectivity of 3.7 %. This comparable to 5 wt % Ni whose enantioselectivity was 3.7 %. Addition of 2 wt % gold leaches 224 ppm of nickel and gave an enantioselectivity of 1.3 %. Further increasing the gold loading to 4 and 8 wt % results in leaching of 583 ppm and 611 ppm respectively, producing enantioselectivities that are similar to monometallic 10 wt % Ni. EXAFS data for these systems shows no gold/nickel interaction and no NiO present. These catalysts are effectively monometallic nickel. HRTEM micrographs for this system showed extensive sintering of gold. With increasing gold loading, less alloyed Au/Ni particles were found within the silica support. This is due to the weak interaction between silica and gold.

**Table 5-2** Quantity of leached nickel (ppm) of various bimetallic Au/Ni silica supported catalysts after modification and percentage enantioselectivity (% ee) post-hydrogenation.

wt. % Au	wt. % Ni	Support	Reduction <sup>A</sup>	Leached Ni (ppm) <sup>B</sup>	% ee <sup>C</sup>	% conversion of MAA
-	5	SiO <sub>2</sub>	Hydrazine	-	-	-
-	10	SiO <sub>2</sub>	Hydrazine	-	-	-
1	5	SiO <sub>2</sub>	Hydrazine	602	2.1	83
2	5	SiO <sub>2</sub>	Hydrazine	381	3.5	50
4	5	SiO <sub>2</sub>	Hydrazine	271	3.9	56
8	5	SiO <sub>2</sub>	Hydrazine	202	10.0	47
-	5	SiO <sub>2</sub>	H <sub>2</sub>	593	3.7	98
-	10	SiO <sub>2</sub>	H <sub>2</sub>	959	5.9	99
1	5	SiO <sub>2</sub>	H <sub>2</sub>	194	3.7	-
2	5	SiO <sub>2</sub>	H <sub>2</sub>	224	1.3	52
4	5	SiO <sub>2</sub>	H <sub>2</sub>	583	4.8	-
8	5	SiO <sub>2</sub>	H <sub>2</sub>	611	5.3	-
-	5	SBA-15	Hydrazine	-	-	-
-	10	SBA-15	Hydrazine	-	-	-
1	5	SBA-15	Hydrazine	443	2.5	88
2	5	SBA-15	Hydrazine	321	3.9	68
4	5	SBA-15	Hydrazine	201	8.1	85
8	5	SBA-15	Hydrazine	247	5.9	80
-	5	SBA-15	H <sub>2</sub>	456	3.8	89
-	10	SBA-15	H <sub>2</sub>	648	6.4	97
1	5	SBA-15	H <sub>2</sub>	293	2.1	93
2	5	SBA-15	H <sub>2</sub>	273	2.6	-
4	5	SBA-15	H <sub>2</sub>	204	5.9	60
8	5	SBA-15	H <sub>2</sub>	308	4.3	71

<sup>A</sup> Hydrogen reduction temperature was 823 K.

<sup>B</sup> The silica supported catalysts were modified with (*R,R*)-tartaric acid and sodium bromide and maintained at pH 5.1 with sodium hydroxide for an hour and a half at 373 K.

<sup>C</sup> 0.5 grams of supported catalyst, 20 mL of THF and 2.5 grams of methylacetoacetate was hydrogenated at 353 K for 24 hours. The pressure of hydrogen was 10 bar.

SBA-15 silica supported catalysts that were hydrogen reduced gave lower enantioselectivities compared to reduction with hydrazine hydrate. The catalyst with a Ni loading of 5 wt. % leached 456 ppm of nickel and gave an enantioselectivity of 3.8 %. Increasing nickel to 10 wt. % leached 648 ppm of nickel and gave an enantioselectivity of 6.4 %. Addition of gold to this system reduced nickel leaching and gave measurable enantioselectivities. For example, addition of 4 wt % gold to this catalyst reduced the nickel leaching to 204 ppm and with corresponding enantioselectivity of 5.9 %. However, a further increase of gold to 8 wt % increased leaching to 308 ppm and reduced enantioselectivity to 4.3 %. This can be partly attributed to sintering of gold during thermal treatment. While an increase in leached nickel and reduced enantioselectivity occurred, this is still substantially better than its counterpart SiO<sub>2</sub> at this gold loading. This indicates that SBA-15 was able to better contain the nanoparticles during thermal treatment compared to SiO<sub>2</sub>.

The main conclusions from AAS & GC studies include:

1. The presence of gold in this bimetallic system had a significant effect on the extent of nickel leaching; reducing it to half the original amount leached in some cases.
2. Hydrazine hydrate reduction regardless of which support gave higher enantioselectivities and successfully reduced nickel leaching. Reduction with hydrazine hydrate does not induce sintering like hydrogen reduction at 853 K. This in turn led to gold being successful encapsulation within the silica supports.
3. Hydrogen reduced SiO<sub>2</sub> catalysts successfully reduced the leaching of nickel upon addition of gold at low loadings. Higher loadings gave enantioselectivities and quantities of leached nickel similar to those of monometallic nickel due to the sintering of gold.

4. Hydrogen reduced SBA-15 catalysts gave similar enantioselectivities to SiO<sub>2</sub>. However, SBA-15 at higher gold loadings was better able withstand the sintering of gold and contain the nanoparticles within its mesoporous channels.

## 5.4 DISCUSSION

### 5.4.1 PARTICLES SIZE & MORPHOLOGY VERSUS PREPARATION METHOD

Overall, reduction with hydrazine hydrate produces a combination of Ni, NiO, Ni/NiO core/shell structures, alloyed Au/Ni particles and large faceted Au particles. The latter being predominantly located on the surface of the silica supports. There was no evidence of Au/Ni core/shell structures. Reduction with hydrazine hydrate gives a wide range of particle sizes varying from 3-25 nm in diameter. The particles were found to have different geometrical shapes ranging from spherical, hexagonal to large faceted particles. Particles smaller than 5 nm tended to be ill-defined and more cluster-like in appearance. Gold particles tended to spherical when less than 15 nm in diameter and faceted when greater than 15 nm in diameter. Nickel and nickel oxide particles were mainly spherical ranging in size from 2-15 nm. Alloyed Au/Ni particles were also spherical and ranged in diameter from 3-9 nm.

SiO<sub>2</sub> supported Au/Ni bimetallic catalysts reduced with hydrazine hydrate gave uniformly and homogeneously dispersed particles. The majority of the particles upon reduction were located within the support. Modification of these catalysts induced massive leaching of nickel nanoparticles. This was clearly evident with HRTEM as the particles could be imaged residing on the exterior of the support. Hydrogenation of these catalysts induced agglomeration of these leached nanoparticles.

SBA-15 supported Au/Ni bimetallic catalysts reduced with hydrazine hydrate had clusters of agglomerated particles to the exterior of the support for those particles too large to enter the nano-channels. This increased with higher gold loadings. Many faceted gold particles ~15-25 nm in diameter were situated directly on the surface of the support. Within the mesoporous channels, particles were uniformly and homogeneously dispersed with an average diameter of ~6-9 nm. Particles tended to be spherical while others clustered together and were elongated along the spatial direction of the channel axis. These varied in length from 10-30 nm. This suggests that the metal particles are in contact with the channel walls and that, if more gold is available than necessary for the formation of a spherical particle with the diameter of the channel, the particle will elongate with the growth directed by the spatial restrictions of the channel walls. It also implies the SBA-15 channel walls are strong enough to contain the spherical particles, directing them along the channel axis. This is in agreement with Chao and co-workers who incorporated gold into mesoporous SBA-15 functionalized with positively charged groups. The gold catalyst was reduced with sodium boride.<sup>[37]</sup>

Calcination of the Au/Ni bimetallic catalysts in air for five hours and reduction in hydrogen at 823 K for two hours produces an array of Ni, NiO, Au and alloyed Au/Ni particles for both SBA-15 and SiO<sub>2</sub>. No core/shell structures could be clearly determined; however some nickel particles had a thin surrounding layer. It is postulated that the nickel particles once removed from the furnace were stabilised by a thin oxide layer which could not be readily observed by TEM.

The particles were found to have different geometrical shapes ranging from spherical, hexagonal, to large faceted particles. Smaller particles less than 5 nm in diameter are poorly defined and cluster-like in appearance. Reduction with hydrogen gave a wide range of particle sizes varying from 3-25 nm in diameter with clusters of ~500 nm observed to

the exterior of mesoporous SBA-15. SiO<sub>2</sub> supported catalysts exhibited a wider range of particles sizes, with nanoparticles ranging from 3-65 nm in diameter and clusters as large as ~500 nm to the exterior of the support. Predominantly, Ni particles were very large ~25-65 nm in diameter.

With hydrogen reduction two processes occurred; deposition of particles to the external surface and secondly confinement within the support. In the former case, severe sintering due to thermal treatment is inevitable due to poor metal-support interaction and the presence of chloride which promotes mobility of the gold particles. Gold chloride was used as a precursor and chloride is known to be detrimental in obtaining small gold particle sizes.<sup>[21]</sup> Large clusters to the exterior of the support ranging up to ~500 nm in diameter were observed. As a consequence; both mesoporous SBA-15 and SiO<sub>2</sub> supported catalysts did not exhibit many large faceted gold particles as these had agglomerated into large clusters. In the case of confinement within support; these particles are homogeneously and uniformly dispersed even when subjected to thermal treatment. Majority of these particles were spherical in shape and others (in the case of SBA-15) were elongated along the channels walls ~10-30 nm in length. Au/Ni alloy formation was favoured at low gold loadings with hydrogen reduction. With regard to SBA-15; the nano-channels were able to confine the nanoparticles at low loadings and less so at higher gold loadings.

#### **5.4.2 COMPOSITION OF NANOPARTICLES VERSUS PREPARATION METHOD**

Gold cannot form a bulk alloy with nickel at room temperature due to a large miscibility gap. However, surface alloys are energetically favourable as proven by STM studies.<sup>[22-24]</sup> Chapter 3 of this thesis also provided evidence of surface alloy formation. Deposition of nickel onto Au {111} and subsequent annealing demonstrated surface alloy formation

which was stable up to 570 K as measured by MEIS. The synthesis of Au/Ni bimetallic supported catalysts can potentially produce two types of structures. Core/shell; where gold coats a nickel particle or alternatively an Au/Ni surface alloy. The latter is an intermixing of gold with the outermost layer of the nickel particle forming a surface alloy. TEM and EXAFS data point to alloy formation. The extent of alloy formation in this study primarily depended upon gold loading and reduction method implemented.

Reduction of the Au/Ni bimetallic catalysts with hydrazine hydrate for both supports produces a mixture of Ni, NiO, Ni/NiO core/shell structures, alloyed Au/Ni particles and large faceted Au particles. No interaction between Au and NiO was observed with TEM. EXAFS studies of SiO<sub>2</sub> supported hydrazine hydrate reduced catalysts revealed a Ni-Au interaction for 2, 4 and 8 wt % Au/Ni catalysts. Increasing the gold loading gives a general decrease in nickel leaching while concurrently increases enantioselectivity. Overall, the highest enantioselectivities was achieved with this system and reduction method.

Reduction of the Au/Ni bimetallic catalysts with hydrogen for both supports produces a mixture of Ni, NiO, large faceted Au particles and alloyed Au/Ni particles. Au/Ni alloy formation was found to be dependent on gold loading. No interaction between Au and NiO was observed with TEM. In addition, no Ni/NiO core/shell structures could be clearly determined. However, some nickel particles did have a thin surrounding layer but this could not be resolved clearly. As mentioned previously, this could have originated from removal of the catalysts from the furnace enabling a thin oxide layer to coat the particles.

The dependency of alloy formation with gold loading when hydrogen reduced is related to use of chloride in the gold precursor which induces sintering during thermal treatment. Overall, calcination in air for five hours at 823 K and reduction in hydrogen for two hours at 823 K was instrumental in creating large particles. It is probable that calcination for five

hours was too severe and promoted mobility of the particles which in turn led to extensive sintering of gold. With higher gold loadings, it is probable that the precursor is in less contact with the support and consequently migrates more easily which accounts for the larger particle size. This in turn can lead to agglomeration of clusters ranging up to ~500 nm in diameter. At very high gold loadings of 8 wt. % this had an adverse effect with little to no alloy formation as determined with TEM and EDS.

EXAFS supported this phenomenon with hydrogen reduced Au/Ni bimetallic SiO<sub>2</sub> supported catalysts (table 5-1). Low gold loadings of 2 wt. % led to a Ni-Au interaction with a coordination number of 2.85. This catalyst had mixed quantities of Ni and NiO present also and reduced leaching to almost half that of its monometallic nickel counterpart (table 5-2). Increasing the gold loading to 4 and 8 wt. % led to no Ni-Au interaction. TEM shows large clusters ~500 nm to the exterior of the support. Consequently, these bimetallic catalysts had effectively only nickel particles within the support and acted accordingly; leaching substantial amounts of nickel after chiral modification comparable to that of monometallic 5 wt. % Ni.

Of interest, Heald and co-workers examined MgAl<sub>2</sub>O<sub>4</sub> supported Au-Ni catalysts for hydrocarbon steam reforming.<sup>[38]</sup> Characterisation with Au L<sub>III</sub> -edge EXAFS showed that with increasing gold loading (0.2-1 % Au) a decrease in Au-Ni interaction occurred with a subsequent increase in Au-Au interaction.

For all Au/Ni bimetallic catalysts regardless of support, HRTEM micrographs showed no change in morphology or particle size after chiral modification or hydrogenation procedures. However, the composition of such catalysts did alter as proven by EDS for hydrazine hydrate reduced catalysts (figures 5-7, 5-11). There was a sizeable decrease of nickel present in the EDS spectra after chiral modification. A further decrease in nickel

was evident after hydrogenation of the catalysts. The latter suggesting the participation of nickel in the hydrogenation reaction.

Due to extensive sintering of gold with hydrogen reduction for both supports; EDS spectra post-modification and hydrogenation were difficult to interrupt and were consequently not included.

For all silica supported bimetallic catalysts; predominantly the (111) and (200) planes of Ni, NiO, Au and alloyed Au/Ni particles were imaged with TEM. This stems from Bragg's Law where the structure of cubic crystals imposes selection rules that determine which x-ray beams are scattered from a crystal lattice. Using Bragg's Law, the lattice spacing of cubic crystals can be determined and from this one can derive selection rules for the Miller indices of different cubic Bravais lattices.

### 5.4.3 INFLUENCE OF SUPPORT

The influence of the support is paramount in the synthesis of these Au/Ni catalysts. It not only dictates particle growth and dispersion, it also affects the catalyst resistance to sintering. With mesoporous SBA-15, particles tended to be spherical but cluster together along the channel axis reaching lengths of ~60 nm. This has a twofold effect. Firstly, while it is commendable that the channel walls were able to contain these particles and direct them along the channel axis, it questions the ability of the chiral modifier (*R,R*)-tartaric acid to access them during the modification process and raises the prospect of pore blockage. Adsorption isotherms would be a potential method to determine the latter.

SiO<sub>2</sub> conversely, when reduced with hydrazine hydrate had better dispersions of gold/nickel and consequently was more selective than SBA-15. An enantioselectivity of 10.0 % was attained for 8 wt. % Au/Ni with 202 ppm of nickel leached. When reduced with hydrogen, SiO<sub>2</sub> at high gold loadings of 4-8 wt. % was unable to prevent the gold

particles from sintering. This in turn led to extensive leaching 583 ppm and 611 ppm of nickel with corresponding enantioselectivities of 4.8 and 5.3 % respectively due to the lack of gold present. EXAFS & TEM analysis showed no alloy formation at these loadings when reduced with hydrogen. In contrast, SBA-15 when hydrogen reduced at higher gold loadings was better able to confine the particles within the nano-channels, leaching half the amount of nickel compared to its counterpart.

#### **5.4.4 INFLUENCE OF GOLD ON NI –BASED CATALYSIS**

This study examined silica supported bimetallic Au/Ni preparative routes as a function of reduction method. The purpose of this study was to ascertain the potential use of gold in this catalytic system, focusing on the retardation of nickel leaching. It was found that the presence of gold in this system had a profound effect. Overall, with increasing gold loading, less nickel was leached into the modifying solution. This is of huge importance as it extends the lifetime of the catalyst. Concurrently, an increase in enantioselectivity was achieved. The highest enantioselectivity achieved was 10.0 % for 8 wt. % Au/5 wt. % Ni/SiO<sub>2</sub> reduced with hydrazine hydrate. It is thought the larger particle sizes produced with the SiO<sub>2</sub> support (3-65 nm) is a contributing factor.

The low enantioselectivities achieved for aforementioned catalysts is related to the low nickel loadings used. Common dispersions for nickel catalysts are 2-5 wt. % with nanoparticles ranging from 5-25 nm. It is generally believed that there is an optimum beyond which an increase in nickel content does not produce any increased selectivity. This is typically between 15-20 wt. %. However, methylacetoacetate hydrogenation is an exception. Many studies have investigated the effect of crystallite size of nickel catalysts on enantioselectivity. The reaction is therefore structure sensitive. Catalysts with a larger crystallite size ~50 nm had higher enantioselective abilities. This is attributed to tartaric

acid adsorbing strongly and more regularly on ordered nickel atoms on the surface of a large crystallite sizes of nickel.<sup>[28]</sup> The nickel loadings for such catalysts are usually 40-60 wt %.

Gold influenced the activity of the silica supported bimetallic Au/Ni catalysts. It is evident from table 5-2 that the presence of gold decreased the activity of catalysts at higher gold loadings particularly when supported on SiO<sub>2</sub>.

Very surprisingly, hydrazine hydrate could not reduce 5 or 10 wt. % nickel catalysts supported on SBA-15 or SiO<sub>2</sub>. The reduction procedure of these monometallic catalysts was repeated on numerous occasions and each time it was noted that the nanoparticles never changed colour from blue to translucent to black. Black is an indication of metallic nickel particles.

Bettahar and co-workers also experienced this phenomenon. This group report that the reduction of nickel acetate by aqueous hydrazine hydrate is prevented due to use of a silica support with high surface area.<sup>[30-33]</sup> A similar observation was reported by Bozon-Verduraz and co-workers for PdCl<sub>2</sub> reduction by hydrazine in the presence of high surface area silica (380 m<sup>2</sup>/g<sup>-1</sup>).<sup>[39]</sup> Both groups attributed this phenomenon to the lack of defects sites for the catalytic reduction of the precursor ions. The surface acidity of high surface area silica may also be a contributing factor. Hydrazine hydrate reduction requires a pH of 10-12 for the reduction process to proceed and it is possible the acidity of these silica supports may be preventing nickel ion reduction. The supports in question have a surface area of 280 m<sup>2</sup>/g for SiO<sub>2</sub> and between 250 to 600 m<sup>2</sup>/g for SBA-15.

From this study, it was found that the addition of gold to this nickel system led to the successful reduction of the bimetallic nanoparticles within the high surface area silica supports with hydrazine hydrate. It is postulated that raising the pH to 10-12 facilitated

the interaction of the alloyed Au/Ni particles with the silica support enabling the reduction to proceed. Typically, the deposition of negatively charged metal precursors ( $[\text{AuCl}_4]^-$  in this instance) on negatively charged silica surfaces leads to poor support-metal interaction which in turn leads to the formation of large particles. However, Ichikawa and co-workers found that impregnating gold onto a mesoporous HMM-2 support for 24 hrs, pH adjusted to 11.7 led after hydrogen reduction at 473 K to 3.2 nm gold particles.<sup>[40]</sup>

In this study, regardless of support or reduction method; alloyed Au/Ni nanoparticles were imaged in copious amounts by HRTEM ranging in diameter from 3-9 nm and were successfully encapsulated within the silica supports. No alloyed Au/Ni particles were captured by TEM residing on the surface of these supports. Of interest, the bimetallic catalysts upon impregnation varied in colour intensity. Various shades of yellow were obtained depending on the concentration of gold present. During reduction with hydrazine hydrate the bimetallic catalysts turn from yellow (indication of  $\text{Au}^{\text{III}}$ ) to purple (presence of  $\text{Au}^0$ ).<sup>[21]</sup>

## 5.5 IMPLICATIONS FOR ENANTIOSELECTIVE CATALYSIS

The enantioselective hydrogenation of methylacetoactate to *R*-methyl-3-hydroxybutyrate over modified Raney nickel catalysts is a peculiar catalyst in that the degree of enantioselectivity is hugely dependent upon the modification conditions. The effects of temperature, time, pH and use of co-modifiers are all intertwined.<sup>[36]</sup> In addition, unmodified nickel sites on the catalyst surface are known to catalyse a racemic reaction competitively with the enantioselective reaction; lowering the overall enantioselective yield.<sup>[36]</sup> Modification of the nickel catalysts is a corrosive process and is prone to the leaching of nickel into the modifying solution. This lowers the lifetime of the catalyst with

the added burden that nickel waste is detrimental to the environment and costly to dispose of. This is one of the many factors hindering the industrial scale up of these catalysts.

The aim of this study was to ascertain the potential application of gold to this system in a bid to quench the unmodified nickel sites and retard nickel leaching. Since Raney nickel systems have high enantioselective capabilities but low activities; the application of alternative supports is a formidable task. Silica supports were implemented in this study due to their inert character which enables a detailed characterisation of the nanoparticles encapsulated within these supports. While, the presence of alloyed Au/Ni particles in this catalytic system proved to be less active; they certainly demonstrated to be more robust to nickel leaching than monometallic nickel catalysts. The author is fully aware of the shortcomings of the present study i.e. low enantioselectivities but believes with further work examining the modification conditions and reduction methods (e.g. use of lower temperatures in hydrogen reduction to reduce the sintering of gold); the potential use of this silica supported bimetallic system in enantioselective catalysis could be immense.

## 5.6 SUMMARY

Bimetallic Au/Ni nanoparticles supported on amorphous silica and mesoporous SBA-15 were synthesised in this study as a function of reduction method. These catalysts were then modified by the adsorption of the chiral ligand, (*R,R*)-tartaric acid and tested for their activity and enantioselectivity with respect to methylacetoacetate hydrogenation. EXAFS and TEM proved to be a powerful combination in the characterisation of the prepared bimetallic Au/Ni catalysts. An array of Ni, NiO, Au and alloyed Au/Ni particles were successfully encapsulated within the silica supports. With hydrazine reduction, particle sizes ranged from 3-25 nm in diameter. For hydrogen reduction, particles sizes varied from 3-65 nm with clusters up to ~500 nm in diameter situated on the surface of the silica

supports. Nickel leaching was clearly evident after the chiral modification process as captured by HRTEM.

Reduction with hydrazine hydrate produces a Ni-Au interaction as confirmed by EXAFS. Conversely, EXAFS data indicated a Ni-Au interaction at low gold loadings and none at higher gold loadings for SiO<sub>2</sub> supported catalysts when reduced with hydrogen. This is attributed to the sintering of gold during thermal treatment.

AAS studies illustrated gold's profound effect on the extent of nickel leaching; reducing to half the amount of monometallic nickel in some cases while concurrently increasing the enantioselectivity. Overall, the measured enantioselectivities were low and this can in part be attributed to the small nickel loadings used. The presence of gold lowered the activity of the catalysts when supported on SiO<sub>2</sub>.

## BIBLIOGRAPHY

- [1] [www.rsc.org/pdf/books/colloidsc.pdf](http://www.rsc.org/pdf/books/colloidsc.pdf)
- [2] G. Schmid. *Cluster and Colloids, From theory to Applications*. VCH. (1995) 484.
- [3] J. H. Sinfelt. *J. of Cat.* **29** (1973) 309.
- [4] C. T. Campbell. *Annu. Rev. Phys. Chem.* **41** (1990) 777.
- [5] N. Toshima & T. Yonezawa. *New J. Chem.* (1998) 1179.
- [6] K. Chao, M. Cheng, Y. Ho & P. Liu. *Catalysis Today*. **97** (2004) 49.
- [7] C. Yang, P. Liu, C. Chiu & K. J. Chao. *Chem. Mater.* **15** (2003) 275.
- [8] J. Zhu, Z. Konya, V. F. Puentes, I. Kiricsi, C. X. Miao, J. W. Ager, A. P. Alivisatos & G. A. Somorjai. *Langmuir*. **19** (2003) 4396.
- [9] C. Yang, H. Wustefeld, M. Kalwei & F. Schuth. *Studies Sur. Sci. & Catal.* **154** (2004) 2574.
- [10] Z. Konya, V. F. Puentes, I. Kiricsi, J. Zhu, J. W. Ager, M. K. Ko, H. Frei, P. Alivisatos & G. A. Somorjai. *Chem. Mater.* **15** (2003) 1242.
- [11] W. R. Glomm & G. Oye. *J. of Dispersion Sci. & Tech.* **26** (2005) 729.
- [12] A. Taguchi & F. Schuth. *Microporous & Mesoporous Materials*. **77** (2005) 1.
- [13] C. T. Kresge, M. E. Leonowicz, W. J. Roth, J. C. Vartuli & J. S. Beck. *Nature*. **359** (1992) 710.

- [14] J. S. Beck, J. C. Vartuli, W. J. Roth, M. E. Leonowicz, C. T. Kresge, K. D. Schmitt, C. T. W. Chu, D. H. Olson, E. W. Sheppard, S. B. McCullen, J. B. Higgins & J. L. Schlenker. *J. Am. Chem. Soc.* **114** (1992) 10834.
- [15] T. Linssen, K. Cassiers, P. Cool & E. F. Vansant. *Advances in Colloid & Interface Science.* **103** (2003) 121.
- [16] Q. Huo, R. Leon, P. M. Petroff & G. D. Stucky. *Science* **268** (1995) 1324.
- [17] D. Zhao, Q. Huo, J. Feng, B. F. Chmelka & G. D. Stucky. *J. Am. Chem. Soc.* **120** (1998) 6024.
- [18] L. van de Water & T. Maschmeyer. *Topics in Catalysis.* **29** (2004) 67.
- [19] D. Zhao, J. Feng, Q. Huo, J. Feng, N. Melosh, G. H. Fredrickson, B. F. Chmelka & G. D. Stucky. *Science.* **279** (1998) 548.
- [20] M. Haruta & M. Date. *Applied Catalysis.* **222** (2001) 427.
- [21] G. C. Bond, C. Louis & D. T. Thompson. *Catalysis by Gold. Catalytic Science Series- vol 6* (2006). Series Editor: G. J. Hutchings.
- [22] F. Basenbacher, I. Chorkendorff, B. S. Clausen, B. Hammer, A. M. Molenbroek, J. K. Norskov & I. Stensgaard. *Science.* **279** (1998) 1913.
- [23] I. Chorkendorff, J. K. Norskov & B. S. Clausen. *J. Phys. Chem. B.* **105** (2001) 5450.
- [24] L. Pleth Nielsen, F. Basenbacher, I. Stensgaard & E. Laegsgaard. *Phys. Rev. Lett.* **71** (1993) 754.
- [25] N. C. Triantafyllopoulos & S. G. Neophytides. *J. Catal.* **239** (2006) 187.

- [26] G. Yuan, J. Lopez, C. Louis, L. Delannoy & M. A. Keane. *Catal. Commun.* **6** (2005) 555.
- [27] G. Yuan, C. Louis, L. Delannoy & M. A. Keane. *J. Catal.* **247** (2007) 256.
- [28] Y. Izumi. *Advan Cat.* **32** (1983) 215.
- [29] G. Schmid, A. Lehnert, J. Malm & J. Bovin. *Angew. Chem. Int. Ed. Engl.* **30** (1991) 7.
- [30] A. Boudjahem, S. Monteverdi, M. Mercy, D. Ghanbaja & M. M. Bettahaer. *Catal. Lett.* **84** (2002) 115.
- [31] A. Boudjahem, S. Monteverdi, M. Mercy & M. M. Bettahaer. *Catal. Lett.* **97** (2004) 177.
- [32] A. Boudjahem, S. Monteverdi, M. Mercy & M. M. Bettahaer. *Langmuir.* **20** (2004) 208.
- [33] A. Boudjahem, S. Monteverdi, M. Mercy & M. M. Bettahaer. *J. Catal.* **221** (2004) 325.
- [34] PhD. Thesis. Dr. R. Hodgkins. University of St- Andrews.
- [35] D. B. Williams & C. B. Carter. *Transmission Electron Microscopy: Basics*. Springer Publications. 1998.
- [36] J. W. Niemantsverdriet. *Spectroscopy in Catalysis; An Introduction*. Wiley-VCH. 2006. ISBN 978-3-527-31651-9.
- [37] C. Yang, M. Kalwei, F. Schuth & K. Chao. *Applied Catalysis A: General.* **254** (2003) 289-296.

- [38] Y. Chin, D. L. King, H. Roh, Y. Wang & S. M. Heald. *J. Catal.* **244** (2006) 153-162.
- [39] A. Bensalem, G. Shafeev & F. Bozon-Verduraz. *Catal. Lett.* **18** (1993) 165-171.
- [40] A. Fukuoka, H. Araki, J.I. Kimura, Y. Sakamoto, T. Higuchi, N. Sugimoto, S. Inagaki & M. Ichikawa. *J. Mater. Chem.* **14** (2004) 752.

# Chapter 6

## *Conclusions and Outlook*

### **SYNOPSIS**

*The overall conclusions of this research project are present in the following Chapter. Future work is discussed.*

## 6.1 CONCLUSIONS

This research forms part of a larger project aimed at the creation of selective Au/Ni catalysts in relation to the nickel catalysed enantioselective hydrogenation of  $\beta$ -ketoesters. A range of Au/Ni catalysts were synthesised and tested for their activity and enantioselectivity with respect to the aforementioned reaction. In addition, surface science UHV based model studies and were undertaken to investigate the submonolayer and monolayer deposited of nickel onto Au{111} and subsequent annealing to produce a range of surface and near subsurface alloys. The aforementioned surfaces were then modified with the chiral amino acid, (*S*)-glutamic. The main conclusions of this research project are as follows:

1. Ni grows via Stranski-Krastanov growth mechanism when deposited at 300 K on Au{111}. However; second layer growth begins prior to completion of the first layer; with areas of the gold surface still exposed.
2. Deposition of  $\sim 4$  ML of Ni on Au{111} and progressive annealing of the surface to 350-600 K produced a range of bimetallic surfaces manifested in the form of Moiré and triangular misfit dislocations.
3. Medium Energy Ion Scattering displayed Au/Ni alloy formation when  $\sim 8$  ML of nickel is deposited on a Au{111} surface and progressively annealed to 540 K. The compositional data for the 1-, 2- and 3-layer geometries showed a composition of 0.47 ML Au in the top surface layer. Further annealing to 570-600 K initiates the progressive reduction of nickel in the bimetallic system as it diffuses to the bulk. By 630 K, the surface resembles that of clean gold.
4. For Ni/Au surface alloys on Au{111}, the adsorption of (*S*)-glutamic acid results

in segregation of Ni to the surface. This may be beneficial in terms of the enantioselectivity of Ni/Au catalysts since chirally modified regions (which should be highly enantioselective) should be Ni rich and would therefore be anticipated to have a higher hydrogenation activity than un-modified regions (which should form a racemic mixture of products) which should be relatively enriched in Au.

5. It was shown that the amino acid, (*S*)-glutamic acid corrodes 2D nickel islands grown in the elbows of the Au{111} herringbone reconstruction and that subsequent thermal treatment results in the formation of extended 1D chains. It was concluded that the composition of these 1D chains most likely consist of nickel (II) pyroglutamate. In addition, it was shown that the extent of corrosion of the 2D islands depends strongly on their initial size. This particle size dependent behaviour may be relevant to understanding the chiral modification of nickel nanoparticles by (*S*)-glutamic acid which is an interesting example of a method of producing an enantioselective heterogeneous catalyst for the hydrogenation of  $\beta$ -ketoesters.
6. The addition of Au to the Ni catalysts strongly alters the extent to which Ni is leached from the catalysts during chiral modification and during the catalytic reaction while preserving the activity of the catalysts – this may have significant implications in terms of catalyst lifetime considerations.

## 1.1 OUTLOOK

A natural progression of this research project would be to investigate the interaction of the  $\beta$ -ketoester, methylacetoacetate with Au/Ni bimetallic surfaces modified with (*S*)-glutamic acid using a range of surface science techniques. In addition, analogous experiments involving (*R*)-glutamic acid would be of huge interest. Furthermore, the

author believes it is important to gain an atomistic picture of the solid/ liquid interface of this Au/Ni bimetallic system chirally modified with the amino acid, (*S*)-glutamic acid. Experiments utilising Electrochemical STM would also be an exciting prospect. Concerning the synthesis of Au/Ni catalysts, further work examining the modification conditions and reduction methods is essential as the potential use of this silica supported bimetallic system in enantioselective catalysis could be immense.